

Vector Wave Propagation Method

Ein Beitrag zum elektromagnetischen Optikrechnen

Inauguraldissertation

zur Erlangung des akademischen Grades
eines Doktors der Naturwissenschaften
der Universität Mannheim

vorgelegt von

Dipl.-Inf. Matthias Wilhelm Fertig

aus Mannheim

Mannheim, 2011

Dekan: Prof. Dr.-Ing. Wolfgang Effelsberg Universität Mannheim
Referent: Prof. Dr. rer. nat. Karl-Heinz Brenner Universität Heidelberg
Korreferent: Prof. Dr.-Ing. Elmar Griese Universität Siegen

Tag der mündlichen Prüfung: 18. März 2011

Abstract

Based on the Rayleigh-Sommerfeld diffraction integral and the scalar Wave Propagation Method (WPM), the Vector Wave Propagation Method (VWPM) is introduced in the thesis. It provides a full vectorial and three-dimensional treatment of electromagnetic fields over the full range of spatial frequencies. A model for evanescent modes from [1] is utilized and eligible configurations of the complex propagation vector are identified to calculate total internal reflection, evanescent coupling and to maintain the conservation law. The unidirectional VWPM is extended to bidirectional propagation of vectorial three-dimensional electromagnetic fields. Totally internal reflected waves and evanescent waves are derived from complex Fresnel coefficients and the complex propagation vector. Due to the superposition of locally deformed plane waves, the runtime of the WPM is higher than the runtime of the BPM and therefore an efficient parallel algorithm is desirable. A parallel algorithm with a time-complexity that scales linear with the number of threads is presented. The parallel algorithm contains a minimum sequence of non-parallel code which possesses a time complexity of the one- or two-dimensional Fast Fourier Transformation. The VWPM and the multithreaded VWPM utilize the vectorial version of the Plane Wave Decomposition (PWD) in homogeneous medium without loss of accuracy to further increase the simulation speed.

The analysis of sampling-induced deviations in the amplitude shows that the sampling in the aperture needs to meet the Whitaker-Kotelnikov-Shannon (WKS) sampling theorem to provide an accurate reproduction of the electromagnetic vector field. Furthermore, the accuracy of the amplitude depends on the sampling in the axis of propagation. A criterion for the sampling in the axis of propagation, considering the simulated wavelength, is proposed to minimize the deviation in the amplitude to the results from

theory. The analysis of the zero order diffraction efficiency in a discretized oblique interface shows the relationship of the amplitude deviations to the discretization in the axis of propagation. The normalized sampling rate is introduced. It provides a sampling criterion to achieve a minimum deviation of the simulated amplitude to the results from theory. A plurality of simulations of an oblique layer with different sampling rates are performed to evaluate the theory. The stability of the algorithm and the maintenance of the conservation law is analyzed by investigating the power flux. The results from the VWPM are compared to the results from theory for different polarizations, propagation angles and representative interface configurations. In agreement to the observations in several cited publications, the generation and treatment of evanescent modes is identified being critical for the stability of the algorithm and the maintenance of the conservation law. Several techniques of stabilization are presented and it is shown that the model of evanescent waves provides an elegant way to ensure stability and extend the VWPM to evanescent modes.

The VWPM is utilized to investigate the effect of micrometer gratings on the local absorption in thin film solar cells and to find a solution for an enhanced absorption over a wide range of wavelengths and spatial frequencies. In a simulation model, the angle of incidence of the electromagnetic vector wave, the period and the duty cycle of one- and two-dimensional micrometer gratings are varied to identify an optimized geometry and analyze its influence on the local absorption. The use of one- or two-dimensional gratings is part of various other research activities as published in [80, 81, 82, 83].

Zusammenfassung

Auf Basis des Rayleigh-Sommerfeld Beugungsintegrals und der skalaren *Wave Propagation Method* (WPM) präsentiert diese Arbeit die *Vector Wave Propagation Method* (VWPM). Die VWPM ist ein propagatives Simulationsverfahren zur Berechnung dreidimensionaler Vektorfelder ohne paraxiale Einschränkung und über den gesamten spatialen Frequenzbereich. Evaneszente Fourier-Moden sind nach der Theorie in [1] modelliert. Die Erweiterung der unidirektionalen zur bidirektionalen VWPM berechnet reflektierte dreidimensionale Vektorfelder über die komplexen Propagationsvektoren und die komplexen Fresnel-Koeffizienten. Spezielle Konfigurationen der komplexen Propagationsvektoren werden für die Berechnung von Totalreflexion, evaneszenter Kopplung (optischer Tunneleffekt) und zur Energieerhaltung eingesetzt (reduzierter Propagator). Die Laufzeit der VWPM ist aufgrund der Überlagerung lokal deformierter Planwellen höher als die der *Beam Propagation Method* (BPM). Der präsentierte parallele Algorithmus skaliert linear mit der Anzahl der Prozesse (Threads). Der nicht-parallelen Anteil Programmcode ist minimal und hat die Zeitkomplexität der ein- oder zweidimensionalen Fast-Fourier-Transformation. Für die Ausbreitung im homogenen Medium wird zur weiteren Reduktion der Simulationsdauer die *Plane Wave Decomposition* ohne Verlust an Rechengenauigkeit eingesetzt.

Die Analyse der Rechengenauigkeit und deren Abhängigkeit zu den Abstraten in der Apertur und entlang der Propagationsachse zeigt, dass zur exakten Reproduktion des elektromagnetischen Feldes in der Apertur das *Whitaker-Kotelnikov-Shannon* (WKS) Abtasttheorems zu berücksichtigen ist. Im Zusammenhang mit der Abtastung entlang der Propagationsachse wird die *normierte Abtastrate* mit Abtastbedingung eingeführt, um den Amplitudenfehler bei diskretisierten schrägen Grenzflächen zu minimieren.

Die Analyse der nullten Beugungsordnung des Phasenelements diskretisierter schräger Grenzfläche zeigt die Beziehung der Rechengenauigkeit zur Abtastrate. Eine Reihe von Simulationen veranschaulichen die Theorie und liefern die Überprüfung am Beispiel. Der Energiefluss durch Grenzflächen ist Grundlage für die Beurteilung der Stabilität des Algorithmus und der Energieerhaltung. Die Simulationsergebnisse für unterschiedliche Polarisierungen und Ausbreitungswinkel in repräsentativen Systemkonfigurationen werden mit den Ergebnissen der Theorie verglichen. Die vorliegende Arbeit zeigt in Übereinstimmung mit der Literatur, dass die Behandlung der evaneszenten (quergedämpften) Fourier-Moden problematisch für die Stabilität des Algorithmus und die Energieerhaltungseigenschaften ist. Die Arbeit präsentiert unterschiedliche Ansätze zur Stabilisierung und verifiziert diese qualitativ. Die Verwendung des reduzierten Propagators erlaubt die Berechnung evaneszenter Fourier-Moden und stabilisiert den Algorithmus.

Die Anwendbarkeit der VWPM wird in einem praktischen Optimierungsproblem nachgewiesen. Ziel ist die Maximierung der lokalen Absorption in Dünnschicht-Solarzellen über ein maximales Winkelspektrum durch Verwendung von optimierten resonanten Phasengittern. Anhand eines Simulationsmodells wird durch Parametervariationen eine optimierte Geometrie ermittelt. Darüberhinaus ist die Verwendung von ein- oder zweidimensionalen resonanten Phasengittern Bestandteil weiterer Forschungsaktivitäten [80, 81, 82, 83].

Vorwort

Die vorliegende Arbeit entstand in den Jahren 2007 bis 2011 neben meiner Tätigkeit als Entwicklungsingenieur in der Mikroprozessorentwicklung bei der IBM Forschung und Entwicklung GmbH in Böblingen. Die Untersuchungen zur optischen Taktverteilung in den Jahren 2005/2006 und der daraus resultierende Kontakt zum IBM Zürich Research Laboratory in Rüschlikon, sowie die Kontakte aus meiner Studienzeit an den Lehrstuhl für Rechnerarchitektur und den Lehrstuhl für Optoelektronik der Universität Heidelberg waren Ausgangspunkt für die Arbeiten zur Silizium Photonik in Böblingen und für diese Dissertation. Die Forschungsarbeit zu optischen on-chip Detektoren und die für die Detektoroptimierung nötigen Simulationen der Ausbreitung elektromagnetischer Wellen lieferte die Motivation für die vorliegende Dissertation.

Altdorf und Mannheim
März 2011

Matthias Fertig

Danksagung

Für die Unterstützung danke ich Thomas Pflüger, Dieter Wendel, Dr. Cordt Starke, Stefan Wald, Dr. Reinhard Ernst, Dr. Andre Hertwig und Dr. Peter Roth von der IBM Forschung und Entwicklung GmbH in Böblingen; sowie Dr. Thomas Morf, Dr. Nikolaj Moll, Dr. Thilo Stöferle, Dr. Jonas Weiss, Dr. Martin Schmatz, Dr. Bert Offrein und Dr. Thomas Toifl vom IBM Zürich Research Laboratory in der Schweiz für die hervorragende Zusammenarbeit. Ebenso danke ich Dr. Bastian Trauter, Max Auer und Herrn Professor Dr. Brenner vom Lehrstuhl für Optoelektronik des Zentralen Instituts für Technische Informatik der Universität Heidelberg für die hervorragende Zusammenarbeit.

Mein besonderer Dank gilt Herrn Professor Dr. Brenner für die Möglichkeit diese Dissertation zu schreiben; für die Betreuung und die zahlreichen Ideen.

Ebenso gilt mein Dank Herrn Professor Dr. Elmar Griese vom Lehrstuhl für Theoretische Elektrotechnik und Photonik der Universität Siegen für die Erstellung des Zweitgutachtens.

Vielen Dank auch an alle Kolleginnen und Kollegen des Lehrstuhls für Optoelektronik; insbesondere an Frau Dr. Xiyuan Liu für das Korrekturlesen einzelner Passagen.

Mein ganz besonderer Dank gilt meiner Mutter und meinen Brüdern Andreas und Stephan. Sie haben mir über so manche Hürde hinweg geholfen.

Contents

1	Simulation methods	7
1.1	RCWA and FDTD	10
1.1.1	Finite difference time domain method	12
1.1.2	Rigorous coupled wave analysis	14
1.2	BPM and WPM	16
1.2.1	Beam Propagation Method	18
1.2.2	Wave Propagation Method	20
1.3	Ray tracing	21
2	Fundamentals	23
2.1	The scalar and vector wave equation	25
2.1.1	Homogeneous wave equation	28
2.1.2	Propagation constant	30
2.1.3	Polarization	30
2.1.4	Transversality	32
2.2	Irradiance	33
2.3	Poynting vector	34
2.4	Power flux	35
2.5	Absorption in homogeneous media	35
2.6	Absorption in inhomogeneous media	36
2.7	Discrete Fourier transformation	38

2.7.1	Forward Fourier transformation	39
2.7.2	Inverse Fourier transformation	39
2.8	Spatial sampling and propagation angle	40
2.9	Plane Wave Decomposition	41
2.9.1	Convolution theorem	42
2.10	Reflection and transmission	43
2.11	Evanescent waves	45
2.11.1	Complex propagation constant	46
2.11.2	Evanescent decay	47
2.11.3	Energy flux of evanescent waves	48
2.11.4	Optical tunneling	49
2.11.5	Fresnel coefficients in the evanescent case	49
2.12	Reflectance and transmittance	51
3	Vector Wave Propagation Method	53
3.1	Split step propagation scheme	55
3.2	Definition of the input system	57
3.3	Scalar Wave Propagation Method	57
3.4	Vector Wave Propagation Method	59
3.4.1	Lateral field dependence	60
3.4.2	Transfer at the interface	60
3.4.3	Propagation step	62
3.5	Algorithm of the VWPM	63
3.5.1	VWPM in homogeneous media	65
3.6	Magnetic vector and Poynting vector	66
3.7	2D simulation of refraction at a prism	67
3.8	3D Simulation of a perfect asphere	70
3.9	3D Simulation of a 2D grating	71
3.10	Evanescent modes	73

CONTENTS

ix

3.10.1	Internal reflection and transmission	75
3.10.2	External reflection and transmission	77
3.10.3	Propagation of evanescent modes	78
3.10.4	Algorithm for evanescent modes	78
3.11	Simulation of evanescent waves	79
4	Vectorial split step propagation	81
4.1	Vectorial Beam Propagation Method	82
4.1.1	Transfer matrix of transmission	83
4.1.2	Diffraction in homogeneous medium	84
4.1.3	Phase adjustment in inhomogeneous medium	85
4.2	3D simulation of a 2D grating	86
5	Bidirectional Vector Wave Propagation Method	89
5.1	Bidirectional VWPM	96
5.1.1	Transfer matrix of transmission	98
5.1.2	Bidirectional propagation	98
5.1.3	Transfer matrix of reflection	99
5.2	Bidirectional algorithm	101
5.3	3D-Simulation of a 2D-grating	104
5.4	2D simulation of a dielectric boundary	107
5.5	2D simulation of a resonator	109
5.6	2D simulation of an oblique interfaces	110
5.7	Transfer of evanescent modes	112
5.8	Algorithm for evanescent modes	113
5.9	3D-Simulation of a 2D-grating with evanescent modes	114
6	Sampling	119
6.1	Sampling in the aperture	120
6.2	Sampling in the axis of propagation	124

6.2.1	Thin element analysis	125
6.2.2	Normalized sampling rate	129
6.2.3	Application of the normalized sampling rate	129
7	Conservation of energy	135
7.1	Power flux	136
7.2	Homogeneous loss- or gainless medium	136
7.2.1	TE-polarized wave	136
7.2.2	TM-polarized wave	138
7.2.3	Power flux	140
7.2.4	Total power flux	140
7.2.5	Power flux of a Gaussian beam	141
7.3	Inhomogeneous medium	142
7.3.1	Longitudinal index variations	142
7.3.2	TE-polarized waves	143
7.3.3	TM-polarized waves	146
7.3.4	Total power flux	149
7.3.5	Lateral index variation	150
7.3.6	Generation of evanescent modes in the WPM and BPM from local discontinuities	153
7.3.7	Power flux in a waveguide	155
7.4	Stabilization of the VWPM	159
7.4.1	Low pass filtering	161
7.4.2	Clipping at the evanescent boundary	166
7.4.3	Energy-balanced clipping	167
7.4.4	Clipping at the evanescent boundary in vacuum	170
7.4.5	Sampling-induced clipping	172
7.4.6	Transfer of evanescent modes	174
7.5	Homogeneous lossy- or gaining medium	177

8	Grating enhanced local absorption	179
8.1	Detection of light	181
8.2	Solar cells	183
8.3	Micro-structured geometries	186
8.4	Optimization of local absorption with the VWPM	188
8.4.1	Input system	189
8.4.2	Number of reflections	190
8.4.3	Absorption rates without a grating	191
8.4.4	One-dimensional gratings	193
8.4.5	Twodimensional gratings	197
8.4.6	Angle of incidence versus wavelength	199
8.4.7	Optimized two-dimensional grating	200
8.5	Conclusion	201
9	Summary and closing	203
9.1	Closing	209
	Appendices	210
A	Fundamentals	225
A.1	Speed of light	225
A.2	Transversality	226
A.3	Discrete spatial derivatives	227
A.4	Absorption coefficient	228
A.5	Evanescient modes	228
A.6	Snell's law	229
A.7	Total internal reflection	229
A.8	Fresnel coefficients for evanescent waves	230
A.9	Energy flux in evanescent waves	231

B	Vector wave propagation method	233
B.1	Complex Fresnel coefficients of transmission	233
B.2	Transfer matrix of transmission	235
B.3	Magnetic vector	237
B.4	Energy Flux	238
B.5	Fresnel coefficients of reflection	239
B.6	Transfer matrix of reflection	240
B.7	Energy flux of a TE-polarized wave in homogeneous medium	242
B.8	Energy flux of a TM-polarized wave in homogeneous medium	243
C	Multithreaded bidirectional VWPM	249
C.1	Multithreaded wave propagation	249
C.1.1	Spatial and spectral parallelism	250
C.1.2	Spectral parallelism	250
C.1.3	Spatial parallelism	251
C.2	Algorithm	251
C.3	Time-Complexity	255
C.3.1	Selected scenarios	256
C.4	Multithreaded split step propagation	257

Computational optics

Nowadays, the simulation and analysis of case studies is part of every operational task to proof a principle, optimize a design, develop and verify an innovative approach, estimate the quality of a new idea and plan the next steps in a project. Simulation is essential in every research and development discipline, especially if the intrinsic effects and interdependencies are not obvious. So, simulation plays also a key role in optical engineering.

The field of optics provides a huge pool of principles of operation which more and more contribute to innovative products in a wide range of applications. The operability of the solutions and their entire development process thereby mainly depends on the engineering tools, their accuracy, efficiency and flexibility. The enhancement of simulators significantly contributes to the project cycle and hence allows a quicker and more efficient analysis and design of systems with steadily increasing complexity. In the semiconductor industry, the field of micro- and nano-optics became more and more important in the last decade and is a steadily growing area of research. Due to the shrinking feature sizes of the semiconductor technology and the increasing demand for micro- and nano-optical devices, the modeling of electromagnetic effects becomes more and more important. Hence, the knowledge about electromagnetism and the interaction of electromagnetic waves with a medium or a geometry is essential for the research and development of innovative on-chip optical components.

The trend in the semiconductor industry to integrate more and more functionality, shrink the feature sizes of the technology and speed up the designs ends up in the dilemma that electric solutions cannot provide the

expected performance. The high integration rates cause significant design problems due to thermal hot spots and power consumption. Hence, the design process needs to consider these factors. Special techniques like clock-gating or switching of operation modes on thermal sensor feedback is utilized to reduce heating and power consumption. The tremendous density of transistors in combination with the demand for higher frequencies and performance yields to a theoretic heat density higher than on the sun surface. This further increases the demand for alternative solutions. The investigation of new technologies and innovative solutions is therefore a key factor to stay competitive and introduce leading edge technologies to the market. A good example for the change from electrical to optical technology is the evolution of interconnect networks. The evolution in wide area networks (WAN) in the seventies, system area networks (SAN) in the eighties, board interconnects in the nineties will most likely continue with optical chip interconnects in the next generations of computer systems. The expertise of optical and electrical engineering seems to be suitable to proof Moore's Law again. The high demand for system speed, bandwidth and low power consumption demands new technologies and the tremendous pressure of the market will speed up their use in innovative products.

In the next decades, when optical interconnects become available directly on a microprocessor chip, the manipulation of light on the chip is the next logical step in the evolution of semiconductor chips. An exact timeframe can be hardly predicted since the integrated use of electric, optical and electro-optical components on a chip is comparable to the step from bipolar to CMOS. The cost effort for such a change is very high because the required modifications affect the entire design and manufacturing process. The limitations of the existing solutions and the promising benefits of optics will bring electrical and optical engineering closer together. Therefore,

the interdisciplinary skill of development engineers and researchers is essential and a vital competitive advantage.

In optical engineering, the successful development of innovative ideas more and more depends on the understanding of the fundamental electromagnetic principles and the existence of flexible, fast and efficient simulators which are compatible with or provide interfaces to the tools which are used in the semiconductor industry. Hence, the development of efficient simulators and design methodologies is of major importance. Optical engineering may furthermore play a key role in serving the increasing demand on energy and in a larger scope the independence from fossil fuels. The optical engineering, as a catalyzer for other technologies, provides the chance for economic growth and technologic evolution for various technologies. In this context, optics is a facet of *Green IT* because for example the development of efficient photovoltaic solutions preserves the environment and reduces the pollution of the environment. The combined engagement of politics, economics and technology might be able to pursue the solutions of one of the most important problems of our and the next generations and optical engineering is one of the tools to succeed.

Motivation

The optical theory provides closed numeric solutions for some simplified and idealized problems, but a closed numeric solution for complex problems from the daily practice are not available. Hence, numeric simulation methods need to be developed. The field of optical simulation provides a wide variety of methods, the modeling of light as a ray or a wave, the

vectorial capabilities of electromagnetic fields, its polarization and so on. The Fourier-based electromagnetic (EM) simulators are in the scope of the thesis. They are distinguished by the propagation scheme which is applied. The *split step propagation scheme* (i.e. an approximation of the Rayleigh-Sommerfeld diffraction integral), which is utilized in the Beam Propagation Methods (BPM) [13] is distinguished from the *wave propagation scheme* (i.e. the exact solution of the Rayleigh-Sommerfeld diffraction integral) which is utilized in the Wave Propagation Method (WPM) [31].

As the Beam Propagation Method (BPM) is limited to small propagation angles and small index variations, a plurality of different optimizations exist which reduce the error for wide-angle propagation. Due to the inherent approximation in the split step propagation scheme, none of these optimizations really overcome the paraxial limitation. Hence, the results from a simulation of lenses with a high numeric aperture (NA), from gratings and beam splitters, Mach-Zehnder Interferometers or even a simple refraction through a prism is not exact as shown in the thesis. With the space- and frequency-dependent solution of the Rayleigh-Sommerfeld diffraction integral, as applied in the WPM, these angle- and index-restrictions do not exist. The scalar WPM in [31] is accurate for propagation angles up to 85 degrees. It calculates scalar electromagnetic fields and does not utilize a model for evanescent waves. The thesis shows that an accurate solution of the diffraction integral in its vectorial form is not possible with the split step propagation scheme due to the strict separation of spatial and frequency domain which introduces severe problems to the vectorial transformation at interfaces. A serial and parallel algorithm of a vectorial Wave Propagation Method is introduced, which calculates the bidirectional propagation of modes over the entire range of spatial frequencies, without loss of accuracy.

Structure of the thesis

Chapter 1 provides a classification of the main optical simulation methods and briefly describes their principle of operation and the field of application. It shows the gap in existing electromagnetic wave simulators, which is filled by the VWPM. Chapter 2 presents the nomenclature and the fundamentals of the electromagnetic theory which is used in the thesis.

The *Vector Wave Propagation Method* (VWPM) is introduced in chapter 3 and the extension to bidirectional wave propagation is performed in chapter 5, introducing the *bidirectional VWPM*. The application of the vectorial transformations to the split step propagation scheme in the BPM is investigated in chapter 4 and the multithreaded, bidirectional VWPM is presented in Appendix C.

The sampling requirements and the relations to the accuracy of the VWPM are analyzed in chapter 6. The energy conservation of the VWPM is examined in chapter 7. In chapter 8, the VWPM is applied to an optimization problem in order to enhance the local absorption in thin layers (i.e. thin film solar cells) over a maximum range of spatial frequencies by using one- or two-dimensional micrometer gratings. Chapter 9 gives a summary of the presented topics.

In Appendix A, some of the basic transformations from chapter 2 are shown and Appendix B provides some detailed algebraic transformations from chapter 3 and 5.

Chapter 1

Simulation methods

Maxwells' equations provide the most profound and comprehensive theoretic analysis of electromagnetism but an exact solution is only available for a very small subset of problems. The problems for which such a closed solution exists are primarily of academic interest and of low importance for the product development. Hence, numeric methods are required.

In a numeric optical simulation of electromagnetic (EM) waves, Maxwells' equations are rigorously solved or approximated to compute the distribution of EM fields to, for example, determine interdependencies of an electromagnetic wave with a geometric structure. In order to find an answer to a technical problem, analyze an innovative approach or get insight into intrinsic properties of a system, a large diversity of algorithms, modifications, extensions, simplifications and optimizations exist. This chapter gives a brief introduction to the most popular numeric simulation methods in optics and puts emphasis on some of the existing modifications if a significant

relation to this thesis exists. Figure 1.1 shows a classification of simulation methods in inhomogeneous medium. Dependent on the application and if diffraction can be neglected or not, a simulation method models an electromagnetic field as a wave or ray. In this thesis, electromagnetic fields are always waves, which are distinguished by their vectorial or scalar capabilities. A scalar treatment of EM waves imposes severe limitations to the simulator since it cannot consider all types of polarization, Fresnel's equations for TE and TM modes and all other effects which belong to the vectorial character of two- or three-dimensional EM waves. Simulators are furthermore classified by their capability of simulating unidirectional or bidirectional propagation. This criterion is unique to simulators which define an axis of propagation and derive the propagation of the EM wave along this axis in an iterative algorithm. If the simulator evolves the propagating EM wave from a time-dependent analysis, the corresponding method is classified by its space \mathbf{r} and time t dependent computation. In opposition, all methods which are based on an analysis of spatial frequency \mathbf{k} or temporal frequency ω define a second group of simulators.

The Beam Propagation Method (BPM), Rigorous Coupled Wave Analysis (RCWA), and the Wave Propagation Method (WPM) are methods of the (\mathbf{k}, ω) -domain while the FDTD utilizes a space- and time-dependent consideration of the electromagnetic theory and is therefore a method in the (\mathbf{r}, t) -domain. The Beam Propagation Method (BPM) is part of the vectorial branch since several vectorial extensions of the conventional, scalar, algorithm exist. The RCWA and FDTD simulate EM vector waves while scalar and vectorial simulators are available for the BPM. The WPM is utilized for the simulation of scalar EM waves up to now and this thesis makes the wave propagation scheme usable for the uni- and bidirectional simulation of vector waves over the entire range of spatial frequencies.

Even if vectorial version of the BPM are known in literature, it is shown in chapter 4 that a vectorial BPM cannot provide an exact solution of the time- and frequency-dependent diffraction integral due to the separation of spatial and frequency domain in the split step propagation algorithm. The wave propagation scheme applies an accurate solution of the vectorial or scalar diffraction integral and thereby overcomes the limitations as shown in [31] for scalar propagation up to 85 degrees. With the Vector Wave Propagation Method (VWPM), the wave propagation scheme is extended to full vectorial propagation, considering the propagation of vectorial EM waves along a predefined axis of propagation without approximation.

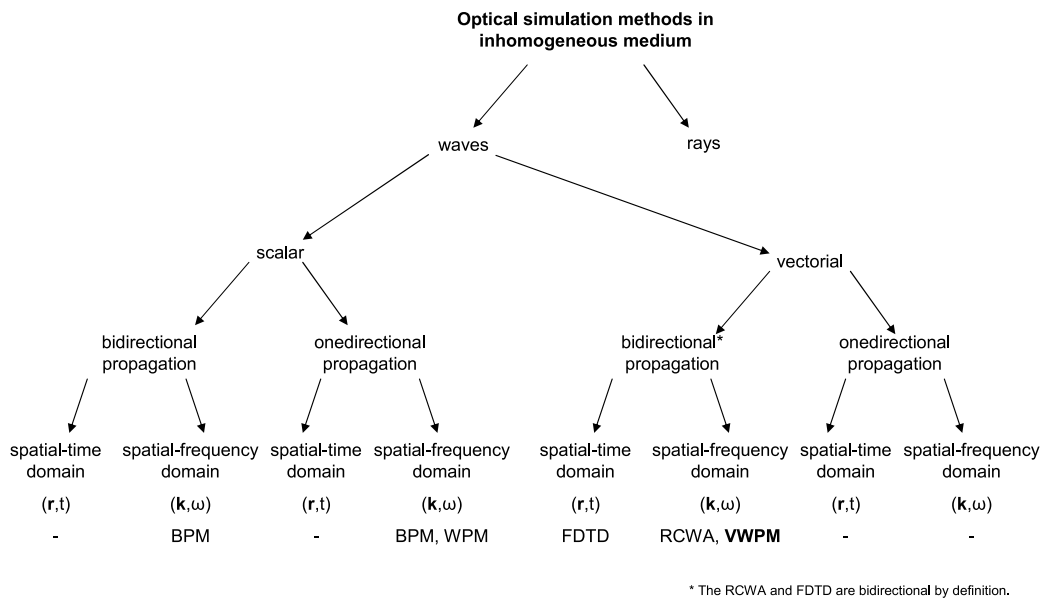


Figure 1.1: *Classification of simulation methods in inhomogeneous medium.*

1.1 RCWA and FDTD

The Rigorous Coupled Wave Analysis (RCWA) and the Finite Difference Time Domain (FDTD) are rigorous methods to compute the distribution of electromagnetic fields in a system, described by a distribution of the (complex) refractive index. While the RCWA provides a two- or three-dimensional rigorous solution of the diffraction problem through periodic grating structures, the FDTD rigorously solves Maxwell's equations in the time domain in an orthogonal discrete two- or three-dimensional grid as exemplary shown in figure 1.2.

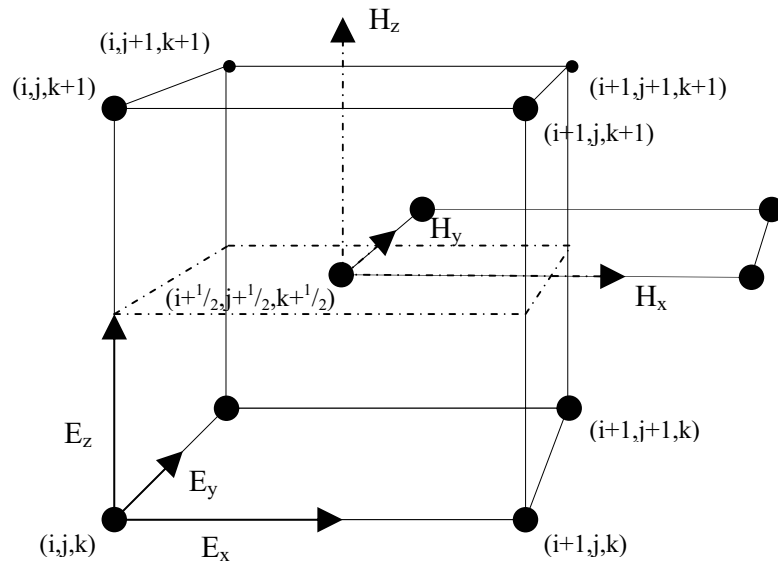


Figure 1.2: *The Yee lattice as utilized in the FDTD method.*

Each point on the grid represents a location in space with a set of associated parameters of the medium. The electric field E [V/m] and magnetic field H [A/m] is derived from the boundary conditions and the elec-

tromagnetic theory at each point. In the Finite Element Approach non-orthogonal or non-uniform grids are utilized which are adapted to the space-derivatives in the system. Locations with high gradients are modeled by a fine mesh while small gradients or homogeneous areas allow a coarse mesh, if low deviations in the EM field can be expected. The three methods are compared in [33].

In some algorithms, an Eigenvalue problem of the form $\mathbf{M}^{m \times n} \cdot \mathbf{u}_n = b\mathbf{u}_n$ is solved (i.e. RCWA), where b is an eigenvalue of the $m \times n$ -matrix $\mathbf{M}^{m \times n}$, corresponding to the n -dimensional eigenvector \mathbf{u}_n . The solution is obtained from the Eigenmodes of the system by solving the characteristic equation $\det((\mathbf{M} - b\mathbf{I}) \cdot \mathbf{u}) = 0$. The solution of a high order $m \times n$ -matrix \mathbf{M} in a vector or scalar equation is required to derive the stationary state of the EM-field. Especially in a three-dimensional simulation, the solution of the Eigenvalue problem requires a significant amount memory because the entire system, represented by the high order matrix \mathbf{M} and the n -dimensional Eigenvectors \mathbf{u}_n , has to be stored and processed at once to derive the steady state. In the three-dimensional case, the computation time grows in the order of $\mathcal{O}(n^6)$, with n is the number of modes, and special hardware acceleration techniques are desirable.

In the FDTD, finite difference equations in the time domain rigorously solve Maxwells' equations and iterate until a steady state has been reached. The electric and magnetic field is calculated at equidistant discrete positions on an orthogonal grid from the time deviations which are described by discrete difference equations. The solution from finite differences is quite time consuming because the steady state of the EM field at a time t has to be determined by iterating the finite difference equations. The strength of rigorous methods is the high accuracy for near-field calculations (i.e.

dimensions in the sub-wavelength range) and the three-dimensional propagation of EM fields. A profound introduction to rigorous methods can be found in [3, 5].

1.1.1 Finite difference time domain method

The basic algorithm of the finite difference time domain (FDTD) method has been developed by Yee [6] in 1966. It is an iterative simulation method in the time domain which uses linear center-difference representations of the continuous partial differential equation on a two or three-dimensional grid as shown in figure 1.2. The algorithm applies the *finite difference algorithm* of the *partial time and space derivative* to each point on the grid which is influenced by electromagnetic disturbances. In the two-dimensional case and for a TE-polarized electromagnetic field in free space, Maxwells' equations become

$$\begin{aligned}\frac{\partial E_x}{\partial t} &= -\frac{1}{\epsilon_0} \frac{\partial H_y}{\partial z} \\ \frac{\partial H_y}{\partial t} &= -\frac{1}{\mu_0} \frac{\partial E_x}{\partial z}\end{aligned}$$

The updates for the electric and magnetic fields are separated in space and time by half a step and derived from the surrounding locations by their interaction according to Maxwells' curl equations and the partial derivatives of space and time. The simulation time is mainly determined by the convergence of the algorithm to compute the EM field at all locations on the grid for a given time t . The two-dimensional central difference approx-

imation of the spatial and temporal derivatives becomes

$$\frac{E_x^{t+1/2}(k) - E_x^{t-1/2}(z)}{\delta t} = -\frac{1}{\epsilon_0} \frac{H_y^t(z + 1/2) - H_y^t(z - 1/2)}{\delta z}$$

$$\frac{H_y^{t+1}(z + 1/2) - H_y^t(z + 1/2)}{\delta t} = -\frac{1}{\mu_0} \frac{E_x^{t+1/2}(z + 1) - E_x^{t+1/2}(z)}{\delta z}$$

The electromagnetic wave is assumed to propagate in an infinite medium and thus the definition of an aperture introduces system boundaries in the henceforth space-limited problem. An electromagnetic wave which reaches such a system boundary gets reflected back into the medium which cause problems in simulations expecting an infinite scene. The *open-region FDTD* implements the *perfectly matched layers* (PML) algorithm to avoid reflections. This technique was originally developed by Berenger in 1994 [7] and extended by Gedney in 1996 [8]. It uses a set of non-physical equations with high attenuation for canceling electromagnetic contributors at the system boundary. In case of an absorbing term, the PML needs to be composed by several layers that gradually introduce absorption. Another approach is the cancellation in so called *absorbing boundary conditions* (ABC) which have been developed by Tavlove and Hagness in 2005 [3]. ABC introduces a term with opposite sign to completely cancel the field entering the layer. The most commonly used techniques for open-region FDTD modeling are the Mur ABC (1981) [9], the Liao ABC (1984) [10] and various PML formulations.

One of the strengths of FDTD is the simulation of a wide range of frequencies in a single run. This is useful when resonance frequencies are not exactly known. The method allows an arbitrary distribution of material all over the system without restrictions on periodicity or any other implication on the refractive index. For example, the effects of apertures and shielding can be directly investigated. The FDTD requires a system to be discretized

by a sufficiently fine grid in order to apply the partial derivatives with appropriate accuracy. Moreover, the grid has to resolve the smallest geometric feature and the smallest wavelength. These requirements causes significant computation times for large scenes and thereby limit the applicability to small inputs. In case of far-field observations, a post-processing is required which has been introduced by Tavlove and Hagness in 2005 [3]. The Yee algorithm has been adapted to various electro-magnetic compatibility (EMC) applications, extended to second order accuracy, modified for applicability to larger systems, merged with hybrid grid approaches to just name some of the enhancements.

1.1.2 Rigorous coupled wave analysis

The Rigorous Coupled Wave Analysis (RCWA) was developed by Burkhardt [11] in 1966. In its most basic and two-dimensional form, it assumes a plane wave input, simple periodic structures in the lateral direction and a uniform refractive index in the axis of propagation. These, mostly rectangular, periodic gratings allow the RCWA an easy separation of space variables and a treatment with the Fourier analysis. The RCWA treats the periodic part of the solution by Fourier expansions of modes (i.e. space harmonics or spatial frequencies). With the Fourier expansion, the partial differential equations transforms to one or more ordinary differential equations by separating a predefined axis of propagation - in most cases the z -axis of a Cartesian coordinate system - from the three-dimensional wave equation. The numeric solution requires a discretization which raises the question of aliasing to the henceforth space-limited problem. The computation time of the RCWA is determined by the Eigenvalue decomposition which is per-

formed to solve the characteristic equation. In order to enhance the convergence with higher mode numbers, a more efficient algorithm has been presented by Kraaij in 2006 [12].

The RCWA algorithm is a conceptually straight forward solution of a characteristic equation, considering boundary conditions which yield the solution and the field in the system under investigation. The method is applicable to periodic geometries and optical diffraction problems. Its strength is the accuracy for near-field analysis and the computation of vectorial field distributions in two and three-dimensions. The RCWA requires a sufficiently high number of samples in the Fourier transformation of the system to consider high order spatial frequencies in the refractive index distribution. An adequate number of modes (i.e. Eigenvalues) are required to simulate the desired number of spatial frequencies of the EM field. The computation time is based on a modal analysis, with n is the number of modes. The propagation of the EM field is derived from equations considering complex exponentials and reflection and transmission coefficients in two or three dimensions. The solution is then obtained from the boundary conditions (i.e. the incident light and the system definition).

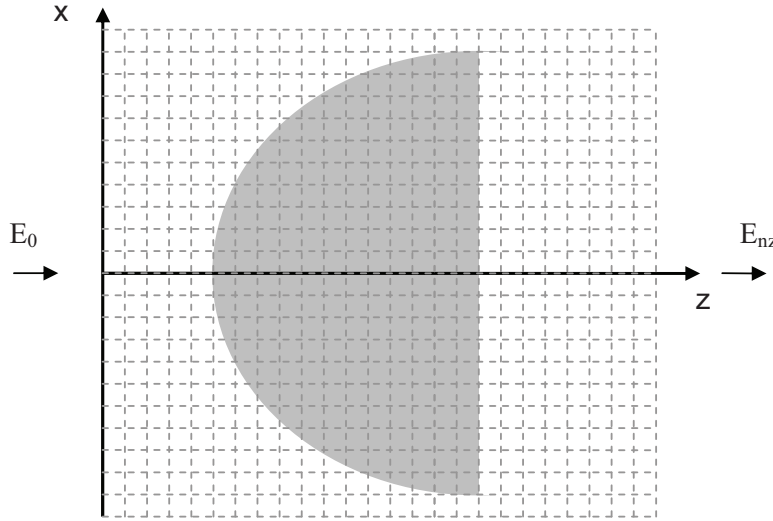
Due to the matrix representation of the entire problem, a high number of modes consumes a lot of memory and the simulation time in the three-dimensional case grows in the order of $\mathcal{O}(n^6)$. Hence, the number of modes is a limiting factor and optimizations of the algorithm for a hardware-assisted acceleration on single instruction multiple data (SIMD) and/or multiple instruction multiple data (MIMD) architectures are of high interest for the practical use of the three-dimensional RCWA.

1.2 BPM and WPM

The Beam Propagation method (BPM) [13] and the Wave Propagation Method (WPM) [31] are members of the Fast Fourier Methods due to their good performance in practical computation and the use of the Fast Fourier Transformation. The underlying physics is based on the intuitive view of an EM wave as a complex exponential, which is obtained from the solution of the scalar or vector wave equation. The complex exponential evolves from transformations of Maxwells' equations, using the constitutive equations (also called medium equations or material equations) followed by a separation of a space variable in the three-dimensional Helmholtz equation which defines the axis of propagation - in most cases the z -axis - as shown in chapter 2. The partial differential equation (PDE) $\nabla^2 u(x, y, z) + k^2 u(x, y, z) = 0$ is thereby reduced to an ordinary differential equation (ODE) $\partial^2 u(x, y, z) / \partial x^2 + \partial^2 u(x, y, z) / \partial y^2 - 2ik \partial u(x, y, z) / \partial z = 0$ for an axis of propagation z .

In the BPM and WPM, a formerly continuous system is split into a certain number of layers along this axis of propagation, determined by the discretization in the axis of propagation. Each layer is expected to be homogeneous along the axis of propagation and is accepted to be inhomogeneous in the other, lateral, directions of the two- or three-dimensional space. Since it is not always possible to gain a homogeneous index distribution in the axis of propagation as shown in figure 1.3, locations with an inhomogeneous refractive index in the axis of propagation are supposed to be replaced by a suitable average refractive index. The average index is suitable, when an optical path length (OPL) through the continuous system

Figure 1.3: *Two-dimensional discretization of a scene in electromagnetic wave simulators with z is the predefined axis of propagation.*



is replaced by a uniform refractive index n_u such that

$$\int n_u dz \approx \int n(\mathbf{r}) dz$$

and then $n_u \approx \int n(\mathbf{r}) dz / \int 1 dz$. Another intuitive uniform refractive index along the axis of propagation is obtained from the normalized sum of weighted volumes

$$n_u \approx \frac{1}{\Delta V} \sum_{i=0}^{N-1} (v_i n_i) \quad (1.1)$$

with N is the number of different refractive indices in a voxel $\Delta V = \Delta x \Delta y \Delta z$ and with $v_i [m^3]$ which is the partial volume for this index in ΔV .

A two-dimensional simulation in a Cartesian coordinate system calculates the EM field in a one-dimensional layer per iteration, perpendicular to the

axis of propagation, including the distribution of the refractive index. In a three-dimensional simulation, each layer is defined by a plane surface, comprising a two-dimensional index distribution. The simulation starts with the first layer and ends after all layers have been processed. The algorithm is iterative and the result of a layer is the input for the calculation of the next layer. The propagation along the separated space variable is based on the *Rayleigh Sommerfeld* integral (eq. 2.60) and diffraction effects (i.e. illumination of the geometric shadow) are calculated. The original algorithms of the BPM and WPM are unidirectional and scalar, considering only the forward propagating fields and neglecting all reflected fields.

1.2.1 Beam Propagation Method

One of the most popular methods utilizing the split step propagation scheme is the Beam Propagation Method (BPM) which was introduced by Feith and Fleck [13] in 1978. With a complexity of $\mathcal{O}(n)$ in the two-dimensional and $\mathcal{O}(n^2)$ in the three-dimensional case, the BPM is a fast method using the forward and inverse Fourier transformation in each iteration. n is the number of modes.

The propagation in the BPM is calculated according to the split-step propagation scheme. It is called split-step propagation because the propagation through one layer is split into a first step in the frequency domain after the Fourier transformation ($\tilde{u} = \mathcal{F}(u)$) of a space-dependent scalar electric field $u(\mathbf{x})$ and a second step in the spatial domain after an inverse Fourier transformation ($\mathcal{F}^{-1}(\tilde{u})$) of the spectrum $\tilde{u}(\nu)$. It is exactly this split-step propagation that is the reason for the remarkable speed but at the same

time it provides also the reason for the limitation of the BPM to paraxial propagation and small index variations. It makes the method unusable to calculate the exact solution of the scalar or vectorial Rayleigh-Sommerfeld diffraction integral and effects which rely on the vectorial treatment of EM waves.

The BPM was primarily designed for the simulation of waveguides or other systems that allow the paraxial approximation without significant loss of accuracy. In addition to the paraxial limitation, the BPM is limited to small index variations as shown in chapter 3. With the paraxial limitation, the stability is ensured if evanescent waves are damped or clipped [45, 29]. The limitations make the BPM unusable for an exact simulation of high order modes which propagate through lenses with a high numeric aperture (NA) or any other systems which are traversed by high order spatial frequencies or which possess an evanescent character. Therefore, various optimizations for the calculation of wide-angles were published.

A wide-angle BPM was introduced by Hadley in [14] to enable the BPM for non-paraxial propagation. Changbao presented a three-dimensional wide-angle BPM in [15] for optical waveguide structures. A semi vectorial wide-angle BPM was presented by Lee in [16]. The BPM was extended to very-wide angles in [17] but the error that arises from the separation of the propagation operator is more or less persistent in all those extensions. Most wide-angle extensions utilize the higher order Pade equation $\sqrt{1+X} = N_m(X)/D_n(X)$, with N is a m -th order polynomial and D is a n -th order polynomial to approximate the square root $\sqrt{1 - (k_x^2 + k_y^2)/n^2/k_0^2}$ in the complex exponential propagator. Several vector extensions of the BPM had been presented by Yamauchi [18], Liu [19] and Perez [20]. Yamauchi introduced a modified semi vectorial beam propagation method

retaining the longitudinal field component, Liu published the analysis of polarized modes of rib waveguides with a semi vectorial BPM and Perez presented a fully-vectorial three-dimensional extension of the BPM. A third class of extensions is based on the finite element (FE) approach as published by Tsui [21], Stern [22], Pinheiro [23] and Obayya [24]. The FE-based extensions of the BPM are optimized for scalar, semi vectorial and full-vectorial fields as well as numerically efficient methods in the order of citation. The fourth and last class of extensions in this brief overview of BPM-based methods is the multi grid approach that is used to reduce computational effort at regions in a system that allow a reduced degree of accuracy. Sewell has introduced a multi grid method for electromagnetic computation in [25]. Additional extensions of the BPM to bidirectional propagation [26, 27] and evanescent waves [28] are known. All enhancements are based on approximations which more or less reproduce the complex exponential phasor and its square root in the argument. Not any overcomes both limitations, the paraxial limitation and the limitation to small index variations as shown in [53]. Therefore, an exact solution of the diffraction integral is required, which overcomes the limitation of the split step propagation scheme. In the scalar case, this is achieved with the Wave Propagation Method (WPM).

1.2.2 Wave Propagation Method

The scalar wave propagation method (WPM) was introduced by Brenner and Singer in 1993 [31]. It utilizes a space and frequency dependent solution of the scalar diffraction integral, called the *wave propagation scheme* this thesis, in comparison to the split step propagation scheme. Due to

the equitable consideration of the space- and frequency-dependency in the diffraction integral, the WPM is not limited to paraxial propagation or a small index variation. The inverse Fourier transformation then can not be used to derive the spatial field distribution from the spectrum. This causes an increase in the time complexity, which is in $\mathcal{O}(n^2)$ for the two-dimensional WPM and in $\mathcal{O}(n^4)$ for the three-dimensional case, with n is the number of modes. The original WPM in [31] calculates the unidirectional propagation of scalar electromagnetic fields and does not model evanescent modes. The WPM provides exact results for propagation angles up to 85 degrees and hence the Fresnel coefficients can no longer be neglected and a vectorial approach is therefore perfectly reasonable. The scalar WPM scheme is used in a commercial software package [34] to calculate aspheric lenses or arbitrary phase elements that do not allow a simple analytic treatment. Even if the WPM provides significant advantages, no known extensions or enhancements are documented in the literature up to now.

1.3 Ray tracing

If diffraction effects can be neglected, ray optics or Gaussian optics are used to calculate the propagation of electromagnetic fields. These methods are used in ray tracing to monitor the trace of light. According to *Fermat's principle or the shortest time*, the path taken by light between two points is the direct path.

The strength of ray tracing is the calculation of large and very complex scenes (i.e. object or zoom lens systems for cameras or telescopes)

with high propagation distances and large geometries compared to the applied wavelength. In this scope, the diffraction effects are negligible and the treatment of light as a ray is absolutely sufficient. In order to reduce the computational effort, the three-dimensional scene is often reduced to a simplified, two-dimensional model, called *meridional ray tracing* [1]. The meridian is defined by a plane surface $(\mathbf{x} - \mathbf{p}) \cdot \mathbf{n} = 0$ in the three-dimensional space, with \mathbf{p} is a point in the plane and \mathbf{n} is the surface normal. All rays propagate in the predefined surface and thereby the three-dimensional problem is reduced to the two-dimensional vector algebra, which consumes less resources and is much faster.

Snell's law and the Fresnel's coefficients can be derived from Fermat's principle and several ray tracers are extended to consider amplitudes and their transformations at interfaces. The electromagnetic theory and the electromagnetic effects like they appear in near field scenarios is out of the scope of the method.

Chapter 2

Fundamentals

Maxwells' equations describe the fundamental theory of electromagnetism, couple electric and magnetic field and formulate the basic physical laws governing the electric field E and the magnetic field strength H . As one of the central observations of the electromagnetic (EM) theory, the relationship of electric and magnetic field shows that a time-varying electric field produces a time-varying magnetic field. This dependency is precisely the root cause for the existence of EM waves.

An EM wave consists of an electric field vector \mathbf{E} [V/m] and the magnetic vector \mathbf{H} [A/m] (also called magnetic field strength, magnetic field intensity, auxiliary magnetic field or magnetizing field). Besides \mathbf{E} and \mathbf{H} the other two quantities in Maxwells' equations are the electric displacement \mathbf{D} [C/m^2] and the magnetic flux density (magnetic induction, magnetic field) \mathbf{B} [$Vs/m^2 = N/A/m = T$ (*Tesla*)].

These four quantities are the basis for the fundamental electromagnetic theory which are condensed in the four Maxwell equations in its differential form

$$\nabla \cdot \mathbf{D} = \rho_v \quad (2.1)$$

$$\nabla \cdot \mathbf{B} = 0 \quad (2.2)$$

$$\nabla \times \mathbf{E} = -\frac{\partial \mathbf{B}}{\partial t} \quad (2.3)$$

$$\nabla \times \frac{\mathbf{B}}{\mu\mu_0} = \mathbf{J}_c + \frac{\partial \mathbf{D}}{\partial t} \quad (2.4)$$

where \mathbf{J}_c [A/m^2] is the electric current density and ρ_v [C/m^3] denotes the charge density. The equations 2.3 and 2.4 show the coupling between electric and magnetic fields. The *constitutive relations* or *material equations*

$$\mathbf{B} = \mu\mu_0\mathbf{H} \quad (2.5)$$

$$\mathbf{D} = \epsilon\epsilon_0\mathbf{E} \quad (2.6)$$

couple the electric and magnetic field. In case of a linear, homogeneous and isotropic medium, the permittivity ϵ [F/m] and the permeability of the medium μ [H/m] are constant. ϵ_0 [$As/V/m$] and μ_0 [$Vs/A/m$] are the electric and magnetic field constants in the vacuum. A medium is called *linear* when its properties does not depend on the amplitude, it is called *homogeneous* when its properties are not a function of space and a medium is called *isotropic* when the properties are the same for all directions. This thesis focuses on systems which are formed by linear and isotropic media.

2.1 The scalar and vector wave equation

The *vector wave equation* for a linear, homogeneous and isotropic medium is derived from Maxwells' equations by taking the curl (∇) of both sides of equation 2.3 and using the first equation of the constitutive relations 2.5

$$\nabla \times \nabla \times \mathbf{E} = -\frac{\partial}{\partial t}(\nabla \times \mathbf{B}) = \frac{\partial}{\partial t}(\nabla \times -\mu\mu_0\mathbf{H}) \quad (2.7)$$

Using the vector identities

$$\begin{aligned} \Delta \mathbf{v} &= \nabla^2 \mathbf{v} = \nabla \cdot (\nabla \cdot \mathbf{v}) \\ \nabla \times \nabla \times \mathbf{v} &= \text{grad}(\nabla \cdot \mathbf{v}) - \nabla^2 \mathbf{v} \\ \text{grad}(u) &= \begin{pmatrix} \partial/\partial x \\ \partial/\partial y \\ \partial/\partial z \end{pmatrix} u, \quad \nabla \times \mathbf{v} = \begin{pmatrix} \partial/\partial x \\ \partial/\partial y \\ \partial/\partial z \end{pmatrix} \times \begin{pmatrix} v_x \\ v_y \\ v_z \end{pmatrix} \end{aligned} \quad (2.8)$$

and the second constitutive equation 2.6, the expression transforms to

$$\nabla^2 \mathbf{E} - \mu\mu_0\epsilon\epsilon_0 \frac{\partial^2 \mathbf{E}}{\partial t^2} = \mu\mu_0 \frac{\partial \mathbf{J}_c}{\partial t} + \text{grad}(\nabla \cdot \mathbf{E}) \quad (2.9)$$

for a homogeneous medium (i.e. $\epsilon = \text{const}$). The space independence of the electric permittivity ϵ allows a reformulation of equation 2.1 to

$$\nabla \cdot \mathbf{E} = \frac{\rho_v}{\epsilon\epsilon_0} \quad (2.10)$$

The second constitutive equation 2.6 provides a way to substitute the nested curl operators and the equation is transformed to

$$\nabla^2 \mathbf{E} - \mu\mu_0\epsilon\epsilon_0 \frac{\partial^2 \mathbf{E}}{\partial t^2} = \mu\mu_0 \frac{\partial \mathbf{J}_c}{\partial t} + \text{grad}\left(\frac{\rho_v}{\epsilon\epsilon_0}\right) \quad (2.11)$$

In a conducting medium, the electric current density \mathbf{J} is $\sigma\mathbf{E}$ and then the first time derivative of \mathbf{J} transforms to $-\mu\mu_0\sigma \partial\mathbf{E}/\partial t$ with σ [A/V/m] is the

specific conductivity of the medium. This is the *vector wave equation* for linear homogeneous and isotropic medium, characterized by ϵ and μ . In a non-conducting and source-free medium, \mathbf{J}_c and ρ_v are zero and equation 2.11 transforms to

$$\nabla^2 \mathbf{E} - \mu\mu_0\epsilon\epsilon_0 \frac{\partial^2 \mathbf{E}}{\partial t^2} = 0 \quad (2.12)$$

which is the *homogeneous vector wave equation in a source-free medium*. Using the equation for a continuous motion $F(x, t) = x - vt$ in equation 2.12, the Laplacian of a function F is $\partial^2 F / \partial t^2 = 1/v^2 \partial^2 F / \partial x^2$ and the quantity $\mu\mu_0\epsilon\epsilon_0$ relates to the velocity v [m/s] of the EM wave in the medium by

$$v = \frac{1}{\sqrt{\mu\mu_0\epsilon\epsilon_0}} \quad (2.13)$$

See Appendix A for more information on the speed of light and the relation to the electric and magnetic susceptibility.

Equation 2.12 then transforms to

$$\nabla^2 \mathbf{E} - \frac{1}{v^2} \frac{\partial^2 \mathbf{E}}{\partial t^2} = 0 \quad (2.14)$$

and with $\mathbf{E} = \mathbf{E}_0 \exp(i(\mathbf{k} \cdot \mathbf{r} - \omega t))$ the *Helmholtz equation*

$$(\nabla^2 + k^2) \cdot \mathbf{E} = 0 \quad (2.15)$$

is obtained, with $k = |\mathbf{k}| = \omega/c$. Due to the linearity of the operators, the equation is equivalent to three scalar wave equations - one for every vector component of the field vector \mathbf{E} . The vectorial amplitude is of the form

$$\mathbf{E}_0 = E_{x,0} \cdot \mathbf{e}_x + E_{y,0} \cdot \mathbf{e}_y + E_{z,0} \cdot \mathbf{e}_z \quad (2.16)$$

where \mathbf{e}_x , \mathbf{e}_y and \mathbf{e}_z are the vectors of unity in a three-dimensional Cartesian coordinate system. The Laplacian is

$$\Delta = \nabla^2 = \nabla \cdot \nabla = \frac{d^2}{dx^2} + \frac{d^2}{dy^2} + \frac{d^2}{dz^2} \quad (2.17)$$

and then the the three scalar wave equations for the vector components E_x , E_y and E_z are

$$\begin{aligned}\frac{\partial E_x}{\partial x^2} + \frac{\partial E_x}{\partial y^2} + \frac{\partial E_x}{\partial z^2} &= \frac{1}{v^2} \frac{\partial^2 E_x}{\partial t^2} \\ \frac{\partial E_y}{\partial x^2} + \frac{\partial E_y}{\partial y^2} + \frac{\partial E_y}{\partial z^2} &= \frac{1}{v^2} \frac{\partial^2 E_y}{\partial t^2} \\ \frac{\partial E_z}{\partial x^2} + \frac{\partial E_z}{\partial y^2} + \frac{\partial E_z}{\partial z^2} &= \frac{1}{v^2} \frac{\partial^2 E_z}{\partial t^2}\end{aligned}\quad (2.18)$$

If $\epsilon(\mathbf{r})$ and $\mu(\mathbf{r})$ are space-dependent, the expression

$$0 = \nabla \times \left(\frac{1}{\mu_0 \mu(\mathbf{r})} (\nabla \times \mathbf{E}) \right) + \frac{\partial}{\partial t} \left(\mathbf{J}_c + \frac{\partial \mathbf{D}}{\partial t} \right) \quad (2.19)$$

is obtained by applying equation 2.5 to equation 2.3, dividing by $1/\mu(\mathbf{r})/\mu_0$, taking the curl on both sides the expression. Using the relations

$$\begin{aligned}\nabla \times (u\mathbf{v}) &= u(\nabla \times \mathbf{v}) + (\text{grad } u) \times \mathbf{v} \quad (i) \\ \nabla \times (\nabla \times \mathbf{v}) &= \text{grad}(\nabla \cdot \mathbf{v}) - \nabla^2 \mathbf{v} \quad (ii)\end{aligned}\quad (2.20)$$

and assuming a non-conducting medium with $\mathbf{J}_c = \sigma \mathbf{E} = 0$ and σ [A/V/m] is the specific conductivity, the expression transforms to

$$\Delta \mathbf{E} - \frac{\epsilon(\mathbf{r})\mu(\mathbf{r})}{c_0^2} \frac{\partial^2 \mathbf{E}}{\partial t^2} + (\nabla(\ln \mu(\mathbf{r})) \times (\nabla \times \mathbf{E}) + \nabla(\mathbf{E} \cdot \nabla(\ln \epsilon(\mathbf{r}))) = 0 \quad (2.21)$$

with $u = 1/\mu_0/\mu(\mathbf{r})$ and $\mathbf{v} = \nabla \times \mathbf{E}$ in equation 2.20.i and $\mathbf{v} = \mathbf{E}$ in 2.20.ii. Considering the space-dependency of $\epsilon_0\epsilon(\mathbf{r})$, and assuming a charge-free volume, equation 2.6 transforms according to $\nabla(u\mathbf{v}) = u\nabla\mathbf{v} + \mathbf{v} \cdot \text{grad } u$ and

$$0 = \rho_v = \nabla(\epsilon_0\epsilon(\mathbf{r})\mathbf{E}) = \epsilon_0\epsilon(\mathbf{r})(\nabla \cdot \mathbf{E}) + \mathbf{E} \cdot \text{grad}(\epsilon_0\epsilon(\mathbf{r})) \quad (2.22)$$

is obtained. A replacement of $\text{grad}(\nabla \cdot \mathbf{E})$ then yields the inhomogeneous wave equation

$$\Delta \mathbf{E} - \frac{\epsilon(\mathbf{r})\mu(\mathbf{r})}{c_0^2} \frac{\partial^2 \mathbf{E}}{\partial t^2} = - \left[\frac{\nabla\mu(\mathbf{r})}{\mu(\mathbf{r})} \times (\nabla \times \mathbf{E}) + \nabla \cdot \left(\frac{\nabla\epsilon(\mathbf{r})}{\epsilon(\mathbf{r})} \cdot \mathbf{E} \right) \right] \quad (2.23)$$

with c_0 is the speed of light in vacuum and $n(\mathbf{r}) = \sqrt{\epsilon(\mathbf{r})}$, assuming $\mu(\mathbf{r}) = 1$. In [1], the term $1/x$ is replaced by $\text{grad}(\ln(x))$ to obtain a vector. In a non-magnetizing medium, $\mu(\mathbf{r}) = 1$ and the gradient is then zero. The deviation to the wave equation in a homogeneous medium reduces then to $-\nabla(\mathbf{E}\nabla(\epsilon_0/\epsilon(\mathbf{r}))/\epsilon_0/\epsilon(\mathbf{r}))$. Again, $\nabla(\epsilon_0/\epsilon(\mathbf{r}))/\epsilon_0/\epsilon(\mathbf{r})$ is replaced by $\nabla(\ln(\epsilon_0\epsilon(\mathbf{r})))$. In case of an exponential dependency of the permittivity to the position $\epsilon(\mathbf{r}) = \exp(\mathbf{a} \cdot \mathbf{r})$, the resulting field shows a linear shift of the partial derivatives of \mathbf{E} and the deviation to the homogeneous wave equation is then

$$\begin{aligned}
 \nabla \cdot \left(\frac{\nabla \epsilon(\mathbf{r})}{\epsilon(\mathbf{r})} \cdot \mathbf{E} \right) &= \nabla \cdot (\mathbf{E} \cdot \nabla(\ln \epsilon(\mathbf{r}))) \\
 &= \nabla \cdot (\mathbf{E} \cdot \nabla(\ln(e^{a_x x + a_y y + a_z z}))) \\
 &= \nabla \cdot (\mathbf{E} \cdot \nabla(a_x x + a_y y + a_z z)) \\
 &= \nabla \cdot (\mathbf{E} \cdot \mathbf{a})
 \end{aligned} \tag{2.24}$$

This illustrates that the term $\nabla(\mathbf{E}\nabla(\epsilon_0/\epsilon(\mathbf{r}))/\epsilon_0/\epsilon(\mathbf{r}))$ for inhomogeneous medium is negligible for small changes in the refractive index.

2.1.1 Homogeneous wave equation

The solution of each equation in 2.18 yields the *scalar wave equation* in its simplest form

$$\begin{aligned}
 E_x(\mathbf{r}, t) &= E_{x,0} \cdot e^{i(\mathbf{k} \cdot \mathbf{r} - \omega t)} \\
 E_y(\mathbf{r}, t) &= E_{y,0} \cdot e^{i(\mathbf{k} \cdot \mathbf{r} - \omega t)} \\
 E_z(\mathbf{r}, t) &= E_{z,0} \cdot e^{i(\mathbf{k} \cdot \mathbf{r} - \omega t)}
 \end{aligned} \tag{2.25}$$

with the time t [s], the circular frequency ω [rad/s], the *propagation vector*

$$\mathbf{k} = \begin{pmatrix} k_x \\ k_y \\ k_z \end{pmatrix} [1/m] \quad (2.26)$$

and the space vector

$$\mathbf{r} = \begin{pmatrix} x \\ y \\ z \end{pmatrix} [m] \quad (2.27)$$

A homogeneous scalar wave equation is subsequently of the form

$$E(\mathbf{r}, t) = \hat{E}_0 \cdot e^{i(\mathbf{k} \cdot \mathbf{r} - \omega t)} \quad (2.28)$$

with the complex scalar amplitude \hat{E}_0 . The vectorial reformulation of equation 2.18 then gives the *homogeneous vector wave equation*

$$\mathbf{E}(\mathbf{r}) = \hat{\mathbf{E}}_0 \cdot e^{i(\mathbf{k} \cdot \mathbf{r} - \omega t)} \quad (2.29)$$

with the complex vectorial amplitude

$$\hat{\mathbf{E}}_0(\mathbf{r}, t) = \begin{pmatrix} \hat{E}_{x,0} \\ \hat{E}_{y,0} \\ \hat{E}_{z,0} \end{pmatrix} [V/m] \quad (2.30)$$

The physical quantities (i.e. electric and magnetic field strength) of the scalar and vector wave equations are obtained by taking the real part of the complex wave equations.

2.1.2 Propagation constant

The *propagation constant* $k = nk_0 = 2\pi n/\lambda$ [rad/m] = [1/m] is the length of the propagation vector $\mathbf{k} = ks$ which is related to the wave velocity v by

$$v = \frac{c}{\sqrt{\epsilon}} = \frac{c}{n} = \frac{\omega}{k} \quad (2.31)$$

with $s = \mathbf{k}/k$ and $k = |\mathbf{k}|$.

2.1.3 Polarization

The complex vector amplitude $\hat{\mathbf{E}}$ in equation 2.30 can be transformed to

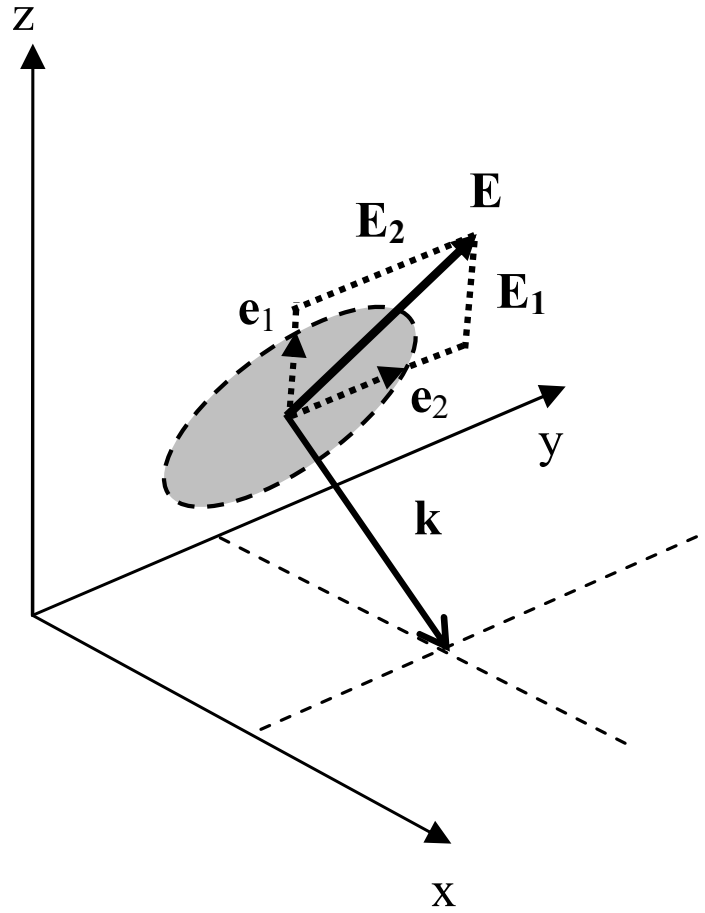
$$\hat{\mathbf{E}}(\mathbf{r}, t) = \begin{pmatrix} E_x \\ E_y \\ E_z \end{pmatrix} = \hat{E}_1 \mathbf{e}_1 + \hat{E}_2 \mathbf{e}_2 e^{i\phi_p} \text{ [V/m]} \quad (2.32)$$

with the real-valued vectors of unity $\mathbf{e}_1, \mathbf{e}_2$ and with $\mathbf{e}_1 \cdot \mathbf{e}_2 = 0$. The vectors \mathbf{e}_1 and \mathbf{e}_2 are furthermore perpendicular to the propagation vector, but not necessarily align with the unity vectors for TE- and TM- polarization as shown in figure 2.1. The phase difference ϕ_p between the two complex values \hat{E}_1 and \hat{E}_2 determine the polarization of the electromagnetic vector wave according to table 2.1.

The polarization vector of unit length \mathbf{u} and the propagation vector of unit length s can then be expressed in terms of the Euler angles in a Cartesian coordinate system according to

$$\mathbf{u} = \frac{\mathbf{E}}{|\mathbf{E}|} = \begin{pmatrix} \cos \psi \cos \theta \cos \phi - \sin \psi \sin \phi \\ \cos \psi \cos \theta \cos \phi + \sin \psi \sin \phi \\ -\cos \psi \sin \theta \end{pmatrix} \quad (2.33)$$

Figure 2.1: Geometry of the polarization angle.

Table 2.1: Phase differences ϕ_p and the related types of polarization.

phase [rad]	type of polarization
$\phi_p = 0$	linear
$0 < \phi_p < \pi/2$	elliptic
$\phi_p = \pi/2$	circular
$\pi/2 < \phi_p < \pi$	elliptic
$\phi_p = \pi$	linear

and

$$\mathbf{s} = \frac{\mathbf{k}}{|\mathbf{k}|} = \begin{pmatrix} \cos \rho \sin \theta \\ \sin \rho \sin \theta \\ \cos \theta \end{pmatrix} \quad (2.34)$$

with θ is the angle of incidence, ϕ is the yaw angle and ψ is the rotation of \mathbf{E} around the vector \mathbf{s} .

2.1.4 Transversality

The constitutive equation 2.6 in a homogeneous medium in the absence of charges states that the divergence of the electric displacement is $\nabla \cdot \mathbf{D} = \text{div}(\mathbf{D}) = \text{div}(\epsilon_0 \epsilon \mathbf{E}) = \epsilon_0 \epsilon \text{div}(\mathbf{E}) = 0$. This yields the *transversality condition* for the electric field $i\epsilon_0 \epsilon \mathbf{k} \cdot \mathbf{E} = 0$ and the z-component of the electric field vector $\hat{\mathbf{E}}$ is then

$$\hat{E}_z = -\frac{\hat{E}_x k_x + \hat{E}_y k_y}{k_z} \quad (2.35)$$

In case of a space dependent $\epsilon(\mathbf{r})$, the divergence of the electric displacement $\text{div}(\mathbf{D})$ transforms to $\nabla \cdot \mathbf{D} = \text{grad}(\epsilon_0 \epsilon(\mathbf{r})) \cdot \mathbf{E} + \epsilon_0 \epsilon(\mathbf{r})(\nabla \cdot \mathbf{E})$ and then

$$\hat{E}_z = -\frac{\hat{E}_x(k_x - i/\epsilon \partial\epsilon/\partial x) + \hat{E}_y(k_y - i/\epsilon \partial\epsilon/\partial y)}{k_z} \quad (2.36)$$

with $\partial\epsilon/\partial x$ and $\partial\epsilon/\partial y$ are the spatial derivatives of $\epsilon(\mathbf{r})$. Appendix A presents a discrete approximation (i.e. the linear symmetric average) of the spatial derivatives $\partial\epsilon/\partial x$ and $\partial\epsilon/\partial y$ as utilized in the program code of the VWPM.

2.2 Irradiance

The irradiance I [W/m^2], also called intensity, is the power per area unit of an an EM-wave. The irradiance is the quantity which is measured by optical detectors and is proportional to the squared amplitude of the electric field vector and inverse proportional to the impedance of the vacuum $1/(\mu_0 c_0) = Z_0 = \sqrt{\mu_0/\epsilon_0} = 376.82[\Omega]$

$$\begin{aligned}
 I(\mathbf{r}) &= |\langle \mathbf{S} \rangle_T| \\
 &= \left| \frac{1}{2} \text{Re} \left(\mathbf{E}(\mathbf{r}) \times \sqrt{\frac{\hat{\epsilon}(\mathbf{r})\epsilon_0}{\hat{\mu}(\mathbf{r})\mu_0}} (\mathbf{s} \times \mathbf{E}^*(\mathbf{r})) \right) \right| \\
 &= \left| \frac{\epsilon_0}{2\mu_0} \text{Re} \left(\left(\sqrt{\frac{\hat{\epsilon}(\mathbf{r})}{\hat{\mu}(\mathbf{r})}} (\mathbf{E}(\mathbf{r}) \cdot \mathbf{E}^*(\mathbf{r})) \right) \mathbf{s} \right) \right| \\
 &= \frac{1}{2} \frac{|\text{Re}(\hat{n}(\mathbf{r}))|}{\mu_0 c} |\mathbf{E}(\mathbf{r})|^2 \\
 &= \frac{|n(\mathbf{r})|}{2Z_0} E^2(\mathbf{r}) \tag{2.37}
 \end{aligned}$$

with $\hat{\mu}(\mathbf{r}) = 1$, $E(\mathbf{r})$ is the absolute of $\mathbf{E}(\mathbf{r})$ and $\mathbf{E}^*(\mathbf{r})$ is the conjugate complex of $\mathbf{E}(\mathbf{r})$. $\text{Re}()$ returns the real part of a complex quantity. The factor $1/2$ (i.e. $(1/\sqrt{2})^2$) originates from the time average computation (i.e. $\langle \cdot \rangle_T$) which is required to get the effective irradiance of the oscillating electric field. $n(\mathbf{r})$ is the space dependent real part of the complex refractive index $\hat{n}(\mathbf{r}) = n(\mathbf{r}) + i\kappa(\mathbf{r})$ at location \mathbf{r} .

2.3 Poynting vector

The absolute of the Poynting vector \mathbf{S} is the irradiance. For complex fields, it is derived from the time average vector product of \mathbf{E} and \mathbf{H}^*

$$\langle \mathbf{S} \rangle_T = \frac{1}{2} \text{Re} \{ \mathbf{E} \times \mathbf{H}^* \} \quad (2.38)$$

where \mathbf{H}^* is the conjugate complex of \mathbf{H} . \mathbf{S} combines the information of the direction $\mathbf{s} = \mathbf{k}/|\mathbf{k}|$ in the propagation vector with the power of an electromagnetic (EM) wave per area in Watts per square meter, which is contained in the irradiance $I = |\langle \mathbf{S} \rangle_T| [W/m^2]$. So, the direction of \mathbf{S} is equal to the direction of the propagation vector and its length is equal to the intensity of the field

$$\frac{\mathbf{S}}{I} = \frac{\mathbf{k}}{k} = \mathbf{s} \quad (2.39)$$

For plane waves, \mathbf{H} can be derived from \mathbf{E} according to

$$\mathbf{H} = \sqrt{\frac{\epsilon\epsilon_0}{\mu\mu_0}} \cdot (\mathbf{s} \times \mathbf{E}) = \frac{n}{\mu Z_0} \cdot (\mathbf{s} \times \mathbf{E}) \quad (2.40)$$

Since an EM wave is an oscillating field, the time average $\langle \cdot \rangle_T = 1/T \int_T (\cdot) dt$ is again necessary to compute the effective value of \mathbf{E} and \mathbf{H} . Substituting the magnetic vector \mathbf{H} , the Poynting vector can then be fully expressed by the electric field and the refractive index of the medium. In average time, the irradiance of an EM-wave is then

$$\langle \mathbf{S} \rangle_T = \frac{1}{2} \text{Re} \left\{ \mathbf{E} \times \left(\sqrt{\frac{\epsilon\epsilon_0}{\mu\mu_0}} (\mathbf{s} \times \mathbf{E}) \right)^* \right\} \quad (2.41)$$

2.4 Power flux

Starting with the Poynting vector \mathbf{S} , the energy flux of an EM-wave which is carried in a vertical direction through an interface can be obtained. The power flux P [W] or energy flux per time $\partial W/\partial t$ [J/s]

$$P = \frac{\partial W}{\partial t} = \int \mathbf{S} \cdot d\mathbf{A} \quad (2.42)$$

through a surface with the normal $d\mathbf{A} = \mathbf{n}dA$ and an area dA [m^2] is a conserved quantity across interfaces according to the conservation law in equation 2.78.

2.5 Absorption in homogeneous media

The absorbing medium is characterized by its complex dielectric permittivity $\hat{\epsilon} = \epsilon_r + i\epsilon_i$ which is coupled to the complex refractive index $\hat{n} = n + i\kappa$ according to $\hat{\epsilon} = \hat{n}^2$ (with $\hat{\mu} = 1$) and then

$$\begin{aligned} \epsilon_r &= n^2 - \kappa^2 \\ \epsilon_i &= 2n\kappa \end{aligned} \quad (2.43)$$

The refractive index computes from the dielectric permittivity according to

$$\begin{aligned} n &= \pm \sqrt{\frac{\sqrt{\epsilon_r^2 + \epsilon_i^2} + \epsilon_r}{2}} \\ \kappa &= \pm \sqrt{\frac{\sqrt{\epsilon_r^2 + \epsilon_i^2} - \epsilon_r}{2}} \end{aligned} \quad (2.44)$$

An interesting observation is the ambiguity (i.e. \pm) of the refractive index n , when derived from the dielectric permittivity. In this thesis, the positive solution of the square root is taken whenever n or κ are used. Deriving the wavenumber k from the complex refractive index according to $k = (n + i\kappa)k_0 = \hat{n}k_0$ and using the relationship $I \approx E^2$, the absorption coefficient $\alpha = 2\kappa k_0$ is obtained as shown in appendix A. The imaginary part of \hat{n} is therefore responsible for the exponential attenuation of EM-waves in an absorbing medium.

2.6 Absorption in inhomogeneous media

An elegant derivation of the local absorption from the spatial distribution of the electric field $\mathbf{E}(\mathbf{r})$ and the refractive index $n(\mathbf{r})$ is introduced in [30]. There, the time derivative of the energy density $(\partial w_e + \partial w_m)/\partial t$, with the electric w_e and magnetic w_m energy, is utilized to compute the *local absorption of energy*. It is derived from the divergence of the Poynting vector $\text{div}(\mathbf{S}) = \nabla \cdot \mathbf{S}$ according to the Poynting theorem

$$\begin{aligned} \mu\mu_0 (\nabla \cdot \mathbf{S}) &= \nabla \cdot (\mathbf{E} \times (\mu\mu_0 \mathbf{H}^*)) \\ &= \mu\mu_0 \mathbf{H}^* \cdot (\nabla \times \mathbf{E}) - \mathbf{E} \cdot (\nabla \times (\mu\mu_0 \mathbf{H}^*)) \end{aligned} \quad (2.45)$$

Using Maxwells' equations in the differential form

$$\begin{aligned} \nabla \times \mathbf{E} &= -\mu_0\mu \frac{\partial \mathbf{H}}{\partial t} \\ \nabla \times \mathbf{H} &= \mathbf{J}_c + \epsilon\epsilon_0 \frac{\partial \mathbf{E}}{\partial t} \end{aligned} \quad (2.46)$$

in the time average of the Poynting vector $\langle S \rangle_T = 1/2 \text{Re}(\mathbf{E} \times \mathbf{H}^*)$, the expression transforms to

$$\mu\mu_0 (\nabla \cdot \mathbf{S}) = -\frac{\mu\mu_0}{4} \left(\mathbf{H}^* \frac{\partial \mathbf{H}}{\partial t} \right) - \frac{1}{4} \left(\mathbf{E} (\mathbf{J}_c + \epsilon\epsilon_0 \frac{\partial \mathbf{E}}{\partial t})^* + \mathbf{E}^* \cdot (\mathbf{J}_c + \epsilon\epsilon_0 \frac{\partial \mathbf{E}}{\partial t}) \right) \quad (2.47)$$

Using $\mathbf{F} \partial \mathbf{F} / \partial t = 1/2 \cdot \partial \mathbf{F}^2 / \partial t$, which is valid for all vector fields with a complex exponential phasor, and considering the complex nature of the electric permittivity $\hat{\epsilon} = \epsilon_r + i\epsilon_i$ and assuming a monochromatic field which is proportional to $\exp(i\omega t)$, the expression is then

$$\nabla \cdot \mathbf{S} + \frac{\mu\mu_0}{4} \frac{\partial}{\partial t} |\mathbf{H}|^2 + \frac{\epsilon_r \epsilon_0}{4} \frac{\partial}{\partial t} |\mathbf{E}|^2 = -\frac{1}{2} \text{Re}(\mathbf{E} \cdot \mathbf{J}_c^*) + \frac{\epsilon_i \epsilon_0}{2} \omega |\mathbf{E}|^2 \quad (2.48)$$

where $\text{Re}()$ denotes the real part of a complex quantity. This expression contains the time derivative of the electric and magnetic energy density

$$\begin{aligned} \frac{(\partial w_e + \partial w_m)}{\partial t} &= \frac{\mu\mu_0}{4} \frac{\partial}{\partial t} |\mathbf{H}|^2 + \frac{\epsilon_r \epsilon_0}{4} \frac{\partial}{\partial t} |\mathbf{E}|^2 \\ &= -\nabla \cdot \mathbf{S} - \frac{1}{2} \text{Re}(\mathbf{E} \cdot \mathbf{J}_c^*) + \frac{\epsilon_i \epsilon_0}{2} \omega |\mathbf{E}|^2 \end{aligned} \quad (2.49)$$

which describes the change of the electromagnetic energy per area unit and time [$J/m^2/s = W/m^2$]. The electric current density \mathbf{J}_c can be neglected for high frequencies and then the equation for the stationary state (i.e. $(\partial w_e + \partial w_m)/\partial t = 0$) transforms to

$$\nabla \cdot \mathbf{S} = \frac{\epsilon_i \epsilon_0}{2} \omega |\mathbf{E}|^2 \quad (2.50)$$

Taking the positive value from equation 2.44, the imaginary part of the electric permittivity can be transformed and the stationary energy per area is then

$$\nabla \cdot \mathbf{S} = n\kappa\epsilon_0\omega |\mathbf{E}|^2 \quad (2.51)$$

Finally, the area-dependent vector equation can be transformed to a volume-specific number according to the Gaussian law

$$\iint \mathbf{S} d\mathbf{A} = \iiint n(\mathbf{r})\kappa(\mathbf{r})\epsilon_0\omega|\mathbf{E}(\mathbf{r})|^2 d^3\mathbf{r} \quad (2.52)$$

An infinitesimal unit of volume dV absorbs the energy $n(\mathbf{r})\kappa(\mathbf{r})\epsilon_0\omega|\mathbf{E}(\mathbf{r})|^2$. The integral over the volume V then yields the total energy in V .

2.7 Discrete Fourier transformation

The discrete Fourier transformation plays a central role in the Fast Fourier simulators and in *Fourier optics*. While the Fourier analysis in electrical engineering operates on time-dependent signals, the spectrum of a spatial field distribution or of a spatial distribution of the refractive index is computed in Fourier optics. The input is a spatial distribution $\mathbf{E}(\mathbf{r})$ in an aperture $A = XY$, with side lengths X in the x-axis and Y in the y-axis. The number of samples n_x and n_y in the two-dimensional aperture defines the minimum distance for a periodic appearance of light and the input signal is assumed to be continued periodically to $\pm\infty$. The forward Fourier transformation \mathcal{F} computes the spectrum $\tilde{\mathbf{E}}(\mathbf{k})$ and $\mathbf{k} = 2\pi\boldsymbol{\nu}$ is called the spatial frequency.

In a discrete system, the two-dimensional index of the location (l, m) and of the spatial frequency (p, q) is related to the space vector $\mathbf{r} = (x \ y)^T$ and the two-dimensional transversal propagation vector $\mathbf{k}_\perp = (k_x \ k_y)^T$ according

to

$$\begin{aligned} x(l) &= lX/n_x \quad , \quad y(m) = mY/n_y \\ k_x(p) &= p2\pi/X \quad , \quad k_y(q) = q2\pi/Y \end{aligned} \quad (2.53)$$

with the superscript T indicates the transposed of a vector.

2.7.1 Forward Fourier transformation

In the discrete case, a two-dimensional spectrum $\tilde{\mathbf{E}}(p, q)$ of a discrete two-dimensional field distribution $\mathbf{E}(l, m)$ with $(p, l) \in N_x$ and $(q, m) \in N_y$ and $N_x = \{0, 1, \dots, n_x - 1\}$ and $N_y = \{0, 1, \dots, n_y - 1\}$ is

$$\tilde{\mathbf{E}}(p, q) = \sum_{l=0}^{n_x-1} \sum_{m=0}^{n_y-1} \mathbf{E}(l, m) e^{-i2\pi \frac{lp+mq}{n_x n_y}} \quad (2.54)$$

2.7.2 Inverse Fourier transformation

The Fourier coefficients $\tilde{\mathbf{E}}(p, q)$ in the spectrum of an EM-field provide the complex amplitudes of corresponding plane waves $\exp(+i2\pi(pl + qm)/n_x/n_y)$ which are needed to spatial field \mathbf{E} at a position (l, m) . The sum of all plane waves yields the inverse discrete Fourier transformation according to

$$\mathbf{E}(l, m) = \frac{1}{n_x n_y} \sum_{p=0}^{n_x-1} \sum_{q=0}^{n_y-1} \tilde{\mathbf{E}}(p, q) e^{+i2\pi \frac{lp+mq}{n_x n_y}} \quad (2.55)$$

With equation 2.54, the spectrum of an EM field in an aperture $A = n_x \delta x n_y \delta y = XY$ is computed and by using equation 2.55 the spatial field

distribution is retrieved from a spectrum. The relationship of the two representations of \mathbf{E} in the spatial domain and in the spectral domain is described by the correspondence operator

$$\mathbf{E} \circ \bullet \tilde{\mathbf{E}} \quad (2.56)$$

2.8 Spatial sampling and propagation angle

In a discretized two-dimensional aperture, the two-dimensional index (p, q) corresponds to a transversal propagation vector according to

$$\begin{pmatrix} k_x \\ k_y \end{pmatrix} = \begin{pmatrix} p\delta k_x \\ q\delta k_y \end{pmatrix} \quad (2.57)$$

with frequency increments $\delta k_x = 2\pi/X$ and $\delta k_y = 2\pi/Y$. From the length of the transversal propagation vector $\delta k_{\perp} = \sqrt{\delta k_x^2 + \delta k_y^2}$, the angular increment in the two-dimensional case is

$$\delta\theta = \sin^{-1}\left(\frac{\delta k_{\perp}}{k}\right) \quad (2.58)$$

with $k = 2\pi n/\lambda$, which is the length of the propagation vector. As a result of the sampling in the aperture, the number of discrete angles of incidence and transmission in the spectrum and on the discretized circle of unity is determined.

Example

A propagating TM-mode, with $\theta_e = \pi/9$ and a sampling of $n_x = 128$ in an aperture $X = 8$ discretizes the unit circle into 128 frequency increments of

$\delta k_x = 2\pi/X = 0.125$ [rad] which is equal to an angle increment of 7.181 degrees, obtained from

$$\begin{aligned}\delta\theta &= \sin^{-1}\left(\frac{\delta k_{\perp}}{k}\right) \\ &= \sin^{-1}\left(\sqrt{\left(\frac{\lambda}{X}\right)^2 + \left(\frac{\lambda}{Y}\right)^2}\right)\end{aligned}\quad (2.59)$$

With this increment, the angle of incidence $\theta_e = \pi/9$ is ideally reproduced from the index $p_e = 2.785$ and the angle of transmission θ_t from the index $p_t = 1.375$ according to Snell's law in equation 2.66. Since only whole numbers are possible in the discrete calculation, the spectrum consists of a multitude of coefficients which develop the correct angle of incidence from a superposition of modes with a different spatial frequency \mathbf{k}_{\perp} and amplitude $\tilde{\mathbf{E}}(\mathbf{k}_{\perp})$ according to the inverse Fourier transformation.

2.9 Plane Wave Decomposition

Taking the electric field at a position z , $E(\mathbf{k}_{\perp}; z)$, the field distribution at a distance $z + \delta z$ is derived from the spectrum of the field $\tilde{\mathbf{E}}(\mathbf{k}_{\perp}; z)$ with the *plane wave decomposition*

$$\begin{aligned}\mathbf{E}(\mathbf{r}_{\perp}; z + \delta z) &= \frac{1}{2\pi} \iint \tilde{\mathbf{E}}(\mathbf{k}_{\perp}; z) e^{i\phi z} e^{i\mathbf{k}_{\perp} \cdot \mathbf{r}_{\perp}} \frac{d^2\mathbf{k}_{\perp}}{(2\pi)^2} \\ &= \frac{1}{2\pi} \iint \tilde{\mathbf{E}}(\mathbf{k}_{\perp}; z) \tilde{H}(\mathbf{k}_{\perp}; \delta z) e^{i\mathbf{k}_{\perp} \cdot \mathbf{r}_{\perp}} \frac{d^2\mathbf{k}_{\perp}}{(2\pi)^2} \\ &= \mathcal{F}^{-1} \left\{ \tilde{\mathbf{E}}(\mathbf{k}_{\perp}; z) \tilde{H}(\mathbf{k}_{\perp}; \delta z) \right\}\end{aligned}\quad (2.60)$$

$\tilde{H}(\mathbf{k}_{\perp}; \delta z)$ is the *spatial frequency transfer function of propagation* [4] which describes the propagation of an electric field \mathbf{E} from z over a distance δz

to $z + \delta z$. There, the phase of a spectral component (k_x, k_y) is shifted by

$$\begin{aligned}\phi_z &= \delta z k_z(k_x, k_y) \\ &= \delta z \sqrt{k^2 - (k_x^2 + k_y^2)} \\ &= \delta z \sqrt{n^2 k_0^2 - k_\perp^2}\end{aligned}\quad (2.61)$$

with $k_0 = 2\pi/\lambda_0$. In the discrete case, the propagation through a homogeneous medium (i.e. $n = \text{const}$) over a distance δz from a starting point z of an EM-wave is then

$$\begin{aligned}\mathbf{E}(m\delta x, n\delta y; (z+1)\delta z) &= \frac{1}{n_x n_y} \sum_{p=0}^{n_x-1} \sum_{q=0}^{n_y-1} \tilde{\mathbf{E}}(p\delta k_x, q\delta k_y; \delta z) e^{+i\phi_z(p\delta k_x, q\delta k_y)} e^{+i2\pi \frac{lp+mq}{n_x n_y}} \\ &= \mathcal{F}^{-1} \left\{ \tilde{\mathbf{E}}(z) e^{+i\phi_z(p\delta k_x, q\delta k_y)} \right\}\end{aligned}\quad (2.62)$$

equal to the vectorial diffraction integral [52].

2.9.1 Convolution theorem

In the convolution theorem, transformations in the spectral domain are expressed in the spatial domain. It provides a correspondence for equation 2.60 in the spatial and spectral domain

$$\mathbf{E}(\mathbf{r}_\perp; z) * H(\mathbf{r}_\perp; \delta z) \circ \bullet \tilde{\mathbf{E}}(\mathbf{k}_\perp; z) \tilde{H}(\mathbf{k}_\perp; \delta z) \quad (2.63)$$

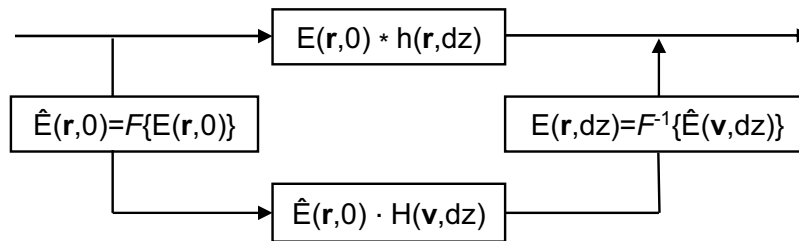
with the *convolution integral*

$$\mathbf{E}(\mathbf{r}_\perp; z) * H(\mathbf{r}_\perp; \delta z) = \int_X \int_Y \mathbf{E}(\mathbf{r}_\perp; z) \cdot H(\mathbf{r}_\perp - \mathbf{r}'_\perp; \delta z) d^2 \mathbf{r}'_\perp \quad (2.64)$$

Weyl has shown in [38] that $H(\mathbf{r}_\perp; \delta z)$ is the spherical wave of the form

$$\mathbf{E}(\mathbf{r}, t) = \frac{\mathbf{E}_0}{r} \cdot e^{i(kr - \omega t)} \quad (2.65)$$

Figure 2.2: A convolution in the spatial domain is dual to a multiplication of the two Fourier transformed (convolution theorem).

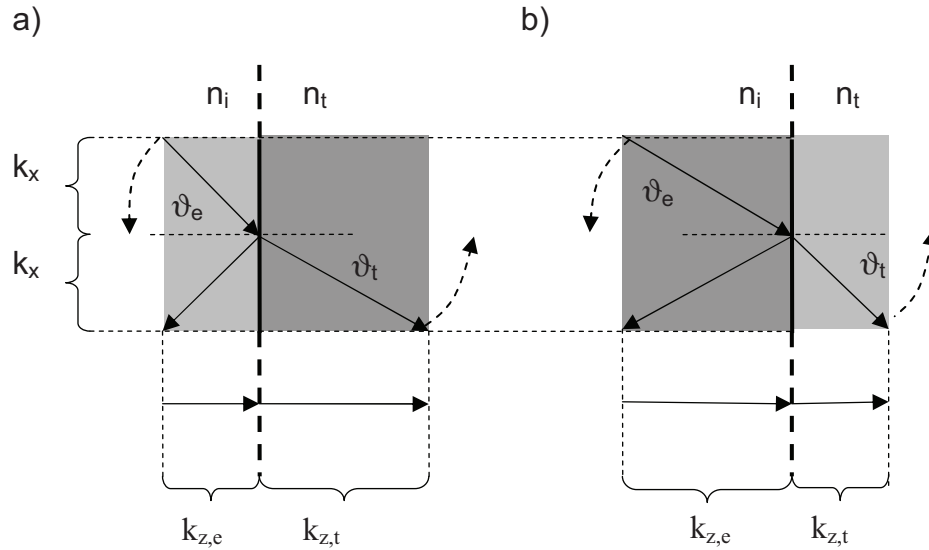


with $k = |\mathbf{k}|$ and $r = |\mathbf{r}|$ in agreement with Huygen's principle. The central statement of the convolution theorem is that a multiplication in the spectral domain corresponds to a convolution in the spatial domain. With this observation, the computationally expensive convolution can be substituted by a simple multiplication and a forward and inverse Fourier transformation as shown in figure 2.2. This theorem is dual and hence a convolution of a spectrum can be replaced by a multiplication in the spatial domain as shown in [39].

2.10 Reflection and transmission

At a boundary with a refractive index $\hat{n}_e = n_e + i\kappa_e$ before and a refractive index $\hat{n}_t = n_t + i\kappa_t$ behind the interface, the electromagnetic wave changes its speed from $v_e = c/n_e$ to $v_t = c/n_t$ with the real and imaginary part of the refractive index to be derived from the electric permittivity according to equation 2.44. The frequency ω remains constant across the interface, because the relationship $\mathbf{E}_e + \mathbf{E}_r = \mathbf{E}_t$ requires $(\mathbf{k}_e \cdot \mathbf{r} - \omega_e t) = (\mathbf{k}_r \cdot \mathbf{r} - \omega_r t) =$

Figure 2.3: *EM wave at a boundary. (a) $n_e < n_t$. (b) $n_e > n_t$. The variation in the light's speed causes a change in k_z .*



$(\mathbf{k}_t \cdot \mathbf{r} - \omega_t t)$ to be met for all times t and all locations \mathbf{r} . Hence, the wave vector \mathbf{k} changes across the interface and the speed of light is $v_e = \omega/k_e$ and $v_t = \omega/k_t$.

Since the transversal subvector \mathbf{k}_\perp of \mathbf{k} is constant across the boundary due to the law of continuity, the z-component $k_z = \sqrt{(nk_0)^2 - k_\perp^2}$ changes as shown in figure 2.3. From this observation, Snell's law

$$n_e \sin \theta_e = n_t \sin \theta_t \quad (2.66)$$

and in combination with the conservation law, the Fresnel coefficients of

transmission

$$\begin{aligned} t_{TE} &= \frac{2n_e \cos \theta_e}{n_e \cos \theta_e + n_t \cos \theta_t} = \frac{E_t}{E_e} \\ t_{TM} &= \frac{2n_e \cos \theta_e}{n_t \cos \theta_e + n_e \cos \theta_t} = \frac{E_t}{E_e} \end{aligned} \quad (2.67)$$

and reflection

$$\begin{aligned} r_{TE} &= \frac{n_e \cos \theta_e - n_t \cos \theta_t}{n_e \cos \theta_e + n_t \cos \theta_t} = \frac{E_r}{E_e} \\ r_{TM} &= \frac{n_t \cos \theta_e - n_e \cos \theta_t}{n_t \cos \theta_e + n_e \cos \theta_t} = \frac{E_r}{E_e} \end{aligned} \quad (2.68)$$

are obtained. Appendix A provides more details on Fresnel's coefficients for evanescent waves. There, the z-component of the propagation vector is then a purely imaginary quantity.

2.11 Evanescent waves

The angle of incidence θ_e varies between 0 [rad] and $\pi/2$ [rad]. In case of external refraction, the angle of transmission θ_t is always smaller or equal (i.e. vertical incidence) than the angle of incidence θ_e . The maximum angle of refraction is then $\sin \theta_t^{max} = n_e/n_t$, obtained from equation 2.66 with $\theta_e = \pi/2$. For internal refraction, the angle of transmission is always greater than or equal to the angle of incidence. The critical angle of incidence $\sin \theta_c = n_t/n_e$ is then obtained from equation 2.66, using $\theta_t = \pi/2$. For $n_t < n_e$ and $\theta_e > \theta_c$, equation 2.66 yields $\sin \theta_t = n_e/n_t \sin \theta_e > 1$. Consequently, a complex angle of transmission is then needed to prove Snell's law. This brings in a complex z-component of the propagation vector by using $\sin^2 \theta_t = n_e^2/n_t^2 \sin^2 \theta_e$ in $k_{z,t}^2 = n_t^2 k_0^2 \cos^2 \theta_t = n_t^2 k_0^2 (1 - \sin^2 \theta_t)$. A

reordering of the index of refraction then yields

$$k_{z,t} = ik_0 \sqrt{\sin\theta_e - \frac{n_t^2}{n_e^2}} = i\sqrt{k_\perp^2 - n_t^2 k_0^2} \quad (2.69)$$

if $\sin\theta_t > 1$ or $k_\perp^2 > n_t^2 k_0^2$ (i.e. the evanescent case). Since k_\perp is supposed to remain continuous across interfaces, the transformation k_z at an interface determines the change in the angle of incidence as described by Snell's law (eq. 2.66). In case of *internal reflection* in plot (b) of figure 2.3, the critical angle of *total internal reflection* (TIR) θ_c

$$\sin\theta_c = \frac{n_t}{n_e} \quad (2.70)$$

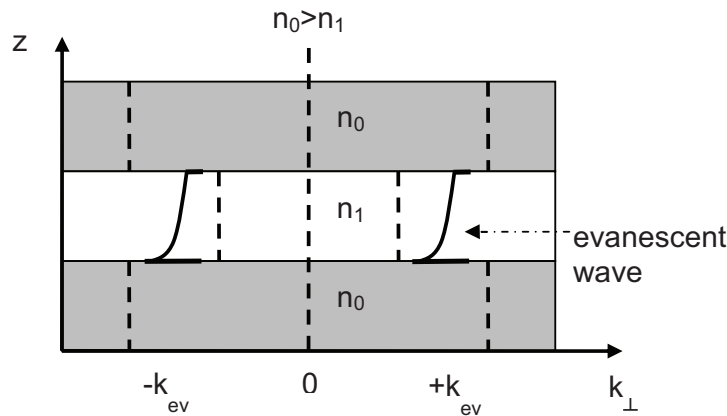
corresponds to the spectral boundary for evanescent waves at an interface as shown in Appendix A. Evanescent waves are obtained for $\theta_e > \theta_c$ and the z-component of the propagation vector is then purely imaginary as shown in equation 2.69 and 2.71. An evanescent wave is not transversal since components of the electric field vector are parallel to the propagation vector as shown in [1]. In case of $k_\perp = nk_0$, the propagation vector is parallel to the interface and $k_{z,t}$ is zero. The transmitted wave then propagates along the interface, the surface normal is perpendicular to the propagation vector and the energy flux through the interface is zero.

2.11.1 Complex propagation constant

The z-component of the complex \hat{k} is categorized into

$$\begin{aligned} \hat{k}_z &= \sqrt{(nk_0)^2 - k_\perp^2} + i0 \Leftrightarrow k_\perp < nk_0 \quad (i) \\ \hat{k}_z &= 0 + i0 \Leftrightarrow k_\perp = nk_0 \quad (ii) \\ \hat{k}_z &= 0 + i\sqrt{k_\perp^2 - (nk_0)^2} \Leftrightarrow k_\perp > nk_0 \quad (iii) \end{aligned} \quad (2.71)$$

Figure 2.4: *Evanescent coupling, optical tunneling, frustrated total internal reflection (FTIR) at two adjacent interfaces. The electromagnetic wave propagates from bottom up.*



the *propagation case i*, the *evanescent boundary ii* and the *evanescent case iii*. The evanescent boundary $k_{\perp} = n_t k_0$ is indicated by the dashed lines in figure 2.4 to the left and right of the center-frequency $k_{\perp} = 0$. The evanescent boundary does not describe an evanescent but a propagating wave.

2.11.2 Evanescent decay

In the evanescent case (i.e. $k_{\perp} > n_t^2 k_0^2$), the z -component of the propagation vector of an evanescent wave is a purely imaginary quantity $\hat{k}_z = i\sqrt{k_{\perp}^2 - (nk_0)^2} = +i\gamma_z$. Inserting the complex phase argument into equation 2.12 then causes a laterally propagating and a longitudinally

damped *evanescent wave* since $i^2 = -1$), commonly known as an evanescent wave or laterally damped wave

$$\begin{aligned}\mathbf{E}_{ev}(\mathbf{r}) &= \mathbf{E}_t \cdot e^{i\mathbf{k}\cdot\mathbf{r}} \\ &= \mathbf{E}_t \cdot e^{i(k_x x + k_y y + i\gamma z)} \\ &= \mathbf{E}_t \cdot e^{i\mathbf{k}_\perp \cdot \mathbf{r}_\perp} \cdot e^{-\gamma z}\end{aligned}\quad (2.72)$$

Evanescent waves are supposed to decay even in the absence of absorption, caused by the complex solution of $\cos \theta_t$. The amplitude \mathbf{E}_t of the evanescent wave is then

$$\mathbf{E}_t = \begin{pmatrix} E_x \\ E_y \\ E_z \end{pmatrix} = \begin{pmatrix} i \cos \theta_t \hat{t}_{TM}(\mathbf{E}_e \cdot \mathbf{e}_{TM}) \\ \hat{t}_{TE}(\mathbf{E}_e \cdot \mathbf{e}_{TE}) \\ \sin \theta_t \hat{t}_{TM}(\mathbf{E}_e \cdot \mathbf{e}_{TM}) \end{pmatrix}\quad (2.73)$$

as shown in [1] and [55]. $\mathbf{e}_{TE} = (\mathbf{s} \times \mathbf{n})$ is the vector of unity perpendicular to the plane of incidence with \mathbf{n} is the surface normal of the boundary. The expression is obtained from the insertion of the complex cosines into the vectorial components of the transmitted vector amplitude as shown in Appendix A.

2.11.3 Energy flux of evanescent waves

For all $\theta_e > \theta_c$, the propagation vector is parallel to the interface and the scalar product with the surface normal is zero. Therefore, the energy flux $\mathbf{S} \cdot d\mathbf{A}$ of evanescent waves is zero and the conservation law $1 + \mathcal{R} = \mathcal{T}$ is preserved. Second, evanescent waves carry no energy because the complex solution of the propagation constant yields an imaginary cosines and a phase shift of $\pi/2$ between E_x and H_y as well as E_y and H_x as shown

in appendix A. The energy flux in time average $\langle S_z \rangle_T = 1/T \int_0^T S_z dt$, with $S_z = E_x H_y + E_y H_x$ is the z-component of the Poynting vector, is then zero. Another argumentation for the zero energy flux of evanescent waves is given in [2]. There, the evanescent wave is described to "circulate back and forth across the interface, resulting on the average in a zero net flow through the boundary into the second medium".

2.11.4 Optical tunneling

In case of two boundaries in close proximity and the first boundary providing internal, the second boundary external reflection as shown in figure 2.4, the evanescent wave couples across the short distance before it decays completely. This effect is called *frustrated total internal reflection* (FTIR) or *optical tunneling* and is used for ring resonators and add-drop filters. This coupling can be explained by the complex medium coefficients $\hat{n} = n + i\kappa$ and that the propagation constant is not truly parallel in case of evanescent waves in lossy or gaining medium as shown in [36].

2.11.5 Fresnel coefficients in the evanescent case

In the evanescent case, the *reflected wave* is derived from Fresnel's coefficients of reflection

$$\begin{aligned}\hat{r}_{TE} &= \frac{k_{z,e} - i\gamma_{z,t}}{k_{z,e} + i\gamma_{z,t}} \\ \hat{r}_{TM} &= \frac{k_{z,e}n_t^2 - i\gamma_{z,t}n_e^2}{k_{z,e}n_t^2 + i\gamma_{z,t}n_e^2}\end{aligned}\quad (2.74)$$

by inserting the complex $\hat{k}_{z,t} = +i\gamma_{z,t}$ into equation 2.68. The Fresnel reflection coefficients are then complex quantities of the form c/c^* with a magnitude of $|c/c^*| = 1$ for all $\theta_e > \theta_c$. In case of total internal reflection and complex Fresnel coefficients of reflection, the reflected wave experiences a phase shift, the so called *Goos Hähnchen Shift*. In the evanescent case, the Fresnel transmission coefficients are again derived from the conservation law $t_{TE} = 1 + r_{TE}$ and $t_{TM} = n_e/n_t(1 + r_{TM})$ according to

$$\begin{aligned}
 \hat{t}_{TE} &= 1 + \frac{k_{z,e} - i\gamma_{z,t}}{k_{z,e} + i\gamma_{z,t}} \\
 &= \frac{k_{z,e} + i\gamma_{z,t} + k_{z,e} - i\gamma_{z,t}}{k_{z,e} + i\gamma_{z,t}} = \frac{2k_{z,e}}{k_{z,e} + i\gamma_{z,t}} \\
 \hat{t}_{TM} &= \frac{n_e}{n_t} \left(1 + \frac{k_{z,e}n_t^2 - i\gamma_{z,t}n_e^2}{k_{z,e}n_t^2 + i\gamma_{z,t}n_e^2} \right) \\
 &= \frac{n_e}{n_t} \left(\frac{2k_{z,e}n_t^2}{k_{z,e}n_t^2 + i\gamma_{z,t}n_e^2} \right) \\
 &= \frac{2k_{z,e}n_en_t}{k_{z,e}n_t^2 + i\gamma_{z,t}n_e^2} \tag{2.75}
 \end{aligned}$$

For the evanescent boundary (i.e. $k_{bot} = nk_0$), the transmission coefficients are $\hat{t}_{TE} = 2$ and $\hat{t}_{TM} = 2n_e/n_t$. The expressions are also obtained by inserting the complex z-components of the propagation vector into equation 2.67 which corresponds to the results in [55]. In case of a absorbing or gaining medium on either or both sides of the boundary, the equations are simply extended to the complex quantities $\hat{n}_e = n_e + ik_e$, $\hat{n}_t = n_t + ik_t$, $\hat{k}_{z,e} = k_{z,e} + i\gamma_{z,e}$ and $\hat{k}_{z,t} = k_{z,t} + i\gamma_{z,t}$. Then the propagation vector is not perfectly parallel to the interface as shown in [36]. In this case, no discrete critical angle exist, because Fresnel's coefficients of reflection experience a gradual turn from purely real to complex values. For lossless or gainless medium, this change is a discrete point and the coefficients abruptly become complex quantities once the critical angle is exceeded.

2.12 Reflectance and transmittance

For real-valued $k_{z,e} = \text{Re}(\hat{k}_{z,e})$ and $k_{z,t} = \text{Re}(\hat{k}_{z,e})$, the transmitted and reflected irradiance of a wave is coupled by the transmittance

$$\begin{aligned}\mathcal{T}_{TE} &= |t_{TE}|^2 \frac{n_t \cos \theta_t}{n_e \cos \theta_e} = |t_{TE}|^2 \frac{k_{z,t}}{k_{z,e}} \\ \mathcal{T}_{TM} &= |t_{TM}|^2 \frac{n_t \cos \theta_t}{n_e \cos \theta_e} = |t_{TM}|^2 \frac{k_{z,t}}{k_{z,e}}\end{aligned}\quad (2.76)$$

and the reflectance

$$\begin{aligned}\mathcal{R}_{TE} &= |r_{TE}|^2 \\ \mathcal{R}_{TM} &= |r_{TM}|^2\end{aligned}\quad (2.77)$$

and the law of conservation states

$$1 + \mathcal{R} = \mathcal{T}\quad (2.78)$$

for the irradiance of the TE and TM component of an electromagnetic field. The absorptance \mathcal{A} is then the loss in a volume by means of absorption. It is determined by

$$\mathcal{A} = 1 - \mathcal{R} - \mathcal{T}\quad (2.79)$$

In case of total internal reflection and evanescent waves, Fresnel's coefficients of reflection are of the form c/c^* , with c is a complex quantity. Then, the squared magnitude cc^* is unity, the reflectance is unity and the transmittance is zero. This agrees to the observation that evanescent waves do not carry energy across the interface.

Chapter 3

Vector Wave Propagation Method

Split step propagation methods like the beam propagation method (BPM) have been primarily developed for simulating light propagation in waveguides. By applying the distributed propagation operator, which is derived from the slowly varying complex exponential envelope approximation of the Helmholtz equation, propagation methods are typically restricted to forward propagation, small index variations and the paraxial regime.

In the original BPM scheme by Feit and Fleck [13], the propagation operator is split into a homogeneous medium propagation in the averaged refractive index and a thin element transmission through the index variation. With the application of propagation methods to more general optical components, such as gradient index media, aspheric lenses and gratings, there is much interest in removing these restrictions.

The scalar wave propagation method (WPM) has been introduced by Brenner and Singer in 1993 [31] in order to overcome the restrictions to paraxial propagation and small index variations in the BPM. Instead of splitting the propagation operator, the WPM decomposes a field distribution into its plane wave components and performs a non-paraxial plane-wave propagation in an inhomogeneous medium for each plane wave component. The field is then calculated as a sum over all plane wave components according to the Rayleigh-Sommerfeld integral. Since this sum cannot be performed by an inverse FFT, the calculation time of the WPM grows with $\mathcal{O}(N^2)$ in the two-dimensional case, whereas the BPM calculation time of the split step propagation scheme is proportional to $\mathcal{O}(N)$, taking N as the number of spatial samples.

In [31], the accuracy of the scalar WPM was validated for propagation angles up to 85 degrees and also for large index steps. The original scalar WPM extended the range of spatial frequencies significantly and hence vectorial effects cannot be longer neglected. A vectorial WPM is desirable. In the Vector Wave Propagation Method (VWPM), the wave propagation scheme is utilized to compute the propagation of three-dimensional vector fields by considering the polarization dependent Fresnel transmission coefficients. The accuracy of this approach is validated by transmission through a prism and by comparison with the focal distribution from vectorial Debye theory. Furthermore, the field distribution in a binary phase Ronchi in the range of a few wavelengths is compared to the results from RCWA.

3.1 Split step propagation scheme

An analysis of the original beam propagation method (BPM), as an example for the split step propagation scheme, serves to illustrate the differences introduced in the WPM. It provides some of the reasons to extend the scalar WPM to three-dimensional vector-fields and introduces an optimization of the WPM and VWPM for efficient light propagation in a homogeneous media.

The BPM uses a separation of the refractive index $n = \bar{n} + \delta n$. The separation of n provides the ability to calculate the propagation in the homogeneous averaged refractive index \bar{n} for all spatial frequencies in a single step of calculation by multiplication with the *diffraction operator* $\tilde{\mathcal{D}}$. The diffraction operator has to be applied in the Fourier space to consider the spatial frequencies $k_x = 2\pi\nu_x$ and $k_y = 2\pi\nu_y$ of the *plane wave decomposition* (PWD) [35]. The separation of the refractive index introduces two sources of error to the calculation of k_z

$$\begin{aligned}
\sqrt{n^2 k_0^2 - k_\perp^2} &= \sqrt{(\bar{n} + \delta n)^2 k_0^2 - k_\perp^2} \\
&= \sqrt{\bar{n}^2 k_0^2 - k_\perp^2 + 2\bar{n} \delta n k_0^2 + \delta n^2 k_0^2} \\
&= \sqrt{\bar{n}^2 k_0^2 - k_\perp^2} \cdot \sqrt{1 + \frac{2\bar{n} \delta n k_0^2 + \delta n^2 k_0^2}{\bar{n}^2 k_0^2 - k_\perp^2}} \\
&= \sqrt{\bar{n}^2 k_0^2 - k_\perp^2} \cdot \left(1 + \frac{\bar{n} \delta n k_0^2}{\bar{n}^2 k_0^2 - k_\perp^2} + \mathcal{O}(\delta n^2) \right) \\
&\approx^{(1)} \sqrt{\bar{n}^2 k_0^2 - k_\perp^2} + \frac{\bar{n} \delta n k_0^2}{\sqrt{\bar{n}^2 k_0^2 - k_\perp^2}} \\
&\approx^{(2)} \sqrt{\bar{n}^2 k_0^2 - k_\perp^2} + \frac{\bar{n} \delta n k_0^2}{\bar{n} k_0} \\
&= \sqrt{\bar{n}^2 k_0^2 - k_\perp^2} + k_0 \delta n = k_z
\end{aligned} \tag{3.1}$$

A first error $\approx^{(1)}$ arises from the approximation of the square root by the linear part of its binomial expansion to separate the entire term into two fractions that depend on \bar{n} and δn . This error is in $\mathcal{O}(\delta n^2)$ and is responsible for the angle indiscriminate propagation through the index variation δn . A second error $\approx^{(2)}$ is caused by the paraxial approximation ($k_z^2 \gg k_x^2 + k_y^2$) that is necessary to reduce the term and make it usable in the split step scheme. The diffraction operator $\tilde{\mathcal{D}}$ and phase shift operator \mathcal{S} are

$$\tilde{\mathcal{D}}(\mathbf{k}_\perp) = \tilde{\mathcal{D}}(k_x, k_y) = e^{i\sqrt{(\bar{n}k_0)^2 - (k_x^2 + k_y^2)}\delta z} \quad (3.2)$$

and

$$\mathcal{S}(\mathbf{r}_\perp) = \mathcal{S}(x, y) = e^{i\delta n(x,y)k_0\delta z} \quad (3.3)$$

The approximation of the phase shift is then applied to Rayleigh's diffraction integral (eq. 2.60). The separation of the constant and variable term in the complex exponential function yields equation (3.4). It applies the phase change along the axis of propagation for a distance δz with the *diffraction operator* $\tilde{\mathcal{D}}$ and the phase shift which is caused by the change in the refractive index in the *phase shift operator* \mathcal{S} .

$$u(\mathbf{r}_\perp; z + \delta z) = \mathcal{F}^{-1} \left[\mathcal{F}(u(\mathbf{r}_\perp; z)) \underbrace{e^{i\delta z\sqrt{\bar{n}^2 k_0^2 - k_\perp^2}}}_{\tilde{\mathcal{D}}} \right] \underbrace{e^{i\delta z\delta n(\mathbf{r}_\perp; z)k_0}}_{\mathcal{S}} \quad (3.4)$$

The computation power of computer systems was low in former days and the calculation of a square root took a significant amount of CPU-time. Therefore, the *Fresnel approximation*

$$\sqrt{\bar{n}^2 k_0^2 - k_\perp^2} + k_0\delta n \approx^{Fresnel} \bar{n}k_0 - \frac{k_\perp^2}{2\bar{n}k_0} + k_0\delta n \quad (3.5)$$

was applied to reduce the computation time. Nowadays this is no longer necessary and the left side of equation 3.5 is used.

3.2 Definition of the input system

Let a system be defined by its distribution of the refractive index $\hat{n}(x, y; z(j)) = \hat{n}_j(x, y) = n_j + i\kappa_j \in \mathcal{C}$ (eq. 3.6). The index j denotes the layer under investigation and n_z is the number of iterations of the simulation along the z -axis, the axis of propagation. Each layer j has an incident layer $j - 1$. The refractive index at a location (x, y) in the j -th layer is then

$$\hat{n}(x, y; z(j)) = n(x, y; z(j)) + i\kappa(x, y; z(j)) \quad (3.6)$$

or simply

$$\hat{n}_j(\mathbf{r}_\perp) = n_j(\mathbf{r}_\perp) + i\kappa_j(\mathbf{r}_\perp) \quad (3.7)$$

The aperture is defined by the XY -plane and has the physical dimensions $X = n_x\delta x$ and $Y = n_y\delta y$. The numbers of samples are defined by $n_x = X/\delta x$, $n_y = Y/\delta y$ and $n_z = Z/\delta z$. An incident wave is supposed to propagate through the system $\mathcal{N} \in \mathcal{C}^{n_x \times n_y \times n_z}$, with \mathcal{C} is a complex number.

3.3 Scalar Wave Propagation Method

The scalar wave propagation method also uses the the Fourier transformation $\mathcal{F}(\cdot)$ of the incident scalar field $u_0(\mathbf{r})$ is

$$\tilde{u}_0(\mathbf{k}_\perp) = \iint u_0(\mathbf{r}_\perp) e^{-i\mathbf{k}_\perp \mathbf{r}_\perp} d^2\mathbf{r}_\perp \quad (3.8)$$

where the three-dimensional and the lateral positions and spatial frequencies are given by

$$\mathbf{r} = \begin{pmatrix} x \\ y \\ z \end{pmatrix}, \quad \mathbf{r}_\perp = \begin{pmatrix} x \\ y \end{pmatrix}, \quad \mathbf{k} = \begin{pmatrix} k_x \\ k_y \\ k_z \end{pmatrix}, \quad \mathbf{k}_\perp = \begin{pmatrix} k_x \\ k_y \end{pmatrix} \quad (3.9)$$

The spatial frequencies are related to the propagation vector by $\mathbf{k} = 2\pi\nu$ and the lateral subvector $\mathbf{k}_\perp = 2\pi\nu_\perp$. The spectrum of the field distribution in the j -th xy -layer of \mathcal{N} , at $Z = j\delta z$, is then

$$\tilde{u}_j(\mathbf{k}_\perp) = \iint u_j(\mathbf{r}_\perp) \cdot e^{-i\mathbf{k}_\perp \cdot \mathbf{r}_\perp} d^2\mathbf{r}_\perp \quad (3.10)$$

\tilde{u}_j is the plane wave decomposition of u_j . The term *plane wave decomposition* (PWD) provides the key idea of the wave propagation method because it emphasizes the decomposition of a field $E(\mathbf{r})$ into its plane waves components by the Fourier transformation. Each mode (i.e. Fourier coefficient) contains the amplitude of a related plane wave $w_j(\mathbf{k}_\perp, \mathbf{r}_\perp) = \tilde{u}_j(\mathbf{k}_\perp) \exp(i\mathbf{k}_\perp \cdot \mathbf{r}_\perp)$ to reproduce the original pattern by superposition. The propagation over a distance δz along the axis of propagation z of each plane wave component is then performed by transmission through an inhomogeneous (i.e. a position and frequency-dependent) phase element

$$\mathcal{P}_j(\mathbf{k}_\perp, \mathbf{r}_\perp) = e^{i\delta z \sqrt{n_j^2(\mathbf{r}_\perp)k_0^2 - \mathbf{k}_\perp^2}} \quad (3.11)$$

with $k_0 = 2\pi\nu_0 = 2\pi/\lambda_0$ and λ_0 is the vacuum wavelength. Since the phase shift also depends on the local distribution of the refractive index $n_j(\mathbf{r}_\perp)$, a simple inverse Fourier transformation is not possible to calculate the propagated field. A summation (integration) of all deformed plane waves $w_{j-1}\mathcal{P}_j$ over the entire spectrum and aperture is necessary to obtain the electric field at a distance $j\delta z$ from the field distribution at $(j-1)\delta z$. Unlike the BPM, the transmission through the locally varying refractive index

$n_j(\mathbf{r}_\perp)$ depends on the angle of propagation (i.e. the spatial frequency) of each plane wave component. The propagated field in layer j at a distance $j\delta z$ is

$$u_j(\mathbf{r}_\perp) = \frac{1}{A} \iint w_{j-1}(\mathbf{k}_\perp, \mathbf{r}_\perp) \mathcal{P}_j(\mathbf{k}_\perp, \mathbf{r}_\perp) \frac{d^2\mathbf{k}_\perp}{(2\pi)^2} \quad (3.12)$$

with $A = XY$. This is the central equation of the wave propagation scheme. Note that in a homogeneous medium, equation 3.12 is equal to the PWD.

3.4 Vector Wave Propagation Method

The *vector wave propagation method* (VWPM) assumes that a vector field \mathbf{E}_e has traversed an incident layer. At the interface between the incident (i.e. subscript 'e') and transmitted (i.e. subscript 't') layer, the change in the refractive index introduces a boundary that requires a separation of the field into its TE- and TM- components. The vectorial field just before the interface is decomposed into its Fourier components

$$\tilde{\mathbf{E}}_e(\mathbf{k}_\perp) = \begin{pmatrix} \tilde{E}_{x,e}(\mathbf{k}_\perp) \\ \tilde{E}_{y,e}(\mathbf{k}_\perp) \\ \tilde{E}_{z,e}(\mathbf{k}_\perp) \end{pmatrix} = \iint \mathbf{E}_e(\mathbf{r}_\perp) e^{i\mathbf{k}_\perp \cdot \mathbf{r}_\perp} d^2\mathbf{r}_\perp \quad (3.13)$$

Each component \mathbf{k}_\perp represents a plane wave, which is called a *mode*,

$$\mathbf{W}_e(\mathbf{k}_\perp, \mathbf{r}_\perp) = \tilde{\mathbf{E}}_e(\mathbf{k}_\perp) \exp(+i(\mathbf{k}_\perp \cdot \mathbf{r}_\perp + k_{z,e}z)) \quad (3.14)$$

with $k_{z,e} = \sqrt{(n_e(\mathbf{r}_\perp)k_0)^2 - \mathbf{k}_\perp^2}$. As indicated by the plus in the exponent, it is important to take the positive solution from the square root and apply a positive propagation vector \mathbf{k} in order to compute the field as described by the Fresnel and not the Lensef theory [36].

3.4.1 Lateral field dependence

In the absence of charges, $\text{div}(\mathbf{D}) = 0$ and the x-, y- and z-components of $\mathbf{W}_e(\mathbf{r}_\perp, \mathbf{k}_\perp)$ are depending on each other according to the medium equation. The z-component is then related to the lateral components by solving

$$0 = \text{grad}(\epsilon(\mathbf{r}_\perp)) \cdot \mathbf{W}_e(\mathbf{k}_\perp, \mathbf{r}_\perp) + \epsilon(\mathbf{r}_\perp) \text{div}(\mathbf{W}_e(\mathbf{k}_\perp, \mathbf{r}_\perp)) \quad (3.15)$$

for each plane wave component. Using $\text{div}(\mathbf{W}_e(\mathbf{k}_\perp, \mathbf{r}_\perp)) = i\mathbf{k} \cdot \mathbf{W}_e(\mathbf{k}_\perp, \mathbf{r}_\perp)$, the z-component of the E-field is then

$$\begin{aligned} \tilde{E}_{z,e} &= \frac{(i\epsilon_{x,e}/\epsilon - k_x)\tilde{E}_x + (i\epsilon_{y,e}/\epsilon - k_y)\tilde{E}_y}{k_{z,e}} \\ &= -\frac{k'_{x,e}\tilde{E}_x + k'_{y,e}\tilde{E}_y}{k_{z,e}} \end{aligned} \quad (3.16)$$

where $\epsilon_{x,e} = \partial\epsilon_e/\partial x$ and $\epsilon_{y,e} = \partial\epsilon_e/\partial y$ are the x- and y-components of the gradient of ϵ in the incident layer. The z-component of the gradient is zero since it is assumed that $\epsilon(\mathbf{r}_\perp)$ in each layer varies only in the lateral and not in the longitudinal z-direction. With equation 3.16, it is sufficient in equation 3.13 to consider only the x- and y-components of the transform. Two and three-dimensional vectors are distinguished by $\mathbf{E}^{(2)}$ and \mathbf{E} .

3.4.2 Transfer at the interface

The transfer at the interface between the incident and transmitted layer requires a separation of the field into its TE- and TM-field components. Each component is then weighted by the Fresnel transmission coefficients and the results are combined using the transmitted vectors of unity for

TE- and TM-polarization. The vectorial plane wave amplitude behind the interface can be expressed by

$$\tilde{\mathbf{E}}_t(\mathbf{k}_\perp) = t_{TE} \tilde{E}_{TE,t} \mathbf{e}_{TE} + t_{TM} \tilde{E}_{TM,t} \mathbf{e}_{TM,t} \quad (3.17)$$

where the TE- and TM-field components are given by

$$\tilde{E}_{TE,t}(\mathbf{k}_\perp) = \tilde{\mathbf{E}}_t \cdot \mathbf{e}_{TE} \quad (3.18)$$

$$\tilde{E}_{TM,t}(\mathbf{k}_\perp) = \tilde{\mathbf{E}}_e \cdot \mathbf{e}_{TM,e} \quad (3.19)$$

and the unity vectors of TE- and TM-polarization before and behind the interface are given by

$$\mathbf{e}_{TE} = \mathbf{e}_{TE,t} = \mathbf{e}_{TE,e} = \frac{(\mathbf{e}_z \times \mathbf{k}_e)}{|\mathbf{e}_z \times \mathbf{k}_e|} = \frac{1}{k_\perp} \begin{pmatrix} -k_y \\ k_x \\ 0 \end{pmatrix} \quad (3.20)$$

and

$$\mathbf{e}_{TM,e} = \frac{(\mathbf{e}_{TE} \times \mathbf{k}_e)}{|\mathbf{e}_{TE} \times \mathbf{k}_e|} = \frac{1}{n_e(\mathbf{r}_\perp)k_0k_\perp} \begin{pmatrix} k_x k_{z,e} \\ k_y k_{z,e} \\ -k_\perp^2 \end{pmatrix} \quad (3.21)$$

The vector of unity for the TM-polarization behind the interface is given by

$$\mathbf{e}_{TM,t} = \frac{(\mathbf{e}_{TE} \times \mathbf{k}_t)}{|\mathbf{e}_{TE} \times \mathbf{k}_t|} = \frac{1}{n_t(\mathbf{r}_\perp)k_0k_\perp} \begin{pmatrix} k_x k_{z,t} \\ k_y k_{z,t} \\ -k_\perp^2 \end{pmatrix} \quad (3.22)$$

The propagation vectors \mathbf{k}_e and \mathbf{k}_t follow from the continuity of the lateral components $k_{x,e} = k_{x,t}$, $k_{y,e} = k_{y,t}$ and $k_{z,e} = \sqrt{(n_e k_0)^2 - k_\perp^2}$, $k_{z,t} = \sqrt{(n_t k_0)^2 - k_\perp^2}$. Note, that $\mathbf{e}_{TM,e}$ as well as $\mathbf{e}_{TM,t}$ depend on the lateral position, since the index of refraction as well as the z-component of the k-vectors are position dependent. Combining the equations 3.17 to 3.22, the transfer at the interface can be expressed by a matrix operation

$$\tilde{\mathbf{E}}_t^{(2)}(\mathbf{k}_\perp, \mathbf{r}_\perp) = \mathbf{M}(\mathbf{k}_\perp, \mathbf{r}_\perp) \cdot \tilde{\mathbf{E}}_e^{(2)}(\mathbf{k}_\perp) \quad (3.23)$$

$\tilde{\mathbf{E}}_t^{(2)}$ is a lateral subvector of the electric field spectrum $\tilde{\mathbf{E}}_t$ behind the boundary. From a reordering of the equation, the transfer matrix of transmission

$$\mathbf{M}(\mathbf{k}_\perp, \mathbf{r}_\perp) = \frac{1}{k_\perp^2} \begin{pmatrix} k_y^2 t_{TE} + k_x^2 \hat{t}_{TM}(1 - i\hat{\epsilon}_{x,e}) & k_x k_y (\hat{t}_{TM}(1 - i\hat{\epsilon}_{y,e}) - t_{TE}) \\ k_x k_y (\hat{t}_{TM}(1 - i\hat{\epsilon}_{x,e}) - t_{TE}) & k_x^2 t_{TE} + k_y^2 \hat{t}_{TM}(1 - i\hat{\epsilon}_{y,e}) \end{pmatrix} \quad (3.24)$$

is obtained with

$$\hat{\epsilon}_{x,e} = \frac{k_\perp^2}{n_e^4 k_0^2} \frac{\epsilon_{x,e}}{k_x}, \quad \hat{\epsilon}_{y,e} = \frac{k_\perp^2}{n_e^4 k_0^2} \frac{\epsilon_{y,e}}{k_y} \quad (3.25)$$

and

$$\hat{t}_{TM} = \frac{n_e k_{z,t}}{n_t k_{z,e}} t_{TM} \quad (3.26)$$

The Fresnel coefficients for transmission are

$$\begin{aligned} t_{TE} &= \frac{2k_{z,e}}{k_{z,e} + k_{z,t}} \\ t_{TM} &= \frac{2n_e n_t k_{z,e}}{n_j^2 k_{z,e} + n_e^2 k_{z,t}} \end{aligned} \quad (3.27)$$

Using equation 3.26, the modified transmission coefficient for TM polarization can be simplified to

$$\hat{t}_{TM} = \frac{2n_e^2 k_{z,t}}{n_j^2 k_{z,e} + n_e^2 k_{z,t}} \quad (3.28)$$

3.4.3 Propagation step

With equation 3.23, the two-dimensional field contribution behind the interface is known. To complete the propagation through one layer, a propagation of the wave through the inhomogeneous medium with thickness δz

is applied. Considering the interface at the beginning of each layer and at $z = 0$, a component of the electric field which propagated a distance δz is then

$$\mathbf{W}_t^{(2)}(\mathbf{k}_\perp, \mathbf{r}_\perp) = \tilde{\mathbf{E}}_t^{(2)} e^{+i(\mathbf{k}_\perp \cdot \mathbf{r}_\perp + k_{z,t} \delta z)} = \tilde{\mathbf{E}}_t^{(2)} \mathcal{P} e^{+i(\mathbf{k}_\perp \cdot \mathbf{r}_\perp)} \quad (3.29)$$

The propagated z-component is then calculated according to equation 3.16, from the space derivatives $\epsilon_{t,x}$ and $\epsilon_{t,y}$ of ϵ in the layer behind the interface. The resulting field distribution at the end of the layer behind the interface in the aperture $A = XY$ is obtained by a summation of all field components

$$\mathbf{E}_t(\mathbf{r}_\perp) = \frac{1}{A} \iint \mathbf{W}_t(\mathbf{k}_\perp, \mathbf{r}_\perp) \frac{d^2 \mathbf{k}_\perp}{(2\pi)^2} \quad (3.30)$$

3.5 Algorithm of the VWPM

A system \mathcal{N} is split into n_z layers and sampled at n_x and n_y locations. The spatial frequencies $k_x = 2\pi p \delta \nu_x = 2\pi p / (n_x \delta x)$ and $k_y = 2\pi q \delta \nu_y = 2\pi q / (n_y \delta y)$ are determined by the sampling $(\delta x, \delta y)$ in the aperture. Each layer is orthogonal to the axis of propagation.

A vector field is propagating through the system \mathcal{N} layer by layer according to the VWPM equations that have been introduced in the previous section. Each layer j has a layer of incidence $j-1$ and a layer of propagation j . For the first iteration $j = 0$, the incident layer is modeled by a homogeneous medium (i.e. $n_{extern}(x, y) = const$) or by a copy of layer zero.

The incident wave is considered to be positioned directly before of the boundary between layer $j-1$ and j . The *first step* of the j -th iteration in

the z-axis is the plane wave decomposition of the field

$$\mathbf{E}_{j-1}^{(2)}(x, y) = \begin{pmatrix} E_{x,j-1} \\ E_{y,j-1} \end{pmatrix} \xRightarrow{FFT} \begin{pmatrix} \tilde{E}_{x,j-1} \\ \tilde{E}_{y,j-1} \end{pmatrix} = \tilde{\mathbf{E}}_{j-1}^{(2)}(k_x, k_y) \quad (3.31)$$

The *second step* applies the transformation matrix \mathbf{M}_j for each spatial frequency $\mathbf{k}_\perp = (k_x, k_y) = (p\delta k_x, q\delta k_y)$ and all locations $\mathbf{r}_\perp = (x, y) = (m\delta x, n\delta y)$ in the aperture. The transmitted plane wave components for electric field vector are derived from the spectrum according to

$$\begin{pmatrix} EX_j(p, q, m, n) \\ EY_j(p, q, m, n) \end{pmatrix} := \mathbf{M}_j \cdot \tilde{\mathbf{E}}_{j-1}^{(2)} \quad (3.32)$$

The spatial derivatives $\epsilon_{j-1,x}$, $\epsilon_{j-1,y}$ and $\epsilon_{j,x}$, $\epsilon_{j,y}$ are derived from the symmetric average

$$\begin{aligned} \epsilon_{j,x}(m, n) &= \frac{n_j^2((m+1)\delta x, n\delta y) - n_j^2((m-1)\delta x, n\delta y)}{2\delta x} \\ \epsilon_{j,y}(m, n) &= \frac{n_j^2(m\delta x, (n+1)\delta y) - n_j^2(m\delta x, (n-1)\delta y)}{2\delta y} \end{aligned} \quad (3.33)$$

The propagated electric field $\tilde{\mathbf{W}}_j$ through the position- and frequency-dependent phase element is again described by equation 3.29. The propagated magnetic field vector of a spatial frequency is then derived from the x - and y -component of the electric field according to

$$\begin{pmatrix} HX_j(p, q, m, n) \\ HY_j(p, q, m, n) \\ HZ_j(p, q, m, n) \end{pmatrix} := \mathbf{T}_j \cdot \begin{pmatrix} WX_j(p, q, m, n) \\ WY_j(p, q, m, n) \end{pmatrix} \quad (3.34)$$

The z-component WZ_j is obtained from equation 3.16 in layer j and the three-dimensional electrical field vector $\mathbf{E}(m\delta x, n\delta y)$ and magnetic vector $\mathbf{H}(m\delta x, n\delta y)$ in the transmitted layer j is subsequently obtained by the

summation over each frequency

$$\mathbf{E}_j(x, y) := \frac{1}{n_x n_y} \sum_p \sum_q \begin{pmatrix} W X_j \\ W Y_j \\ W Z_j \end{pmatrix} \quad (3.35)$$

$$\mathbf{H}_j(x, y) := \frac{1}{n_x n_y} \sum_p \sum_q \begin{pmatrix} H X_j \\ H Y_j \\ H Z_j \end{pmatrix} \quad (3.36)$$

3.5.1 VWPM in homogeneous media

In a homogeneous medium, the refractive index is constant and the propagation operator \mathcal{P} is therefore space-independent. For propagation through a homogeneous layer, the VWPM is therefore equal to the vectorial version of the PWD

$$\mathbf{E}_t(\mathbf{r}_\perp) = \mathcal{F}^{-1} \{ \mathbf{M} \cdot \mathcal{F} \{ \mathbf{E}_e(\mathbf{r}_\perp) \} e^{+ik_z(\mathbf{k}_\perp)\delta z} \} \quad (3.37)$$

In the absence of interfaces (i.e. $n_e = n_t \forall \mathbf{r}_\perp$), the matrix \mathbf{M} reduces to the 2x2 unity matrix. In case of vertical incidence, the 2x2 unity matrix is multiplied with the Fresnel coefficients for the TE- or TM-case (i.e. no polarization exists at $\mathbf{k}_\perp = 0$).

3.6 Magnetic vector and Poynting vector

The electric vector \mathbf{E} and magnetic vector \mathbf{H} of a transversal electromagnetic wave are related by transversality

$$\tilde{\mathbf{H}} = \sqrt{\frac{\epsilon\epsilon_0}{\mu\mu_0}} \left(\frac{\mathbf{k}}{k} \times \tilde{\mathbf{E}} \right) \quad (3.38)$$

By using equation 3.16, equation 3.38 is applied to the transversal components of the E-field in order to derive the magnetic vector in the layer behind the interface from a matrix multiplication according to

$$\tilde{\mathbf{H}}_t = \mathbf{T} \cdot \tilde{\mathbf{E}}_t^{(2)} \quad (3.39)$$

with $\tilde{\mathbf{E}}_t^{(2)}$ as the x - and y -components of the three-dimensional spectrum $\tilde{\mathbf{E}}_t$ in the transmitted layer. \mathbf{T} is derived from equation 3.38 as

$$\mathbf{T}(\mathbf{k}_\perp, \mathbf{r}_\perp) = \frac{1}{k_t k_{z,t}} \sqrt{\frac{\epsilon_t \epsilon_0}{\mu_t \mu_0}} \begin{pmatrix} -k'_{x,t} k_y & -(k_y k'_{y,t} + k_{z,t}^2) \\ k_x k'_{x,t} + k_{z,t}^2 & k_x k'_{y,t} \\ -k_y k_{z,t} & k_x k_{z,t} \end{pmatrix} \quad (3.40)$$

The *Poynting vector* \mathbf{S} is then derived from the magnetic field vector $\mathbf{H}_t(\mathbf{r}_\perp) = 1/(2\pi)^2 \iint \tilde{\mathbf{H}}_t(\mathbf{k}_\perp, \mathbf{r}_\perp) e^{i2\pi \mathbf{k}_\perp \cdot \mathbf{r}_\perp} d^2 \mathbf{k}_\perp / (2\pi)^2$ according to

$$\langle \mathbf{S}(\mathbf{r}) \rangle_T = \frac{1}{2} \text{Re} (\mathbf{E}(\mathbf{r}) \times \mathbf{H}^*(\mathbf{r})) \quad (3.41)$$

with \mathbf{H}^* is the complex conjugate of \mathbf{H} . The power flux per area unit $\partial P / \partial A$ [W/m^2] through the boundaries is then the z -component of the Poynting vector

$$\begin{aligned} \frac{\partial P(\mathbf{k}_\perp, \mathbf{r}_\perp)}{\partial A} &= \langle \mathbf{S} \rangle_T \cdot \mathbf{n} = \langle \mathbf{S}_z \rangle_T \\ &= \frac{1}{2} \text{Re} \{ E_x H_y^* - E_y H_x^* \} \\ &= \frac{1}{2} \text{Re} \left\{ E_x \left[\frac{1}{\mu k_0 Z_0} (k_z E_x - k_x E_z) \right]^* - E_y \left[\frac{1}{\mu k_0 Z_0} (k_y E_z - k_x E_y) \right]^* \right\} \end{aligned} \quad (3.42)$$

The total energy flux through a location \mathbf{r}_\perp is then obtained from the integration (summation) over the entire spectrum \mathbf{k}_\perp according to

$$\frac{\partial P(\mathbf{r}_\perp)}{\partial A} = \frac{1}{2Z_0} \iint k_z \mathbf{E} \mathbf{E}^* \frac{d^2 \mathbf{k}_\perp}{(2\pi)^2} \quad (3.43)$$

with $\mu = 1 + i0$. In the discrete case

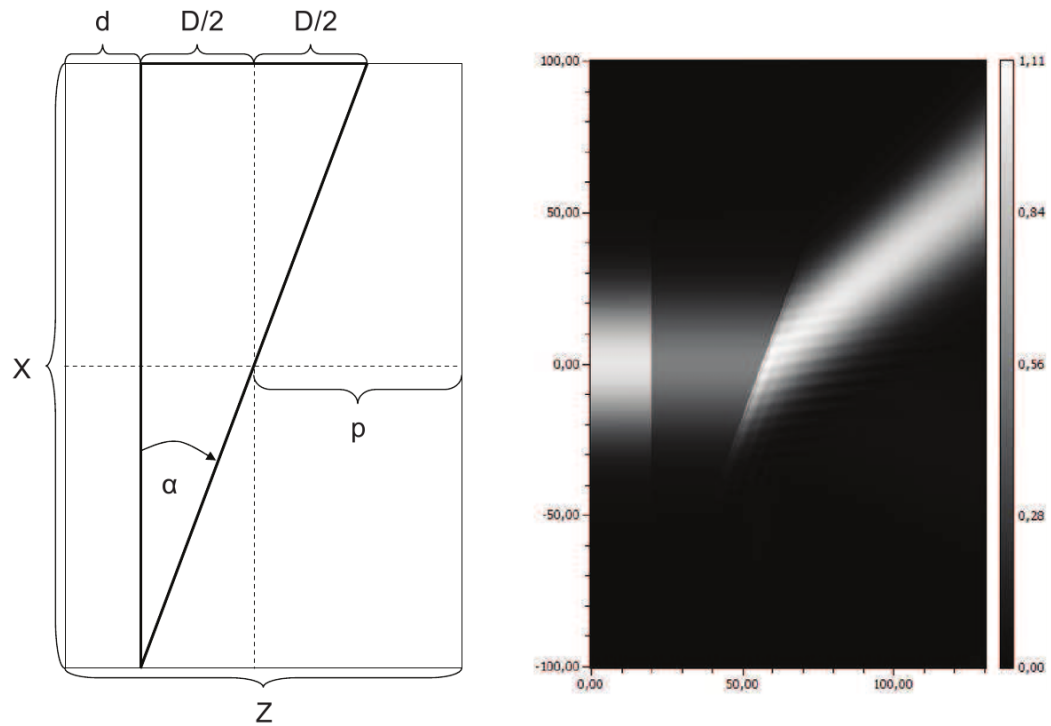
$$P_j(l, m) = \frac{\delta x \delta y}{2Z_0} \sum_p \sum_q \left[k_{z,j} \begin{pmatrix} WX_j \\ WY_j \\ WZ_j \end{pmatrix} \cdot \begin{pmatrix} WX_j \\ WY_j \\ WZ_j \end{pmatrix}^* \right] \quad (3.44)$$

with $\delta x = X/n_x$ and $\delta y = Y/n_y$. The multiplication with $\delta x \delta y$ makes the calculation independent from the number of samples and the entire energy flux through the aperture is then obtained from an integration of equation 3.43 or a summation of equation 3.44 over the locations \mathbf{r}_\perp .

3.7 2D simulation of refraction at a prism

A two-dimensional simulation of a Gaussian beam which propagates through a prism provides an easy and visual way to verify the VWPM. The results are compared to the results from theory and from a vectorial version of the BPM to show the accuracy of the VBPM. The refractive index of the prism is $n_P = 2.5$ and the surrounding refractive index $n = 1$. The back boundary of the prism has a slope of 20 degrees. The aperture has a width of $X = 200 \mu m$ and the Gaussian beam propagates a distance of $Z = 130 \mu m$. The number of samples in the aperture is $N_x = 512$ and in the axis of propagation $N_z = 333$. The thickness of the prism D is $72.8 \mu m$ and the propagation distance after the prism at $x = 0$ is $p = 73.6 \mu m$. d is then $20 \mu m$. The incident Gaussian beam is TE-polarized with a peak

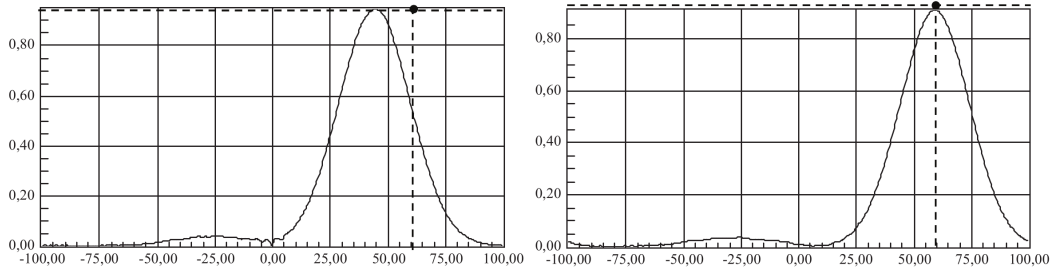
Figure 3.1: 2D simulation of a prism. **Left:** Schematic description and design parameters. **Right:** Propagating Gaussian beam, simulated with the VWPM.



amplitude of 1 V/m . The wavelength is $4 \mu\text{m}$ and the waist diameter is $40 \mu\text{m}$. The beam passes the front boundary at vertical incidence in the center of the aperture. The left subplot of figure 3.1 shows the geometry of the prism and the design parameters of the scene. The right plot shows the amplitude $|\mathbf{E}|$ of the propagating Gaussian beam. Snell's law and the Fresnel coefficients are applied to the two boundaries in the configuration in order to calculate the exact location ($59.1 \mu\text{m}$) and amplitude (0.936 V/m) of the Gaussian beam in the output aperture.

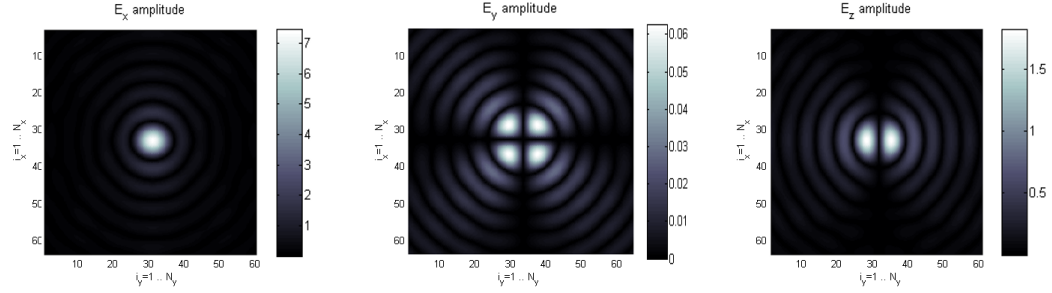
Figure 3.2 compares the amplitudes at $z = 130 \mu\text{m}$, calculated with the

Figure 3.2: **Left:** Propagated Gaussian beam with the VBPM. **Right:** Propagated Gaussian beam with the VWPM. The dashed lines show the exact result from theory.



VBPM (left) and VWPM (right). The dashed lines represent the exact results for amplitude (horizontal line) and position (vertical line). Obviously, the VBPM deviates in the position of the peak. The peak has its maximum at $x = 45.21 \mu m$ with an amplitude of $0.947 V/m$. The amplitude, simulated by the VWPM is shown in the right subplot of figure 3.2. The peak position shows a good match to Snell's theory at $x = 59.375 \mu m$ and the amplitude at $z = 130$ is $0.928 V/m$. The deviation of the position to the exact result in this case is in the range of the sampling. The root cause for the deviation in the amplitude is caused by an increased beam divergence which originates from the larger propagation distance at high refraction angles. No absorption has been considered in the entire scene.

Figure 3.3: Amplitudes E_x (left), E_y (middle) and E_z (right) of the vector field at focal distance (Vectorial Debye theory).



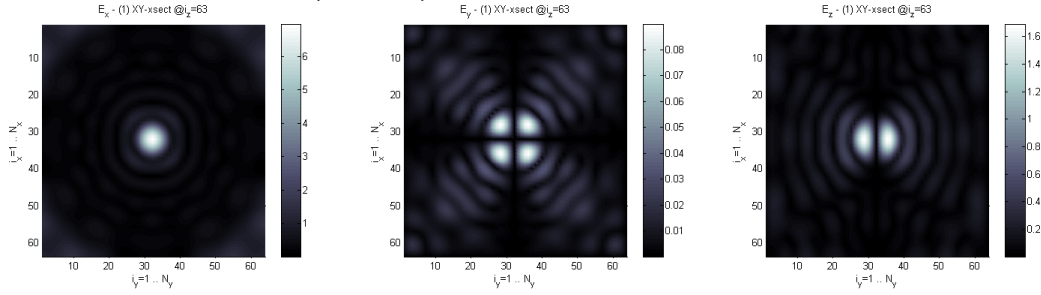
3.8 3D Simulation of a perfect asphere

To show the benefits of non-paraxial propagation, a three-dimensional asphere with a high numeric aperture is simulated. The asphere is designed according to a *theory of perfect aspheres* [37] with an NA of 0.8 and a working distance of $43\mu\text{m}$. The asphere is sampled in a 64^3 grid with $dx = dy = dz = 0.6875\mu\text{m}$. The asphere has a refractive index of 2 and the surrounding volume has a refractive index of vacuum.

The exact field distribution at in the focus can be derived from vectorial Debye theory [37]. Figure 3.3 shows the distribution of the E_x , E_y and E_z -components of the vector field from vectorial Debye theory. The comparison of figure 3.3 with the results from the VWPM in figure 3.4 shows that the basic features are reproduced. The simulated focal spot is very close to the design focus position. The amplitudes show a slight deviation.

Figure 3.5 shows a xz-plot of the TE-electric field distribution. The asphere in this case had a radius of $22\mu\text{m}$, a numeric aperture of 0.8 and a refractive index of $n = 1.5$. The surrounding refractive index was 1 and sampling is $N_x = N_y = N_z = 64$. The figure shows a diffraction limited, un-

Figure 3.4: Amplitudes E_x (left), E_y (middle) and E_z (right) of the vector field at focal distance (VWPM).

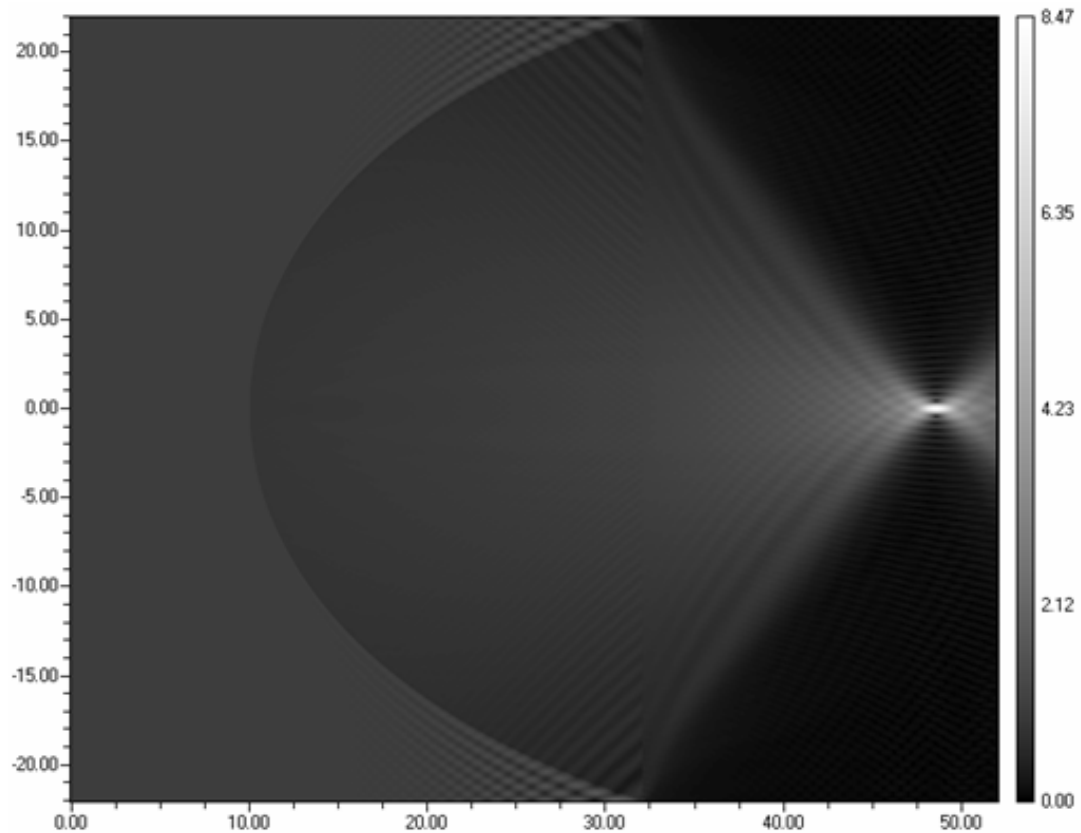


aberrated spot, as is to be expected from a perfect focusing lens. Also the focus location agrees perfectly with ray tracing. As reference, the VBPM was also tried. It showed a longitudinal shift of the focus and a significant spherical aberration.

3.9 3D Simulation of a 2D grating

A third scenario is a high frequency grating, defined by periods p_x , p_y and widths w_x , w_y in the x - and y -axis. The widths determine the duty-cycle of the grating. The height of the grating is h . The refractive index of the grating is $n_g = 1.5$ and the surrounding refractive index is $n = 1$ (i.e. vacuum). The sampling is $dx = dy = dz = 0.125\mu m$. The parameters of the gratings are $p_x = p_y = 8\lambda$, $w_x = w_y = 4\lambda$ and $h = 1\lambda$ for the simulation that is shown in figure 3.6 and $p_x = p_y = 4\lambda$, $w_x = w_y = 2\lambda$ and $h = 1\lambda$ for the simulation in figure 3.7. The incident plane wave has a wavelength of $\lambda = 1\mu m$ and TM polarization for both examples. The angle of incidence is 15 degrees in figure 3.6 and 0 degrees in figure 3.7. The propagated wave shows a well-defined distribution of the field amplitude that is determined by the

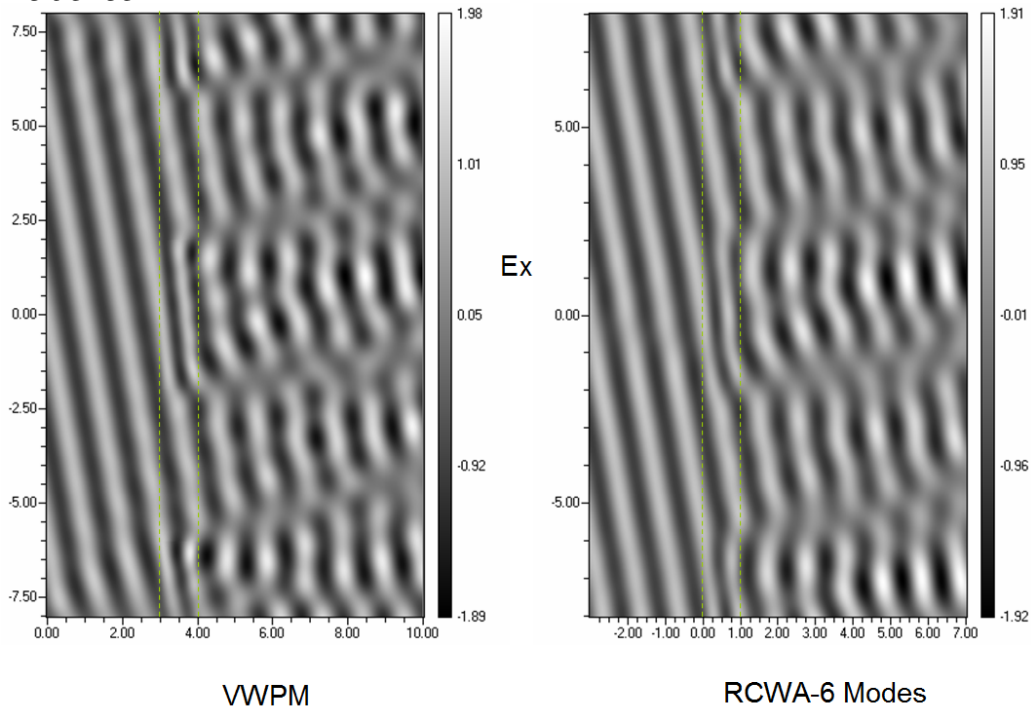
Figure 3.5: Simulation of a perfect asphere with the VWPM. The figure shows the amplitude of the E_y -component of a TE-polarized plane wave which propagates from left to right through a perfect asphere.



grating dimensions.

The vector components of the electric field, calculated by the VWPM are compared to the results of the two-dimensional RCWA. For the RCWA, 6 modes have been used, whereas the VWPM effectively uses 256 modes. Both figures show remarkable agreement. The differences are significant only for the incident region before the grating, which is clear since the VWPM does not yet consider reflections.

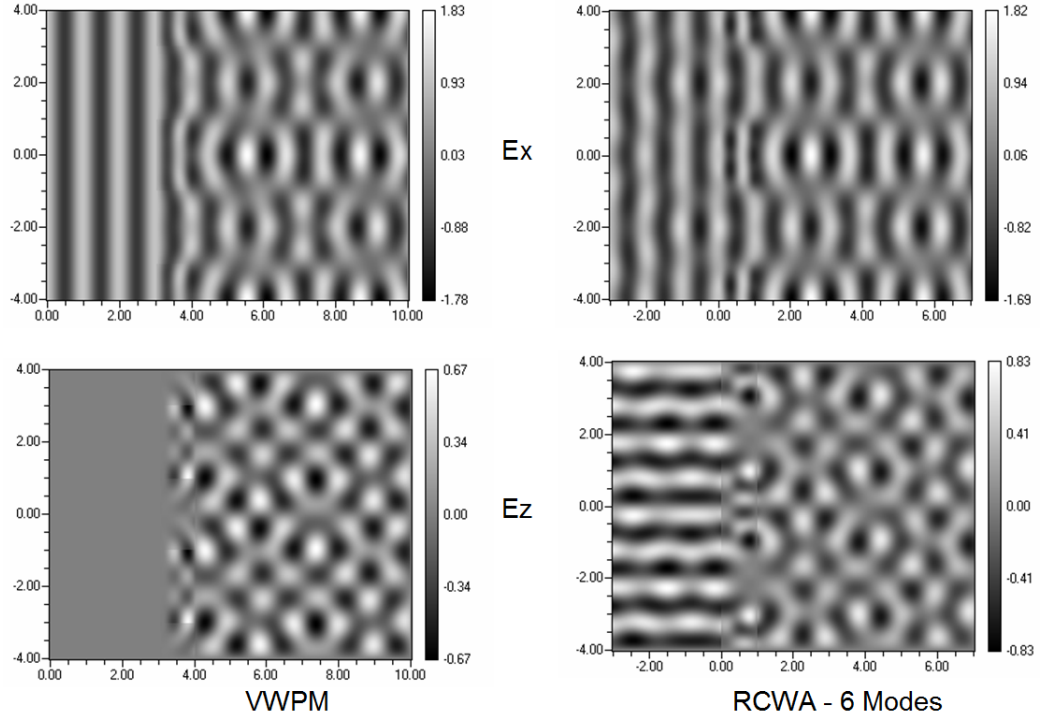
Figure 3.6: Amplitude of the E_x -component of the vector field in the xz -plane simulated with the RCWA (right) and the VWPM (left) for oblique incidence.



3.10 Evanescent modes

According to [1], an evanescent wave is not transversal because parts of the electric field vectors are parallel to the propagation vector. In [2], an evanescent wave is introduced as a wave which does not carry energy because the field oscillates back and forth across the interface, resulting in a zero net energy flux. Obviously, evanescent waves are different and do not possess some of the central assumptions for electromagnetic waves, transversality and the transportation of energy.

Figure 3.7: Amplitude of the E_x (upper row) and E_z -component (lower row) of the TM-polarized vector field in the xz -plane simulated with the RCWA (right) and the VWPM (left) for perpendicular incidence.



For internal reflection (i.e. $n_e > n_t$), a critical angular θ_c is obtained from Snell's law according to equation 2.70. For all $\theta_e > \theta_c$, an evanescent wave is then generated which propagates along the interface and decays exponentially and perpendicular to the interface as introduced in chapter 2. The evanescent boundary $k_{\perp} = n_e(\mathbf{r}_{\perp})k_0$ shifts to $k_{\perp} = n_t(\mathbf{r}_{\perp})k_0$ as depicted in figure 2.4. Then, a propagating mode becomes an evanescent mode and vice versa under certain conditions. For internal reflection (i.e. $n_e > n_t$) and $\theta_e > \theta_c$, a propagating mode in the medium with the higher real part of the refractive index becomes an evanescent mode in the medium with the lower real part of the refractive index and the evanescent boundary

Table 3.1: *Evanescent and propagating modes at interfaces.*

Case	inc. mode	trans. mode	Comment
1	prop.	prop.	normal propagation
2	prop.	evan.	total internal reflection
3	evan.	prop.	evanescent coupling (i.e. tunneling)
4	evan.	evan.	transfer of evanescent modes

moves toward the origin of the spatial frequency axis. For external reflection (i.e. $n_t > n_e$) and frequencies above the evanescent boundary before the interface and below the evanescent boundary behind the interface, an evanescent mode in the low-index medium becomes a propagating mode in the high-index medium. The different configurations for evanescent and propagating modes are enumerated in table 3.1.

Case 1 describes propagating waves on both sides of an interface for external and internal refraction. Total internal reflection (TIR) and the generation of an evanescent wave occurs in case 2 and frustrated total internal reflection (FTIR) and the effect of evanescent coupling in case 3. Case 4, the propagation of evanescent waves is only considered in homogeneous medium and no transfer of evanescent-to-evanescent modes is considered in the VWPM.

3.10.1 Internal reflection and transmission

In case 2 and $n_e > n_t$, an evanescent wave is generated by total internal reflection. The amplitude of the evanescent wave behind the interface is

then obtained from equation 2.73 according to

$$\begin{aligned}\tilde{\mathbf{E}}_t(\mathbf{k}_\perp, \mathbf{r}_\perp) &= \begin{pmatrix} \hat{t}_{TM} \hat{k}_{z,t} / k_t (\tilde{\mathbf{E}}_e \cdot \mathbf{e}_{TM}) \\ \hat{t}_{TE} (\tilde{\mathbf{E}}_e \cdot \mathbf{e}_{TE}) \\ \hat{t}_{TM} n_e k_\perp / n_t / k_t (\tilde{\mathbf{E}}_e \cdot \mathbf{e}_{TM}) \end{pmatrix} \\ &= \begin{pmatrix} i \hat{t}_{TM} \gamma_{z,t} / k_t / k_\perp (k_x k_{z,e} E_x + k_y k_{z,e} E_y - k_\perp^2 E_z) \\ \hat{t}_{TE} (k_x E_y - k_y E_x) \\ \hat{t}_{TM} n_e / n_t / k_t (k_x k_{z,e} E_x + k_y k_{z,e} E_y - k_\perp^2 E_z) \end{pmatrix} \quad (3.45)\end{aligned}$$

with \hat{t}_{TE} and \hat{t}_{TM} (eq. 2.75) are the complex Fresnel coefficients of transmission, utilizing the purely imaginary z-component of the propagation vector of the evanescent wave. k_t is the length of the propagation constant behind the interface and $k_\perp = n_e k_0 \sin \theta_e = n_t k_0 \sin \theta_t$, which yields the sines of θ_t . Evanescent waves are not transversal because E_x is purely imaginary and therefore parallel to the propagation vector as shown in [1]. Hence, the z-component of the electric field can not be derived from equation 3.16.

Even in the absence of absorption (i.e. $\kappa = 0$), an evanescent mode is expected to decay exponentially and perpendicular to the interface according to equation 2.72. The locally deformed plane wave \mathbf{W}_t is obtained from the frequency and space dependent phase element using the complex propagation vector according to

$$\begin{aligned}\mathbf{W}_t(\mathbf{k}_\perp, \mathbf{r}_\perp) &= \tilde{\mathbf{E}}_t e^{i\mathbf{k}_\perp \cdot \mathbf{r}_\perp} \mathcal{P}(\mathbf{k}_\perp, \mathbf{r}_\perp) \\ &= \tilde{\mathbf{E}}_t e^{i\mathbf{k}_\perp \cdot \mathbf{r}_\perp} e^{-\gamma_{z,t} \delta z} \quad (3.46)\end{aligned}$$

where $\gamma_{z,t} = \sqrt{k_\perp^2 - n_t^2 k_0^2}$ is the imaginary part of $\hat{k}_{z,t}$. The evanescent wave is then obtained from the integration over the spatial frequencies according to equation 3.30.

For $k_{\perp} = n_t k_0$, θ_e is equal to θ_c and the z-component of the propagation vector is zero. Then, the propagation vector of the transmitted field \mathbf{k}_t is parallel to the interface and the electric field propagates along the boundary and the phase-element is unity (i.e. $\mathcal{S} = \exp(0)$). In case of an absorbing medium, the VWPM assumes a complete decay of the wave due to an infinite propagation distance $\delta z / \cos \theta_t = \delta z k_t / \hat{k}_{z,t} \rightarrow \infty$ for $\hat{k}_{z,t} \rightarrow 0$. A unit phase element $\mathcal{S} = \exp(0) = 1$ is applied to equation 3.46 in the absence of absorption and then the transmitted field propagates parallel to the interface as shown in figure 3.8 on page 80.

At the evanescent boundary $k_{\perp} = n k_0$ and for $k_{z,e} \neq 0$ and $\hat{k}_{z,t} = 0$, the Fresnel transmission coefficients are $t_{TE} = 2$ and $t_{TM} = 2n_e/n_t$. In the TE-case, an increase in the amplitude by a factor of 2 is obtained, which is independent from the refractive index. The Fresnel transmission coefficients are zero for $\hat{k}_{z,e} = 0$ and $k_{z,t} \neq 0$. The denominator of t_{TE} and t_{TM} is zero for $\hat{k}_{z,e} = \hat{k}_{z,t} = 0$ but this corresponds to $n_e = n_t$ and the Fresnel transmission coefficients are then defined to $t_{TE} = 1$ and $t_{TM} = 1$ in the VWPM. In an medium with $\hat{n}_t = n_t + i\kappa_t$ and $\kappa_t > 0$, the propagating mode $k_{z,t} = 0$ is completely absorbed since the VWPM assumes an infinite propagation distance $\exp(-\gamma_{z,t} \delta z n k_0 / k_z) \rightarrow \infty$ for $k_z = 0$. The simulated field distributions agree with the expected results from theory as shown in figure 3.8.

3.10.2 External reflection and transmission

In case 3 and external reflection $n_e < n_t$, a propagating mode is obtained from an evanescent mode and the transmitted electric field vector behind

the interface is again obtained from equation 2.73 according to

$$\tilde{\mathbf{E}}_t^{(2)}(\mathbf{k}_\perp, \mathbf{r}_\perp) = \begin{pmatrix} \hat{t}_{TM} \hat{k}_{z,t} / k_t \tilde{\mathbf{E}}_{e,x} \\ \hat{t}_{TE} \tilde{\mathbf{E}}_{e,y} \end{pmatrix} \quad (3.47)$$

where $\tilde{\mathbf{E}}_{e,x}$ contains the TM- and $\tilde{\mathbf{E}}_{e,y}$ the TE-polarization of the incident evanescent wave before the boundary as defined in equation 3.45. Since the evanescent wave propagates along interface and gets not refracted, the orientation of the TE- and TM-components remains constant and the Fresnel coefficients of transmission are applied to the x-component for the TM-case and to the y-component of the evanescent wave for the TE-case. The propagation of the transmitted field is the obtained from equation 3.29 and the z-component is finally obtained from transversality according to equation 3.16.

3.10.3 Propagation of evanescent modes

In case 4 and for $n_{j-1}(\mathbf{r}_\perp) = n_j(\mathbf{r}_\perp)$, the complex propagation vector is applied to the space- and frequency-dependent phase element $\mathcal{P} = \exp(-\gamma_{z,t} \delta z)$ is applied to equation 3.29. If $n_{j-1}(\mathbf{r}_\perp) = n_j(\mathbf{r}_\perp), \forall \mathbf{r}_\perp$ the plane wave decomposition (PWD) is utilized and the propagated evanescent wave is obtained from $\mathbf{E}_t(\mathbf{r}_\perp) = \mathcal{F}^{-1} \{ \mathcal{F} \{ \mathbf{E}_e(\mathbf{r}_\perp) \} \mathcal{P} \}$.

3.10.4 Algorithm for evanescent modes

For case 1 in table 3.1, the algorithm in section 3.5 is applied. The algorithm is modified for case 2 and 3 by replacing the transfer at the interface

Table 3.2: Complex phasor $\mathcal{P}(\mathbf{k}, \mathbf{r})$ for propagation in the VWPM.

Case	$\hat{k}_{z,j-1}$	$\hat{k}_{z,j}$	$n_{j-1} > n_j$	$n_{j-1} = n_j$	$n_{j-1} < n_j$
1	$k_{z,j-1}$	$k_{z,j}$	$\mathcal{P} = e^{ik_{z,j}\delta z}$	PWD	$\mathcal{P} = e^{ik_{z,j}\delta z}$
2	$k_{z,j-1}$	$i\gamma_{z,j}$	$\mathcal{P} = e^{-\gamma_z\delta z}$	–	$\mathcal{P} = 0$
3	$i\gamma_{z,j-1}$	$k_{z,j}$	$\mathcal{P} = 0$	–	$\mathcal{P} = e^{ik_{z,j}\delta z}$
4	$i\gamma_{z,j-1}$	$i\gamma_{z,j}$	$\mathcal{P} = 0$	PWD	$\mathcal{P} = 0$

with equation 2.73 and the space and frequency dependent phase element evolves from the complex propagation constant as shown in table 3.2. All modes which belong to case 4 are only considered in the absence of interfaces along the axis of propagation and then the plane wave decomposition (PWD) is applied. Evanescent waves (i.e. $\theta_e > \theta_c$) do not transfer power across an interface as shown in chapter 2 and therefore all evanescent modes are negligible in the calculation of the energy flux.

3.11 Simulation of evanescent waves

Let a TE-polarized plane wave of unit amplitude and at with 1. $\theta_e = \theta_c = 65.38$ degrees and 2. greater than 65.38 degrees propagate through a medium with $\hat{n}_e = 1.1 + i0$ and $\hat{n}_t = 1 + i0$. The aperture is $X = Z = 16 [\mu m]$ and $n_x = n_z = 256$. For the first case, the transmitted wave propagates along the interface as shown in figure 3.8. In the second case, the transmitted electric field is evanescent and therefore decays exponentially in the axis of propagation as shown in figure 3.9.

Figure 3.8: *Simulation of a propagating wave with $\theta_e = \theta_c$ in a lossless medium with the VWPM.*

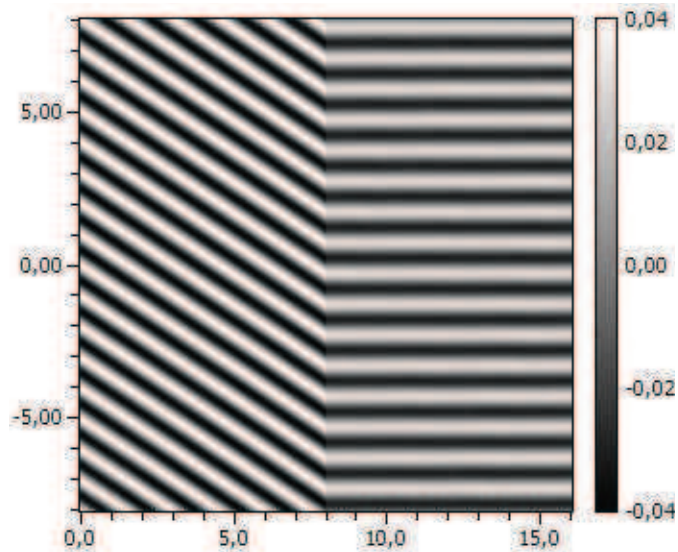
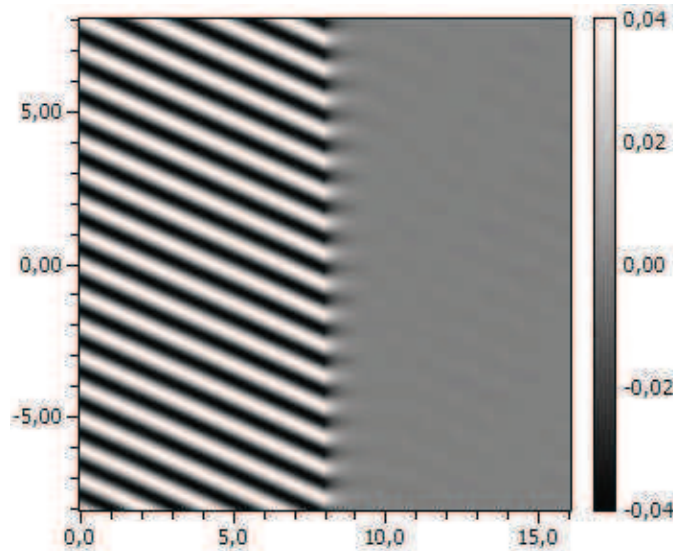


Figure 3.9: *Simulation of an evanescent wave with $\theta_e > \theta_c$ with the VWPM.*



Chapter 4

Vectorial split step propagation

The treatment of electromagnetic (EM) vector waves in the VWPM according to the wave propagation scheme (eq. 3.12) raises the question, if a vectorial treatment is also possible with the split step propagation scheme (eq. 3.4). This chapter provides the analysis of the vectorial calculation of electromagnetic field propagation with the Beam Propagation Method (BPM). It shows that an unapproximated solution of the vectorial diffraction integral is not possible and that the benefit of a vectorial split step propagation method is low due to the paraxial limitation.

The theory of the BPM has been introduced in chapter 3 and the same nomenclature is now used to derive its vectorial version. A vectorial split step propagation scheme then evolves from the following sequence. In the j -th step of calculation, the frequency dependent phase shift is applied to the spectrum of the electric field from layer j , $\tilde{\mathbf{E}}_j(\mathbf{k}_\perp)$, which is the transmitted spectrum in layer $j - 1$, $\tilde{\mathbf{E}}_{j-1}(\mathbf{k}_\perp)$, transformed according to the transfer

of vector waves at interfaces as shown in chapter 3. In agreement with the split step propagation algorithm, the mean average refractive index before the boundary \bar{n}_{j-1} and behind the boundary \bar{n}_j is applied to Snell's law and Fresnel's equations to obtain the transfer matrix of transmission. The purely frequency dependent phase adjustment is then performed by the scalar complex diffraction operator $\tilde{\mathcal{D}}(\mathbf{k}_\perp)$ (eq. 3.2). The z-component E_z is then derived from the diffracted spectrum according to equation 3.16) and the inverse Fourier transformation of the henceforth three-dimensional transmitted and diffracted spectrum yields the propagated field through a homogeneous layer in the spatial domain. The phase adjustment in the inhomogeneous medium is then performed by using the purely space-dependent phase adjustment operator $\mathcal{S}(\mathbf{r}_\perp)$ (eq. 3.3) to consider the inhomogeneities in layer j . The propagated wave in layer j is then obtained which provides the input for iteration $j + 1$.

In the vectorial split step propagation, the transfer at the interface, using a transfer matrix, is the central extension compared to the scalar equivalent. It is important to consider that the transfer at the interface is performed in the spatial frequency domain, utilizing the mean average refractive indices.

4.1 Vectorial Beam Propagation Method

For the vectorial version of the BPM, the algorithm is extended by one additional step - the transfer of the vectorial wave at the interface. In agreement with split step propagation and in order to be able to calculate and apply Fresnel's equations, the transfer at the interface needs to be performed in the spatial frequency domain. The two-dimensional sub-vector

of the vectorial spectrum $\tilde{\mathbf{E}}_e^{(2)}$ is multiplied with the transfer matrix $\hat{\mathbf{M}}(\mathbf{k}_\perp)$, which is derived from equation 3.17, using the mean average refractive indices \bar{n}_e and \bar{n}_t . The propagated vector field $\mathbf{E}_t(\mathbf{r})$ is then derived from $\mathbf{E}_e^{(2)}(\mathbf{r})$ according to the Vectorial Beam Propagation Method (VBPM) in equation 4.6.

4.1.1 Transfer matrix of transmission

For two homogeneous layers with the refractive indices \bar{n}_e and \bar{n}_t , the transfer of the TM-component at the interface is independent from the spatial derivatives ϵ_x and ϵ_y because $grad(\epsilon) = 0$. The replacement of \tilde{E}_z in equation 3.17 then yields

$$\begin{aligned} E_{TM,e} &= \frac{1}{k_\perp \bar{k}_e} \left(\tilde{E}_x \left(k_x \bar{k}_{z,e} + \frac{k_\perp^2}{k_{z,e}} k_x \right) + \tilde{E}_y \left(k_y \bar{k}_{z,e} + \frac{k_\perp^2}{k_{z,e}} k_y \right) \right) \\ &= \frac{\bar{k}_e}{k_\perp \bar{k}_{z,e}} \left(\tilde{E}_x k_x + \tilde{E}_y k_y \right) \end{aligned}$$

The TE-component in equation 3.17 remains unchanged and inserting the modified expression for \tilde{E}_z into the TM-component (eq. 3.21 and eq. 3.22), the transmitted electric field vector is then

$$\begin{aligned} \tilde{\mathbf{E}}_t(\mathbf{k}_\perp, \mathbf{r}_\perp) &= \frac{\tilde{E}_x}{k_\perp^2} \left(-k_y \bar{t}_{TE} \begin{pmatrix} -k_y \\ k_x \\ 0 \end{pmatrix} + \frac{\bar{k}_e k_x}{\bar{k}_t \bar{k}_{z,e}} \bar{t}_{TM} \begin{pmatrix} k_x \bar{k}_{z,t} \\ k_y \bar{k}_{z,t} \\ -k_\perp^2 \end{pmatrix} \right) + \\ &\quad \frac{\tilde{E}_y}{k_\perp^2} \left(k_x \bar{t}_{TE} \begin{pmatrix} -k_y \\ k_x \\ 0 \end{pmatrix} + \frac{\bar{k}_e k_y}{\bar{k}_t \bar{k}_{z,e}} \bar{t}_{TM} \begin{pmatrix} k_x \bar{k}_{z,t} \\ k_y \bar{k}_{z,t} \\ -k_\perp^2 \end{pmatrix} \right) \end{aligned}$$

This expression depends only on the transversal components \tilde{E}_x and \tilde{E}_y of the electrical field vector. The reordering by the transversal components

\tilde{E}_x and \tilde{E}_y gives the space-independent *transfer matrix of transmission in homogeneous medium* $\bar{\mathbf{M}}$ for the transmission into the layer behind the interface

$$\bar{\mathbf{M}}(\mathbf{k}_\perp) = \frac{1}{k_\perp^2} \begin{pmatrix} k_y^2 \bar{t}_{TE} + b k_x^2 \bar{t}_{TM} & k_x k_y (b \bar{t}_{TM} - \bar{t}_{TE}) \\ k_x k_y (b \bar{t}_{TM} - \bar{t}_{TE}) & k_x^2 \bar{t}_{TE} + b k_y^2 \bar{t}_{TM} \end{pmatrix} \quad (4.1)$$

with $b = \bar{t}'_{TM}/\bar{t}_{TM}$ yields the modified transmission coefficient

$$\bar{t}'_{TM} = \frac{\bar{n}_e \bar{k}_{z,t}}{\bar{n}_t \bar{k}_{z,e}} \bar{t}_{TM}$$

and $\bar{\mathbf{M}}$ then transforms to

$$\bar{\mathbf{M}}(\mathbf{k}_\perp) = \frac{1}{k_\perp^2} \begin{pmatrix} k_y^2 \bar{t}_{TE} + k_x^2 \bar{t}'_{TM} & k_x k_y (\bar{t}'_{TM} - \bar{t}_{TE}) \\ k_x k_y (\bar{t}'_{TM} - \bar{t}_{TE}) & k_x^2 \bar{t}_{TE} + k_y^2 \bar{t}'_{TM} \end{pmatrix} \quad (4.2)$$

The bar indicates that the average refractive index is taken, causing the space-independence for the propagation with the diffraction operator (eq. 3.2) as proposed by the split step propagation scheme. With a similar calculation, the transfer matrix of reflection $\bar{\mathbf{R}}$ for a bidirectional Vector Beam Propagation Method (VBPM)

$$\bar{\mathbf{R}}(\mathbf{k}_\perp) = \frac{1}{k_\perp^2} \begin{pmatrix} k_y^2 \bar{r}_{TE} + k_x^2 \bar{r}_{TM} & k_x k_y (\bar{r}_{TM} + \bar{r}_{TE}) \\ k_x k_y (\bar{r}_{TM} - \bar{r}_{TE}) & k_y^2 \bar{r}_{TM} + k_x^2 \bar{r}_{TE} \end{pmatrix} \quad (4.3)$$

is obtained.

4.1.2 Diffraction in homogeneous medium

To complete the calculation in the spatial frequency domain, the propagation through the homogeneous medium with thickness δz is calculated by

using the diffraction operator \mathcal{D}

$$\begin{aligned}\mathbf{W}_t(\mathbf{k}) &= e^{+i(\bar{k}_{z,t}\delta z + \mathbf{k}_\perp \cdot \mathbf{r}_\perp)} \tilde{\mathbf{E}}_t(\mathbf{k}_\perp) \\ &= \tilde{\mathcal{D}}(\mathbf{k}_\perp) \tilde{\mathbf{E}}_t(\mathbf{k}_\perp) e^{+i\mathbf{k}_\perp \cdot \mathbf{r}_\perp}\end{aligned}\quad (4.4)$$

with $\bar{k}_{z,t}(\mathbf{k}_\perp) = \sqrt{(\bar{n}_t k_0)^2 - \mathbf{k}_\perp \cdot \mathbf{k}_\perp^*}$, which is independent from the position \mathbf{r}_\perp and only depends on the spatial frequency \mathbf{k}_\perp and $\mathbf{k}_\perp \cdot \mathbf{k}_\perp^*$ is the squared absolute of \mathbf{k}_\perp . The field distribution after a propagation through the homogeneous medium at the end of the layer behind the interface is then obtained from the integration of all plane waves over the two-dimensional spectrum \mathbf{k}_\perp

$$\begin{aligned}\mathbf{E}_t(\mathbf{r}_\perp) &= \frac{1}{A} \iint \mathbf{W}_t \frac{d^2\mathbf{k}_\perp}{(2\pi)^2} \\ &= \mathcal{F}^{-1} \left\{ \tilde{\mathbf{E}}_t(\mathbf{k}_\perp) e^{+i\bar{k}_{z,t}\delta z} \right\}\end{aligned}\quad (4.5)$$

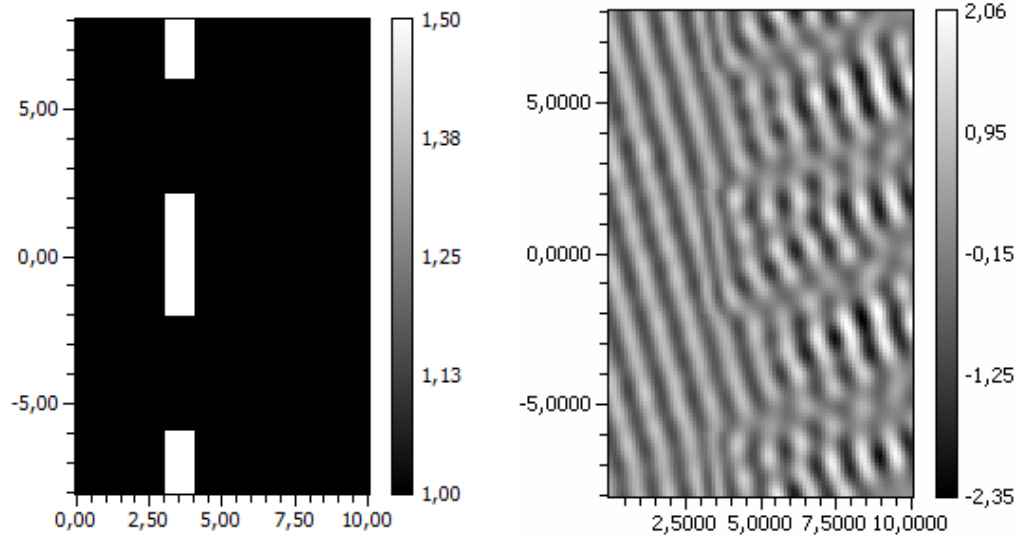
which is equal to the inverse Fourier transformation. $A = XY$ is the aperture of the system.

4.1.3 Phase adjustment in inhomogeneous medium

The propagation through the layer behind the boundary is then finished by performing the phase adjustment from the application of the purely space dependent phase shift operator \mathcal{S} (eq. 4.6). This phase adjustment can be neglected in case of a homogeneous layer behind the interface since $0 = n_t(\mathbf{r}_\perp) - \bar{n}_t$ and then $\mathcal{S} = 1$ for all locations \mathbf{r}_\perp in the aperture.

In case of a propagation through a homogeneous layer, the plane wave decomposition (PWD) which has been introduced in section 2.9, is obtained

Figure 4.1: *Simulation of the $8\lambda-4\lambda-1\lambda$ -grating from chapter 3 with the vectorial BPM.*



and the central equation of the Vector Beam Propagation Method (VBPM)

$$\mathbf{E}_t = S \mathcal{F}^{-1} \left\{ \tilde{\mathcal{D}} (\bar{\mathbf{M}} \cdot \mathcal{F} \{ \mathbf{E}_e^{(2)} \}) \right\} \quad (4.6)$$

reduces to the vectorial Plane Wave Decomposition (PWD)

$$\mathbf{E}_t = \mathcal{F}^{-1} \left\{ \tilde{\mathcal{D}} (\bar{\mathbf{M}} \cdot \mathcal{F} \{ \mathbf{E}_e^{(2)} \}) \right\} \quad (4.7)$$

4.2 3D simulation of a 2D grating

The simulation of the two-dimensional grating from chapter 3 is now performed with the Vector Beam Propagation Method and the result is shown in figure 4.1. The comparison to the results from RCWA on page 73 shows

that the distribution of the electric field is slightly different and that the scale deviates.

Even if the distribution of the electric field shows a correlation to the results from the RCWA and the VWPM, the Beam Propagation Method still possesses an inherent error for the propagation of high order modes as shown in the simulation of a prism in chapter 3 and in [53] for the simulation of waveguides with a tilt up to 20 degrees. The Fresnel coefficients cannot be correctly applied in the spatial frequency domain by using the mean average of the refractive index in the spectral domain as also shown in figure 3.2.

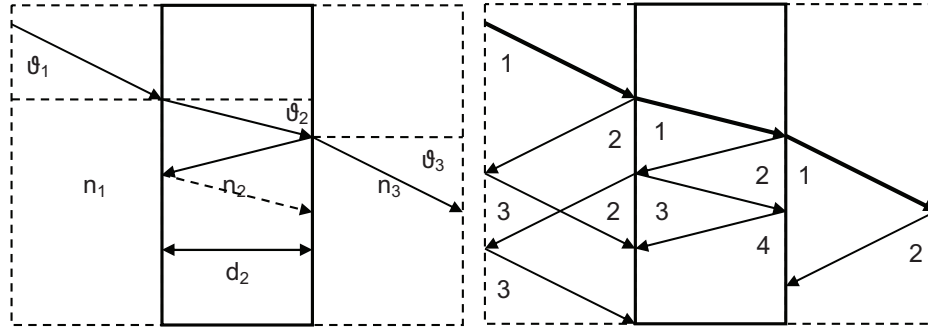
Since Fresnel's coefficients start to vary for large propagation angles and therefore the calculation of vectorial effects with the paraxial split step propagation scheme does not provide a significant benefit.

Chapter 5

Bidirectional Vector Wave Propagation Method

Unidirectional propagation methods calculate the propagation of waves in just one direction. In case of multilayer systems, multiple reflections occur and the results deviate to the exact results from theory because not all forward propagating waves are considered. Each layer generates fractions of the incident field which are traveling back and forth, generating themselves fractions of fields and so forth. This chapter provides an analysis of the forward and backward propagating fields in a resonator to estimate the error in the simulation with a uni-directional propagation method. The observations on the convergence of the electric field in a single resonator are applied to coupled resonators in order to approximate the number of iterations which are necessary for the convergence of the electromagnetic (EM) field in a bidirectional simulation.

Figure 5.1: Angles, refractive index, layer thickness (left) and the numbering of the iterations (right) in a Fabry-Perot resonator.



In a single Fabry-Perot resonator with n_1 is the refractive index before the resonant layer, n_2 is the refractive index in the resonator and n_3 is the refractive index behind the resonant layer as shown in figure 5.1, the fractions of back and forward propagating fields contribute to the field distribution before (i.e. sum of all reflected waves) and behind (i.e. sum of all transmitted waves) the resonator. An electromagnetic wave with an angle of incidence θ_1 traverses the resonator at an angle of θ_2 and then leaves the resonator at an angle θ_3 according to Snell's law (eq. 2.66). The layer has a thickness d_2 and the index (u, v) of the Fresnel's coefficients of transmission $t_{u,v}$ and reflection $r_{u,v}$ indicate the incident layer (u) and the transmitted layer (v) with the refractive index n_u and n_v . The reflection coefficients are symmetric by means of $r_{u,v} = -r_{v,u}$ and the propagation through n_2 with a thickness d_2 at an angle of θ_2 introduces a phase shift of $\phi_2 = k_2 d_2 / \cos \theta_2$ with $k_2 = n_2 k_0$.

The following analysis calculates the remainder for an infinite number of reflections in a resonator to a consideration of p forward propagating beams (i.e. $2p$ iterations) and then derives a criterion for p at an allowed devia-

tion a in the electric field. In this context, the term *iteration* describes all beams which propagate in one direction through one or more resonators as shown in the right subplot of 5.1. The second iteration describes the first reflected beam through all resonators and so on. After $2p$ iterations, the number of beams in each layers is equal and the scalar amplitude in the resonant layer n_2 directly before the interface to layer n_3 is composed from the sum of p forward propagating beams according to

$$\begin{aligned} A_2(p) &= t_{1,2}e^{i\phi_2} + t_{1,2}r_{2,3}r_{2,1}e^{i3\phi_2} + \cdots + t_{1,2}(r_{2,3}r_{2,1})^{p-1}e^{i2(p-1)\phi_2} \\ &= t_{1,2}e^{i\phi_2} \sum_{m=0}^{p-1} (r_{2,3}r_{2,1})^m e^{i2m\phi_2} \end{aligned} \quad (5.1)$$

If the resonator is back-illuminated, additional forward propagating beams need to be considered according to

$$\begin{aligned} A_2^-(p) &= t_{3,2}r_{2,1}e^{i2\phi_2} + t_{3,2}r_{2,1}r_{2,3}r_{2,1}e^{i4\phi_2} + \cdots + t_{3,2}r_{2,1}(r_{2,3}r_{2,1})^{p-1}e^{i3p\phi_2} \\ &= t_{3,2}r_{2,1}e^{i2\phi_2} \sum_{m=0}^{p-1} (r_{2,3}r_{2,1})^m e^{i3m\phi_2} \end{aligned} \quad (5.2)$$

The index 2 in $A_2(p)$ and $A_2^-(p)$ indicates the resonant layer. Fresnel's coefficients are given in terms of θ_1 , θ_2 and θ_3 as well as n_1 , n_2 and n_3 (eq. 3.27). These expressions are transformed and in the general case the field in the j -th resonator which consists of p forward propagating waves is then

$$\begin{aligned} A_j(p) &= t_{j-1,j} \left[\left(\frac{1 - (r_{j,j+1}r_{j,j-1})^p e^{i2\phi_j p}}{1 - r_{j,j+1}r_{j,j-1} e^{i2\phi_j}} \right) \right] \\ A_j^-(p) &= t_{j+1,j} r_{j,j-1} \left[\left(\frac{1 - (r_{j,j+1}r_{j,j-1})^p e^{i3\phi_j p}}{1 - r_{j,j+1}r_{j,j-1} e^{i3\phi_j}} \right) \right] \end{aligned} \quad (5.3)$$

obtained from the series $\sum_{m=0}^p q^m = (1 - q)^p / (1 - q)$ as shown in [1]. In the limit $p \rightarrow \infty$, the amplitude of the electric field at the end of the j -th

resonator, directly at the interface to the adjacent layer $j + 1$, is

$$\begin{aligned}\lim_{p \rightarrow \infty} A_j(p) &= \frac{t_{j-1,j}}{1 - r_{j,j+1}r_{j,j-1}e^{i2\phi_j}} = A_j^\infty \\ \lim_{p \rightarrow \infty} A_j^-(p) &= \frac{t_{j+1,j}r_{j,j-1}}{1 - r_{j,j+1}r_{j,j-1}e^{i3\phi_j}} = A_j^{-\infty}\end{aligned}\quad (5.4)$$

obtained from the series $\sum_{m=0}^{\infty} q^m = 1/(1 - q)$. The field distribution directly before the back boundary of a resonator after $2p$ iterations (i.e. $2p$ iterations are needed to consider p forward propagating waves), which is illuminated by a forward propagating field E_{j-1} at the front and a backward propagating field E_{j+1}^- at the back boundary is then

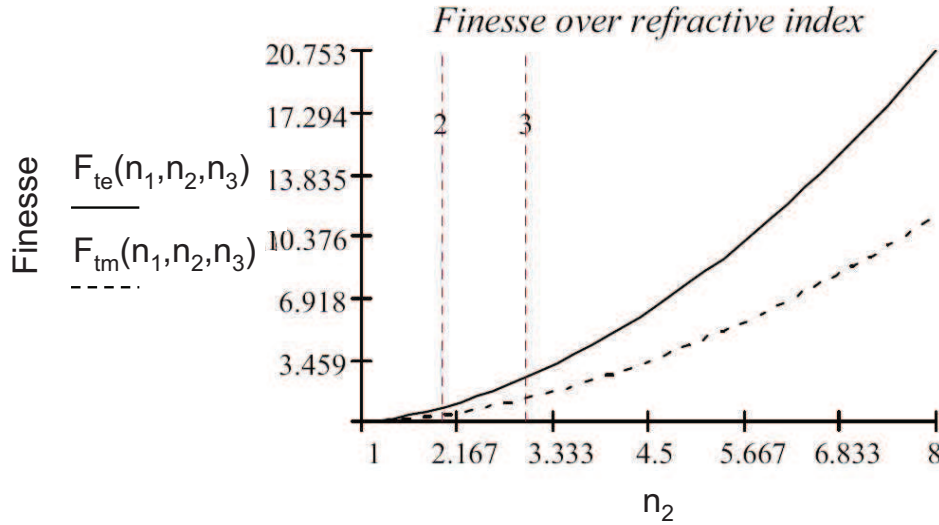
$$E_j(p) = A_j(p)E_{j-1} + A_j^-(p)E_{j+1}^-e^{i\phi_{j+1}} \quad (5.5)$$

E_{j+1}^- is assumed to originate from a position directly before the interface to layer $j + 2$ to accommodate with the assumptions in the VWPM. The transmittance of a resonator is then

$$\begin{aligned}T_j &= A_j^\infty A_j^{\infty*} \\ &= \frac{t_{j-1,j}^2}{(1 - r_{j,j+1}r_{j+1,j})^2 + 4r_{j,j+1}r_{j,j-1} \sin^2 \phi_j} \\ &= \frac{t_{j-1,j}^2}{1 + F_j \sin^2 \phi_j/2}\end{aligned}\quad (5.6)$$

with $A_j^{\infty*}$ is the conjugate complex of A_j^∞ and F is the finesse of a resonator. Obviously, the product of the inner reflection coefficients $r_{j,j+1}r_{j,j-1}$ is of major importance for each resonator because it determines the number of traversals of the EM wave through the resonator before it stabilizes. The number of iterations inside a resonator to obtain a stabilized EM field is then described by the *finesse* F . The finesse of the j -th resonator is $F_j = 4r_{j,j+1}r_{j,j-1}/(1 - r_{j,j+1}r_{j,j-1})^2$ as shown in [1]. It is a characterizing metric for a resonator, regardless of the direction of the incident wave and obtained from transformations of the squared amplitude in equation 5.6,

Figure 5.2: Finesse F of a Fabry-Perot resonator over an index change $n_2/n_1 = n_2/n_3$ from 1 to 8.



which is proportional to the intensity. Figure 5.2 shows the finesse for a TE (F_{te}) and TM (F_{tm}) polarized wave with $\theta_1 = 30\pi/180$ in an exemplary range of contrast n_j/n_{j-1} and n_j/n_{j+1} of 1 to 8. The finesse and thereby the number of forward propagating beams increase with a higher index change and the closer the absolute of the product $r_{j,j+1}r_{j,j-1}$ approaches unity. F is singular (i.e. $F = \infty$) for $|r_{j,j+1}r_{j,j-1}| = 1$, but this case is not relevant since it is not possible to obtain $\theta_j > \theta_{cr}$ (eq. 2.70) for $\theta_{j-1} < 90\pi/180$. In figure 5.10 on page 115, $T = t_{2,3}A_2(p)E_0$, with $E_0 = 1$ is plotted over the number of p forward (i.e. T_{tte}, T_{ttm}) and backward (i.e. R_{rte}, R_{rtm}) propagating beams for the TE and TM case. R describes the reflected amplitude directly before the resonator which is obtained from a sum of p reflected beams according to equation 5.3 and as introduced in [1]. The resonator

in figure 5.10 is assumed symmetric with $n_1 = n_3 = 1$ and the contrast $n_2/n_1 = n_2/n_3$ is 1.1, 2 and 3. The figure shows that a higher finesse yields a slower convergence of the electric field and the field in a resonator with a low contrast stabilizes faster and after a smaller number of iterations. The stabilization inside the resonator is independent from the magnitude of the input amplitude as shown in figure 5.11 on page 116. This is perfectly reasonable, since the input amplitude can be factored out from equation 5.1 and 5.2 and the number of steps to the stabilization of the electromagnetic field then only depends on the product $r_{j,j+1}r_{j,j-1}$, which is a function of the angle of incidence θ_j and the refractive index before (n_{j-1}), in (n_j) and behind (n_{j+1}) the resonator. In a simulation of a single resonator with the unidirectional VWPM just the first term (i.e. $p = 1$) is considered and hence the error in a simulation considering a forward propagating plane wave (fig. 5.1) is $A_2^\infty - A_2(1)$. The deviation decreases with an increasing number of iterations and in case of a resonator which is illuminated from both sides, the deviation in the j -th resonator after $2p$ iterations is

$$\begin{aligned} \delta A_j(p) &= A_j^\infty + A_j^{-\infty} - (A_j(p) + A_j^-(p)) \\ &= t_{j-1,j} \frac{(r_{j,j+1}r_{j,j-1})^p e^{i2\phi_j p}}{1 - r_{j,j+1}r_{j,j-1}e^{i2\phi_j}} + t_{j+1,j} r_{j,j-1} \frac{(r_{j,j+1}r_{j,j-1})^p e^{i3\phi_j p}}{1 - r_{j,j+1}r_{j,j-1}e^{i3\phi_j}} \end{aligned} \quad (5.7)$$

In case of a series of N coupled resonators, every beam inside a resonator contributes to the input field of the neighboring resonators. Hence, the number of beams increases exponentially with the number of iterations until the amplitudes stabilize. The stabilization of the amplitude in each resonator requires a constant number of iterations after the input amplitude has been stabilized as shown in the previous section. The important question for the stabilization of the electromagnetic field in a series of resonators is therefore the settlement of the input amplitudes from adjacent resonators which can only be achieved by a stabilization of the amplitude

in the neighboring resonators. This shows the strong recursive nature of coupled resonators. Each wave in each layer depends on the waves in every other layer. The number of beams $b(p)$ after the $2p$ -th iteration in an N -layer resonator, considering p forward propagating beams, is

$$\begin{aligned} b(p) &= N + \left(\sum_{i=1}^N i \right)^{2p} \\ &= N + \left(\frac{N(N-1)}{2} \right)^{2p} \end{aligned} \quad (5.8)$$

and the number of beams after $2p$ iterations in each of the N resonators is equal to $b(p)/N$. All amplitudes in the resonators decay simultaneously and stabilize after a variable number of iterations, dependent on the product of the inner reflection coefficients as shown in figure 5.12. The plots show the product of the inner Fresnel coefficients of reflection to the power of the number of forward propagating beams, $|(r_{j,j+1}r_{j,j-1})|^p$, for the TE- and TM-case in resonators with different finesse. The lower the contrast, the lower the inner product and the lower the finesse and the faster the stabilization of the electric field. The resonator with the highest finesse will therefore generate the highest number of beams. Since all resonators contain an equal number of beams after $2p$ iterations, the accuracy is determined by the resonator with the highest finesse. Let the accuracy a of the results be defined by a fraction of E_0 which contributes to the field inside a resonator through reflection. The calculation is supposed to terminate if the field $E_j(p)$ falls below a certain accuracy $a_j = |E_j(p+1)/E_j(p)| = |r_{j,j+1}r_{j,j-1}|$. Since $|(r_{j,j+1}r_{j,j-1})|^p$ is a strictly monotonically decreasing function for $|r_{j,j+1}r_{j,j-1}| < 1$, the delta $E_j(p+1) - E_j(p)$ inside the resonator can only decrease and never increase because all resonators contain the same number of beams after $2p$ iterations. The change in the amplitudes in a resonator will therefore never be greater than a , once this limit has been reached. This observa-

tion yields the *criterion for a minimum number of iterations* in a bidirectional propagation method. From

$$|r_{j,j-1}r_{j,j+1}|^p < a_j \quad (5.9)$$

the number of forward propagating beams is determined by

$$p > \left\lceil \frac{\ln a}{\ln R} \right\rceil \quad (5.10)$$

with $R = \max_{j \in \{1 \dots N-1\}} (|r_{j,j-1}r_{j,j+1}|)$ is the maximum product of the internal reflection coefficients of amplitude and $\lceil \cdot \rceil$ is the rounding up to the next finite integer. This expression can be transformed to

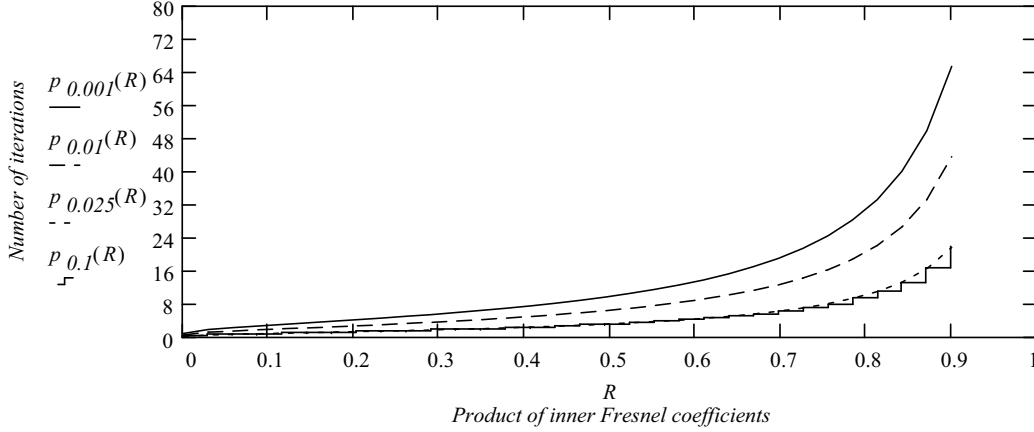
$$p > \lceil \log_R a \rceil \quad (5.11)$$

with p is the number of forward propagating beams and $a = \max_j(a_j)$. The number of iterations is then at least $2p$. The number of iterations in a lossless resonant structure which are required to obtain a maximum deviation of 0.1, 1, 2.5 and 10 percent in the amplitude of the EM field can be obtained from figure 5.3.

5.1 Bidirectional VWPM

The bidirectional VWPM considers forward and backward propagating waves. In each forward iteration over n_z layers of a system \mathcal{N} with a length Z , $n_z = Z/\delta z$ reflected vector waves are generated at every interface. In a second iteration in the opposite direction, the reflected waves are collected at every interface, accumulated to the back-propagating waves and the next n_z reflected waves are generated. A simulation of p forward-propagating waves then requires $2p$ iterations and traverses $2pn_z$ layers.

Figure 5.3: Number of iterations p over the product of the inner Fresnel coefficients R for $a \in \{0.001, 0.01, 0.025, 0.1\}$.



In case of resonant structures, the algorithm terminates after $2p$ iterations, with p is determined from equation 5.11, from an accepted deviation a and from the maximum product of all inner Fresnel coefficients $R = \max_j(R_j) = \max_j(r_{j,j-1}r_{j,j+1})$ with $j \in \{1, \dots, n_z\}$.

Again, the VWPM assumes that at each interface, a vector field \mathbf{E}_e has already traversed the incident layer (i.e. subscript "e"). An interface is formed by a change in the refractive index between the incident layer and the transmitted layer (i.e. subscript "t") which requires a separation of the field into its TE- and TM- components (eq. 3.17).

In the first step of the bidirectional VWPM, the vectorial field just before the interface is decomposed into its Fourier components

$$\tilde{\mathbf{E}}_e^{(2)}(\mathbf{k}_\perp) = \begin{pmatrix} \tilde{E}_{x,e}(\mathbf{k}_\perp) \\ \tilde{E}_{y,e}(\mathbf{k}_\perp) \end{pmatrix} = \mathcal{F} \left\{ \begin{pmatrix} E_{x,e}(\mathbf{r}_\perp) \\ E_{y,e}(\mathbf{r}_\perp) \end{pmatrix} \right\} = \mathbf{E}_e^{(2)}(\mathbf{r}_\perp) \quad (5.12)$$

5.1.1 Transfer matrix of transmission

At an interface (i.e. $n_e \neq n_t$), the EM field requires to be separated into its TE- and TM-field components (eq. 3.17). The transmitted wave $\mathbf{E}_t^{(2)+}$ is calculated from the *transfer matrix of transmission* \mathbf{M} (eq. 3.24)

$$\tilde{\mathbf{E}}_t^{(2)+} = \mathbf{M} \cdot \tilde{\mathbf{E}}_e^{(2)} \quad (5.13)$$

The two-dimensional plane wave component $\tilde{\mathbf{W}}_t^{(2)+}$ which is supposed to propagate through the transmitted layer is then composed from the forward propagating spectrum $\tilde{\mathbf{E}}_t^{(2)+}$ and a backward propagating spectrum $\tilde{\mathbf{E}}_t^{(2)-}$ according to

$$\tilde{\mathbf{W}}_t^{(2)+}(\mathbf{k}_\perp, \mathbf{r}_\perp) = (\tilde{\mathbf{E}}_t^{(2)+} + \tilde{\mathbf{E}}_t^{(2)-})e^{+i\mathbf{k}_\perp \cdot \mathbf{r}_\perp} \quad (5.14)$$

$\tilde{\mathbf{E}}_t^{(2)-}$ is obtained from equation 5.22 which will be obtained from a future step of calculation in the opposite direction. $\tilde{\mathbf{E}}_t^{(2)-}$ is initialized to zero for the first iteration. The incident and transmitted layers change their role when the direction of propagation changes.

5.1.2 Bidirectional propagation

With equation 5.14, the two-dimensional field behind the interface is known. To complete the propagation through the layer behind the interface, a propagation of each wave $\tilde{\mathbf{W}}_t^{(2)+}$ through the inhomogeneous medium with a thickness $\delta z = Z/n_z$ is applied, using the space- and frequency-dependent phase element $\mathcal{P}(\mathbf{r}_\perp, \mathbf{k}_\perp)$ (eq. 3.11) to obtain the propagated spectrum at the end of the layer behind the interface. With equation 3.16 the z-component is then calculated from the space derivatives $\epsilon_{t,x} = \partial\epsilon_t/\partial x$ and

$\epsilon_{t,y} = \partial\epsilon_y/\partial y$ of $\epsilon(\mathbf{r}_\perp)$ in the propagation layer and the resulting three-dimensional field distribution $\mathbf{E}_t(\mathbf{r})$ is finally obtained from the summation of all field components

$$\mathbf{E}_t^+(\mathbf{r}_\perp) = \frac{1}{A} \iint \tilde{\mathbf{W}}_t^+ \mathcal{P} \frac{d^2\mathbf{k}_\perp}{(2\pi)^2} \quad (5.15)$$

with $A = XY$.

5.1.3 Transfer matrix of reflection

The transfer at interface from equation 5.13 yields the forward propagating field \mathbf{E}_t^+ but the interface also generates a reflected spectrum $\tilde{\mathbf{E}}_e^-$ which is obtained from the TE- and TM-components according to

$$\tilde{\mathbf{E}}_e^-(\mathbf{k}_\perp, \mathbf{r}_\perp) = r_{TE} \tilde{E}_{TE,e} \mathbf{e}_{TE,e} + r_{TM} \tilde{E}_{TM,e} \mathbf{e}_{TM,e} \quad (5.16)$$

with

$$\begin{aligned} \tilde{E}_{TE,e}(\mathbf{k}_\perp, \mathbf{r}_\perp) &= \tilde{\mathbf{E}}_e(\mathbf{k}_\perp) \cdot \mathbf{e}_{TE,e}(\mathbf{k}_\perp) \\ \tilde{E}_{TM,e}(\mathbf{k}_\perp, \mathbf{r}_\perp) &= \tilde{\mathbf{E}}_e(\mathbf{k}_\perp) \cdot \mathbf{e}_{TM,e}(\mathbf{k}_\perp) \end{aligned} \quad (5.17)$$

Fresnel's coefficients of reflection for the TE-component r_{TE} and the TM-component r_{TM} are

$$\begin{aligned} r_{TE}(\mathbf{k}_\perp, \mathbf{r}_\perp) &= \frac{k_{z,e} - k_{z,t}}{k_{z,e} + k_{z,t}} \\ r_{TM}(\mathbf{k}_\perp, \mathbf{r}_\perp) &= \frac{n_t^2 k_{z,e} - n_e^2 k_{z,t}}{n_t^2 k_{z,e} + n_e^2 k_{z,t}} \end{aligned} \quad (5.18)$$

derived from the surface normal \mathbf{n} and the propagation vector \mathbf{k} as shown in appendix B.

The vectors of unity for the TE-component e_{TE} and for the TM-component e_{TM} are defined according to equation 3.20 and 3.21. For reflections, e_{TM} does not change at the interface because the refractive index and therefore k_z does not change. In the scalar components of the TE- and TM-component, the z -component $E_{z,e}$ is substituted by equation 3.16. Inserting the scalar TE- and TM-components into equation 5.16 and reordering the expression by the transversal vector components of $\tilde{\mathbf{E}}$, equation 5.16 is then transformed to a matrix multiplication

$$\tilde{\mathbf{E}}_e^-(\mathbf{k}_\perp, \mathbf{r}_\perp) = \mathbf{R} \cdot \tilde{\mathbf{E}}_e^{(2)}(\mathbf{k}_\perp) \quad (5.19)$$

with \mathbf{R} is the *transfer matrix of reflection*

$$\mathbf{R}(\mathbf{k}_\perp, \mathbf{r}_\perp) = \frac{1}{k_\perp^2} \begin{pmatrix} r_{TE}k_y^2 + r_{TM}k_x^2(1 - i\hat{\epsilon}_x) & (r_{TM}(1 - \hat{\epsilon}_y) - r_{TE})k_xk_y \\ (r_{TM}(1 - \hat{\epsilon}_x) - r_{TE})k_xk_y & r_{TE}k_x^2 + r_{TM}k_y^2(1 - i\epsilon_y) \\ -r_{TM}k_x(1 - i\hat{\epsilon}_x)k_\perp^2/k_{z,e} & -r_{TM}k_y(1 - i\hat{\epsilon}_y)k_\perp^2/k_{z,e} \end{pmatrix} \quad (5.20)$$

with $\hat{\epsilon}_x = \epsilon_x k_\perp^2 / \epsilon / k_e^2 / k_x$ and $\hat{\epsilon}_y = \epsilon_y k_\perp^2 / \epsilon / k_e^2 / k_y$. Appendix B shows the detailed calculation. The z -component of $\tilde{\mathbf{E}}_e^-$ is directly obtained from $\tilde{\mathbf{E}}_{\perp,e}^{(2)}$ with the 3×2 -matrix \mathbf{R} , according to equation 3.16. Since the reflected spectrum is processed with equation 5.14, no propagation is necessary and the field distribution is then obtained by the superposition of all plane wave components in the reflected spectrum

$$\mathbf{W}_e^-(\mathbf{k}_\perp, \mathbf{r}_\perp) = \mathbf{E}_e^- e^{+i(\mathbf{k}_\perp \cdot \mathbf{r}_\perp)} \quad (5.21)$$

The spatial distribution of the reflected field is then

$$\mathbf{E}_e^-(\mathbf{r}_\perp) = \frac{1}{A} \iint \mathbf{W}_e^- \frac{d^2 \mathbf{k}_\perp}{(2\pi)^2} \quad (5.22)$$

with $A = XY$.

5.2 Bidirectional algorithm

A system \mathcal{N} is split into n_z layers and sampled at n_x and n_y locations. The spatial frequencies $k_x(p) = 2\pi p\delta\nu_x = 2\pi p/(n_x\delta x)$ and $k_y(q) = 2\pi q\delta\nu_y = 2\pi q/(n_y\delta y)$, with $p \in \{-n_x/2 \dots n_x/2\}$ and $q \in \{-n_y/2 \dots n_y/2\}$ are determined by the sampling $(\delta x, \delta y)$ in the aperture $A = XY$.

A vector field is propagating through the system \mathcal{N} layer by layer according to the bidirectional VWPM equations that have been introduced in the previous section. Each layer j has a layer of incidence $j - 1$ and a layer of propagation j . For the first iteration $j = 0$, the incident layer is modeled by a homogeneous medium (i.e. $n_{extern}(x, y) = const$) or by a copy of layer zero.

The reflected waves $\mathbf{E}^-(\mathbf{r}_\perp)$ at all interfaces are initialized to zero.

In the j -th iteration, the incident wave is positioned in layer $j - 1$ and in direct contact to the boundary with layer j . The *first step* of the j -th iteration is the decomposition of the spatial field into its plane waves (i.e. the Fourier transformation) of the propagating $\mathbf{E}_{j-1}^{(2)}$ and reflected $\mathbf{E}_j^{(2)-}$ field

$$\mathbf{E}_{j-1}^{(2)}(x, y) = \begin{pmatrix} E_{x,j-1} \\ E_{y,j-1} \end{pmatrix} \xRightarrow{FFT} \begin{pmatrix} \tilde{E}_{x,j-1} \\ \tilde{E}_{y,j-1} \end{pmatrix} = \tilde{\mathbf{E}}_{j-1}^{(2)}(k_x, k_y) \quad (5.23)$$

and

$$\mathbf{E}_j^{(2)-}(x, y) = \begin{pmatrix} E_{x,j}^- \\ E_{y,j}^- \end{pmatrix} \xRightarrow{FFT} \begin{pmatrix} EX_j^- \\ EY_j^- \end{pmatrix} = \tilde{\mathbf{E}}_{j-1}^{(2)-}(k_x, k_y) \quad (5.24)$$

with $m \in \{-n_x/2 \dots n_x/2\}$ and $n \in \{-n_y/2 \dots n_y/2\}$. The *second step* applies the transformation matrix of reflection \mathbf{R}_j and transmission \mathbf{M}_j for

each spatial frequency $\mathbf{k}_\perp = (k_x, k_y) = (p\delta k_x, q\delta k_y)$ and all locations $\mathbf{r}_\perp = (x, y) = (m\delta x, n\delta y)$ in the aperture. The reflected plane wave amplitudes are derived from the spectrum according to

$$\begin{pmatrix} EX_{j-1}^-(p, q, m, n) \\ EY_{j-1}^-(p, q, m, n) \end{pmatrix} := \mathbf{R}_j \cdot \tilde{\mathbf{E}}_{j-1}^{(2)} \quad (5.25)$$

and the plane wave in the aperture without propagation is the obtained from the lateral expansion of the complex exponential according to

$$\begin{pmatrix} WX_{j-1}^-(p, q, m, n) \\ WY_{j-1}^-(p, q, m, n) \end{pmatrix} := \begin{pmatrix} EX_{j-1}^- \\ EY_{j-1}^- \end{pmatrix} e^{+i\mathbf{k}_\perp \cdot \mathbf{r}_\perp} \quad (5.26)$$

The transmitted components are derived from

$$\begin{pmatrix} EX_j^+(p, q, m, n) \\ EY_j^+(p, q, m, n) \end{pmatrix} := \mathbf{M}_j \cdot \tilde{\mathbf{E}}_{j-1}^{(2)} \quad (5.27)$$

The reflected two-dimensional spectrum EX_j^- and EY_j^- in layer j (!) is then accumulated to the transmitted spectrum EX_j^+ and EY_j^+ . EX_j^- and the two-dimensional plane wave components are then

$$\begin{pmatrix} WX_j^+(p, q, m, n) \\ WY_j^+(p, q, m, n) \end{pmatrix} := \left(\begin{pmatrix} EX_j^+ \\ EY_j^+ \end{pmatrix} + \begin{pmatrix} EX_j^- \\ EY_j^- \end{pmatrix} \right) e^{+i\mathbf{k}_\perp \cdot \mathbf{r}_\perp} \quad (5.28)$$

With WX_j^+ and WY_j^+ , the spectrum behind the interface is known and the propagation of a distance δz along the z-axis is then obtained according to equation 5.15 from a multiplication with the position and frequency-dependent phase element

$$\begin{pmatrix} EX_j^+(p, q, m, n) \\ EY_j^+(p, q, m, n) \end{pmatrix} := \begin{pmatrix} WX_j^+ \\ WY_j^+ \end{pmatrix} \mathcal{P} \quad (5.29)$$

The propagated magnetic field vector of a spatial frequency is derived from

the x - and y -component of the electric field according to

$$\begin{pmatrix} HX_j(p, q, m, n) \\ HY_j(p, q, m, n) \\ HZ_j(p, q, m, n) \end{pmatrix} := \mathbf{T}_j \cdot \begin{pmatrix} EX_j^+ \\ EY_j^+ \end{pmatrix} \quad (5.30)$$

and the z -component EZ_j^+ in layer j is then obtained from equation 3.16. The summation over all deformed plane waves of the three-dimensional electric \mathbf{E}_j and magnetic \mathbf{H}_j field in layer j then yields the distribution of the electromagnetic field

$$\mathbf{E}_j(x, y) := \frac{1}{n_x n_y} \sum_p \sum_q \begin{pmatrix} EX_j^+ \\ EY_j^+ \\ EZ_j^+ \end{pmatrix} \quad (5.31)$$

and

$$\mathbf{H}_j(x, y) := \frac{1}{n_x n_y} \sum_p \sum_q \begin{pmatrix} HX_j^+ \\ HY_j^+ \\ HZ_j^+ \end{pmatrix} \quad (5.32)$$

The summation of all reflected electric field components from equation 5.26 then yields the reflected field in layer $j - 1$

$$\mathbf{E}_{j-1}^-(x, y) := \frac{1}{n_x n_y} \sum_p \sum_q \begin{pmatrix} WX_{j-1}^- \\ WY_{j-1}^- \\ WZ_{j-1}^- \end{pmatrix} \quad (5.33)$$

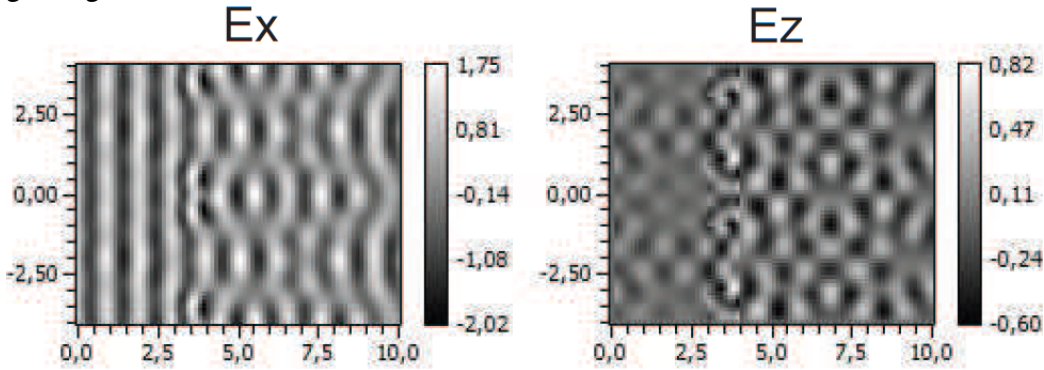
The reflected field distribution is stored and then retrieved in a processing step in the opposite direction. With this algorithm the $(j - 1)$ -th reflected contributes to the processing of the j -th layer in the opposite direction. In the program code, the index $j - 1$ is replaced with $j - d$ with $d \in \{-1, 1\}$, which indicates the direction of propagation. The algorithm iterates with an increasing sequence of layers for $d = 1$ and with a decreasing order

of layers for $d = -1$. d is negated (i.e. $d = -d$) if $j = 1$ or $j = n_z$. The algorithm terminates if all reflected fields are zero or smaller than a configurable threshold, or if a certain number of reflection have been simulated (eq. 5.11).

5.3 3D-Simulation of a 2D-grating

The results of the simulation of a 2D-grating in chapter 3 on page 71 shows that the unidirectional method does not calculate reflected fields. With the bidirectional VWPM, the reflected field is calculated according to the presented algorithm. In the following simulation, the configuration of the grating is identical to the scenario in chapter 3. In a first simulation with the bidirectional VWPM, the electric field distribution in a two-dimensional grating with a pitch $p_x = p_y = 4\lambda$, a width $w_x = w_y = 2\lambda$ and a height $h = \lambda$, as it was introduced in chapter 3, is investigated. The incident plane vector wave is again TM-polarized, has a unit amplitude and propagates with vertical incidence (i.e. $\theta = 0$). The refractive index of the grating is $\hat{n}_g = 1.5 + i0$ and the index of the surrounding medium is $\hat{n}_s = 1 + i0$. A comparison of the results from a simulation with the bidirectional VWPM in figure 5.4 to the results from the RCWA in figure 3.7 on page 74 shows a significant difference in the reflected field before the grating. The sampling which is used in the simulation with the VWPM does not exactly meet the case $\theta_e = \theta_c$ (i.e. $\mathbf{k}_\perp = nk_0$) and hence also not $\mathcal{P} = \exp(0) = 1$. In case of a discretization which perfectly meets the evanescent boundary, the wave propagates along the interface as shown in figure 3.9 on page 80. A superposition with the reflected wave then yields the depicted field distribution from the RCWA. The deviation in the reflected field does not occur in the

Figure 5.4: x -component in the yz -plane (left) and z -component in the xz -plane (right) of the electric field from the bidirectional simulation of a 2D grating.



simulation of a second grating in figure 5.5. In this case, the sampling which is used in the RCWA and the VWPM do both not exactly meet the critical angle of incidence

$$\mathbf{k}_{\perp} = \sin \theta_c = \frac{n_t}{n_e} \quad (5.34)$$

with $n_e > n_t$ (i.e. internal reflection). Then, the reflected field does not contain the backward propagating wave at the evanescent boundary.

In a second scenario, a GaAs-grating with a period of 5λ , a height $h = 0.3 \text{ } [\mu\text{m}] \approx \lambda/3$ and a refractive index of $3.647 + i0.025$ is positioned at $Z = 2.5 \text{ } [\mu\text{m}]$ in a medium with $3.647 + i0$ before the grating and $1 + i0$ behind the grating. A TM-polarized plane wave propagates a distance of $Z = 5 \text{ } [\mu\text{m}]$ in an aperture $X = Y = 5 \text{ } [\mu\text{m}]$. The scene is sampled with $n_x = n_y = n_z = 256$ and the simulation then calculates 2^{16} modes in a three-dimensional simulation. The electric field distribution of the x and z -component is compared to the results from an RCWA with 4 modes. The patterns show a good coincidence as shown in figure 5.5. The deviation

of the maximum and minimum amplitude is 0.0074 and -0.0713 for the x-component of the electric field vector and ± 0.0043 for the z-component.

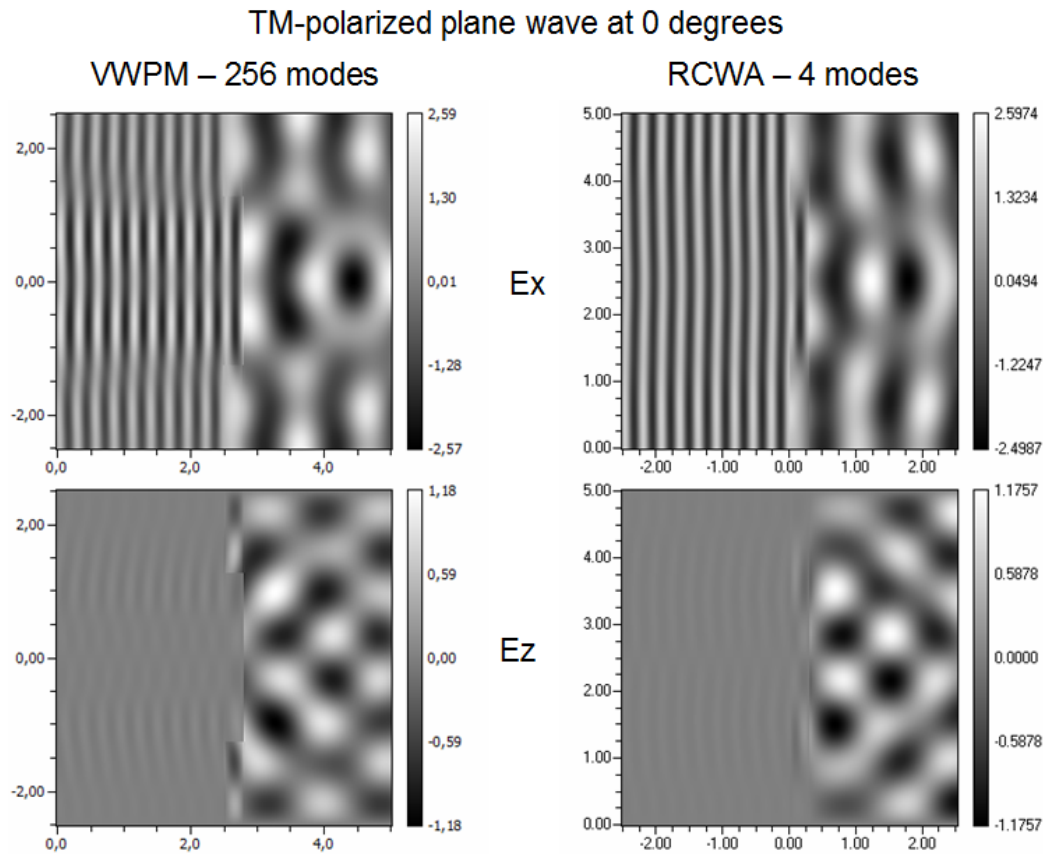
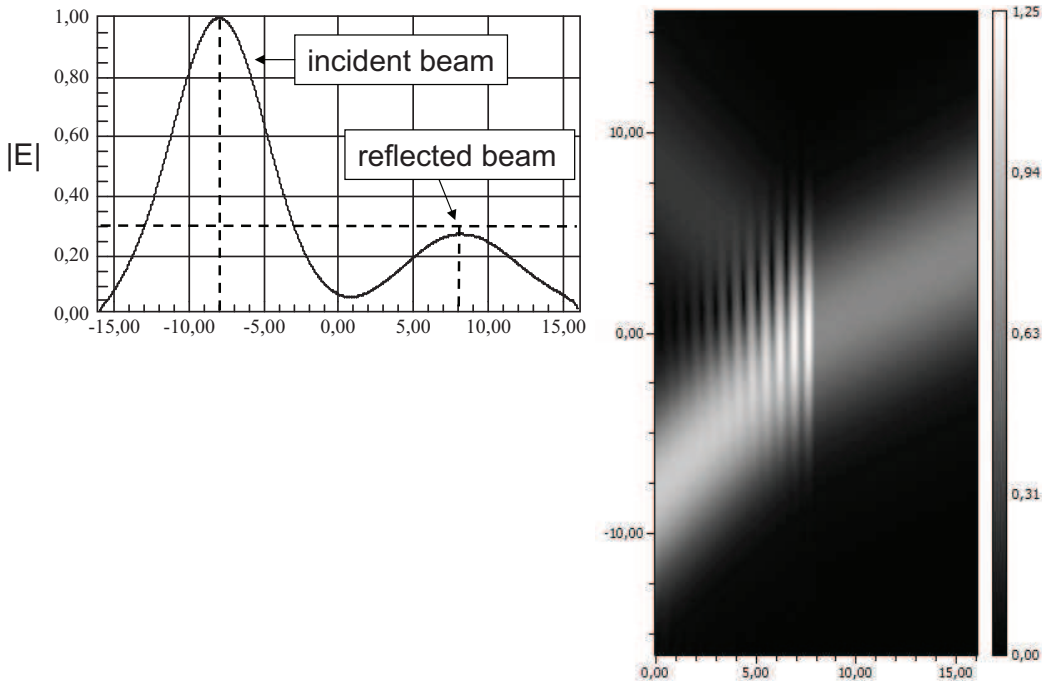


Figure 5.5: Bidirectional simulation of a 1D GaAs-grating with the VWPM (left) and the RCWA (right).

Figure 5.6: Amplitude of a reflected TE-polarized Gaussian beam at 45° at $z = 0$, simulated with the bidirectional VWPM.



5.4 2D simulation of a dielectric boundary

Let a single boundary be defined by a refractive index of $\hat{n}_e = 1 + i0$ before and $\hat{n}_t = 1.5 + i0$ behind the interface. A TE-polarized Gaussian beam with a unit amplitude, an angle of incidence of 45° and a waist of $\sigma_x = 8 [\mu m]$ propagates $5 [\mu m]$ and is then reflected at the boundary. According to Fresnel's reflection coefficient for a TE-polarized electric field, the amplitude of the reflected wave is equal to $|E_y^-| = |r_{TE} E_y| [V/m]$ and due to the unit amplitude, the coefficient of reflection equals to the reflected

amplitude $|E_y^-| = |r_{TE}| = 0.303 [V/m]$. With an angle of incidence of 45 degrees and a shift of $X_e = -8 [\mu m]$ in the aperture, the peak of the Gaussian beam at $Z = 0 [\mu m]$ is expected to be mirrored at $X = 0 [\mu m]$ and the reflected peak is then positioned at $X_r = 8 [\mu m]$. The simulation with the bidirectional VWPM, using $n_x = 512$, $n_z = 256$, $X = 32$ and $Z = 16$ shows that the results agree with the theory as shown in figure 5.6. The horizontal and vertical dashed lines indicate the exact amplitude and the exact location of the gaussian peak from theory.

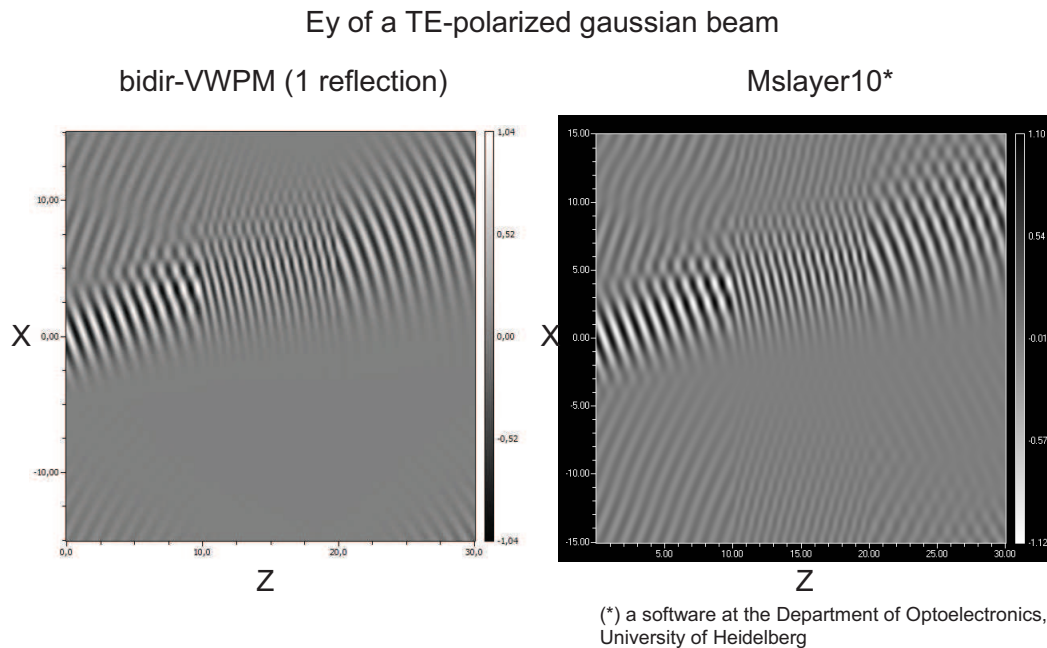


Figure 5.7: E-Field in a resonator simulated with the VWPM (left) and MSlayer10 (right).

5.5 2D simulation of a resonator

The simulation of a resonator with a thickness of $10 [\mu m]$ and a refractive index of $1.5 + i0$, with $10 [\mu m]$ of vacuum before and behind the resonator shows that the electric field distribution is shown in figure 5.7. The result of the simulation with the bidirectional VWPM correlates well to the results from a simulation with MSlayer10, a software which utilizes matrix multiplications according to the multilayer theory. The incident wave is TE-polarized, has a wavelength of $1 [\mu m]$, an amplitude of $E_0 = 1 [V/m]$ and the angle of incidence θ_i is 20 degrees. The propagation angle inside the resonator is then $\theta_t = 13.18$ (eq. 2.66) and the product of the inner Fresnel reflection coefficients for the TE-case is $R = -0.047$. In order to obtain a deviation of 1 per-mill (i.e. 0.001) to the exact results from theory, the number of iterations is then $p = \lceil \ln_{|-0.047|} 0.001 \rceil = 3$, obtained from equation 5.11. Table 5.1 shows the change of the maximum amplitude and the deviation of the amplitude if one, two, three and ten reflected waves are considered. The deviation of the amplitude is below the desired accuracy after three iterations and the changes of the amplitude are below $E_0 \cdot 10^{-5}$ if ten and more reflected waves are considered. A comparison to the results from the multilayer theory in the right subplot of figure 5.7 shows that the deviation is -0.06 for the maximum and 0.08 for the minimum amplitude.

Table 5.1: *Maximum amplitude and deviation of the amplitude for one, two, three and ten reflected waves in the resonator in figure 5.7.*

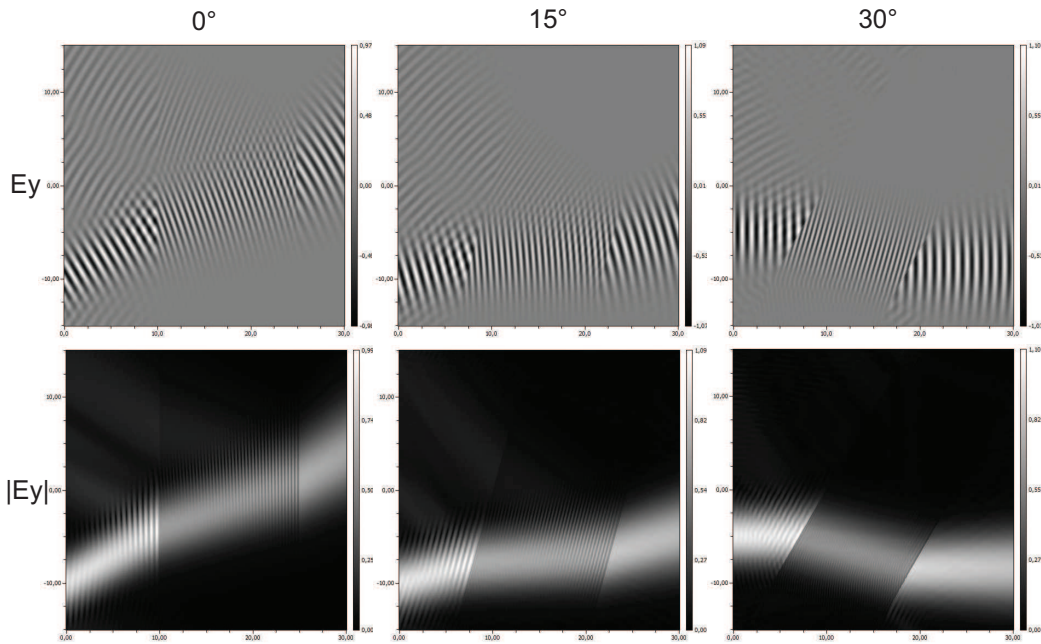
Num. of reflected waves	$\max(E (\mathbf{r}))$	$ \delta(\max(E (\mathbf{r}))) $
0	0.93964	—
1	1.05030	0.11066
2	1.05050	0.0002
3	1.05058	0.00008
10	1.05058	$< 10^{-5}$

5.6 2D simulation of an oblique interfaces

Ideally, the results of a simulation should be invariant to a rotation of the scene but with the predefinition of the z-axis as the axis of propagation, some interesting effects are obtained in a simulation with the bidirectional VWPM. Let a Gaussian beam with a wavelength of $1 [\mu m]$ and a waist of $5 [\mu m]$ propagate through a homogeneous layer with a thickness of $30 [\mu m]$ and a refractive index of $n_l = 1.5 + i0$. The TE-polarized Gaussian beam propagates a distance of $Z = 30 [\mu m]$ in an aperture $X = 30 [\mu m]$. The angle of incidence of the Gaussian beam to the homogeneous layer is 30 degrees.

In a simulation of a vertical layer in the left subplot of figure 5.8, the bidirectional simulation shows two parallel reflected beams which originate from the first and second interface. If the scene and the incident beam are

Figure 5.8: 2D simulation of a slanted homogeneous layer with the bidirectional VWPM at 0 degrees (left), 15 degrees (middle) and 30 degrees (right).



clockwise rotated by 15 degrees, the real part of E_y and the amplitude in the middle subplots of figure 5.8 still show two parallel reflected beams. After another clockwise rotation about 15 degrees in a clockwise direction, the reflected beams in the resonator are reversed as depicted in the right subplot of figure 5.8. This result is caused by the definition of e_z being the surface normal in the algorithm of the VWPM. With this definition, the angle of incidence at the second boundary has a reversed sign. This causes a reversed angle of reflection for the beam and gives the reason for the results in the right subplots of figure 5.8.

5.7 Transfer of evanescent modes

In case of internal reflection (i.e. $n_e > n_t$), the reflected electric field for propagating spatial frequencies (i.e. $\mathbf{k}_\perp \leq n_e^2 k_0^2$) before and evanescent spatial frequencies (i.e. $\mathbf{k}_\perp > n_t^2 k_0^2$) behind the interface is obtained from a multiplication with the complex-valued transfer matrix of reflection $\hat{\mathbf{R}}$ according to

$$\tilde{\mathbf{E}}_{j-1}^-(\mathbf{k}_\perp, \mathbf{r}_\perp) = \hat{\mathbf{R}}_j \cdot \tilde{\mathbf{E}}_{j-1}^{(2)}(\mathbf{k}_\perp) \quad (5.35)$$

By inserting the complex z-component of the propagation vector in the Fresnel reflection coefficients (eq. 2.74), the complex transfer matrix of reflection

$$\hat{\mathbf{R}}_j(\mathbf{k}_\perp, \mathbf{r}_\perp) = \frac{1}{k_\perp^2} \begin{pmatrix} \hat{r}_{TE} k_y^2 + \hat{r}_{TM} k_x^2 (1 - i\hat{\epsilon}_x) & (\hat{r}_{TM}(1 - \hat{\epsilon}_y) - \hat{r}_{TE}) k_x k_y \\ (\hat{r}_{TM}(1 - \hat{\epsilon}_x) - \hat{r}_{TE}) k_x k_y & \hat{r}_{TE} k_x^2 + \hat{r}_{TM} k_y^2 (1 - i\hat{\epsilon}_y) \\ -\hat{r}_{TM} k_x (1 - i\hat{\epsilon}_x) k_\perp^2 / \hat{k}_{z,e} & -\hat{r}_{TM} k_y (1 - i\hat{\epsilon}_y) k_\perp^2 / \hat{k}_{z,e} \end{pmatrix} \quad (5.36)$$

is obtained from equation 5.16 with \hat{r}_{TE} and \hat{r}_{TM} as defined in equation 2.74. The reflected field \mathbf{E}^- at location \mathbf{r}_\perp directly before the interface is then derived from the integration of the non-propagated (i.e. $\delta z = 0$) complex exponential plane wave components in the aperture $A = XY$

$$\mathbf{W}_e^-(\mathbf{k}_\perp, \mathbf{r}_\perp) = \mathbf{E}_{j-1}^- e^{i\mathbf{k}_\perp \cdot \mathbf{r}_\perp} \quad (5.37)$$

over all transversal spatial frequencies

$$\mathbf{E}_e^-(\mathbf{r}_\perp) = \frac{1}{A} \iint \mathbf{W}_{j-1}^-(\mathbf{k}_\perp, \mathbf{r}_\perp) \frac{d^2 \mathbf{k}_\perp}{(2\pi)^2} \quad (5.38)$$

All reflected and transmitted electric fields are calculated directly before the interface. No reflected wave is calculated for all evanescent spatial

frequencies before the boundary (i.e. $k_{\perp} > n_{j-1}^2 k_0^2$). The evanescent field behind the interface is derived from the evanescent wave model in chapter 3.

5.8 Algorithm for evanescent modes

The transversal components of the electric field E_x and E_y are Fourier transformed according to equation 5.23. In case of a real-valued z-component of the propagation vector before the interface $\hat{k}_{z,e} = k_{z,e} + i0$ and a complex z-component of the propagation vector behind the interface $\hat{k}_{z,t} = 0 + i\gamma_{z,t}$ (i.e. case 2 in table 3.2), the complex transfer matrix of reflection $\hat{\mathbf{R}}_j$ (eq. 5.36) is applied in equation 5.25. The z-component of the reflected field is then derived from the transversality condition (eq. 2.36) and the total internally reflected wave then extends the propagating wave in the opposite direction according to equation 5.28 in the following iteration. A complex-valued z-component of the propagation vector before the interface (i.e. case 3 and 4 in table 3.2) belongs to an evanescent mode and then no reflected field is calculated at the interface. In case 3, the algorithm for evanescent modes in chapter 3 is applied.

5.9 3D-Simulation of a 2D-grating with evanescent modes

With the evanescent wave model, the bidirectional simulation of the phase Ronchi with a pitch of 4λ in chapter 3 shows changes in the z-component of the electric field distribution at the edges of the grating. The changes in the x-component are not significant as shown in figure 5.9, but the magnitude of the z-component shows better agreement with the results from RCWA, shown in figure 3.7.

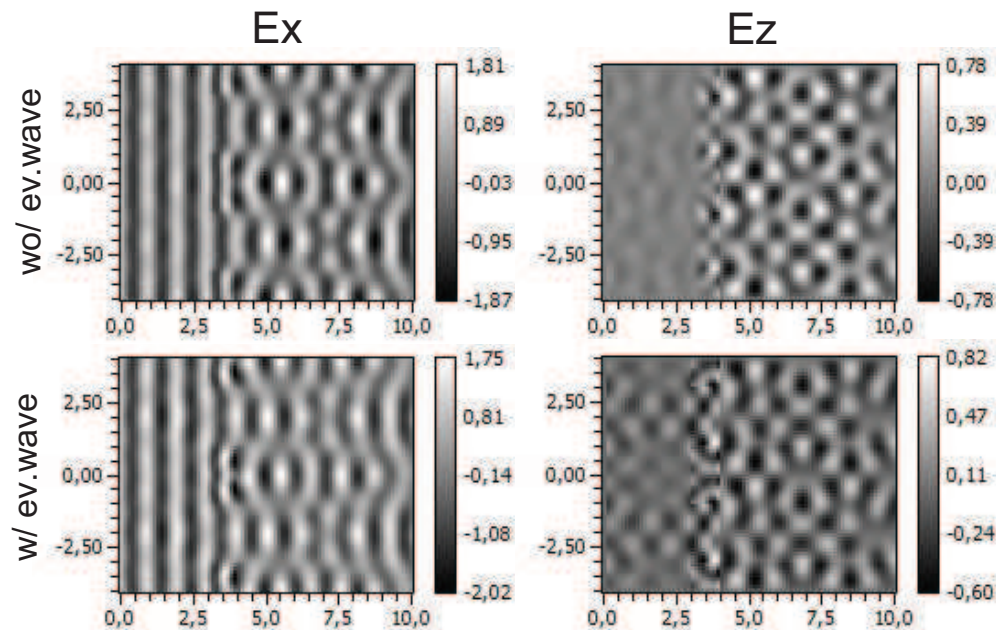


Figure 5.9: 3D simulation of a 4λ - 2λ - 1λ -phase Ronchi without (top) evanescent waves and with (bottom) evanescent waves (bidirectional VWPM).

Figure 5.10: Reflected (R) and Transmitted (T) amplitude before and behind a resonator for a TE (R_{rte}, T_{tte}) and TM (R_{rtm}, T_{ttm}) polarized wave with unit amplitude.

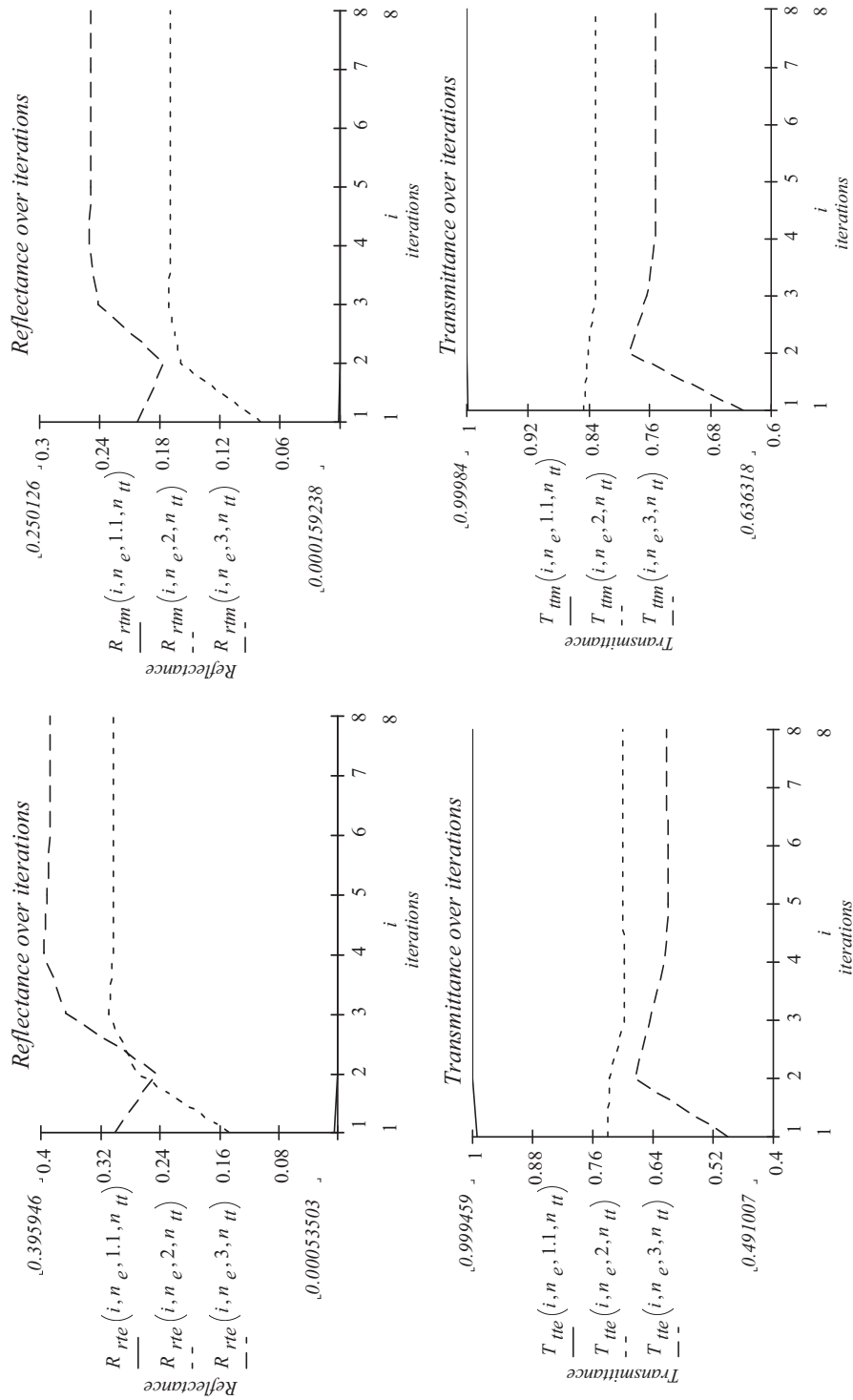
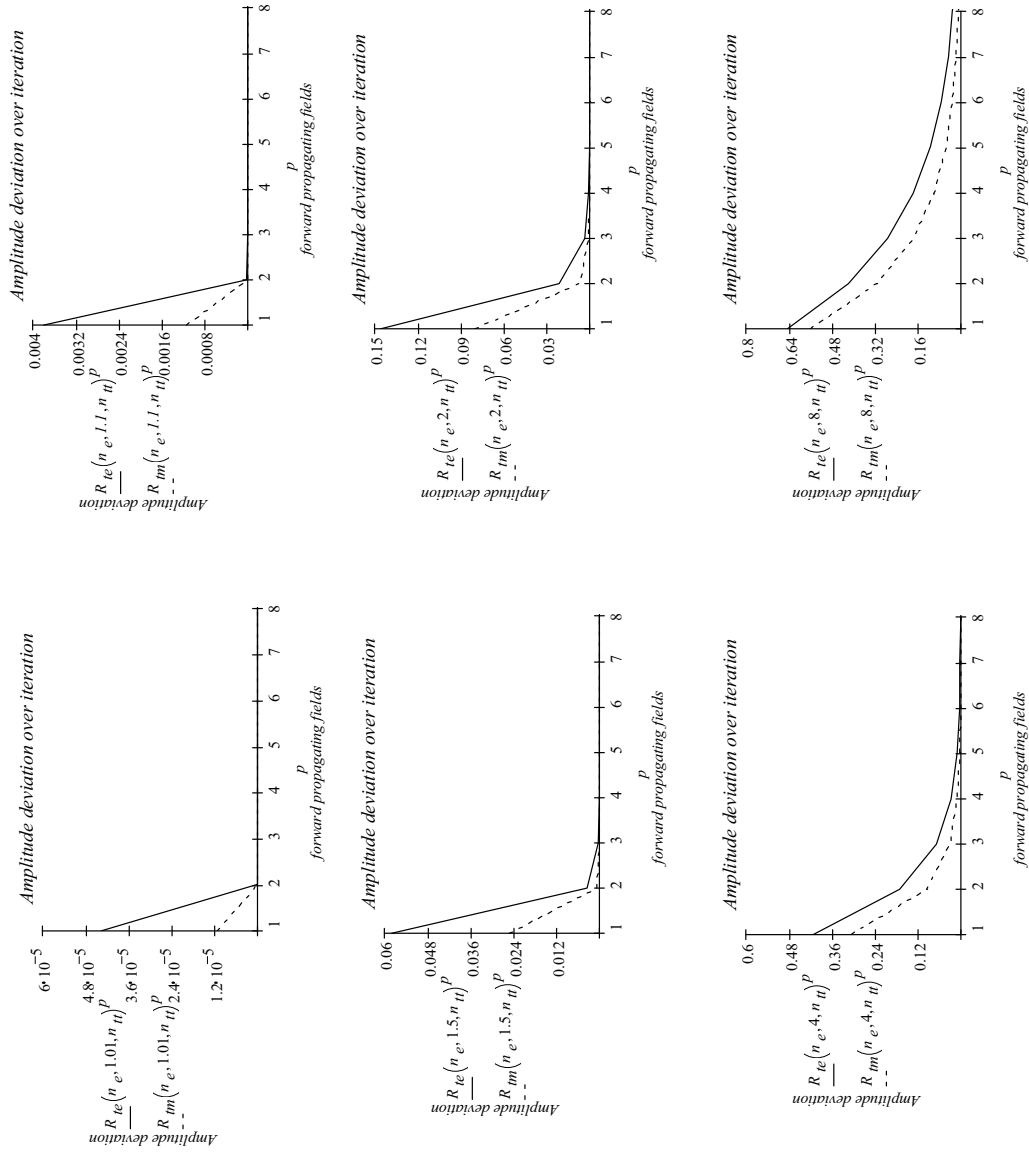


Figure 5.12: Product of the inner reflection coefficients ($R = r_{j,j+1}r_{j,j-1}$) to the power of the number of forward propagating fields p for the TE (R_{te}^p) and TM (R_{tm}^p) case with $E_0 = 1$.



Chapter 6

Sampling

The reduction of the partial differential equation to a ordinary differential equation from the separation of a space variable allows the piecewise solution of the two- or three-dimensional Helmholtz equation (eq. 2.15). The separated variable is then the propagation axis of the electromagnetic field. This allows the use of the Fourier transformation to obtain one- or two-dimensional spectrum of an electromagnetic field and to derive its propagation along the separated space variable from a solution of the scalar or vectorial diffraction integral (eq. 2.60).

In order to ideally reproduce a spatial distribution of a complex electromagnetic (EM) field from its spectrum, the sampling in the aperture has to meet the *Whittaker-Kotelnikow-Shannon (WKS) sampling theorem*, also called the Shannon theorem.

6.1 Sampling in the aperture

According to the sampling theorem, the sufficient condition for exact reconstructibility of a signal from samples at a uniform sampling rate ν_s [1/m] (in samples per meter) is

$$\nu_s > 2B \quad (6.1)$$

with B is the bandwidth of a signal. The space D between two samples is then

$$D = \frac{1}{\nu_s} \quad (6.2)$$

and the discrete electric field is obtained from $\mathbf{E}(mD)$, with $m \in \mathcal{Z}$ (integers).

*If the highest frequency in the original signal is known, the sampling theorem gives the lower bound of the sampling frequency ν_s for which perfect reconstruction can be assured (eq. 6.1). This lower bound to the sampling frequency, $\nu_N = 2B$, is called the *Nyquist rate*.*

*If instead the sampling frequency is known, the theorem gives an upper bound for frequency components, $B < \nu_s/2$, of the signal to allow a perfect reconstruction. This upper bound of the bandwidth is the *Nyquist frequency*.*

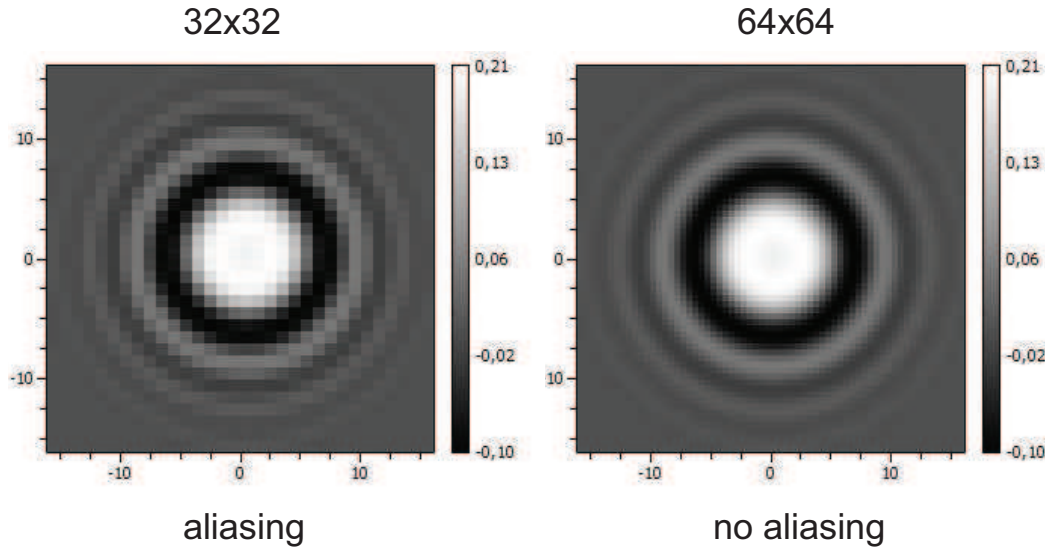
Both cases imply that the signal to be sampled is band-limited. For a band-limited signal, any spectral component which has a frequency above the bandlimit is zero. If the sampling frequency is known, it needs to be assured that the sampled signal is band-limited such that frequency com-

ponents at or above half of the sampling frequency are zero or can be neglected. A band-limitation is usually accomplished with a low-pass filter.

Let a TE-polarized Gaussian beam propagate a distance $Z = 50$ [μm] through vacuum. The aperture is $X = Y = 32$ [μm] and the sampling is $n_x = n_y = 64$ and $n_z = 128$. The wavelength is $\lambda = 1$ [μm] and the waist of the beam is $\sigma_x = \sigma_y = 3$ [μm]. With this sampling rate and aperture size, the Nyquist frequency ν_N is then $n_x/2/X = n_y/2/Y = 10^6$ [$1/\text{m}$]. The bandwidth B of the signal then needs to be limited to $B < \nu_N$ to ensure a proper reconstruction of the signal without aliasing effects in the spectrum. This maximum allowable frequency is obtained from $\sin(\theta_x) = \nu_x \cdot \lambda/n$ which is 1 in vacuum (i.e. $n = 1$) and hence spans the full range of spatial frequencies. In this case, the sampling meets the WKS-sampling theorem and therefore the spectrum of the field at $Z = 40$ [μm] is not affected by an overlap of the baseband with higher order bands due to the periodic repetition of the spectrum, caused by the sampling (i.e. aliasing). Aliasing in the spectrum appears as a distortion (i.e. noise) in the spatial domain as depicted in the right subplot of figure 6.1. With a sampling of $n_x = n_y = 32$, the Nyquist frequency is $\nu_N = 0.5 \cdot 10^6$ [$1/\text{m}$] and the maximum angle of propagation is then limited to $\theta_{max} = 30$ degrees or $\pi/6$. This exceeds the bandwidth of the signal as shown in the left subplot of figure 6.1 and some of the spectral components of the neighboring spectrum crosstalk into the base band.

A higher sampling rate in the aperture avoids aliasing and crosstalk into the base-band of the signal. The signal needs to be band-limited to the Nyquist frequency if a higher sampling is not possible. The maximum angle of propagation is then limited.

Figure 6.1: *Gaussian beam in homogeneous medium. Left: undersampled. Right: sampling meets the WKS sampling theorem. The aliasing in the spectrum becomes visible in the spatial domain for Gaussian beams.*



The Nyquist boundary for the transversal components of the propagation vector (k_x, k_y) in a two-dimensional simulation is

$$\begin{aligned} k_{N,x} &= 2\pi\nu_{N,x} = \pi/\delta x = \pi n_x/X \\ k_{N,y} &= 2\pi\nu_{N,y} = \pi/\delta y = \pi n_y/Y \end{aligned} \quad (6.3)$$

which corresponds to a angle of propagation of ± 90 degrees in a medium with a refractive index of $n = k_{N,x}/k_0 = k_{N,y}/k_0$ (i.e. $k_x = k_y = nk_0$). In a

discrete simulation, the angle of propagation θ for a given index i is then

$$\begin{aligned} p(\theta) &= \frac{nX}{\lambda} \sin \theta \\ q(\theta) &= \frac{nY}{\lambda} \sin \theta \end{aligned} \quad (6.4)$$

with p and q determines the spatial frequency $k_x = 2\pi p/X$ and $k_y = 2\pi q/Y$. The index p and q then corresponds to an angle of propagation

$$\begin{aligned} \theta(p) &= \sin^{-1}\left(p \frac{\lambda}{nX}\right) \\ \theta(q) &= \sin^{-1}\left(q \frac{\lambda}{nY}\right) \end{aligned} \quad (6.5)$$

with n is the real part of the refractive index of the medium. In the discrete algorithm, the *Nyquist index*

$$\begin{aligned} p_N = \frac{n_x}{2} &\Leftrightarrow \nu_x = 1/\delta x = 2/\lambda \Leftrightarrow \delta x = \lambda/2 \\ q_N = \frac{n_y}{2} &\Leftrightarrow \nu_y = 1/\delta y = 2/\lambda \Leftrightarrow \delta y = \lambda/2 \end{aligned} \quad (6.6)$$

then describes the first index which is affected by aliasing. The boundary $n_x/2$ for aliasing is thereby expressed by the constant $\lambda/\delta x = 2$. This agrees with the WKS theorem which states that at least more than two samples per period are required to reproduce a signal with a frequency $1/\lambda$. The index in the discrete simulation needs to be lower than this limit to avoid aliasing and the corresponding maximum angle of propagation θ_N at a given wavelength λ and refractive index n is then given by

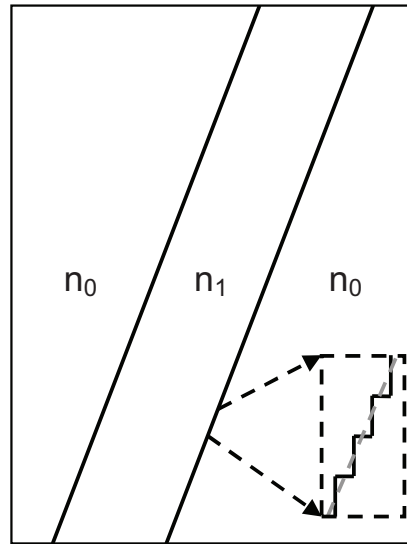
$$\begin{aligned} \theta_{N,p} &= \sin^{-1}\left(p_N \frac{\lambda}{nX}\right) = \sin^{-1}\left(\frac{\lambda}{2n\delta x}\right) \\ \theta_{N,q} &= \sin^{-1}\left(q_N \frac{\lambda}{nY}\right) = \sin^{-1}\left(\frac{\lambda}{2n\delta y}\right) \end{aligned} \quad (6.7)$$

6.2 Sampling in the axis of propagation

The discretization in the axis of propagation (i.e. the z -axis) determines the phase adjustment which is applied to the propagating wave by the space- and frequency-dependent phase element \mathcal{P} (eq. 3.11). In the BPM, WPM and VWPM, the number of samples in the z -axis is not an input to the Fourier transformation and therefore the WKS theorem needs not to be met. But n_z determines the number of points for which the resulting electromagnetic distribution is plotted. If the sampling δz is equal to the wavelength, a plane wave at $\theta = 0$ would appear as a constant. Hence, a fraction of the wavelength which is not an integer seems to be suitable. The number of samples n_z therefore should always determine δz to be a non-integer fraction of the minimum wavelength. n_z therefore depends on the wavelength of the incident wave and the maximum refractive index in the system \mathcal{N} .

The choice of δz furthermore determines the accuracy of the reproduction of the system \mathcal{N} which was defined in section 3.2 on page 57. For a vertical boundary which is completely located in a single layer, the selection of δz has no effect on the discretization of the system, but in case of an oblique boundary the choice of $\delta z = Z/n_z$ determines the shape of the discretized interface and the deviation to the continuous system. The effects on the simulated electromagnetic field are now investigated.

Figure 6.2: *Sawtooth, generated by the discretization in the axis of propagation.*

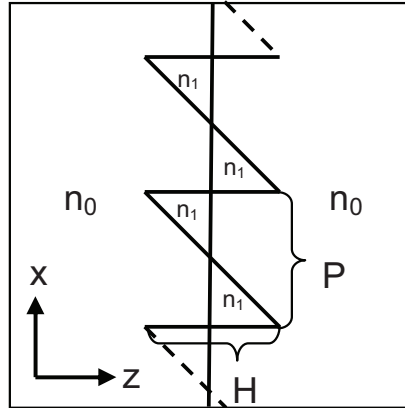


6.2.1 Thin element analysis

Figure 6.2 shows that a sequence of prisms is generated from the discretization of oblique interfaces. The size of the prisms is determined by the sampling interval δz . The phase shift of an electromagnetic wave which passes the discretized interface is different to the phase shift at the continuous interface. In particular, the phase shift varies with the discretization of the interface and thereby with the sampling interval δz .

An electromagnetic wave which passes a continuous interface at perpendicular incidence is supposed to get not refracted according to Snell's law. The zero order spatial frequency (i.e. $k_{\perp} = 0$) is therefore expected to be maintained and all non-zero frequencies ideally remain zero.

Figure 6.3: A thin element model of a discretized oblique interface to investigate the effect of the z -sampling on the zero-order diffraction efficiency.



In order to analyze the effects of discretization in a continuous theory, the scenario in figure 6.2 is translated to a similar configuration, containing a vertical boundary which is modulated by a sawtooth function as shown in figure 6.3. The modified configuration is supposed to envelope the discretized interface in figure 6.2 and then the thin element analysis considers a larger phase modulation. The sawtooth function $h(x)$, with x is a location in the aperture, is then a function of the period P and the maximum height H

$$h(x) = \frac{H}{P}x \quad (6.8)$$

with $H = 2\delta z$, which is determined by the sampling interval δz . The phase

difference of a wave which propagates along the z -axis is then

$$\begin{aligned}\delta\phi_h(x) &= \frac{2\pi}{\lambda}h(x)\delta n \\ &= k_0h(x)(n_1 - n_0) \\ &= k_0h(x)(n_1 - 1)\end{aligned}\quad (6.9)$$

with $n_0 = 1$ is the refractive index of vacuum. This yields the complex phasor of an electromagnetic wave with unit amplitude.

$$u(x, h) = e^{i\delta\phi_h(x)} \quad (6.10)$$

At vertical incidence, the spectrum of a plane wave consists of a single mode, the zero-frequency (i.e. $k_{\perp} = 0$), which is supposed to be maintained across the interface according to Snell's law. The zero order diffraction efficiency c_0 thereby gives a criterion for the deviation of the results from a simulation of a discretized system to the exact results from the continuous theory.

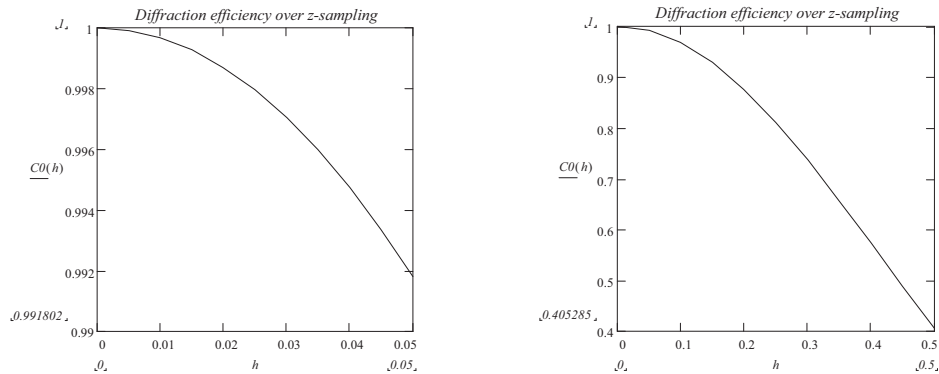
The m -th diffraction order efficiency (DOE) c_m for the thin element in figure 6.3

$$c_m(h) = \left| \int_{-P/2}^{P/2} u(x, h) e^{i\frac{2\pi}{P}mx} dx \right|^2 \quad (6.11)$$

is obtained from an integration of the m -th order spatial frequency m/P over one period P (i.e. from $-P/2$ to $P/2$). It describes the diffractive characteristic of the thin element model which is characterized by the phase function in equation 6.10. The zero DOE is obtained for $m = 0$.

Figure 6.4 shows the zero order diffraction efficiency for a plane wave of unit amplitude and a wavelength of $\lambda = 1$ [nm] which propagates through the thin element in figure 6.3. The number of samples n_z is 2000 and Z is

Figure 6.4: Zero order diffraction efficiency over the sampling interval δz in multiples of the wavelength. Small propagation distances (left) versus large propagation distances (right).



100 $[\mu m]$. The propagation distance δz is then $1/20\lambda$ $[\mu m]$. The height h of the sawtooth varies from 0 to $\delta z = 1/20\lambda = 0.05\lambda$ in the left subplot. The right subplot shows the deviation of the zero order diffraction efficiency for a sampling up to $\delta z = 0.5\lambda$. There, $c_0(h)$ shows a significant drop and the results of the simulation therefore show a significant deviation to the exact results from theory. The diffractive behavior of the discretized interface increases and fractions of the wave behind the interface propagate in higher order modes due to the conservation law. For sampling rates δz which are large fractions of the wavelength, a large deviation in the zero DOE is obtained (i.e. $\delta z = h = H/2$ is in multiples of the wavelength). This yields a large deviation in the amplitude of the simulated electromagnetic wave. The simulation results possess a high accuracy for sampling rates δz which are small fractions of the wavelengths as shown in the left subplot of figure 6.4. The deviation of the amplitude is below one percent at a sampling interval $\delta z \leq 0.05\lambda$. With a sampling $\delta z < 0.5\lambda$ (i.e. more than two samples per wavelength), a deviation of up to 60 percent is obtained.

6.2.2 Normalized sampling rate

Besides the choice of δz , the wavelength λ also contributes to the phase function u (eq. 6.10). The zero order diffraction efficiency $c_0(h)$ is investigated at the wavelengths 0.5, 0.75, 1, 2 and 3 [μm] as shown in figure 6.5 and a high and fast drop (i.e. low accuracy) is obtained for large ratios $\delta z/\lambda$ in the right subplot and a slow drop (i.e. high accuracy) is obtained for small ratios $\delta z/\lambda$ as shown in the left subplot. Obviously, the deviation of the zero order DOE increases with a growing ratio $\delta z_\lambda = \delta z/\lambda$. This is reasonable, because the wavenumber is inverse proportional to the wavelength and therefore a smaller wavelength causes a higher wavenumber which requires a higher sampling rate ν_z . Hence, at a constant sampling interval δz , a smaller wavelength causes a faster drop of the zero order diffraction efficiency and subsequently a higher deviation in the amplitude. The *normalized sampling rate* is then defined as

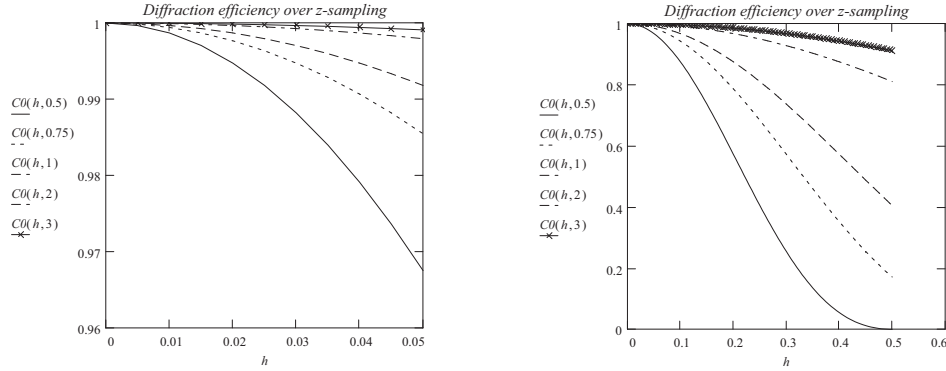
$$\nu_\lambda = \frac{1}{\delta z_\lambda} = \frac{\lambda_0}{n_{max}\delta z} = \lambda_{max} \frac{n_z}{Z} \quad (6.12)$$

with λ_0 is the vacuum wavelength and n_{max} is the maximum real part of the complex refractive index $\hat{n} = n_{max} + i\kappa$. It gives a quantity to identify an appropriate choice of δz to determine the accuracy of the VWPM.

6.2.3 Application of the normalized sampling rate

A simulation of a slanted layer is now performed to evaluate the normalized sampling interval δz_λ and evaluate the accuracy of the results from simulations with the VWPM and a variation in the sampling interval δz .

Figure 6.5: Zero DOE over the propagation distance in multiples of the wavelength λ for wavelengths 0.5, 0.75, 1, 2 and 3 micrometer.



Let a TE-polarized Gaussian beam with unit amplitude propagate from left to right and pass two parallel oblique interfaces at an angle of 20 degrees as shown in figure 6.6. The Gaussian beam possess a negligible spread as shown in the middle (i.e. the real part of \hat{E}_y) and right (i.e. the amplitude of \hat{E}_y) subplot. The amplitude after the first and second interface are obtained from Snell's law and the Fresnel coefficients. According to Snell's law, the angle of transmission is

$$\theta_t = \sin^{-1}\left(\frac{n_i}{n_t} \sin(\theta_i)\right) \quad (6.13)$$

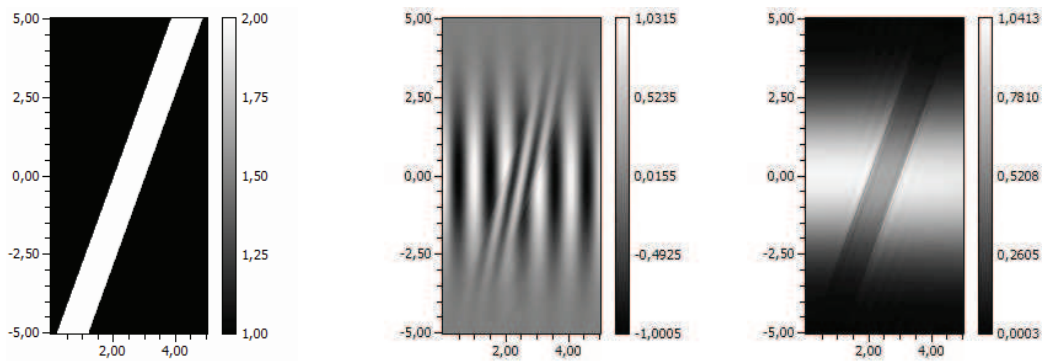
after the first interface and the angle of transmission behind the second boundary is then

$$\theta'_t = \sin^{-1}\left(\frac{n_1}{n_0} \sin\left(\sin^{-1}\left(\frac{n_0}{n_1} \sin(\theta_i)\right)\right)\right) = \theta_i \quad (6.14)$$

Using $n_0 = 1$ and $n_1 = 2$, the expression yields $\theta_t = 9.8$ degrees. The Fresnel coefficients after the first and second boundary are determined from equation 2.67. The incident beam is a TE-polarized π -Gaussian beam, shifted by $(x_0 \ y_0)^T$ in the aperture

$$\mathbf{E}_\pi = \mathbf{E}_0 e^{-\frac{1}{\pi} \left(\frac{(x-x_0)^2}{\sigma_x^2} + \frac{(y-y_0)^2}{\sigma_y^2} \right)} e^{i2\pi \boldsymbol{\nu}_\perp \cdot \mathbf{r}_\perp} \quad (6.15)$$

Figure 6.6: *TE-polarized Gaussian beam traverses a slanted layer (20 degrees) in vacuum (left). (middle) real part of the E_y , (right) amplitude.*



with an amplitude of $\mathbf{E}_0 = 1 [V/m]$, a wavelength of $1 [\mu m]$ and a rotation symmetric, circular waist of $\sigma_x = \sigma_y = 10 [\mu m]$. The thickness of the homogeneous oblique layer is negligible, because the refractive index $n_0 = n_2 = 1$ and $n_1 = 2$ is purely real and the layer is lossless. The dimensions of the scene are $X = Y = Z = 30 [\mu m]$ and the sampling is $n_x = n_y = n_z = 512$. Due to the unit amplitude, the electric field is identical to the Fresnel coefficient after the first and the product of the Fresnel coefficients after the second interface. Furthermore, due to $\lambda = 1 [\mu m]$, the normalized sampling interval δz_λ is equal to the sampling in the axis of propagation δz . According to equations 6.13 and 2.67, the exact ampli-

Table 6.1: Results of the simulation in figure 6.7. Amplitudes from the VWPM and from theory considering the normalized sampling interval δz_λ [-].

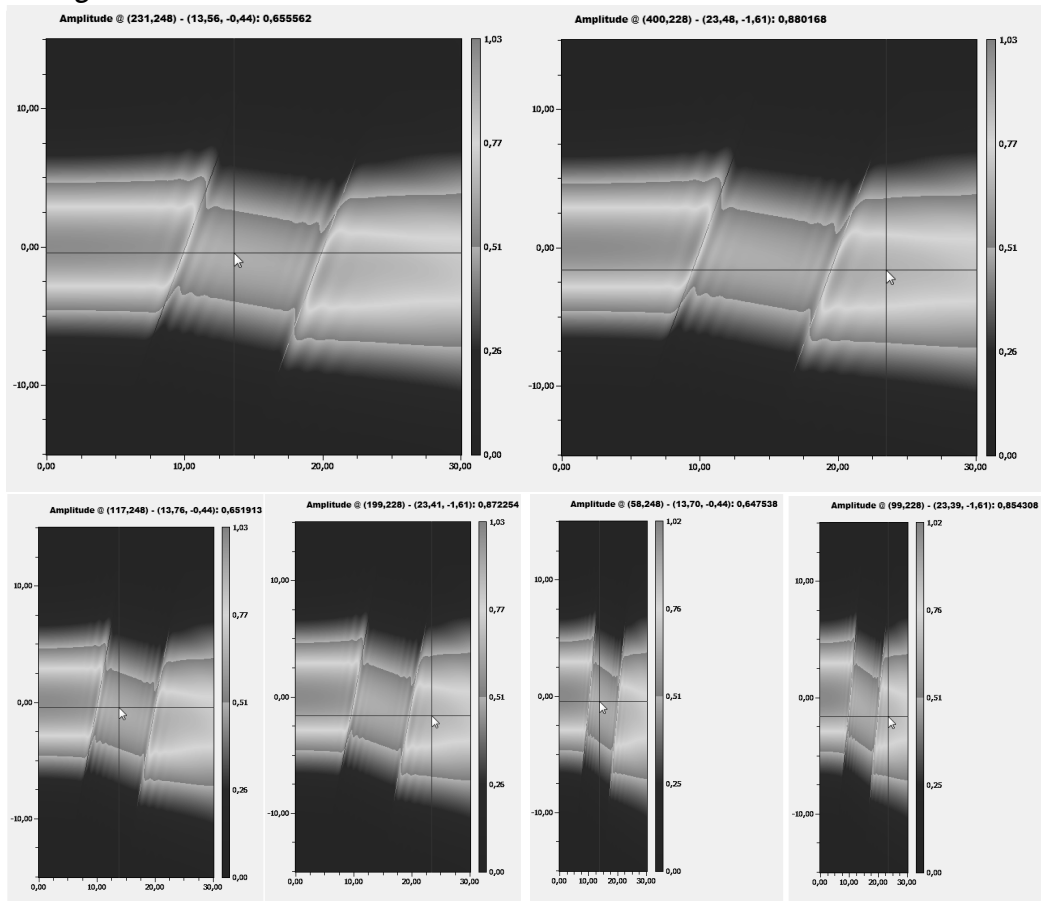
λ [μm]	Z [μm]	n_z [-]	δz_λ [-]	E_{theory}^1 [V/m]	E_{vwpm}^2 [V/m]	$\delta \mathbf{E}$ [%]
1	30	512	0.058	0.646/0.875	0.655/0.880	0.5
1	30	256	0.117	0.646/0.875	0.651/0.872	0.7
1	30	128	0.234	0.646/0.875	0.647/0.854	2.4
1	30	64	0.468	0.646/0.875	0.597/0.809	7.5

tude after the first boundary is 0.646 [V/m] and after the second boundary 0.875 [V/m]. The results from the simulation with the VWPM are shown in figure 6.7. The simulation is performed for three different sampling rates, $n_z \in \{128, 256, 512\}$. The sampling in the aperture $n_x = n_y$ remains constant. The plots utilize a special palette to emphasize the small rate of divergence of the Gaussian beam. The upper two subplots show the the results for a sampling rate of $n_x = 512$ and $n_z = 512$. The lower left two plots utilizes a sampling $n_z = 256$ and the lower right of $n_z = 128$. Table 6.1 summarizes the results which are shown in figure 6.7. Table 6.1 summarizes the amplitude deviations for the simulation in figure 6.7. In agreement to the analysis of the zero order diffraction efficiency, the error in the amplitude increases with an increasing normalized sampling interval. With a sampling of 5.8 percent of the wavelength (i.e. $\delta z_\lambda = 0.058$), the deviation of the simulated amplitude to the results from theory is 0.5 percent. An error of 2.5 percent is obtained from a sampling of $\delta z_\lambda = 0.234$ (i.e. 5 samples per wavelength).

¹Amplitude after the first/second interface of the slanted layer derived from theory

²Amplitude after the first/second interface of the slanted layer with the VWPM

Figure 6.7: Simulation of a slanted boundary of 20 degrees with the VWPM. The number of samples determine the number of pixels ($n_x \times n_z$) of the plots (upper two plots: 512×512 , lower left two plots: 512×256 , lower right two plots: 512×128). A special palette is used to emphasize the low divergence of the Gaussian beam.



Chapter 7

Conservation of energy

The *conservation law* states that a measurable property of an isolated physical system does not change as the system evolves. For electromagnetic waves, this measurable property is the power flux. In this chapter, the analysis of the power flux is utilized to investigate the power conservation and the stability of the VWPM.

According to the conservation law (eq. 2.78), the power flux through an area element $d\mathbf{A} = \mathbf{n}\delta A$ with \mathbf{n} is the surface normal (i.e. the energy flux per time) is $P = W/t = \mathbf{S} \cdot d\mathbf{A}$ [W] and has to be constant in a homogeneous loss- or gainless medium (i.e. $\epsilon_i = \kappa = 0$). In case of reflection and transmission at interfaces, the sum of transmitted P^+ and reflected P^- power flux has to be equal to the incident power flux P_e .

All subsequent equations and calculations assume $\hat{\mu} = 1 + i0$.

7.1 Power flux

The Poynting vector is derived from the real part of the vector product of the electrical field vector \mathbf{E} and the complex conjugate of the magnetic vector \mathbf{H} as shown in eq. 3.41. For plane waves, the magnetic vector can be replaced according to equation 2.40. Then, the Poynting vector completely depends on the electric field according to

$$\begin{aligned} \langle \mathbf{S} \rangle_T &= \frac{1}{2} \text{Re}(\mathbf{E} \times \mathbf{H}^*) \\ &= \frac{1}{2} \text{Re} \left(\begin{pmatrix} E_x \\ E_y \\ E_z \end{pmatrix} \times \left(\frac{1}{Z_0 k_0} \begin{pmatrix} k_y E_z - \hat{k}_z E_y \\ -(k_x E_z - \hat{k}_z E_x) \\ k_x E_y - k_y E_x \end{pmatrix} \right)^* \right) \end{aligned} \quad (7.1)$$

Then, the average power flux per area $\partial P / \partial A$ through an interface is

$$\frac{\partial \tilde{P}(\mathbf{r}_\perp, \mathbf{k}_\perp)}{\partial A} = \langle \mathbf{S} \rangle_T \cdot \mathbf{n} = \langle \mathbf{S} \rangle_T \cdot \mathbf{e}_z = \frac{k_z}{2Z_0 k_0} (\mathbf{E} \mathbf{E}^*) \quad [W/m^2] \quad (7.2)$$

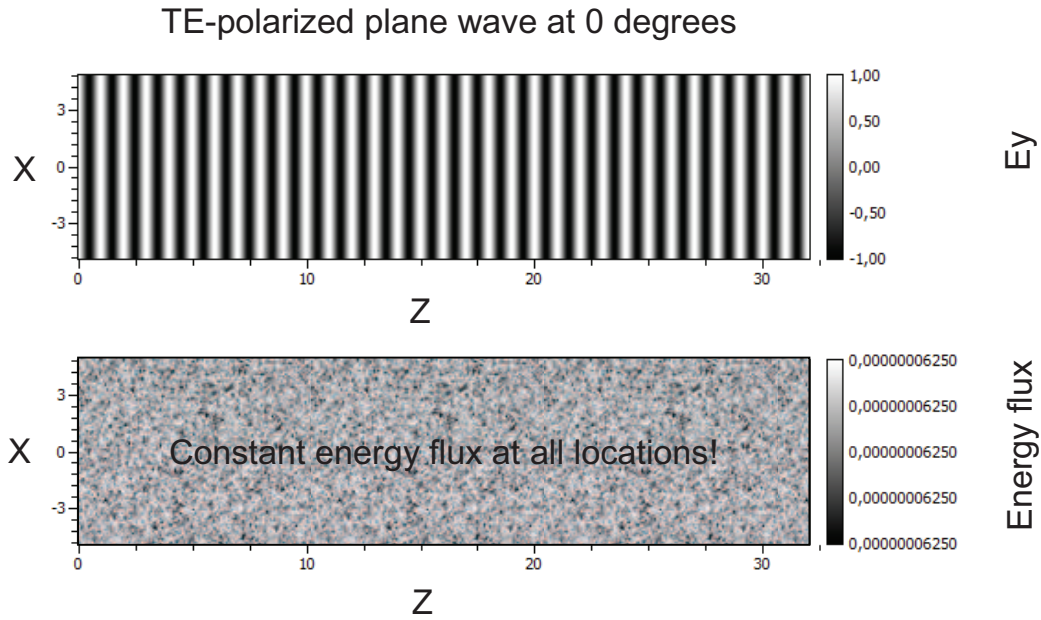
with $\mathbf{n} = \mathbf{e}_z$ is the surface normal at a location \mathbf{r}_\perp and $\hat{\mathbf{k}} = (k_x \ k_y \ \hat{k}_z)^T$. Using equation 3.16 in equation 7.2, the power flux becomes independent from E_z as shown in appendix B.

7.2 Homogeneous loss- or gainless medium

7.2.1 TE-polarized wave

Let the plane of incidence be parallel to the xz-plane. With $\mathbf{n} = \mathbf{e}_z$, the z-component of a TE-polarized electric field vector is zero and the time

Figure 7.1: Real part of the electric field and power flux of a TE-polarized plane wave propagating through vacuum. The power flux is clipped at the eleventh position.



average power flux per area $\partial P_{TE}/\partial A$ is

$$\begin{aligned} \frac{\partial \tilde{P}_{TE}(\mathbf{r}_{\perp}, \mathbf{k}_{\perp})}{\partial A} &= \frac{k_z}{2Z_0 k_0} (\mathbf{E}\mathbf{E}^*) \\ &= \frac{k_z}{2Z_0 k_0} (E_y E_y^*) \quad [W/m^2] \end{aligned} \quad (7.3)$$

derived from equation 7.2 with $(\mathbf{s} \times \mathbf{e}_z) \perp xz\text{-plane}$ and $\hat{k}_z = k_z + i0$ and \mathbf{s} as defined in eq. 2.34.

Let a TE-polarized plane wave with unit amplitude, perpendicular incidence and a wavelength $\lambda = 1$ [μm] propagate a distance $Z = 32$ [μm] through a discretized homogeneous medium in a twodimensional Cartesian xz -coordinate system with $k_y = 0$, $y = 0$, $n_y = 1$ and through an area element $\delta A = \delta x$. With a refractive index $\hat{n} = n + i\kappa = 1 + i0$, an aperture $X = 8$ [μm] and a sampling $\delta x = \delta z = X/128 = Z/512 = 0.625$ [μm], the time average power flux in the twodimensional case $\partial\tilde{P}_{TE}/\partial y$ through the area element δx is then $6.250 \cdot 10^{-8}/2/Z_0$ [W/m], as shown in figure 7.1. This result perfectly agrees with the results from equation 7.3 in the one-dimensional case.

$$\begin{aligned}\frac{\partial P_{TE}}{\partial y} &= \int_0^{\delta x} \frac{\partial P_{TE}(x, 0)}{\partial A} dx \\ &= \frac{nk_0}{2Z_0k_0} \delta x = \frac{\delta x}{2Z_0} = \frac{6.25 \cdot 10^{-8}}{2Z_0} [\text{W}/\text{m}]\end{aligned}$$

7.2.2 TM-polarized wave

Let the plane of incidence be parallel to the xz -plane. The y -component of a TM-polarized wave is then zero due to the transversality of electromagnetic waves. The time average power flux per area $\partial\tilde{P}_{TM}/\partial A$ is then

$$\begin{aligned}\frac{\partial\tilde{P}_{TM}(\mathbf{r}_\perp, \mathbf{k}_\perp)}{\partial A} &= \frac{k_z}{2Z_0k_0} (\mathbf{E}\mathbf{E}^*) \\ &= \frac{k_z}{2Z_0k_0} (E_x E_x^* + E_z E_z^*) \\ &= \frac{k_z}{2Z_0k_0} \left(1 + \frac{k_x^2}{k_z^2}\right) (E_x E_x^*) [\text{W}/\text{m}^2] \quad (7.4)\end{aligned}$$

with $(\mathbf{s} \times \mathbf{e}_z) \perp xz\text{-plane}$ and \mathbf{s} as defined in eq. 2.34. θ is the angle of incidence and

$$\begin{aligned} k_z &= nk_0 \sqrt{1 - \sin^2(\theta)} \\ E_z &= -E_x k_x / k_z \end{aligned} \quad (7.5)$$

Let a TM-polarized plane wave with unit amplitude, an angle of incidence $\theta = 20$ degrees, the plane of incidence parallel to the xz -plane, propagate through homogeneous medium with $\hat{n} = n + i\kappa = 1 + i0$. The time average power flux per meter $\partial P_{TM}(\mathbf{r}_\perp, \pi/9) / \partial y$ through an area element δx is $0.5873 \cdot 10^{-8} / 2 / Z_0$ [W/m], derived from equation 7.4. This agrees with the results from a simulation with the VWPM as shown in figure 7.2.

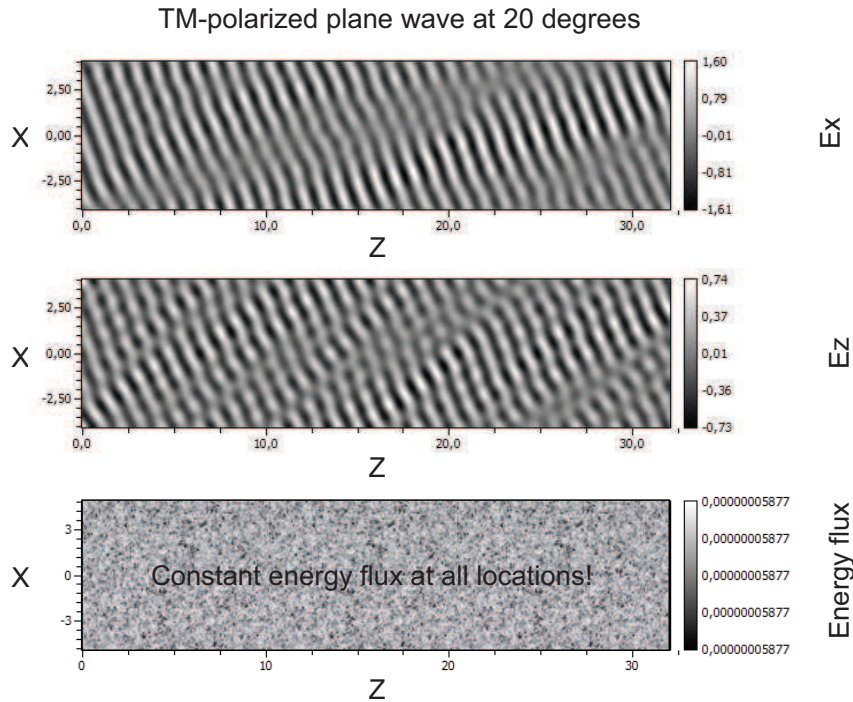


Figure 7.2: *Real parts of the electric field vector and the power flux of a TM-polarized plane wave. The power flux is clipped after the eleventh position.*

7.2.3 Power flux

The time average power flux per area of two propagating waves, the first wave is TE- and the second is TM-polarized, both planes of incidence parallel to the xz -plane, is obtained from a summation of equation 7.3 and 7.4

$$\begin{aligned}
 \frac{\partial \tilde{P}_{TE}}{\partial A} + \frac{\partial \tilde{P}_{TM}}{\partial A} &= \frac{1}{2Z_0 k_0} [(E_y E_y^*) k_z + (E_x E_x^* + E_z E_z^*) k_z] \\
 &= \frac{k_z}{2Z_0 k_0} (\mathbf{E} \mathbf{E}^*) \\
 &= \frac{\partial \tilde{P}(\mathbf{r}_\perp, \mathbf{k}_\perp)}{\partial A} [W/m^2] \tag{7.6}
 \end{aligned}$$

with $(\mathbf{s} \times \mathbf{e}_z) \perp xz\text{-plane}$. A detailed calculation is shown in appendix B.

7.2.4 Total power flux

In case of a wave which is composed from a plurality of modes, the power flux per area cannot be simply obtained from an integration over the spectrum \mathbf{k}_\perp . Due to interferences the field might vanish completely (destructive interference) and the total power flux per area is therefore obtained from

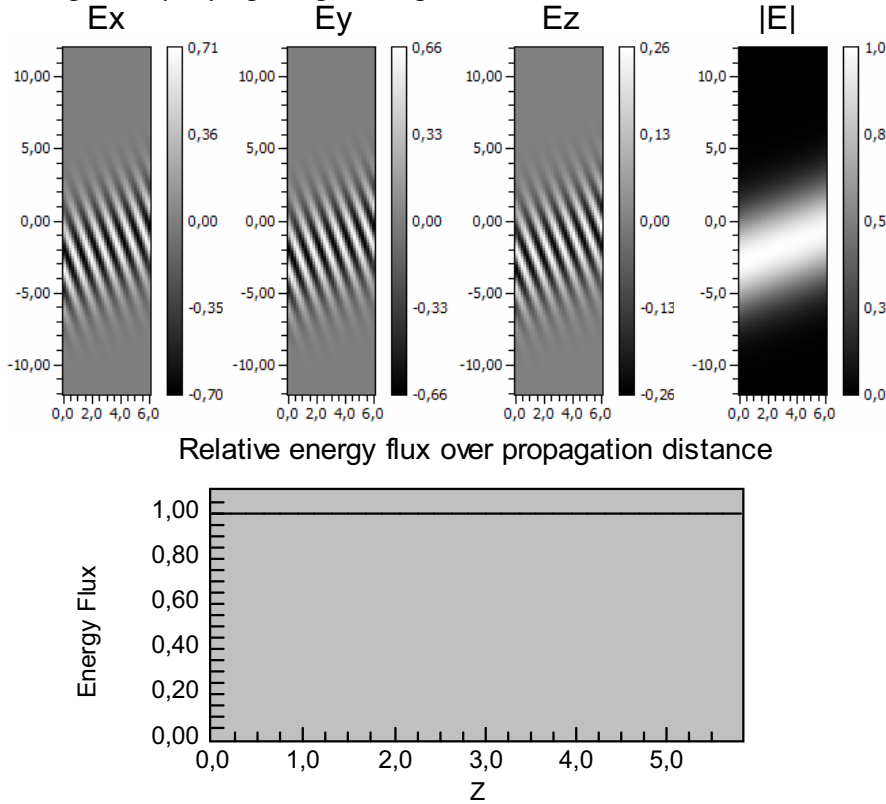
$$\frac{\partial P(\mathbf{r}_\perp)}{\partial A} = \frac{1}{2} \text{Re} \left\{ \left(\int \tilde{\mathbf{E}} e^{i\mathbf{k}\cdot\mathbf{r}} \frac{d^2 \mathbf{k}_\perp}{(2\pi)^2} \right) \times \left(\int \tilde{\mathbf{H}} e^{i\mathbf{k}\cdot\mathbf{r}} \frac{d^2 \mathbf{k}_\perp}{(2\pi)^2} \right)^* \right\} \cdot \mathbf{n} \tag{7.7}$$

and the total power flux through the aperture A is then derived from the integration of $\partial P(\mathbf{r}_\perp)/\partial A$ over the aperture A

$$P = \int_A \frac{\partial P(\mathbf{r}_\perp)}{\partial A} d^2 \mathbf{r}_\perp [W] \tag{7.8}$$

The relative or normalized energy flux is then $0 \leq P/P_e \leq 1$.

Figure 7.3: Power flux of a Gaussian beam with $\phi_p = 0$ and $\psi = 45$ at $\theta = 20$ degrees, propagating through vacuum.



7.2.5 Power flux of a Gaussian beam

Let an linear polarized Gaussian beam with unit amplitude, a waist $\sigma_x = 6 [\mu m]$, a rotation angle $\psi = 45$ degrees (eq. 2.33) and an angle of incidence $\theta = 20$ propagate a distance $Z = 6 [\mu m]$ through a homogeneous lossless medium with $\hat{n} = n + i\kappa = 1 + i0$ and an aperture $X = Y = 24 [\mu m]$. The sampling in the aperture is $n_x = n_y = 128$ and in the axis of propagation $n_z = 32$. The real parts of the electric vector field E_x , E_y and E_z are depicted in figure 7.3. The z-component E_z originates from the oblique in-

idence, $\theta = 20$ degrees. The amplitude $|\mathbf{E}| = \sqrt{\mathbf{E}\mathbf{E}^*}$ is constant as shown in the right subplot due to the absence of absorption (i.e. $\kappa = 0$). Figure 7.3 shows that the power flux of the Gaussian beam remains constant in a simulation with the VWPM in agreement to the theory.

7.3 Inhomogeneous medium

In an inhomogeneous medium, an interface is introduced by a change of the refractive index. A wave which passes the interface is transformed by reflection and transmission. The power flux is then split into a transmitted P^+ and a reflected power flux P^- according to the conservation law (eq. 2.78).

7.3.1 Longitudinal index variations

In this thesis, index variations along the axis of propagation (i.e. the z-axis) are called longitudinal index variations. At such longitudinal index variations between two homogeneous layers, the electric field \mathbf{E} is transformed according to equation 3.24, considering the angle of incidence θ_e , transmission θ_t and the refractive index before $\hat{n}_e = n_e + i\kappa_e$ and behind $\hat{n}_t = n_t + i\kappa_t$ the boundary.

7.3.2 TE-polarized waves

With equation 7.3, the power flux per area of a TE-polarized plane wave behind the interface, propagating in the xz -plane with unit amplitude and *vertical incidence* is

$$\begin{aligned} \frac{\partial P_{TE}^+(\mathbf{r}_\perp, \mathbf{k}_\perp = 0)}{\partial A} &= \frac{n_t}{2Z_0} |t_{TE}|^2 (E_y E_y^*) \\ &= \frac{n_t}{2Z_0} \frac{k_{z,e}}{k_{z,t}} \mathcal{T}_{TE} (E_y E_y^*) \\ &= \frac{n_e}{2Z_0} \mathcal{T}_{TE} (E_y E_y^*) \quad [W/m^2] \end{aligned} \quad (7.9)$$

with $(\mathbf{s} \times \mathbf{e}_z) \perp xz\text{-plane}$, $k_{z,e} = n_e k_0$ and $k_{z,t} = n_t k_0$. $\mathcal{T}_{TE} = k_{z,t}/k_{z,e} |t_{TE}|^2$ is the transmittance for the TE-polarized wave. At vertical incidence (i.e. $k_x = k_y = 0$), where the transfer matrix of transmission possesses a singularity, the transformation of \mathbf{E}_\perp is a simple multiplication with t_{TE} . For *oblique incidence*, the transformation of \mathbf{E}_\perp is given by the transfer matrix of transmission \mathbf{M} (eq. 3.24). The power flux per area of a TE-polarized wave with *oblique incidence* per area is then

$$\frac{\partial \tilde{P}_{TE}^+(\mathbf{r}_\perp, \mathbf{k}_\perp)}{\partial A} = \frac{k_{z,t}}{2Z_0 k_0} |\mathbf{E}_\perp^+|^2 = \frac{k_{z,t}}{2Z_0 k_0} |\mathbf{M} \cdot \mathbf{E}_\perp|^2 \quad [W/m^2] \quad (7.10)$$

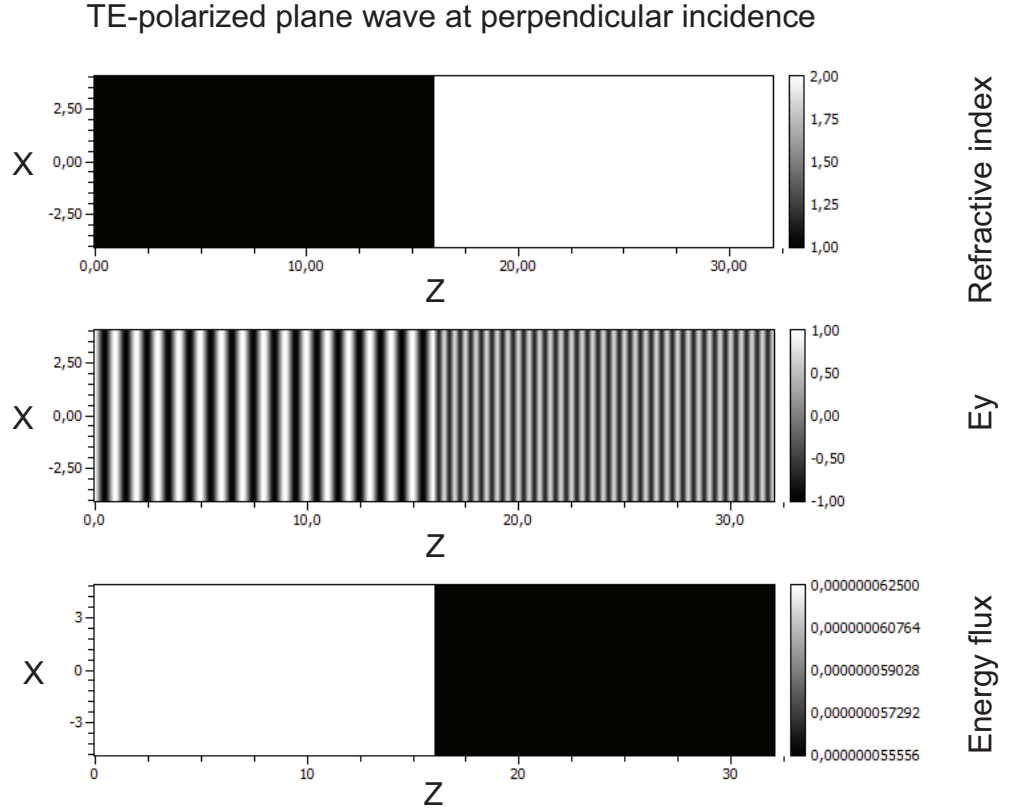
with $k_\perp^2 = k_x^2 + k_y^2$. For a TE-polarized wave at oblique incidence and with the plane of incidence parallel to the xz -plane, the power flux per area is

$$\frac{\partial \tilde{P}_{TE}^+(\mathbf{r}_\perp, \mathbf{k}_\perp)}{\partial A} = \frac{k_{z,t}}{2Z_0 k_0} |t_{TE}|^2 (E_y E_y^*) \quad [W/m^2] \quad (7.11)$$

with $(\mathbf{s} \times \mathbf{e}_z) \perp xz\text{-plane}$ and $k_\perp = k_x$ and $k_t^2 = k_x^2 + k_{z,t}^2$. For *vertical incidence* the expression then simplifies to equation 7.9 and the power flux per area *before the interface* $\partial \tilde{P}_{TE}/\partial A$ is directly obtained from equation 7.3.

Let a TE-polarized plane wave of unit amplitude and perpendicular incidence pass a boundary with $\hat{n}_e = n_e + i\kappa_e = 1 + i0$ and $\hat{n}_t = n_t + i\kappa_t = 2 + i0$.

Figure 7.4: Power flux of a TE-polarized plane wave of unit amplitude and perpendicular incidence passing an interface with $\hat{n}_e = 1$ and $\hat{n}_t = 2$.



For a plane of incidence parallel to the xz -plane and in a discrete two-dimensional simulation, the power flux per meter $\partial P_{TE}/\partial y$ [W/m] behind the interface through an area element δx is

$$\begin{aligned} \frac{\partial P_{TE}^+}{\partial y} &= \int_0^{\delta x} \frac{\partial P_{TE}^+(x, 0)}{\partial A} dx = \frac{\delta x}{2Z_0} |t_{TE}|^2 (E_y E_y^*) n_t \\ &= \frac{\delta x}{2Z_0} n_e \mathcal{T}_{TE}(E_y E_y^*) \quad [W/m] \quad (7.12) \end{aligned}$$

with $(\mathbf{s} \times \mathbf{e}_z) \perp xz$ -plane. Assuming $\delta z = \delta x = X/n_x = 8/128 = Z/n_z = 32/512 = 0.0625$ [$\mu m/sample$], the power flux per meter is then 6.25 .

$10^{-8}/2/Z_0$ [W/m] before and $5.556 \cdot 10^{-8}/2/Z_0$ [W/m] behind the interface. For vertical incidence, the results for the TE- and TM-component are equal because $t_{TE} = t_{TM}$ and $k_{z,e} = n_e k_0$. These results from theory perfectly agree with the results from a simulation with the VWPM as shown in figure 7.4. The reflected power flux $\partial P^-/\partial A$ per area is then derived from the conservation law

$$\frac{\partial \tilde{P}^-}{\partial A} = \frac{\partial \tilde{P}}{\partial A} - \frac{\partial \tilde{P}^+}{\partial A} \quad [W/m^2] \quad (7.13)$$

as shown in appendix B or it can be obtained from equation 7.3 for a TE-polarized wave and from equation 7.4 for a TM-polarized wave by consideration of the transfer matrix of reflection (eq. 5.20).

For *oblique incidence*, the power flux per area of the reflected TE-polarized wave before the boundary is obtained from the replacement of \mathbf{E}_\perp with $\mathbf{E}_\perp^- = \mathbf{R} \cdot \mathbf{E}_\perp$ (eq. 7.3). At *vertical incidence*, the transfer matrix of reflection contains again a singularity and the reflected field is then obtained from a multiplication with the Fresnel reflection coefficients for the TE- or TM-component. The power flux per area of the reflected wave is then

$$\begin{aligned} \frac{\partial P_{TE}^-(\mathbf{r}_\perp, \mathbf{k}_\perp = 0)}{\partial A} &= \frac{n_e}{2Z_0} |r_{TE}|^2 (E_y E_y^*) \\ &= \frac{n_e}{2Z_0} \mathcal{R}_{TE} (E_y E_y^*) \\ &= \frac{n_e}{2Z_0} (1 - \mathcal{T}_{TE}) (E_y E_y^*) \\ &= \frac{\partial \tilde{P}}{\partial A} - \frac{\partial \tilde{P}^+}{\partial A} \quad [W/m^2] \end{aligned} \quad (7.14)$$

with $(\mathbf{s} \times \mathbf{e}_z) \perp xz\text{-plane}$ and $\mathcal{R}_{TE} = |r_{TE}|^2$ is the reflectivity for the TE-component. This agrees with the conservation law.

7.3.3 TM-polarized waves

In case of TM-polarized waves passing an interface at *vertical incidence*, the power flux per area is

$$\begin{aligned}
 \frac{\partial P_{TM}^+(\mathbf{r}_\perp, \mathbf{k}_\perp = 0)}{\partial A} &= \frac{k_t}{2Z_0 k_0} |t_{TM}|^2 (\mathbf{E}\mathbf{E}^*) \\
 &= \frac{n_t}{2Z_0} \frac{k_e}{k_t} \mathcal{T}_{TM}(\mathbf{E}\mathbf{E}^*) \\
 &= \frac{n_e}{2Z_0} \mathcal{T}_{TM}(\mathbf{E}\mathbf{E}^*) [W/m^2] \quad (7.15)
 \end{aligned}$$

with $(\mathbf{s} \times \mathbf{e}_z) \perp xz\text{-plane}$, $k_e = n_e k_0$ and $k_t = n_t k_0$ and $\mathcal{T}_{TM} = k_{z,t}/k_{z,e} |t_{TM}|^2$ is the transmittance of the TM-polarized wave. At vertical incidence, the power flux per area of a TE- and a TM-polarized wave with equal amplitude is identical (eq. 7.9).

At *oblique incidence*, \mathbf{E} transforms according to equation 3.24 at the interface and the transversality in equation 2.36. \mathbf{E} in equation 7.4 is then replaced by \mathbf{E}^+ to obtain the power flux per area of the TM-polarized wave behind the boundary

$$\frac{\partial \tilde{P}_{TM}^+(\mathbf{r}_\perp, \mathbf{k}_\perp \neq 0)}{\partial A} = \frac{k_{z,t}}{2Z_0 k_0} |\mathbf{E}^+|^2 [W/m^2] \quad (7.16)$$

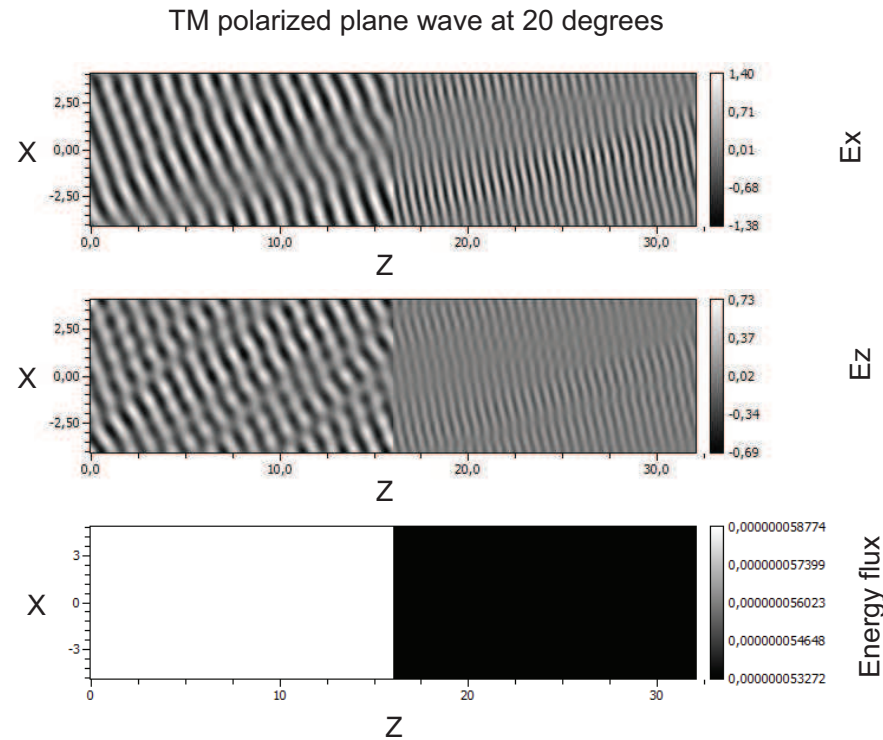
For TM-polarized waves in a twodimensional simulation, propagating in the xz -plane, the power flux per area behind the interface is then

$$\frac{\partial \tilde{P}_{TM}^+(\mathbf{r}_\perp, \mathbf{k}_\perp \neq 0)}{\partial A} = \frac{k_{z,t}}{2Z_0 k_0} \left(1 + \frac{k_x^2}{k_{z,t}^2} \right) |t_{TM}|^2 (E_x E_x^*) [W/m^2] \quad (7.17)$$

with $(\mathbf{s} \times \mathbf{e}_z) \perp xz\text{-plane}$, $k_{z,t}^2 = (n_t k_0)^2 - k_x^2$ and $\mathbf{k}_\perp = k_x$ (i.e. 2D-simulation).

Let a TM-polarized plane wave propagate in a twodimensional discretized system and pass an interface at an angle of incidence $\theta_e = \pi/9$ and with

Figure 7.5: *Power flux of a TM-polarized plane wave of unit amplitude, passing an interface with $\hat{n}_e = 1$ and $\hat{n}_t = 2$ at 20 degrees.*



a plane of incidence parallel to the xz -plane. The power flux per meter $\partial P_{TM}/\partial y$ through an area element δx *before the interface* is $0.5873 \cdot 10^{-8}/2/Z_0$ [W/m], directly obtained from equation 7.4 in section 7.2. The transmitted power flux per meter $\partial P_{TM}^+/\partial y$ is $0.5301 \cdot 10^{-8}/2/Z_0$ [W/m] according to equation 7.17. This agrees with the results from the VWPM ($0.532 \cdot 10^{-8}/2/Z_0$ [W/m]) as depicted in figure 7.5. The deviation of 4 per mill is caused by the amplitude deviation which evolves from the discretization as shown in chapter 6.

The *reflected power flux per area* of the TM-polarized wave is then derived

Table 7.1: *Incident, transmitted and reflected power flux of a TE- and TM-polarized plane waves at a boundary with $\hat{n}_e = 1$ and $\hat{n}_t = 2$.*

E-field		Theory	VWPM	δz_λ
TE, plane, vertical	inc.	$6.255 \cdot 10^{-8}$	$6.255 \cdot 10^{-8}$	0.0625
	tra.	$5.556 \cdot 10^{-8}$	$5.556 \cdot 10^{-8}$	0.0625
	ref.	$0.699 \cdot 10^{-8}$	$0.699 \cdot 10^{-8}$	0.0625
TM, plane, oblique	inc.	$5.873 \cdot 10^{-8}$	$5.873 \cdot 10^{-8}$	0.0625
	tra.	$5.301 \cdot 10^{-8}$	$5.302 \cdot 10^{-8}$	0.0625
	ref.	$0.572 \cdot 10^{-8}$	$0.571 \cdot 10^{-8}$	0.0625

from equation 7.4 by considering the transformation of the electric field at the interface. \mathbf{E} is therefore replaced with \mathbf{E}^- , using the transfer matrix of reflection (eq. 5.20) and transversality (eq 2.36). For a plane of incidence which is parallel to the xz -plane and for vertical incidence, the reflected power flux per area $\partial P_{TM}^- / \partial A$ in a twodimensional simulation is then

$$\begin{aligned}
 \frac{\partial P_{TM}^-(\mathbf{r}_\perp, \mathbf{k}_\perp = 0)}{\partial A} &= \frac{k_e}{2Z_0 k_0} |r_{TM}|^2 (E_x E_x^*) \\
 &= \frac{n_e}{2Z_0} \mathcal{R}_{TM}(E_x E_x^*) \\
 &= \frac{n_e}{2Z_0} (1 - \mathcal{T}_{TM})(E_x E_x^*) \\
 &= \frac{\partial P_{TM}}{\partial A} - \frac{\partial P_{TM}^+}{\partial A} \quad [W/m^2] \quad (7.18)
 \end{aligned}$$

with $(\mathbf{s} \times \mathbf{e}_z) \perp xz\text{-plane}$, $k_e^2 = |\mathbf{k}_e|^2 = (n_e k_0)^2 = k_{z,e}^2 + k_x^2$ and $\mathbf{k}_\perp = k_x$. This agrees to the conservation law. The results of the simulations with a longitudinal index change are summarized in table 7.1.

7.3.4 Total power flux

Again, the total power flux per area behind the interface cannot be simply obtained from an integration of $\partial\tilde{P}^+(\mathbf{r}_\perp, \mathbf{k}_\perp)/\partial A = k_{z,t}/2/Z_0/k_0(\mathbf{E}^+\mathbf{E}^{+*})$ over the spectrum \mathbf{k}_\perp . Interferences need to be considered and the total power flux at a location \mathbf{r}_\perp is then

$$\frac{\partial P(\mathbf{r}_\perp)^+}{\partial A} = \frac{1}{2} \text{Re} \left\{ \left(\int \tilde{\mathbf{E}}^+ e^{i\mathbf{k}\cdot\mathbf{r}} \frac{d^2\mathbf{k}_\perp}{(2\pi)^2} \right) \times \left(\int \tilde{\mathbf{H}}^+ e^{i\mathbf{k}\cdot\mathbf{r}} \frac{d^2\mathbf{k}_\perp}{(2\pi)^2} \right)^* \right\} \quad (7.19)$$

The power flux behind the interface through the entire aperture A is obtained from an integration over \mathbf{r}_\perp

$$P^+ = \int_A \frac{\partial P^+(\mathbf{r}_\perp)}{\partial A} d^2\mathbf{r}_\perp \quad [W] \quad (7.20)$$

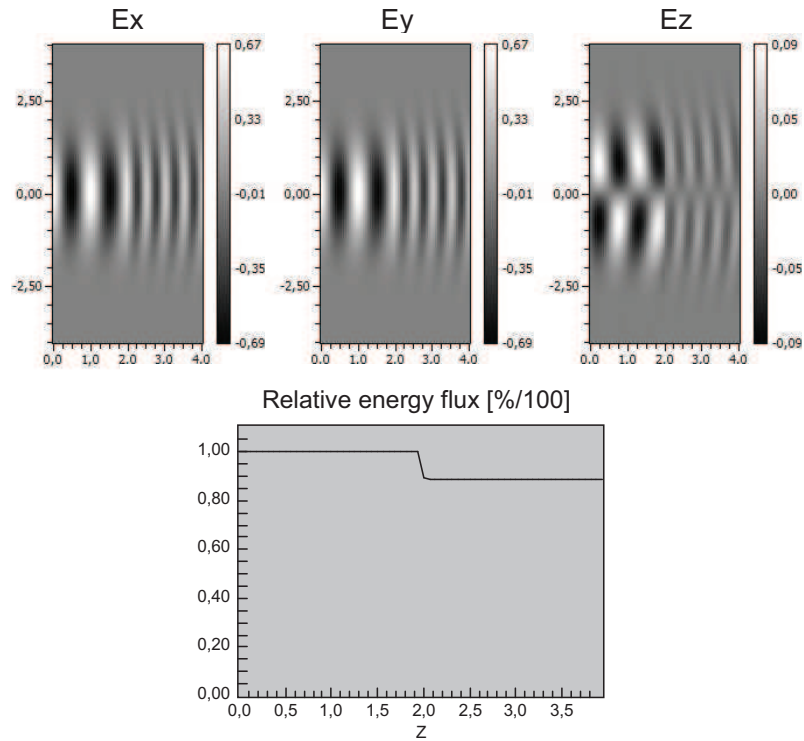
The reflected power flux is then

$$P^- = \int_A \frac{\partial P^-(\mathbf{r}_\perp)}{\partial A} d^2\mathbf{r}_\perp = 1 - P^+ \quad [W] \quad (7.21)$$

according to the conservation law. The power flux of the TE-polarized Gaussian beam at vertical incidence on page 143 then drops by $1 - W^+$. Considering equation 7.17 in equation 7.21, the power flux of the TE-polarized Gaussian beam drops by 11.112 percent (i.e. $1 - 0.888$).

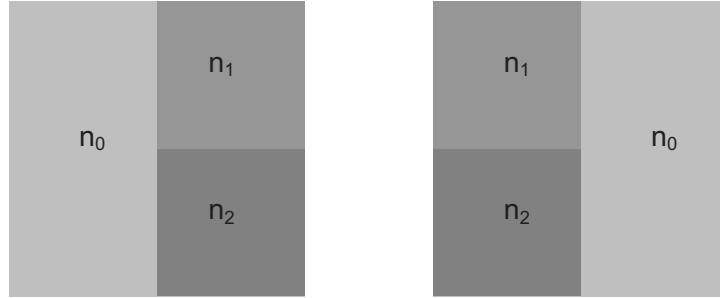
The power flux per area of a propagation linear polarized Gaussian beam with $\phi_p = 0$ and $\psi = 45$ degrees, a waist of $\sigma_x = \sigma_y = 2$ [μm] and a wavelength of 1 [μm] at vertical incidence is calculated with the VWPM. The propagation distance is $Z = 4$ [μm] through the aperture $X = Y = 8$ [μm] with $n_x = n_y = 128$ and $n_z = 64$ as shown in figure 7.6. The simulation result yields a normalized energy flux $P^+/P_e = 0.888$ behind the interface as shown in 7.6. This agrees with the theory and exact results are obtained with the VWPM for a propagation through homogeneous media and for longitudinal index variations.

Figure 7.6: *Real part of the electric field which passes a boundary with $\hat{n}_e = 1$ and $\hat{n}_t = 2$. The normalized power flux P^+ behind the interface is 0.888 [–] behind the interface.*



7.3.5 Lateral index variation

In this thesis, a *lateral index variation* describes a change in the refractive index in the aperture. In contrast to longitudinal index changes, lateral changes in the refractive index are part of to the input of the Fourier transformation. Lateral index changes cause variations in the Fresnel coefficients in the aperture and thereby cause local deformations in the electric field. The following investigation of the dependency of lateral index variations to the power flux is based on two characteristic configurations

Figure 7.7: *Characteristic configurations for lateral index variations.*

which are shown in figure 7.7. All transfers from lateral index changes to homogeneous layers can be reduced to these two base-cells. The wave is assumed to propagate from left to right, entering a lateral index change in the left subplot and leaving a lateral index variation in the right subplot of figure 7.7. Since the power flux through homogeneous medium has been investigated in the last sections, the analysis of the propagation through the right base-cell of figure 7.7 is sufficient to show the effect of lateral inhomogeneities on a propagating electric field.

Let a TE-polarized Gaussian beam of vertical incidence, unit amplitude, a wavelength of $2 \text{ } [\mu\text{m}]$ and a waist of $10 \text{ } [\mu\text{m}]$ propagate a distance $Z = 30 \text{ } [\mu\text{m}]$ through an aperture $X = Y = 15 \text{ } \mu\text{m}$ in a three-dimensional system as shown in figure 7.8. The sampling is $n_z = 512$ and $n_x = n_y = 256$. The Gaussian beam propagates from left to right, enters the lateral index variation at $Z = 0 \text{ } [\mu\text{m}]$ with $n_0 = n_2 = 1$, $n_1 = 2$ and leaves the lateral index change at $Z = 25 \text{ } [\mu\text{m}]$. It then propagates $Z = 5 \text{ } [\mu\text{m}]$

through a homogeneous medium. The normalized sampling interval δz_λ is $n_{max}Z/(n_z\lambda_0) = 2 \cdot 30/(512 \cdot 2) = 0.0586$ and then the deviation in the amplitude is below one percent as shown in chapter 6. Since the wave is TE-polarized, the electric field has no z- and y-component. The spatial Nyquist frequency is $k_{N,x} = \pi/\delta x = 5.362 \cdot 10^7$ [1/m], which corresponds to an angle of propagation greater than 90 (eq. 6.5). This is a sufficient sampling to avoid aliasing. The result of the simulation with the VWPM in the left subplot of figure 7.8 show that the total power flux tends to oscillate while the wave propagates through the lateral index change. It stabilizes immediately after the wave has left the lateral index change and entered the homogeneous medium. Obviously, a lateral index change causes shifts in the power flux which do not occur at longitudinal index changes as shown in the previous sections.

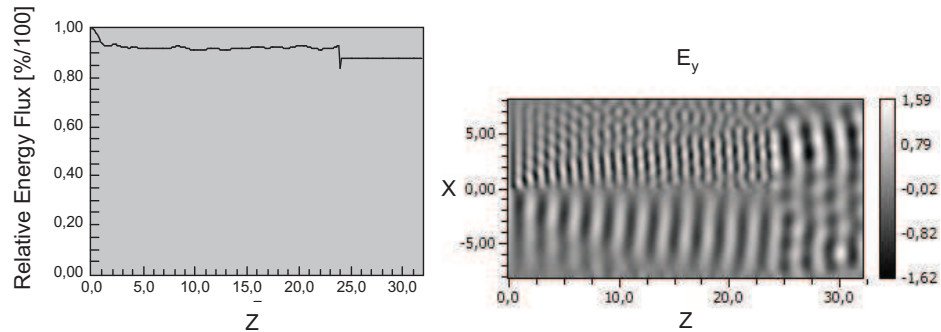


Figure 7.8: A TE-polarized Gaussian beam at perpendicular incidence propagates through a lateral index variation (VWPM).

7.3.6 Generation of evanescent modes in the WPM and BPM from local discontinuities

In the VWPM, the electromagnetic vectorial field in a layer $j - 1$ is first Fourier transformed to obtain the spectrum. If the wave enters a lateral index change as depicted in the left subplot of figure 7.7, discontinuities (i.e. steps) in the electric field are obtained from the space- and frequency-dependent transformation at the interface. The gradients in the electric field thereby depend on the change of the real parts of the refractive index n_1 and n_2 . With a high contrast in the refractive index, the space- and frequency-dependent transfer at the interface potentially results in a discontinuity in the electric field. In the propagation step, the phase is adjusted according to the space dependent optical path length (OPL) $n(\mathbf{r}_\perp)k_0 \cos \theta \delta z$ and the electric field at the end of layer j is obtained. The resulting electric field distribution at the end of layer j is then input to the next step of calculation to obtain the electric field at the end of layer $j + 1$. Thereby, the transfer at the interface and phase adjustment are potential reasons for the generation of discontinuities in the electric field. Since the electric field is Fourier transformed in each step of calculation, evanescent or high order modes are generated from peaks or steps according to *Gibb's phenomenon*. Gibb's phenomenon implies that an infinite number of modes are necessary to ideally reproduce a step function from a superposition of plane waves (i.e. by the inverse Fourier transformation) and an oscillating overshoot appears at the discontinuity. In a bandlimited spectrum, a perfect reconstruction of the discontinuity is impossible and the oscillating peaks at the edges of step functions grow with the number of considered modes. Dependant on the sampling, the oscillations appear in the spectrum as evanescent modes.

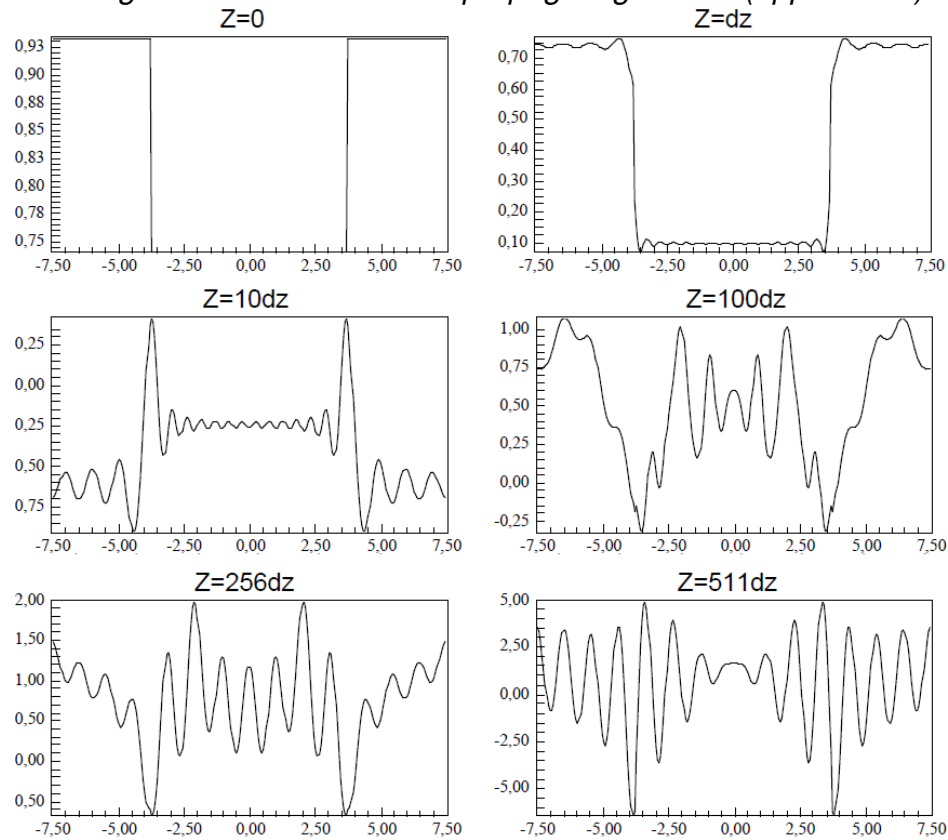
In the split step propagation scheme which is utilized in the BPM, the diffraction operator (eq. 3.2) is applied in homogeneous medium. The spectrum is transformed without considering lateral variations in the refractive index and therefore the inverse Fourier transformation is not affected by local deformations. In inhomogeneous layers, the phase shift operator (eq. 3.3) is applied in the spatial domain, considering the local refractive index $n(\mathbf{r})$ and vertical propagation. Due to the locally varying phase adjustment, a discontinuity in the electric field of two times the amplitude (i.e. $|\mathcal{S}| = 1$ and for $\arg(\mathcal{S}) = \pm\pi/2$) can occur. The discontinuous signal is then input to the Fourier transformation in the next iteration and evanescent modes appear in the spectrum. The treatment of the evanescent modes is critical for the stability and the energy conservation of the BPM as shown in [29] and [45]. In [58], evanescent waves are completely excluded from the algorithm of the BPM to achieve stability. This exclusion of evanescent modes is supported by the limitation of the BPM to paraxial propagation. In [26], the growth of evanescent modes is described, if they are treated as propagating modes in rational approximants of the propagator. It is also reported that the Pade approximants, which are used in wide-angle BPM algorithms in [43] and [45], cannot model the evanescent modes with sufficient accuracy. Instability and the violation of the conservation law are observed. Therefore, modified Pade approximants are proposed, which automatically filter the evanescent modes. Rational approximants that can model or at least suppress the evanescent modes have been also developed in [59]. The replacement of the complex exponential propagator with Pade approximants is suggested, which are zero in the limes $k_{\perp} \rightarrow \infty$ and thereby provide an automated suppression of evanescent modes. Inaccuracies and instability problems are moreover reported in [28], when fields have significant evanescent character. Therefore, a complex representation of the propagation operator by choosing either a complex reference

wave number or a complex representation of the Pade approximation is proposed to model evanescent modes. A stable evolution of propagating and evanescent waves was achieved, reducing the inaccuracy and instability problems. In [29] it is reported that evanescent modes which are excited at lateral interfaces, as for example when a slowly varying waveguide is approximated by a piecewise uniform waveguide, cause instability in the BPM. There, a stabilization was achieved from a damping of evanescent waves by using a layer with high absorption at the system boundaries, which is also assumed in the original paper by Feith and Fleck in [13].

7.3.7 Power flux in a waveguide

A waveguide with a step index profile provides lateral index changes over a sequence of iterations. Let a plane wave propagate a distance $Z = 30$ [μm] from left to right through an aperture $X = 15$ [μm] with a sampling $n_x = 256$, entering a waveguide at $Z = 0$ [μm] with $\hat{n}_{cladding} = 1 + i0$ and $\hat{n}_{core} = 2 + i0$ and leaving the waveguide at $Z = 30$ [μm]. With a sampling $n_z = 512$ the normalized sampling interval δz_λ is 0.058 and the deviation in the amplitude can be expected to be below one percent as shown in chapter 6. The sampling in the aperture allows an angle of propagation up to 90 degrees without aliasing. The electric field distributions of a TE-polarized plane wave with a wavelength of 1 [μm], a unit amplitude and vertical incidence at six z -positions is shown in figure 7.9. In the simulation, the VWPM utilizes a purely complex treatment of the entire range of spatial frequencies as introduced in appendix B. The transfer matrix of transmission (eq. 3.24) and reflection (eq. 5.20) then evolves from the complex Fresnel coefficients (eq. 3.27), the complex refractive index and

Figure 7.9: Amplitude of a TE-polarized plane wave at six locations in the z -axis propagating through a lossless waveguide with a step index profile and treating evanescent modes as propagating modes (appendix B).



the complex propagation vector as described in appendix B to calculate evanescent modes. Thereby, the evanescent modes are calculated by the transfer matrix of transmission and reflection - in the literature this is called 'treated like propagating modes'. At $Z = 0$, the electric field is located in the first layer which is inside the waveguide. At $Z = \delta z$, high order oscillations arise from the Fourier transformation of the discontinuity in the electric field at $Z = 0$ and in the following steps of calculation, the electric field E_y steadily increase as shown in figure 7.9, which shows the real part

of the electric field at the positions $10\delta z$, $100\delta z$ up to $511\delta z$. The power flux increases and the conservation law is violated.

In a second two-dimensional simulation in the same Cartesian xz -coordinate system, a Gaussian beam with a wavelength of $1 [\mu m]$ and a waist of $10 [\mu m]$ propagates through a waveguide with a diameter of $10 [\mu m]$ at perpendicular incidence. The aperture is $X = 40 [\mu m]$ and the propagation distance is $Z = 40 [\mu m]$. The system is discretized with $n_x = n_z = 512$ and the refractive index of the step-index waveguide is $\hat{n}_{core} = 1.5 + i0$ and $\hat{n}_{cladding} = 1 + i0$ (i.e. vacuum). Here, the VWPM treats the evanescent modes like propagating modes (appendix B). Due to the $1/e$ drop of the Gaussian beam, smaller inhomogeneities in the electric field occur at the boundary of the waveguide but the conservation law is again violated by a growing normalized energy flux as shown in figure 7.10. Apparently, the propagating modes are completely overacted by growing high order modes and the electric field distribution at $z = Z$ shows a purely evanescent character. It appears that, in agreement with the observations from the BPM, an electric field with significant evanescent character causes instabilities if the entire range of spatial frequencies is treated as propagating modes, using a purely complex calculation with complex Fresnel coefficients and a complex propagation vector in the calculus of chapter 3 and chapter 5. The occurrence of high order oscillations at locations with local discontinuities of the electric field is part of the Fourier theory and reasoned by Gibb's phenomenon. They arise from the consideration of space-dependent information which introduce local deformations of the electromagnetic field as described in the last section. This effect cannot be removed but it can be reduced and controlled by different techniques.

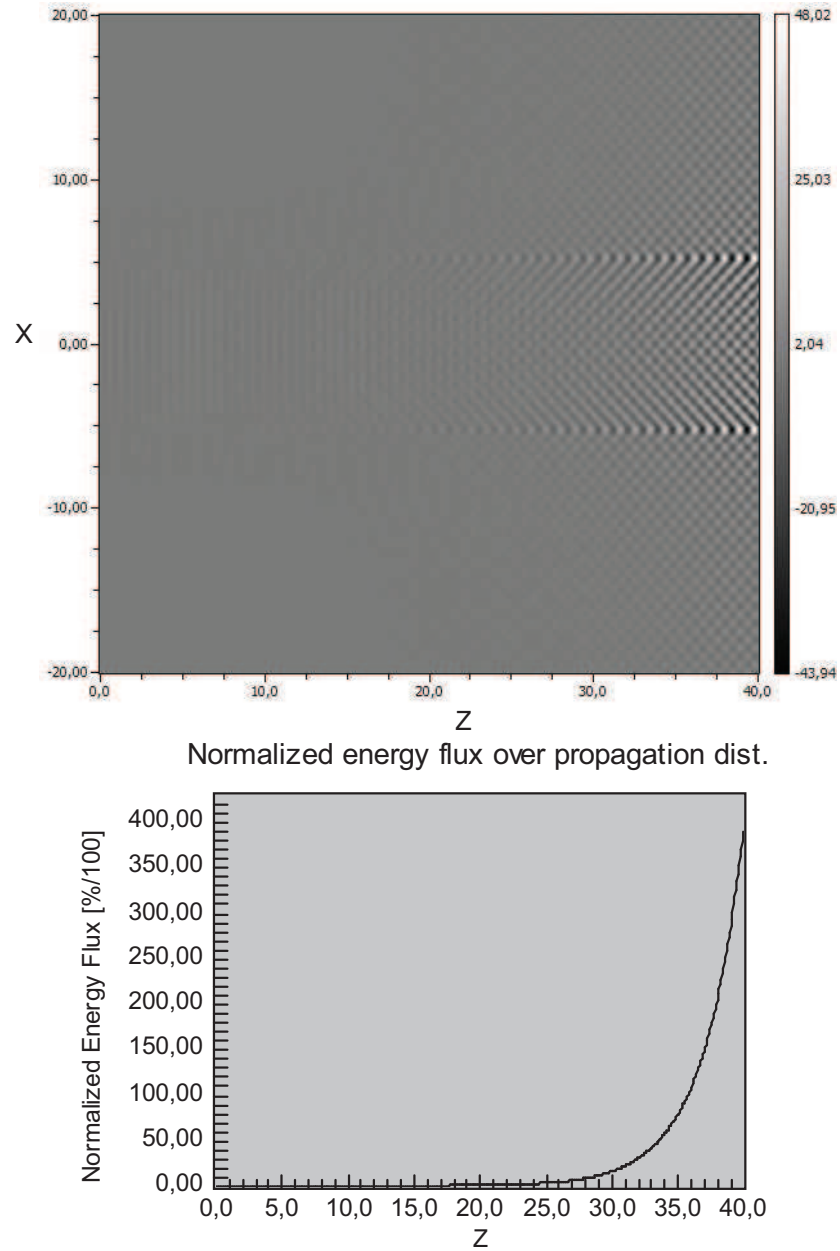


Figure 7.10: Simulation of a TE-polarized Gaussian beam which propagates through a STEP-profile waveguide with $\hat{n}_{core} = 1.5$ and $\hat{n}_{cladding} = 1$ and treating evanescent modes as propagating modes (appendix B).

7.4 Stabilization of the VWPM

According to the observations in the literature and in the last sections, the growth of the power flux evolves from the treatment of evanescent modes like propagating modes. A stabilization of the simulation appears to be possible by suppressing, reducing or controlling the evanescent modes as described for the BPM in various publications. A stabilization can then be achieved by

- a) low pass filtering the system
- b) energy-balanced clipping
- c) clipping
- d) transfer of evanescent modes

While a) operates on the system, the electric field is the subject matter of the stabilization in b), c) and d). In a), a low-pass filtering of the index distribution is performed in order to reduce the gradients in the electric field

$$\begin{aligned}\frac{\partial \mathbf{E}}{\partial x} &= \frac{\mathbf{E}(x + \delta x, y) - \mathbf{E}(x - \delta x, y)}{2\delta x} \\ \frac{\partial \mathbf{E}}{\partial y} &= \frac{\mathbf{E}(x, y + \delta y) - \mathbf{E}(x, y - \delta y)}{2\delta y}\end{aligned}\quad (7.22)$$

from a reduction of the gradient in the index distribution $n(\mathbf{r}_\perp)$. The Fresnel coefficients are thereby smoothed and the electric field is more continuous. This reduces the generation of high order modes and its superposition with propagating modes.

In b), a controlled suppression of modes by considering the conservation law (eq. 7.24) ensures a constant power flux across each boundary in a system which does not possess lateral and longitudinal index variations in a single step of calculation. Starting from the center frequency $k_{\perp} = 0$, the power flux is derived from an integration over the spatial frequencies. High order spatial frequencies which exceed the energy balance are then suppressed. In a lossy medium, a sufficient damping ensures the stability of the calculation and makes a clipping of modes dispensable. The controlled clipping of modes is thereby self-adapting to the absorption in the medium.

In c), a clipping of modes at the evanescent boundary of the medium or in vacuum is proposed. A third clipping technique suppresses all high order modes from a reduction of the sampling rate in the aperture. This sampling-induced clipping suppresses evanescent and high order modes by limiting the maximum angle of propagation. The entire energy of the signal is then contained in propagating modes. Obviously, this method is susceptible to aliasing if the sampling rate is below the Nyquist rate. An anti-aliasing filter is then required, which might limit the propagation of modes to even smaller angles of propagation.

In d), the transfer of evanescent modes with the VWPM, which was introduced in chapter 3 and 5, is applied. It is ensured that all eligible evanescent modes in table 3.2 are modeled according to the theory in [1]. All evanescent-to-evanescent transfers at boundaries are neglected.

7.4.1 Low pass filtering

In a low-pass filtered system, the refractive index $n(\mathbf{r}_\perp)$ at location $\mathbf{r}_\perp = (x \ y)^T$ of a system \mathcal{N} (see section 3.2 on page 57) is obtained from its surrounding locations according to

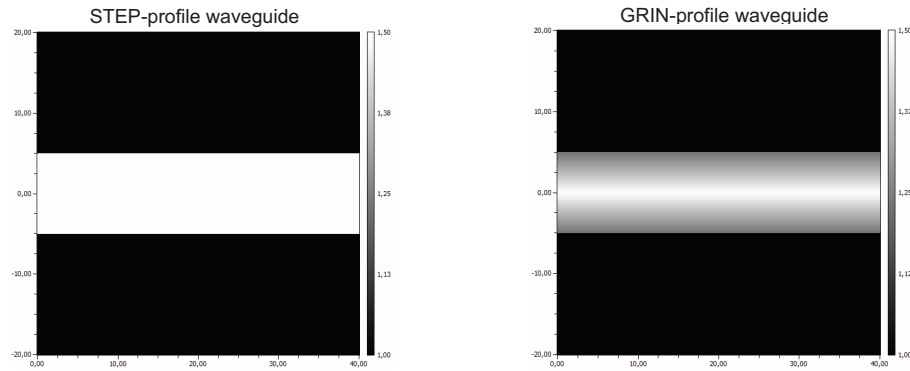
$$n(x, y) = \frac{1}{N} \sum_{i,j \in \{-q, \dots, q\}} a_{i,j} n(x - i, y - j) \quad (7.23)$$

with q defines the order of the filter matrix $A^{2q+1 \times 2q+1}$, $a_{i,j}$ are the elements of the filter matrix and N is the sum of all filter coefficients. The left plot in figure 7.11 shows the filter coefficients of a *local mean average* low-pass filter and the right plot shows the filter coefficients of a *Gaussian filter*. Both filters are rotation symmetric and therefore provide an equalized filtering in the x - and y -direction.

local mean average	Gaussian filter																		
<table border="1" style="border-collapse: collapse; width: 100%; height: 100%;"> <tr><td style="text-align: center;">1</td><td style="text-align: center;">1</td><td style="text-align: center;">1</td></tr> <tr><td style="text-align: center;">1</td><td style="text-align: center;">1</td><td style="text-align: center;">1</td></tr> <tr><td style="text-align: center;">1</td><td style="text-align: center;">1</td><td style="text-align: center;">1</td></tr> </table>	1	1	1	1	1	1	1	1	1	<table border="1" style="border-collapse: collapse; width: 100%; height: 100%;"> <tr><td style="text-align: center;">1</td><td style="text-align: center;">2</td><td style="text-align: center;">1</td></tr> <tr><td style="text-align: center;">2</td><td style="text-align: center;">4</td><td style="text-align: center;">2</td></tr> <tr><td style="text-align: center;">1</td><td style="text-align: center;">2</td><td style="text-align: center;">1</td></tr> </table>	1	2	1	2	4	2	1	2	1
1	1	1																	
1	1	1																	
1	1	1																	
1	2	1																	
2	4	2																	
1	2	1																	

Figure 7.11: Filter matrix $A^{3 \times 3}$ of a local mean average filter (left) and a Gaussian filter (right).

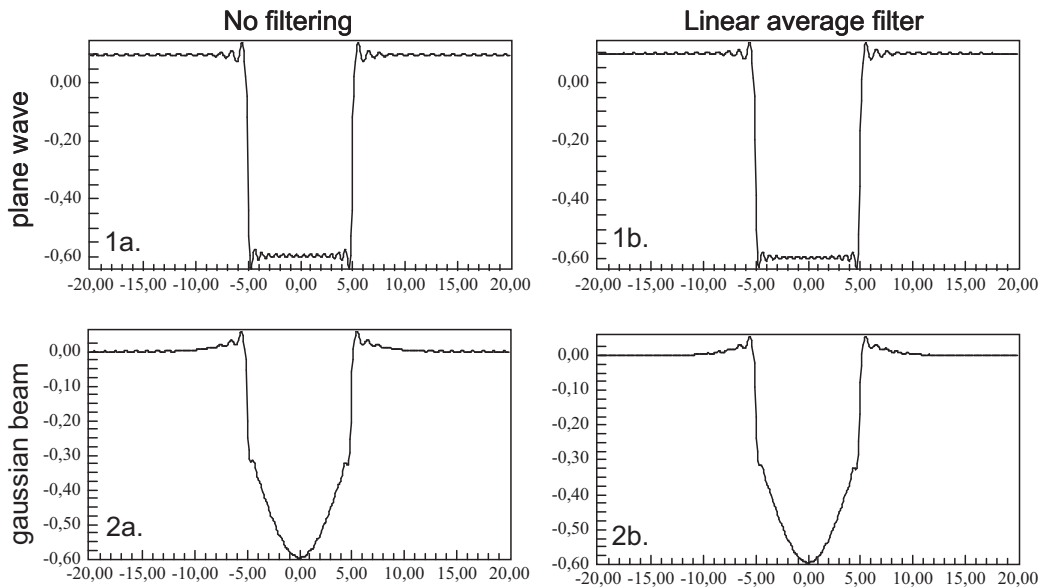
Figure 7.12: *Step-profile waveguide (left) versus GRIN-profile waveguide (right). The contrast $n_{core} : n_{cladding}$ is 1.5.*



Step-profile and GRIN-profile waveguide

Let a TE-polarized plane wave of unit amplitude, vertical incidence and a wavelength of $1 [\mu m]$ propagate through the step-index waveguide in the left subplot of figure 7.12, which has been simulated in section 7.3.7 on page 157. Again, the simulation treats the evanescent modes like propagating modes (appendix B). The real part of E_y in the first layer of the waveguide is compared in figure 7.13. The system is not filtered in subplot 1a and it is filtered with a 3×3 local mean average filter matrix in subplot 1b. In a second scenario, the waveguide is traversed by a Gaussian beam with a waist of $10 [\mu m]$. In subplot 2a of figure 7.13 the system is again not filtered. The system is filtered with a 3×3 local mean average matrix in subplot 2b. The comparison of the results show that the low-pass filtering does not significantly reduce the high order oscillations at the edge of the waveguide. It makes no difference, if the waveguide is traversed by a Gaussian beam or a plane wave. All four scenarios possess a more or less strong increase in the power flux, similar to the results in figure 7.9

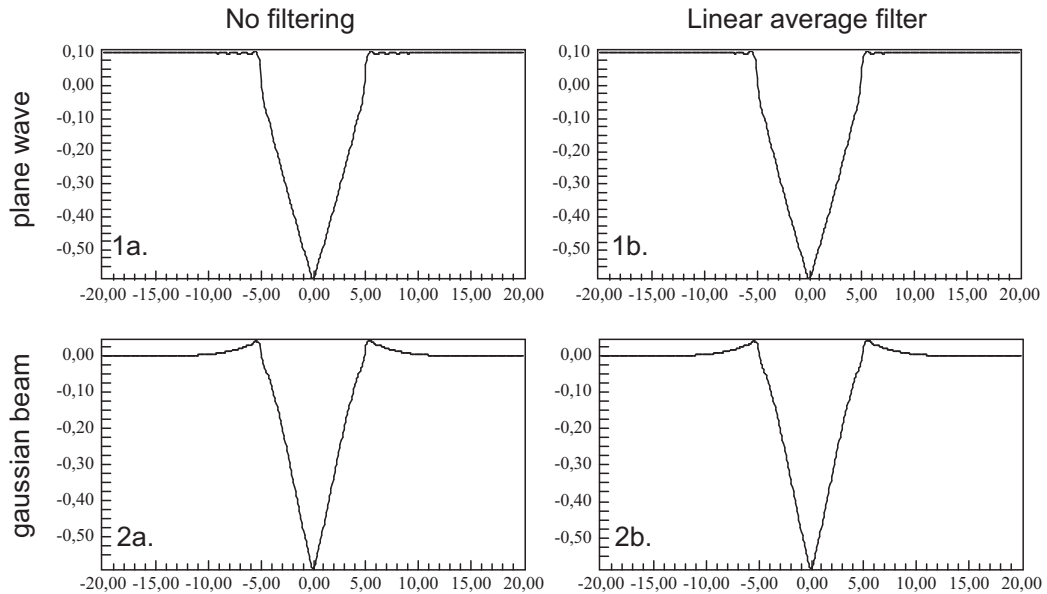
Figure 7.13: *Electric field in the x-axis at $i_z = 2$. Simulation of the step-profile waveguide, treating evanescent modes like propagating modes (appendix B).*



and 7.10.

Next, let the plane wave (top) and the Gaussian beam (bottom) propagate through a GRIN waveguide as shown in the right subplot of figure 7.12. The results of the simulation in figure 7.14 show that a linear average filtering does again not significantly reduce the overshoot at the edge of the waveguide. Again, energy flux grows and the conservation of energy is violated (not shown here, but the results are similar to figure 7.9 and 7.10).

Figure 7.14: *Electric field in the x-axis at $i_z = 2$ (starting from $i_z = 1$). Simulation of the GRIN-profile waveguide, treating evanescent modes as propagating modes (appendix B).*



Low contrast waveguide

A simulation of a low-contrast step index waveguide with an index-ratio of $n_{core} : n_{clad} = 1.1$ appears to be stable in all four cases 1a. to 2b. for the same propagation distance $Z = 40 [\mu m]$ as shown in the left subplot of figure 7.15.

The power flux for a propagation distance $Z = 140 [\mu m]$ is shown in the right subplot of figure 7.15. With a sampling $n_z = 2048$, the normalized

sampling interval $\delta z_\lambda = 0.078125$ and the accuracy in the amplitude is maintained. With the enlarged propagation distance, the energy flux remains constant up to a distance of $120 [\mu m]$. Then, the power starts to grow significantly and the conservation law is violated. It appears that the simulation becomes instable after a sufficiently high number of propagation steps due to an accumulation of a small amplification in the evanescent modes. The root cause for the violation of the conservation law can not be removed by a reduction of the gradients in the electric field from a linear average filtering of the system.

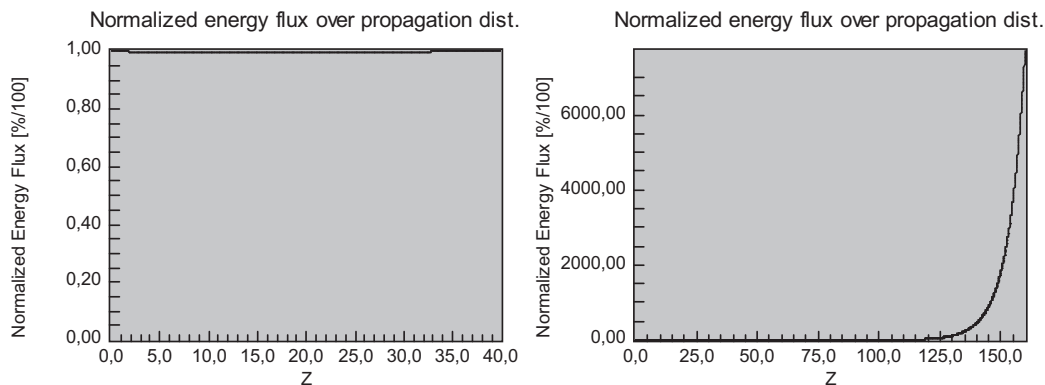
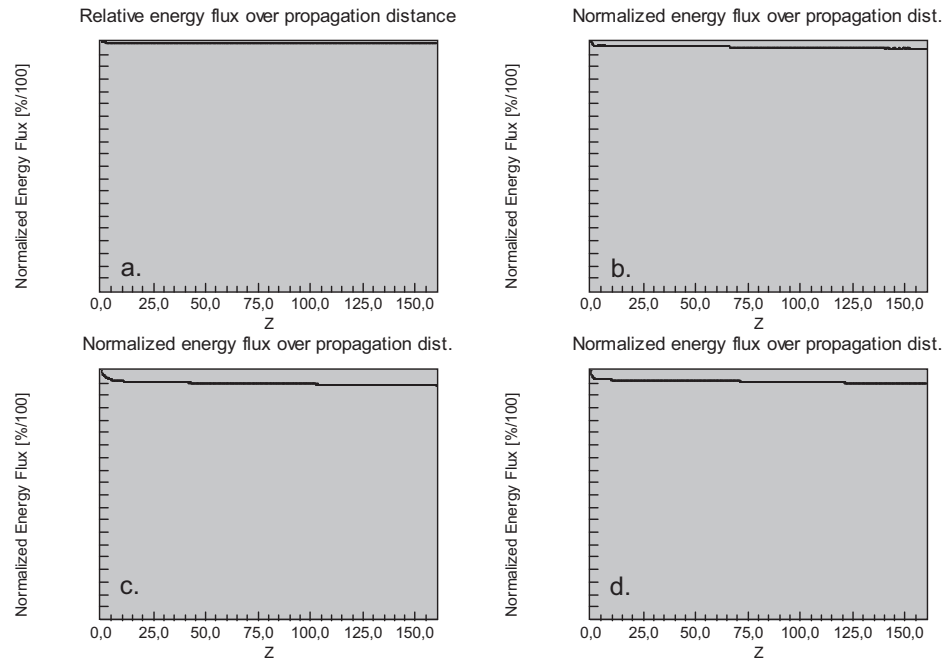


Figure 7.15: *TE-Gaussian beam propagating through a linear filtered step-profile waveguide with $n_{core} : n_{clad} = 1.1$ and a length of $40[\mu m]$ (left) and $160[\mu m]$ (right), treating evanescent modes like propagating modes (appendix B).*

Figure 7.16: *Power flux through a linear average filtered step-profile waveguide with a contrast $n_{core} : n_{clad}$ 1.1 (a.), 1.5 (b.), 2 (c.) and 3 (d.) using a clipping at the evanescent boundary and treating evanescent modes like propagating modes (appendix B).*



7.4.2 Clipping at the evanescent boundary

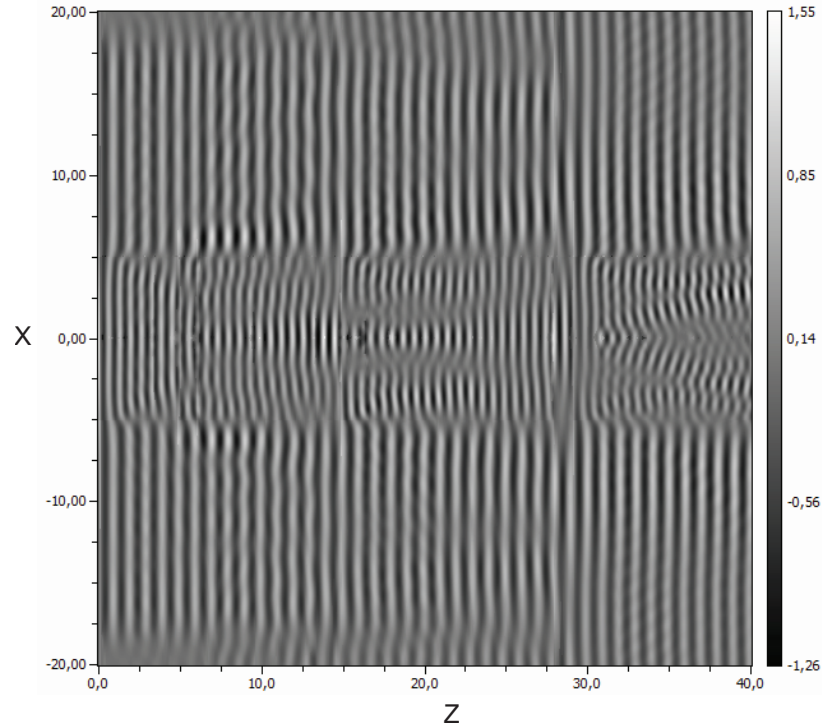
A clipping of spatial frequencies for a propagation above the critical angle θ_c avoids the calculation of evanescent modes. By removing all modes above the space-dependent evanescent boundary $k_{\perp}^2 = n^2(\mathbf{r})k_0^2$, all propagating modes are considered in the calculation. With the space-dependent clipping of modes at the evanescent boundary in the medium, the power flux through the low-contrast waveguide in figure 7.15 is stabilized but a dependency on the lateral index variation is introduced as shown in fig-

Figure 7.16. There, the simulation results for a variation in the contrast of the refractive index $n_{core} : n_{cladding}$ are shown. An increase in the contrast yields a larger drop in the power flux and the violation of the conservation law depends on the lateral index variation in the system. The energy, which is contained in the evanescent modes, increases with the discontinuity in the electric field (i.e. Gibb's phenomenon). A higher contrast introduces a higher step in the electric field and thereby the evanescent character of the propagating electromagnetic field increases. The spatial frequencies above the space-dependent evanescent boundary then comprise a larger fraction of energy which is taken away from the propagating modes according to Parseval's theorem $\int \mathbf{E}^2 d^2\mathbf{r}_\perp \propto 1/A \int \tilde{\mathbf{E}}^2 d^2\mathbf{k}_\perp / (2\pi)^2$. A removal of evanescent modes stabilizes the energy flux and a drop in the power flux is obtained at high contrasts in the refractive index. It is thereby shown, that the treatment of evanescent modes is responsible for the instability in the power conservation and the violation of the conservation law. It is also shown, that the clipping of evanescent modes at the space-dependent boundary yields a loss of power and thereby violates the conservation law. The loss of energy depends on the contrast in the lateral index change. In agreement to the observations in the BPM, the suppression of evanescent modes avoids the instability in the power flux. Since the instability is also observed in the scalar WPM, the vectorial transfer at the interface can not be responsible.

7.4.3 Energy-balanced clipping

Dependent on the contrast of the refractive index, the clipping of modes at the evanescent boundary violates the conservation law as shown in the

Figure 7.17: *Electric field of a plane wave which propagates through a waveguide with $n_{core} : n_{cladding} = 1.5$, using the energy-balanced clipping and treating evanescent modes like propagating modes (appendix B).*



last section. Therefore, an adaptive *energy-balanced clipping of modes* appears reasonable to avoid a violation of the conservation law. The power flux is observed while starting the accumulation of modes (eq. 3.29) from the center frequency $k_{\perp} = 0$ towards the evanescent modes. All modes which exceed the energy balance (eq. 7.24) are then clipped. At every interface, the method assumes a lateral or longitudinal index variation but never both, a longitudinal and a lateral index variation. Thereby, a space-dependent investigation of the conservation law is not necessary and a global energy balance for the transfer from the incident to the transmitted

layer is possible. Furthermore, the controlled clipping of modes does not consider the the multiplication with the space- and frequency-dependent phase element $\mathcal{P}(\mathbf{k}_\perp, \mathbf{r}_\perp)$ and thus the method is applicable to absorbing and non-absorbing media.

The power flux through the STEP-index waveguide in the left subplot of figure 7.12 is stabilized by using the energy balanced clipping as shown in figure 7.18. The corresponding electric field is shown in figure 7.17. It shows irregularities since the spectrum is dynamically the low pass filtered. Hence, the calculation perfectly agrees with the conservation law but depending on the contrast $n_{core} : n_{cladding}$ in the lateral index variation more or less modes are removed and the electric field then shows inhomogeneities. The result in figure 7.18 shows that the power flux in the high-contrast waveguide is perfectly constant in agreement to the conservation law but the electric field shows irregularities. Energy-balanced clipping thereby provides a perfectly constant power flux under all circumstances by definition, but depending on the power flux, more or less spatial frequencies are removed and the resulting distribution of the electric field is discontinuous.

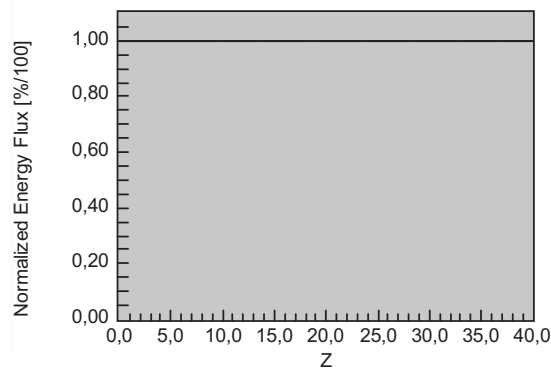
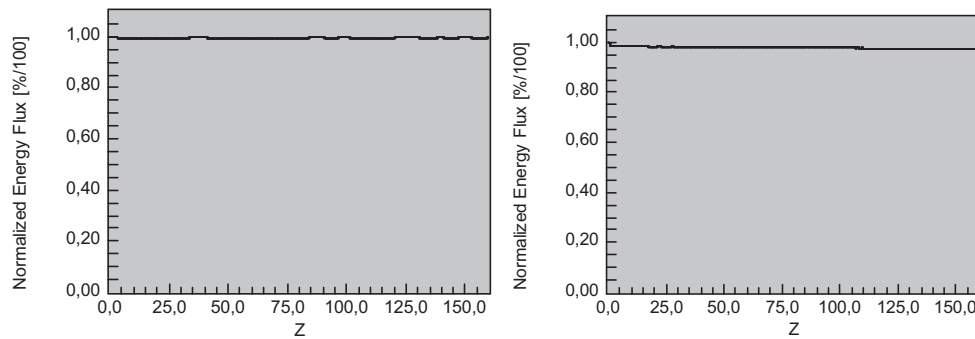


Figure 7.18: *Power flux of the electric field in figure 7.17.*

Figure 7.19: Power flux through a low-contrast waveguide $n_{core} : n_{cladding} = 1.1$ (left) and a waveguide with $n_{core} : n_{cladding} = 1.5$ (right) using clipping at the evanescent boundary in vacuum and treating evanescent modes like propagating modes (appendix B).



7.4.4 Clipping at the evanescent boundary in vacuum

The clipping at the evanescent boundary in section 7.4.2 utilizes a space-dependent suppression of evanescent modes. Now, the high order modes are clipped at the evanescent boundary in vacuum $k_{\perp}^2 = k_0^2$. All modes with a higher spatial frequency are not considered in equation 3.29 and thereby propagating modes are suppressed for $n > 1$. The power flux for the simulation of the waveguide with a low contrast (left) meets the conservation law as shown in figure 7.19. Compared to the results from the energy-balanced clipping, the electric field is continuous for small and medium contrasts as shown in figure 7.20. An increasing drop in the power flux of the electromagnetic wave, which depends on the contrast in the lateral index change, is observed in the right subplot of figure 7.19. The clipping at the evanescent boundary in vacuum provides a usable accuracy in the power flux at low contrasts in the lateral index change.

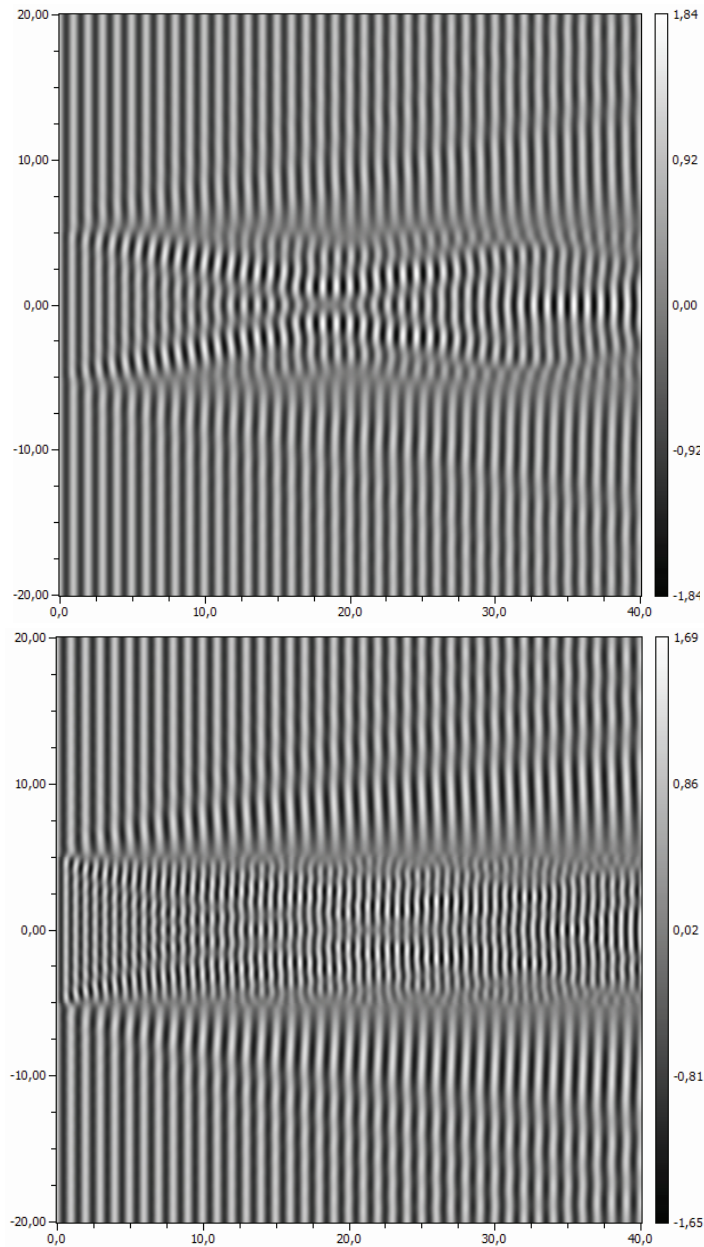
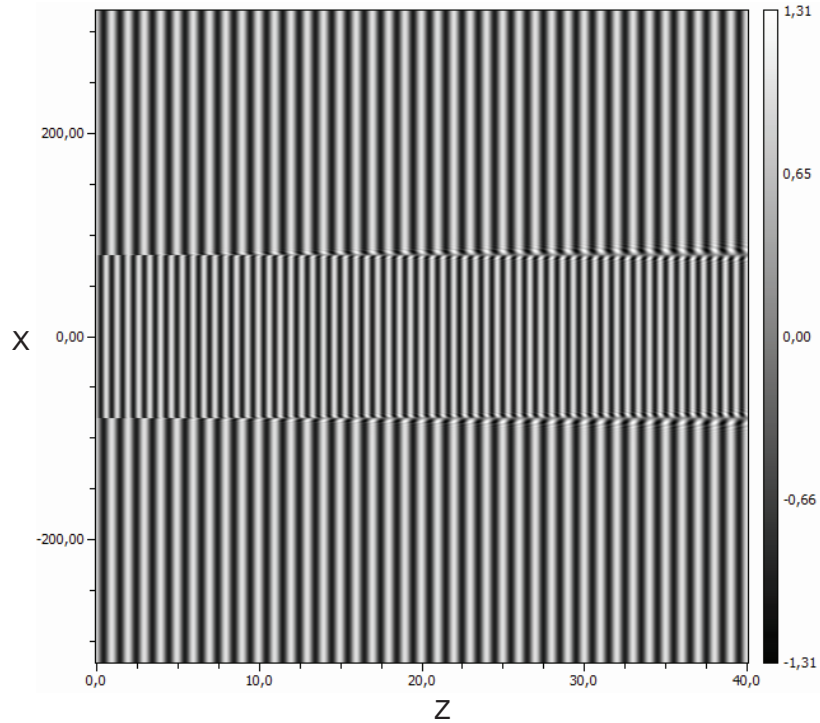


Figure 7.20: *TE-polarized plane wave, propagating through a low-contrast $n_{core} : n_{cladding} = 1.1$ (top) and a contrast $n_{core} : n_{cladding} = 1.5$ (bottom) waveguide, using a clipping at the evanescent boundary in vacuum and treating evanescent waves as propagating waves.*

Figure 7.21: A *TE*-polarized plane wave which propagates through the *STEP*-index waveguide in figure 7.12 using a sampling-induced clipping and treating evanescent modes like propagating modes (appendix B).



7.4.5 Sampling-induced clipping

The last and most simple clipping is the *sampling-induced clipping*. It utilizes the simple fact that lower sampling rates reduce the maximum frequency in the spectrum of the field. It is thereby possible to suppress evanescent modes and limit the spectrum to propagating modes if the maximum frequency in the spectrum is lower than the boundary for evanescent modes $k_{\perp} \leq nk_0, \forall n(\mathbf{r}_{\perp}) \in \mathcal{N}$.

With the sampling-induced clipping, the power flux of the TE-polarized plane wave which propagates through the STEP-index waveguide in figure 7.12 is perfectly constant as shown in figure 7.22. No high order or evanescent modes exist and hence the electric field experiences a hard phase shift at the boundary of the waveguide as depicted in figure 7.21. The method is susceptible for aliasing and induces a paraxial limitation since only a propagation of low order modes is allowed.

Therefore, the sampling-induced clipping is merely of academic interest. It shows that the appearance and treatment of evanescent and high order modes is responsible for the violation of the conservation law in agreement to the results in various publications as described on page 153.

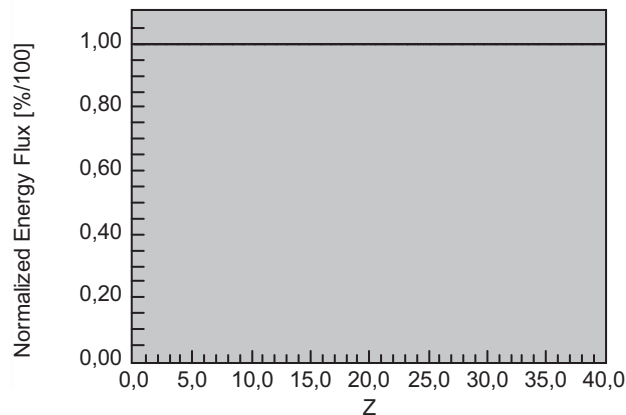


Figure 7.22: *TE-polarized Gaussian beam, propagating through the STEP-index waveguide in figure 7.12 using sampling-induced clipping and treating evanescent modes as propagating modes (appendix B).*

7.4.6 Transfer of evanescent modes

Chapter 3 and 5 introduce the transfer of evanescent modes at interfaces, using the vectorial model of evanescent from [1] which is derived from the complex z-component of the propagation vector. The VWPM identifies eligible configurations for $k_{z,e}$ and $k_{z,t}$ as described in table 3.1. All evanescent modes experience an exponential decay $\exp(-\gamma_{ev}\delta z)$, perpendicular to the interface. They do not contribute to the power flux as described in chapter 2 and in Appendix A. Evanescent modes are therefore not considered in the calculation of the power flux since they do not carry energy across the interface. But they contribute to the total field distribution and thereby to the input of the Fourier transformation.

Let a TE-polarized Gaussian beam with a wavelength of $1.5 [\mu m]$ and a waist of $10 [\mu m]$ propagate through the lossless STEP-index waveguide in figure 7.12. The refractive index of the waveguide is $n_{core} = 1.5 + i0$ and $n_{cladding} = 1 + i0$ and the diameter is $10 [\mu m]$. The aperture of the scene is $X = 40 [\mu m]$, the length of the waveguide is $Z = 160 [\mu m]$ and the scene is sampled with $n_x = 256$ and $n_z = 2048$. With the transfer of evanescent modes in the VWPM, the power flux is constant in agreement with the conservation as shown in figure 7.23.

A comparison to the simulation of the same scene in the right subplot of figure 7.15 shows that the rigorous calculation of evanescent waves by treating evanescent modes like propagating modes (appendix B) violates the conservation law and yields to an instability in the electromagnetic wave. A stabilization is obtained with the transfer of evanescent modes in the VWPM from chapter 3 which suppresses the evanescent-to-evanescent

transfer of modes as shown in table 3.1. Hence, it can be assumed that the evanescent-to-evanescent transfer at interfaces yields to instabilities. With the removal of the evanescent-to-evanescent transfer, the VWPM meets the conservation law.

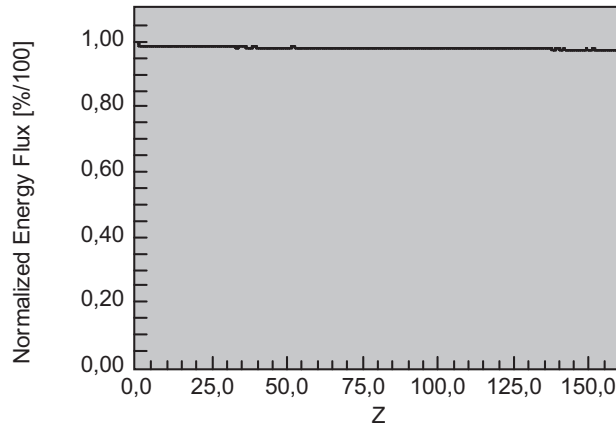


Figure 7.23: *Power flux of a TE-polarized Gaussian beam which propagates through the STEP-waveguide in figure 7.12 using the transfer of evanescent modes in the VWPM from chapter 3.*

Figure 7.24: *Real part (top) and amplitude (bottom) of a TE-polarized Gaussian beam which propagates through the STEP-index waveguide in figure 7.12 using the transfer of evanescent modes of the VWPM from chapter 3.*

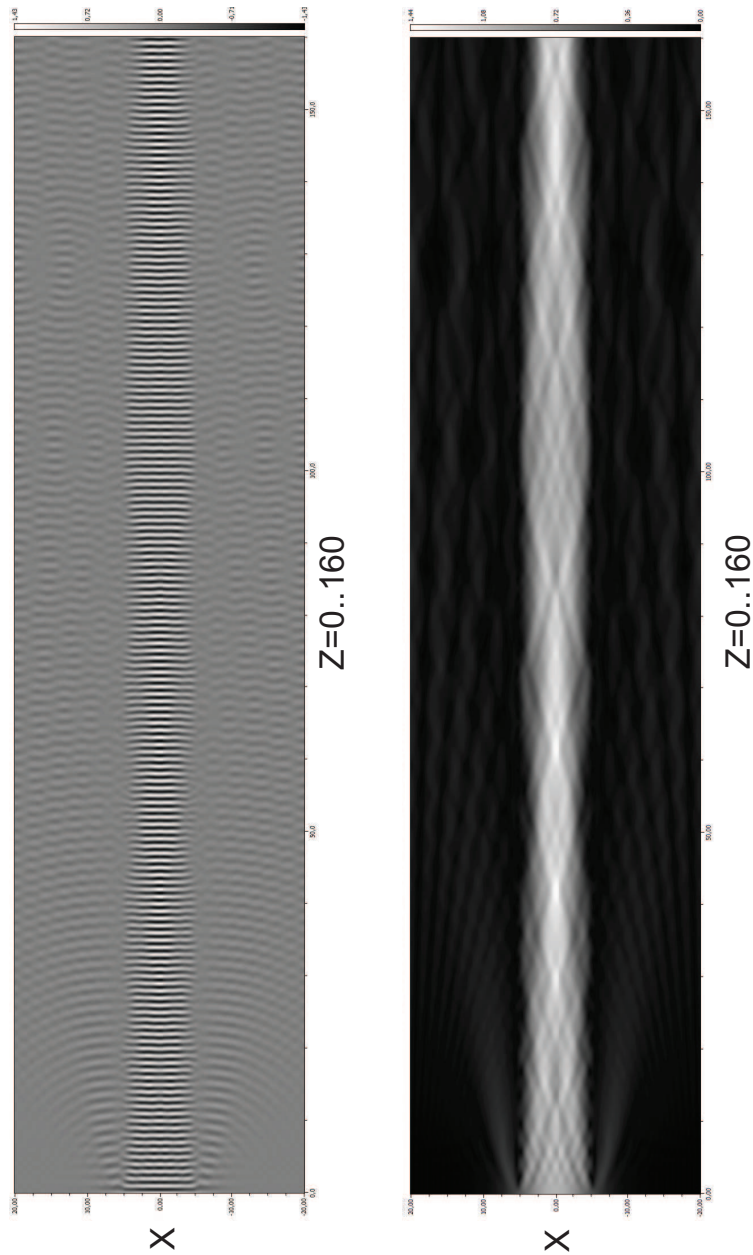
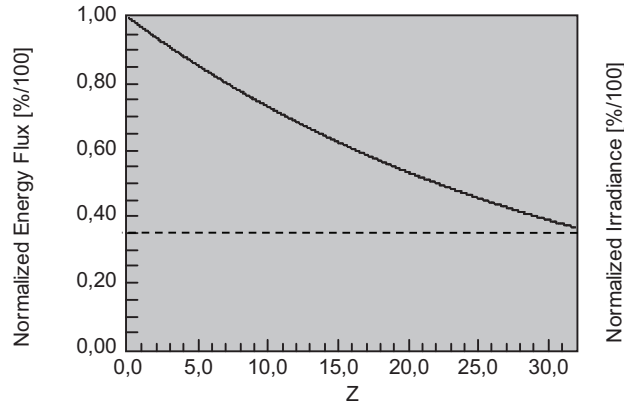


Figure 7.25: Normalized power flux of a TE-polarized plane wave which propagates through a homogeneous absorbing medium with $\hat{n} = 1 + i0.0025$.



7.5 Homogeneous lossy- or gaining medium

In a lossy medium, the absorption of electromagnetic energy needs to be considered. The power balance is then expanded by the absorbed energy

$$P_t = P_e - P_r - P_a \quad (7.24)$$

with P is the incident power, P_r is the reflected power, P_t is the transmitted power and P_a is the absorbed power according to equation 2.52.

In a lossy medium with $\epsilon_i \neq 0$ and $\kappa \neq 0$, the power flux decreases with the absorption length $1/\alpha = 1/(2\kappa k_0)$. A positive sign of κ causes a drop in the amplitude by absorption as shown in Appendix A. The drop in the amplitude is inverse proportional to the cosines of the angle of propagation

$$\frac{|\mathbf{E}_t|}{|\mathbf{E}_e|} = e^{-\kappa k_0 \delta z / \cos \theta} = e^{-\kappa k_0 k_t \delta z / k_{z,t}} \quad (7.25)$$

with κ is the imaginary part of \hat{n} , $k_t = n_t k_0$ and $k_{z,t} = \sqrt{k_t^2 - k_{\perp}^2}$. For a TE-polarized plane wave of unit amplitude which propagates a distance $Z = 32 [\mu m]$ through a medium $1 + i0.0025$, the irradiance and power flux drops by a factor $1/e \approx 37\%$ after an *absorption length* $1/\alpha = 31.82 [\mu m]$ as shown in the simulation with the VWPM in figure 7.25.

Chapter 8

Grating enhanced local absorption

Absorption is the loss of electromagnetic energy in a medium and local absorption considers its space-dependent variation determined by index distribution $n(\mathbf{r})$ and the distribution of the electromagnetic (EM) field.

The local absorption can be obtained from the divergence of the Poynting vector and Maxwell's equations as shown in equation 2.52. With equation 2.43, $\epsilon_i(\mathbf{r}) = 2n(\mathbf{r})\kappa(\mathbf{r})$, the space-dependent absorption of energy in a volume V is obtained from an expression which is independent from the ambiguity in equation 2.52, caused by the two signs in $n = \pm\sqrt{\epsilon}$. Then, the expression in [30] is obtained and the local absorption $P_a [W]$ is

$$P_a(V) = \frac{\omega}{2} \iiint_V \epsilon_0 \epsilon_i(\mathbf{r}) \mathbf{E} \mathbf{E}^* d^3 \mathbf{r} \quad (8.1)$$

with $\omega = ck [1/s]$ is the frequency of an electromagnetic wave with a wave-

length $\lambda = 2\pi/k$. For all practical purposes, a replacement of \mathbf{E} by the product $E_0\mathbf{E}_1$, with \mathbf{E}_1 is the normalized and dimensionless field strength, yields an alternative dimensionless formulation of the local absorption in a volume V

$$P_a(V) = E_0 \frac{\omega}{2} \iiint_V \epsilon_0 \epsilon_i(\mathbf{r}) \mathbf{E}_1(\mathbf{r}) \mathbf{E}_1(\mathbf{r})^* d^3\mathbf{r} \quad (8.2)$$

with $E_0 = |\mathbf{E}_0|$ [V/m] is the amplitude of the incident EM wave. The incident power $P_e(V)$ [W] of an electric field which passes an area element $\delta\mathbf{A}$ with an area $|\delta\mathbf{A}| = A$ [m²] is

$$\begin{aligned} P_e &= \frac{1}{2} \sqrt{\frac{\epsilon\epsilon_0}{\mu\mu_0}} \mathbf{E}_0 \mathbf{E}_0^* A \\ &= \frac{1}{2} \frac{n_e}{c\mu\mu_0} \mathbf{E}_0 \mathbf{E}_0^* A \end{aligned} \quad (8.3)$$

with $\sqrt{\epsilon\epsilon_0\mu\mu_0} = n/c$ and the squared amplitude in a nonmagnetic (i.e. $\mu = 1$) medium is then related to the power according to

$$\begin{aligned} \mathbf{E}_0 \mathbf{E}_0^* &= 2 \frac{c\mu_0}{n_e} \frac{P_e}{A} \\ &= 2 \frac{Z_0}{n_e} \frac{P_e}{A} \text{ [V/m]} \end{aligned} \quad (8.4)$$

with $Z_0 = c_0\mu_0 = \sqrt{\mu_0/\epsilon_0} = 1/c_0/\epsilon_0 = 376.82$ [Ω] is the impedance of the vacuum and $A = XY$.

The substitution of $\mathbf{E}_0\mathbf{E}_0^*$ in equation 8.2 yields a dependency between transmitted P_t and incident P_e power flux

$$P_t(V) = \frac{P_e(V)}{A} \iiint_V 4k_0\kappa_t(\mathbf{r}) \frac{n_t(\mathbf{r})}{n_e(\mathbf{r})} \mathbf{E}_1(\mathbf{r}) \mathbf{E}_1^*(\mathbf{r}) d^3\mathbf{r} \quad (8.5)$$

with $\hat{n}_e = n_e + i\kappa_e$ is the refractive index before and $\hat{n}_t = n_t + i\kappa_t$ is the refractive index behind the interface. The power ratio is then

$$\frac{P_t}{P_e} = \frac{1}{A} \iiint_V 2 \frac{\alpha_t(\mathbf{r})}{n_e(\mathbf{r})} \mathbf{E}_1(\mathbf{r}) \mathbf{E}_1^*(\mathbf{r}) d^3\mathbf{r} \quad (8.6)$$

with $\alpha_t = 2\kappa_t k_0 [1/m]$ is the inverse of the absorption length of the medium. Obviously, the local absorption has a direct relationship to the absorption length $1/\alpha [m]$ for which a drop in the irradiance to $1/e$ is obtained.

Using the nomenclature of the discrete algorithm for the VWPM from chapter 3, equation 8.6 then translates to the sum

$$\frac{P_j}{P_{j-1}} = \frac{\delta z}{n_x n_y} \sum_l \sum_m 2 \frac{\alpha_j(l, m)}{n_{j-1}(l, m)} \mathbf{E}_1(l\delta x, m\delta y) \mathbf{E}_1^*(l\delta x, m\delta y) \quad (8.7)$$

with δz is the sampling width in the z-direction, n_x, n_y is the pixel count (i.e. sampling) in the aperture, \mathbf{E}_1 is the normalized amplitude of the electric field, $j - 1$ is the index of the layer before and j is the index of the layer behind the interface.

8.1 Detection of light

In a silicon detector or solar cell, a depleted region is formed by combining semiconductors with different P- and N-dopants (i.e. PN-junction). A diffusion volume is thereby formed at the contact surface which extends into the semiconductors. This volume provides a lightsensitive region. Once a photon raises the energy state of an electron in the depleted region, the charge is potentially elevated from the valence band into the conduction band. The generated electron-hole pair contributes to the photo current. This is the *photo-electric effect* which was discovered by the German physicist Heinrich Hertz in 1886 and then interpreted with the quantum theory by the German Nobel laureate Albert Einstein in 1905.

The P- and N-dopants in the two semiconductors generate a diffusion volt-

age which prevents some electrons from an immediate recombination. A charge that does not recombine with a hole - the absence of a charge in a P-doped material or a free energetic state in the valence band - can be collected at the contacts of a photo detector or a solar cell. Once the charge is collected at the contacts, it is part of the external photo current. The more charges reach the contacts the merrier the external photo current and the merrier the efficiency of the device.

The *quantum efficiency* $[A/W]$ is defined as the number of elevated charges in Coulomb $[C]$ per second and per watts of incident light, generated by absorption in the depleted volume. The difference between *internal quantum efficiency* and *external quantum efficiency* is simply the loss of current due to recombination. The term *elevated charge* describes the change of the energy level $[eV]$ of an electron which elevates the charge from the valence band into the conduction band. The energy of the electron is then sufficient to overcome the bandgap (i.e. energy gap) in semiconductors which separates the two energy bands. The energy level of the electron elevates above the Fermi-level and the charge occupies a free energetic state in the conduction band. An electron with an energetic state at the Fermi level possesses an equal probability to stay in the valence and the conduction band. An elevated electron increases the internal photo current because it becomes a free floating charge which is not bound to an atom. The energy state of a charge which recombines, falls back to the valence band and becomes a bound electron. The charge then no longer contributes to the external photo current and to the external quantum efficiency. The recombination causes the emission of a photon which is the basic principle of a laser. If an amplified and stimulated emission of a high number of photons is possible, the material is called a lasing medium which can be utilized in a laser.

According to equation 8.1, a maximum absorption can be achieved by a large imaginary part of the refractive index, from a high electric field strength and from a large propagation distance through an absorbing medium. Hence, a geometric structure which provides a high concentration of electromagnetic irradiance and a fast population of the frequency space (i.e. generation of high order modes) provides a maximum local absorption in a certain medium.

8.2 Solar cells

The optimization of solar cells and the development of innovative high absorbing materials is a field of research that becomes more important due to the predictable decrease of fossil energy resources and the ever growing demand for energy. The extensive research created a variety of different solar cells which are classified by certain criteria. The most popular criterion is the material thickness which separates the types of modules into conventional and thin-film solar cells. A second criterion is the material which is used in the absorbing layer. The most popular materials are crystalline semiconductors like Cadmium Telluride (CdS, CdTe, ZnTe heterojunction), Gallium Arsenide (GaAs), Copper Indium Diselenide (CuInSe₂) and Silicon (Si). The structure of these materials can be mono-crystalline, polycrystalline or amorph. The use of organic or polymer materials is suggested in [61] to build flexible, plastic solar cells. So called CIS or CIGS (Chalkopyrite) solar cells are composed from Copper-Indium-Gallium-Diselenid or Copper-Indium-Disulfid to assemble thin film solar cells.

Most modules are made of mono-crystalline silicon (c-Si) or poly-/multi-crystalline silicon (mc-Si). The efficiency of c-Si cells is about 15% to 20% and the power density is in the range of 20 to 50 Watts per kg of material. The manufacturing of such cells necessitates a lot of energy which raises the price and the time for the amortization of cost. The cost-performance ratio and the energy consumption for the manufacturing of multi-crystalline modules is better. An efficiency up to 18,6% is presented in [60]. Crystalline (c-Si) and multi-crystalline (mc-Si) silicon is used in conventional solar cells with an absorbing layer of a thickness of 200 to 400 micrometers [70]. In case of thin-film solar cells, amorphous silicon is assembled with an efficiency of 5% to 9% and a power density of 2000 Watts per kg of material. Due to the use of layers at a thickness in the range of tens of micrometers (i.e. at least 30 micrometers for crystalline silicon is reported in [65]), no shortage in the material up to the range of terawatts exists. The absorption coefficient ($\alpha = 2\kappa k_0$) is ideally in the range of 10^4 [1/cm] to 10^5 [1/cm] in the wavelength region of 350 [nm] to 1000 [nm].

Another type of solar cells are the III-V semiconductor cells (i.e. GaAs). Such solar modules are very temperature insensitive and robust against ultra-violet (UV) radiance. The power efficiency is about 50 Watts per kg of material and the recent world record for III-V semiconductor cells with 41.1% efficiency was presented in [62] with a cost intensive multi-junction device. Such multi-junction devices utilize combinations of Gallium or Indium phosphide (InP/GaP) and Gallium Arsenide (GaAs), GaAs and Germanium or just Germanium to maximize the total depletion volume and provide a high absorption rate over a wide range of wavelengths. The manufacturing of such thin-film solar cells is expensive and therefore the major application area is in space flight.

A cheaper type of thin-film solar cells are the CdTe-cells, where II-VI semiconductors are utilized to commercially assemble solar modules by chemical bath deposition. Efficiencies up to 16% have been presented in [63] and up to 10% are available in commercial modules.

In CIGS(S) (copper, indium, gallium, sulfur, selenium) or CIS cells, I-III-VI semiconductors with a direct bandgap are assembled in thin film modules. The cells belong to the group of Chalkopyrites and provide an efficiency up to 20% as presented in [64]. Modules with an efficiency of 10 to 12% are commercially available.

The use of organic materials in solar cells is limited by their low efficiency of around 6% and the quite short lifetime of the cells of about 5000 hours. Organic thin film solar cells are flexible and can therefore be mounted on curvature shapes or even clothings. The research of new materials with a better lifetime and increased efficiency is promising and preliminary for a commercial success.

In conventional silicon-based solar cells, the absorbing substrate has a thickness of 200 to 400 micrometers and causes about 50% of the cost of solar modules. The reduced weight and cost as well as the efficient use of resources provides the major reason for the research of thin-film solar cells. The absorption of light in thin films provides an interesting application for an optimization by using diffractive geometries. In this chapter, the VWPM is utilized to determine the dimensions of diffractive gratings to obtain an enhanced absorption over a maximum range of wavelengths.

8.3 Micro-structured geometries

Micro structured geometries provide a promising way to enhance the performance of detectors and solar cells as shown in countless publications. The functional principle is based on the reduction of the reflectance and the fast population of the frequency space by diffraction to maximize the local absorption from a concentration and trapping of light. This improvement in the performance can be achieved by two mechanisms - the diffractive and the physical optics approach as explained in [77]. In the *diffractive approach*, the frequency space is filled by oblique propagating transmission orders. The *physical optics* approach utilizes rigorous simulation methods like the rigorous coupled wave analysis (RCWA) or the finite difference time domain (FDTD) method to calculate absorption in subwavelength structures.

In [66, 67, 68, 69, 70, 71], the physical optics approach is investigated. [66] investigates the enhancements of surface texturing with submicron diffractive gratings which are optimized with the RCWA. It is shown that nanostructures reduce the reflections at the air to silicon interface and efficiently couple light into diffraction orders which remain near the interface. The use of crystalline silicon grating structures is investigated in [67] and their calculations predict close to 100% energy coupling into oblique propagating diffraction orders for a certain wavelength. In agreement with the calculations and experimental results in [78], the use of two-dimensional gratings is promising to achieve a maximum coupling for TE- and TM-polarized electromagnetic fields.

A photonic light trap is assembled in [68] from a high contrast in the re-

fractive index to ease the coupling into the cell and prevent the loss by a small angle of total internal reflection. A $\lambda/4$ grating is applied to modulate the frequency space and redirect at least a fraction of the incident light into modes of higher order.

In [69], the use of photonic crystals in thin-film silicon solar cells is proposed to enhance the absorption. The results show a dependency of the coupling efficiency of the nanometer grating to the wavelength and the angle of incidence. The dependency is reasoned by the relation of the subvector k_{\perp} to the angle of incidence and the wavelength according to equation 2.34.

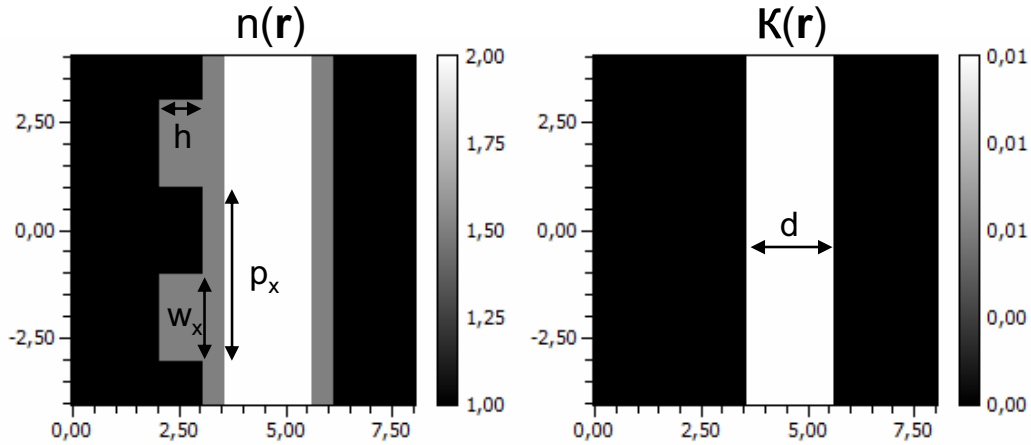
The diffractive approach is analyzed in [72, 73, 74, 76, 77]. One of the very first investigations for the use of micro-grating structures in solar cells was presented in [73]. A Gallium Arsenide grating solar homojunction cell with an efficiency of 25.5% was introduced, based on a P-cell. At that time, the introduced dot-grating structure could not be analyzed in an exhaustive numeric style and therefore the researchers had to rely on measured results. Their measurements showed that a device with a ratio of 18 for the ratio of diffusion length over grating separation provides an efficiency close to 100% for a certain wavelength. The lithographic performance limited the diameter of the dot-grating to 1 micrometer and the smallest grating spacing of a cell with 1% junction coverage was 10 micrometer in 1985. It has been determined that the diffusion length needs to be increased by at least one order of magnitude to make use of the potential of grating geometries. In [74], the use of periodic light-coupler gratings of aluminum-doped zinc oxide (ZnO) was investigated with a finite integration technique (FIT) and through experimental study. An increased height of the grating showed a better diffraction efficiency and an enhanced absorption.

8.4 Optimization of local absorption with the VWPM

The control of the local absorption is of high interest for a multitude of applications like optical detectors, thin film solar cells, electro-optical modulators or in the lithography [80, 81, 82, 83]. Compared to the global consideration of absorption in equation 2.78 which utilizes the difference between incident and transmitted power flux, the local absorption calculates a space dependent loss of power from equation 8.5, by considering the spatial distribution of the electromagnetic field $\mathbf{E}(\mathbf{r})$ and index distribution $\hat{n}(\mathbf{r})$.

In the following parameter optimization, a two-dimensional phase Ronchi is utilized to enhance the local absorption in an absorbing layer by a population of the frequency space which yields an increase in the optical path length (OPL). First the absorbing characteristic of a layer in the absence of a grating is analyzed to obtain a reference. Then, the period (i.e. pitch) of the grating is determined from a parameter variation of the duty cycle w/p , shown in figure 8.1. The simulation is performed for a TE- and a TM-polarized electromagnetic wave and for various angles of incidence. Two periods p_x and p_y with promising absorption rates for the TM- and TE-case are selected from the results. Then, the absorption for two-dimensional gratings and the dependency to the angle of incidence is investigated in a variation of the grating widths w_x and w_y . The widths are then selected from the results and the absorption for a variation in the angle of incidence is compared to the absorption rates in the system without a grating. Due to the increased complexity of the VWPM from $\mathcal{O}(n^2)$ to $\mathcal{O}(n^4)$ in all three-dimensional simulations, the multithreaded version of the VWPM in

Figure 8.1: Distribution of the real n (left) and imaginary κ (right) part of the refractive index for a 4λ grating with an adjacent 1.5λ absorbing layer.



appendix C is utilized.

8.4.1 Input system

The one- or two-dimensional phase Ronchi which was introduced in chapter 3 is slightly modified. The absorbing layer behind the one- or two dimensional phase Ronchi is enclosed by a thin non-absorbing homogeneous layer, for example Silicon (di)Oxide, to obtain a waveguiding structure. The non-absorbing cover-layers at the front- and backside of the absorbing layer therefore possesses a lower refractive index than the absorbing medium to obtain (total) internal reflection.

The one-dimensional grating is defined by the pitch p_x and the width w_x in the x-axis and two-dimensional gratings are defined by a second pair of

parameters, p_y and w_y , defining the grating in the y-direction. For all configurations with $w_x = 0$ and $w_y \neq 0$ or $w_y = 0$ and $w_x \neq 0$ one-dimensional gratings in the y-axis or x-axis are obtained. The two homogeneous non-absorbing layers before and behind the absorbing layer possess a thickness of 0.5λ and a refractive index $n_{clad} = 1.5 + i0$. Thereby an interface with (total) internal reflection is formed. All layers are assumed to possess a wavelength-independent constant refractive index. The absorbing layer has a refractive index $n_{core} = 2 + i0.01$. The micrometer-grating and the two homogeneous layers at the front and back-boundary are made of the same non-absorbing material n_{clad} . The grating has a height $h = \lambda$ and the absorbing layer has a thickness of $d = 2\lambda$ as shown in figure 8.1.

The size of the two-dimensional system is $X = Z = 8 [\mu m]$ and of the three-dimensional system $X = Y = Z = 8 [\mu m]$. The sampling in the two-dimensional scene is $n_x = n_z = 64$ and the three-dimensional system is sampled with $n_x = n_y = n_z = 64$. With a wavelength of $1 [\mu m]$, the normalized sampling interval δz_λ is $0.125 [-]$. This sampling would cause significant amplitude-deviations in case of oblique interfaces as shown in chapter 6, but the grating contains only vertical interfaces and hence the longitudinal sampling does not influence the accuracy of the amplitude as already shown in the comparison of the grating simulations with the VWPM to the results from RCWA in chapter 3.

8.4.2 Number of reflections

According to equation 5.11, $2p = 4$ iterations (i.e. p is the number of forward propagating beams) need to be calculated to obtain an accuracy of

Table 8.1: Number of iterations to obtain an accuracy of $a = 0.01$ of the input amplitude in the system in figure 8.1.

Num. of reflected waves ($2p$)	n_1	n_2	n_3	$R = r_{21}r_{23} $	$p = \lceil \log_R a \rceil$
4	1	1.5	2	0.02	$\lceil 1.183 \rceil$
4	1.5	2	1.5	0.029	$\lceil 1.295 \rceil$

one percent in the amplitude. Table 8.1 shows the product of the inner reflection coefficients $R = |r_{21}r_{23}|$ and the number of required iterations for the two interfaces to limit the maximum deviation $\max_{j \in \{1..n_z-1\}} (E_j(p+1)/E_j(p))$ (chapter 5) to one percent of the input amplitude. In the calculation of the Fresnel coefficients, the angle of incidence is set zero to obtain a maximum transmission into the absorbing layer.

The deviation in the amplitude falls below 0.01 after four iterations as verified in a simulation of a TE-polarized plane wave at vertical incidence which is not depicted in the thesis. The amplitudes and the amplitude deviations for the consideration of zero to five and ten iterations are shown in table 8.2. The deviation reaches the desired limit of one percent of the input amplitude if four or more iterations (i.e. $p = 2$ forward propagating beams) are considered.

8.4.3 Absorption rates without a grating

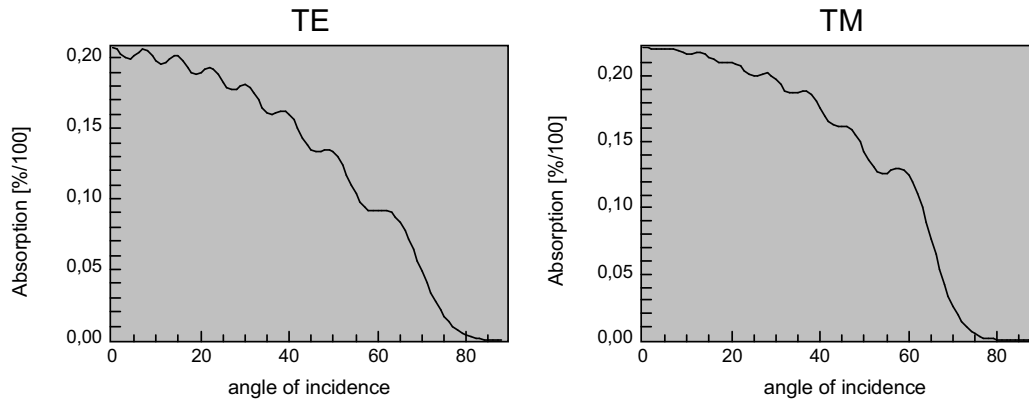
In the absence of a grating, the local absorption shows resonances due to the resonant structure of the layers. The reflectance increases with an

Table 8.2: *The maximum amplitude $E_{max} = \max_{\mathbf{r}}(|E|(\mathbf{r}))$ and its deviation $\delta E_{max} = |E_{max}(p+1) - E_{max}(p)|$ for p to consider one to five and ten iterations. The results are obtained from a simulation of the grating in figure 8.1.*

Iterations	p	E_{max}	δE_{max}
1	1	1.65305	—
2	1	1.66662	0.01357
3	2	1.68387	0.01724
4	2	1.68679	0.00291
5	3	1.68618	0.00061
10	5	1.68605	$< 10^{-4}$

increasing angle of incidence and less electromagnetic radiation enters the absorbing layer. Depending on the finesse of the resonant structure, a certain amount of light travels forth and back inside the absorbing layer as described in chapter 5. The phase relation between forward and backward propagating wave determines if constructive (even multiples of the half wavelength) or destructive (odd multiples of the half wavelength) interference occurs and therefore the resulting absorption rates tend to oscillate as shown in figure 8.2. A maximum absorption is obtained for vertical incidence and the absorption drops by a factor of two at 60 degrees. At 80 degrees no considerable absorption is calculated. The graphs show that the TE-polarized wave drops a little faster than the TM-polarized wave. An equal maximum absorption of 20.73 % for the TE- and TM-case is obtained at vertical incidence. In this case, the plane of incidence reduces to the surface normal, no polarization exists and the Fresnel transmission coefficients are equal for TE- and TM-polarized electromagnetic waves.

Figure 8.2: Absorption rate over the angle of incidence in the absorbing layer with $d = 2\lambda$, $n_{core} = 2 + i0.01$ and without a grating. (Left:) TM-polarized plane wave with unit amplitude. (Right:) TE-polarized plane wave with unit amplitude.



8.4.4 One-dimensional gratings

First, a promising pitch p_x is determined from a parameter variation of p_x and w_x in a two-dimensional simulation of one-dimensional gratings. The pitch p_x varies from 0 to 8λ and the width w_x varies from 0 to p_x . For all cases $w_x \geq p_x$, the absorbing layer is completely covered by a non-absorbing layer with a thickness equal to the height of the grating. The incident wave is TE-polarized in a first and TM-polarized in a second parameter variation. The angle of incidence varies between 0 and 80 degrees in steps of 20 degrees. In case of a TE-polarized wave, the grating aligns with the y-component of the electric field and in the TM-case, the x-component of the electric field is positioned perpendicular to the one-dimensional grating. No grating is obtained for $w_x = 0$.

Figure 8.3 shows the absorption for a parameter variation w_x (y-axis) over p_x (x-axis). In case of a TE-polarized plane wave at vertical incidence, a peak absorption rate of 50 percent is obtained. The peak-absorption decreases with an increasing angle of incidence. At 60 degrees, the maximum absorption is 18 percent and an absorption rate of 1.7 percent is obtained for $\theta = 80$ degrees. The maximum absorption rate in the TM-case is higher than for the TE-case over the entire spectrum of spatial frequencies since the electric field vector for TM is oriented perpendicular to the grating and therefore gets diffracted. The electric field vector of the TE-polarized wave oscillates along the grating and thereby is not affected by diffraction. Figure 8.4 shows the absorption rates for the range of with a high absorption, p_x from 0λ to 3λ and w_x from 0λ to 3λ , and a variation in the angle of incidence from $\theta = 0$ to $\theta = 80$ degrees. With a TM-polarized plane wave of unit amplitude, a maximum absorption of 53 percent is obtained by using vertical incidence for a grating pitch $p_x = 0.8\lambda$ and $w_x = 0.4\lambda$. Here, a high average absorption rate over a wide range of θ is preferred to a maximum absorption at vertical incidence since most solar modules are fix-mounted and do not provide the capability to adjust the panel to maintain vertical incidence. Therefore, from the parameter variation in figure 8.4, a pitch of 2λ for the TE-case and a pitch $p = \lambda$ for the TM-case is selected. The widths for a two-dimensional grating are now determined from a variation of w_x and w_y in a sequence of three-dimensional simulations.

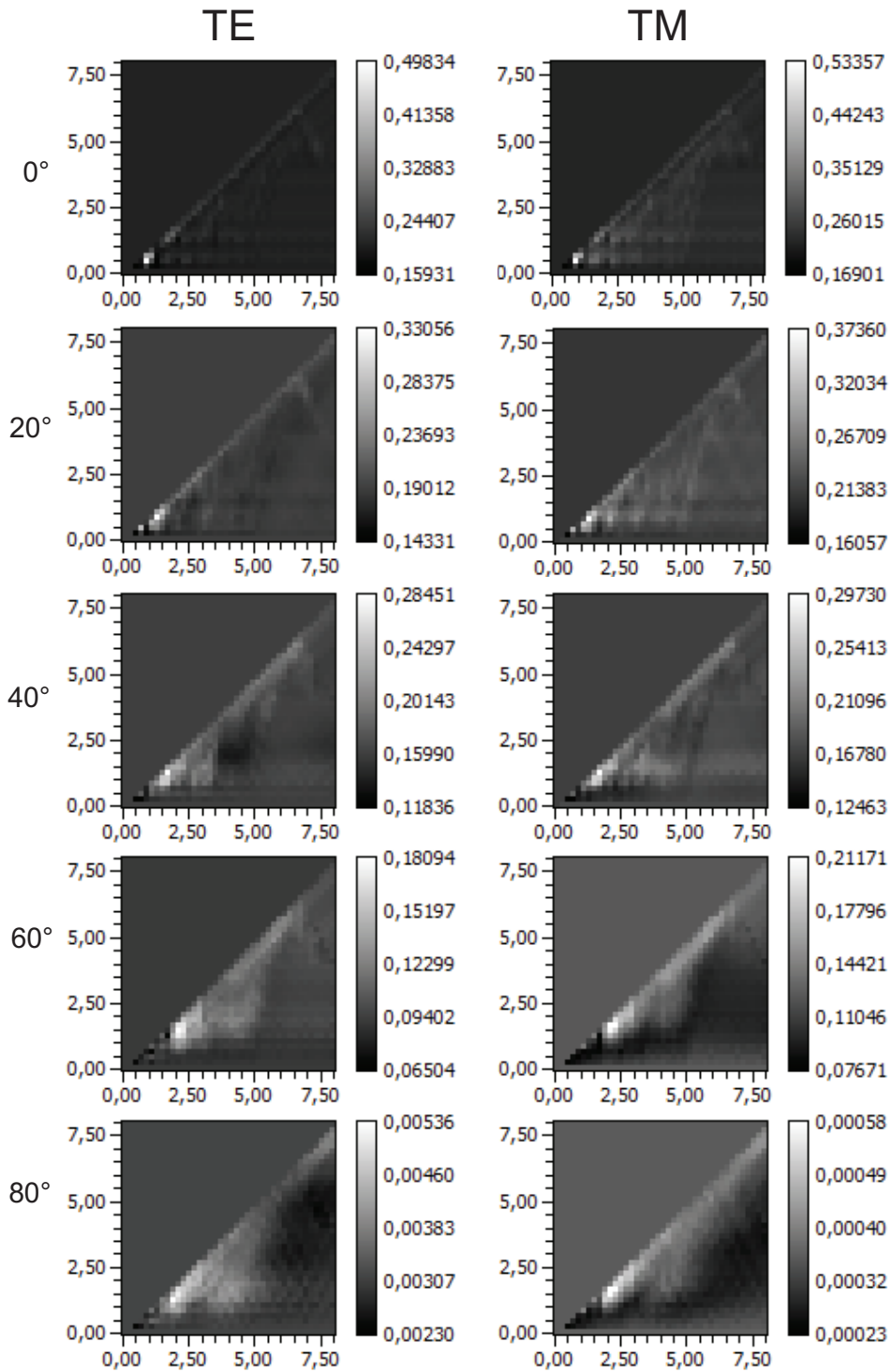


Figure 8.3: Accumulated absorption in the absorbing layer for a variation of pitch w_x (y-axis) over width p_x (x-axis) and for selected angles of incidence θ .

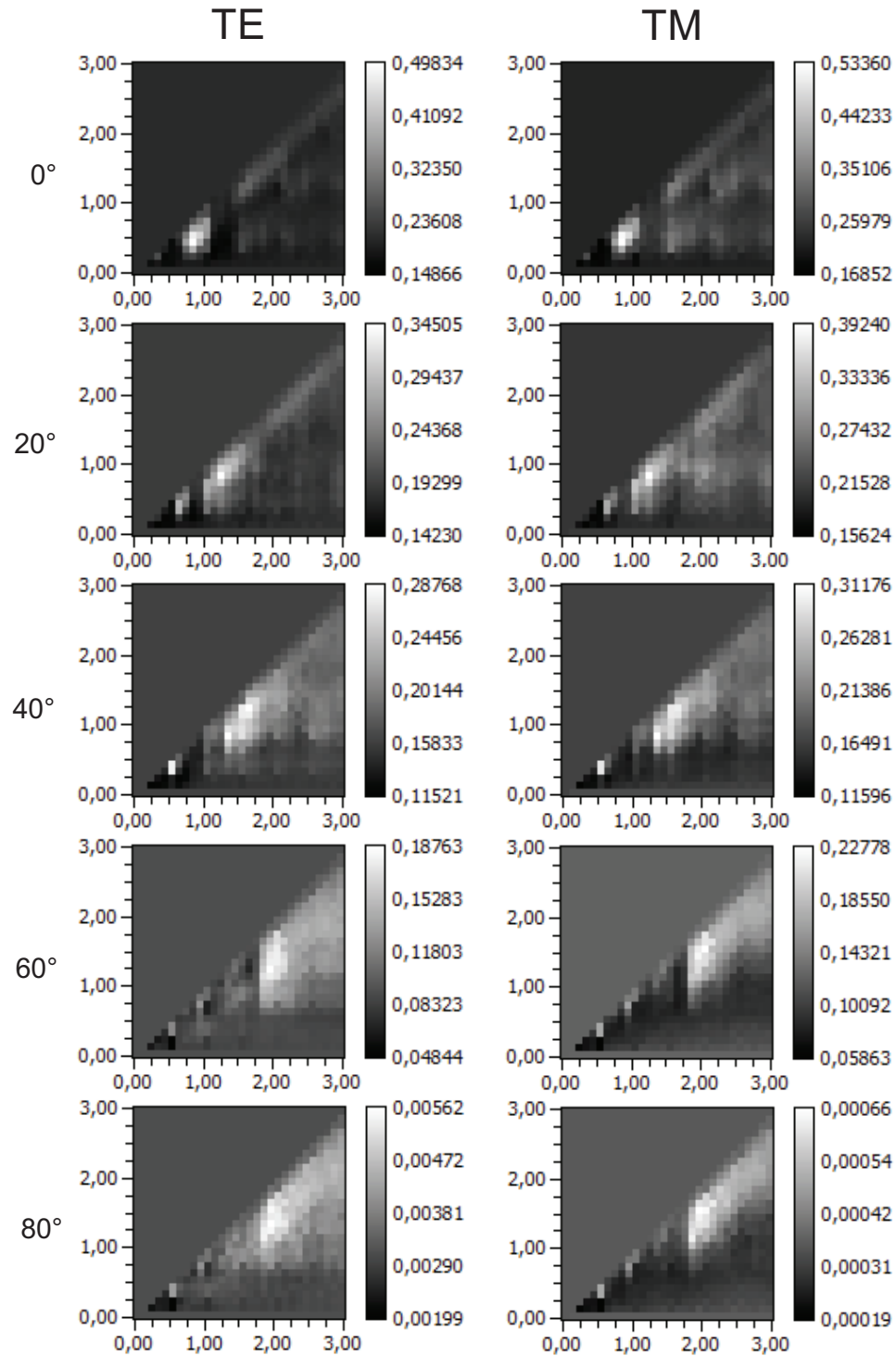


Figure 8.4: Accumulated absorption in the absorbing layer for a variation of pitch w_x (y -axis) over width p_x (x -axis). Left column: TE-polarized plane wave. Right column: TM-polarized plane wave.

8.4.5 Twodimensional gratings

The results from the optimization of one-dimensional gratings in section 8.4.4 show that the absorption in the layer vary with the polarization and the angle of incidence. Gratings with high absorption for a TE-polarized EM field not necessarily possess high absorption rates for a TM-polarized EM field. Hence, the use of two-dimensional gratings, which are optimized in one dimension for absorbing TE-polarized waves and in the second dimension for absorbing TM-polarized waves are promising to further enhance the absorption.

The investigation of the results in figure 8.4 shows that a high average absorption for the TE-polarized wave is obtained from a pitch $p_y = 2\lambda$ and for the TM-polarized wave from a pitch $p_x = \lambda$. In order to determine an optimal duty cycle w/p for the two pitches, let w_y vary from 0 to $p_y = 2\lambda$ and w_x from 0 to $p_x = \lambda$ in steps of 0.1λ . The angle of incidence varies again from 0 to 80 degrees in steps of 20 degrees. The incident wave is TE-polarized in a first and TM-polarized in a second parameter variation.

Figure 8.5 shows the accumulated local absorption rates for the TE-case (left) and TM-case (right) and for an increase in the angle of incidence from top to bottom. At small angles of incidence, the absorption rates show maximum values for the TE- and TM-polarized waves. At higher angles of incidence, the absorption decreases as already observed in section 8.4.4. A high average absorption rate for a maximum range of angles of incidence can be obtained for a widths $w_x = w_y = 0.5\lambda$. The resulting two-dimensional grid with the duty cycles $d_x = 0.5$ and $d_y = 0.25$ is shown in figure 8.6.

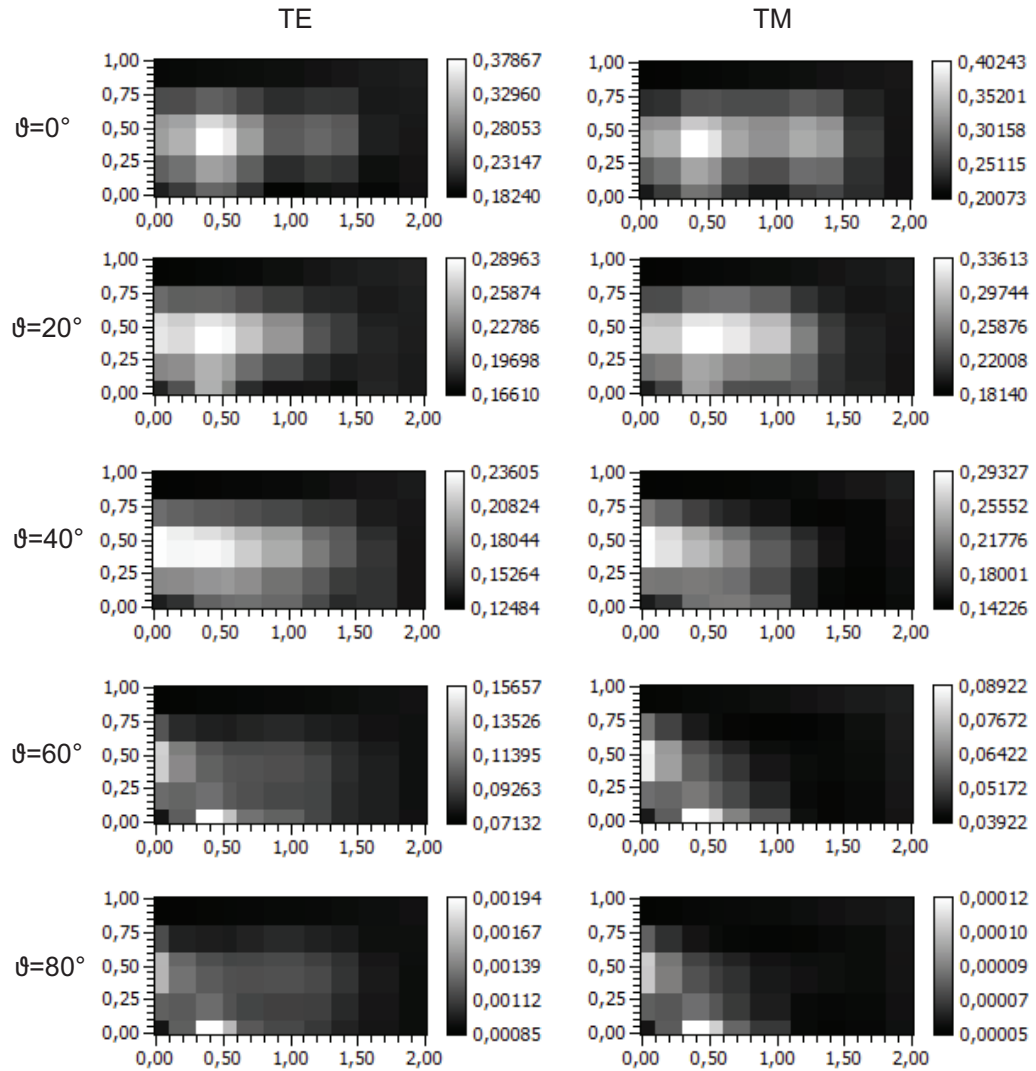
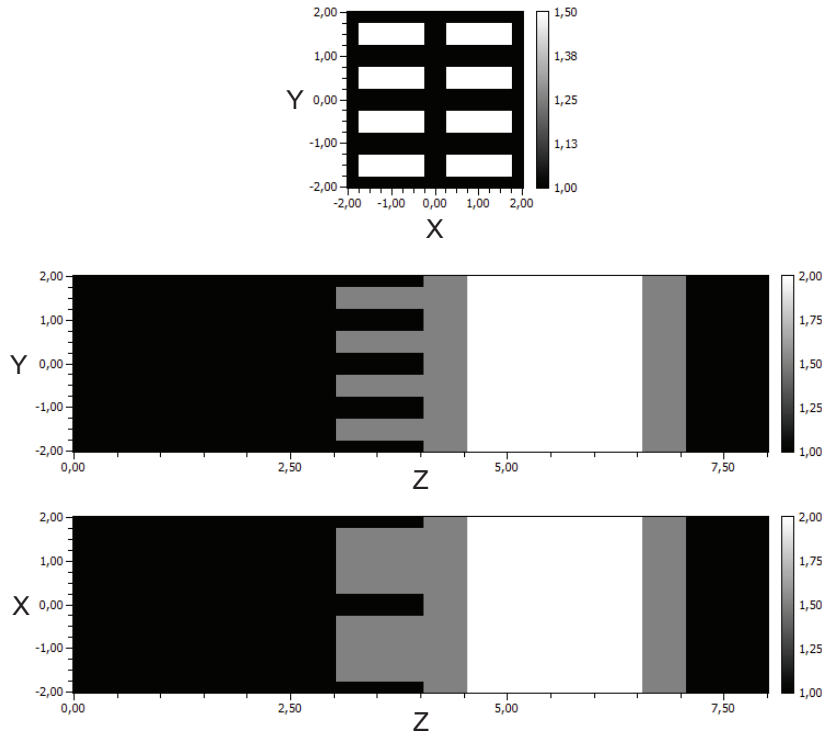


Figure 8.5: Parameter variation w_x (x-axis) over w_y (y-axis) at different angles of incidence.

Figure 8.6: *Optimized two-dimensional grating with $p_y = 2\lambda$, $p_x = \lambda$ and $w_x = w_y = 0.5\lambda$.*



8.4.6 Angle of incidence versus wavelength

Due to the dependency of the local absorption to the angle of incidence, the efficiency of the grating also varies with the wavelength. This dependency between angle of incidence θ and the wavelength λ is also described in [78]. Thereby, a variation of the angle of incidence has the same effect on the transversal component of the propagation vector \mathbf{k}_\perp as a variation in the wavelength since the grating has no sense for the root cause for \mathbf{k}_\perp . Hence, same results are obtained from a variation in the angle of incidence and from a variation of the wavelength. An angle of in-

idence θ_m at a wavelength λ_m then corresponds to an angle of incidence θ_n at a wavelength λ_n according to

$$\frac{\sin \theta_m}{\lambda_m} = \frac{\sin \theta_n}{\lambda_n} \quad (8.8)$$

obtained from $k_{\perp} = 2\pi/\lambda \sin(\theta)$.

8.4.7 Optimized two-dimensional grating

The angle of incidence θ and the wavelength λ of the incident electromagnetic wave are related metrics and therefore a grating which provides a high absorption rate over a wide range of spatial frequencies also yields a high absorption over a corresponding range of wavelengths (eq. 8.8) - presumed that the absorption factor $\alpha = 2\kappa k_0$ does not vary with the wavelength. Here, all properties of the material which depend on the wavelength are neglected since the effect of diffractive gratings on an EM wave is independent from the material in the absorbing layer.

Figure 8.7 shows the absorption rates for the optimized two-dimensional grating in figure 8.6 for a variation of the angle of incidence from 0 to 90 degrees. The upper plots show the absorption rates without grating and the lower plots depict the grating enhanced absorption. In the absence of a grating, the resonant character of the structure is clearly visible. The absorption in the grating enhanced system increases by roughly 50 in average with and a second peak in the absorption rate at $\theta \approx 27$ degrees. The curve of the grating-enhanced system envelopes the conventional system at nearly all angles of incidence. The absorption at high angles of incidence and for TM-polarized modes falls slightly below the absorption of

the system without a grating but the absorption at such high angles is below three percent and thereby does not significantly contribute to the overall system performance.

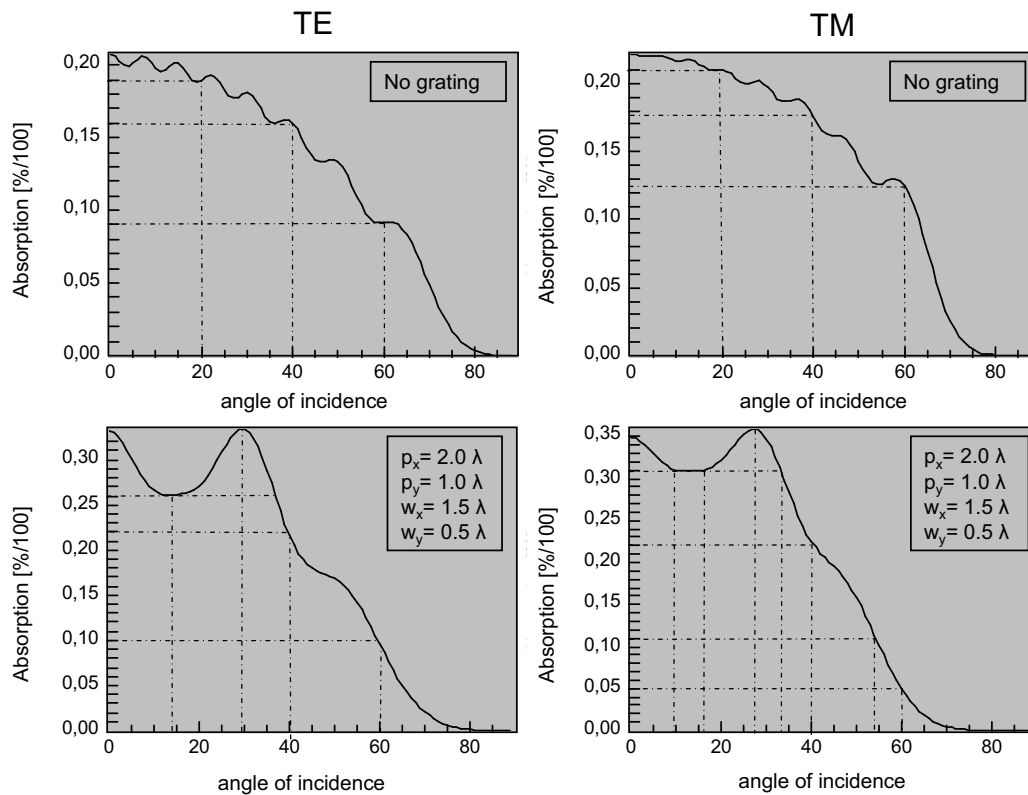


Figure 8.7: Absorption rates over angle of incidence without a grating (top) versus the optimized two-dimensional grating (bottom).

8.5 Conclusion

This chapter shows that the use of two-dimensional micrometer gratings improves the absorption rates in thin absorbing layers. The results of var-

ious parameter variations show that enhancement of the absorption with one-dimensional gratings is sensitive to the polarization and the angle of incidence. As a consequence, it is not possible to obtain a maximum absorption rate for TE- and TM-polarized waves with one-dimensional gratings. Hence, the use of two-dimensional gratings is proposed in agreement with various publications. A parameter set for an enhanced absorption over nearly the entire spectrum is determined with the VWPM. The two-dimensional grating enhances the absorption by roughly 50 percent over nearly the entire spectral range for TE- and TM-polarized electromagnetic fields.

Outlook

With its sensitivity to angle and wavelength as well as polarization, one- or two-dimensional gratings can be furthermore used for wavelength division multiplexing (WDM), add-drop filters, optical detectors or electro-optical modulators as suggested in [80, 81, 82]. In case of WDM or add-drop filters, a grating with a peak absorption at a certain wavelength would be preferred. When used in electro-optical modulators, the dynamics in the material and the influence of a change in the refractive index on the diffraction efficiency of the grating from an applied voltage (i.e. Kerr-Effect, Pockels effect) needs to be considered. A configuration with a high sensitivity in the absorption rates to the applied voltage or to the angle of incidence would then be selected to achieve a maximum effect from the control of the diffraction efficiency of the grating. The reflectivity, transmittivity and absorption can then be controlled. This appears to be a promising approach for optical chip-to-chip communication [82].

Chapter 9

Summary and closing

Fast Fourier methods are efficient to simulate the propagation of electromagnetic fields along a predefined axis of propagation as shown in chapter 1, based on the theoretic fundamentals in chapter 2. The split step propagation scheme, which is utilized in the Beam Propagation Method, cannot overcome the inherent error which arises from the separation of the propagation into two operators, the diffraction operator (eq. 3.2) and the phase adjustment operator (eq. 3.3) as shown in Chapter 3. Hence, all split step propagation methods are more or less limited to paraxial propagation and small index variations and their applicability is therefore limited. The scalar wave propagation method (WPM) [31] utilizes the exact solution of the scalar diffraction integral and therefore yields accurate results for propagation angles of electromagnetic fields up to ± 85 degrees. The WPM is limited to scalar electromagnetic fields and does not model evanescent waves. Since the vectorial effects become significant at high propagation angles, a vectorial version of the WPM is desirable.

The Vector Wave Propagation Method (VWPM) is presented in this thesis. It utilizes a vectorial formulation of the Rayleigh-Sommerfeld diffraction integral to derive the propagation of three-dimensional vector fields from the transformation of its lateral components and from transversality. This reduces the computational effort and ensures transversality. The transfer of evanescent waves in chapter 3 utilizes the model of evanescent waves from [1]. In the VWPM, eligible configurations for the incident and transmitted propagation vector are identified and evanescent-to-evanescent propagation is only considered in the absence of longitudinal changes along the axis of propagation. The magnetic vector, the irradiance, the power flux and the local absorption are derived from the electromagnetic vector fields. With the VWPM, exact results are obtained for the entire range of spatial frequencies as shown in various simulations and by comparing the results to the electromagnetic theory. The simulated field distributions in diffraction gratings show a remarkable agreement with the results from a three-dimensional RCWA and the vectorial Debye theory. With the extension to evanescent frequencies, the VWPM simulates total internal reflection and evanescent waves at interfaces as shown in figure 3.9. Thereby, the applicability of the VWPM is extended to the full range of spatial frequencies without approximation.

Chapter 4 shows that a vectorial version of the split step propagation scheme is not reasonably possible due to the separation of the propagator into two operators. The Fresnel coefficients must be applied in the spatial frequency domain and hence by considering the averaged refractive index. Then, artificial reflections and transmissions occur, which can be only eliminated by considering spatial and spectral information and remove the strict separation of the propagator into two operators. Since the split step propagation scheme is limited to paraxial propagation, where

the vectorial effects are more or less negligible, an extension of the BPM to vector fields is of limited benefit.

The VWPM is extended to bidirectional propagation of three-dimensional electromagnetic vector fields in chapter 5. The bidirectional algorithm iterates forward and backward and calculates the propagation of transmitted and reflected electromagnetic vector fields along the axis of propagation. The field distributions in one or two-dimensional gratings show remarkable agreement with the results from RCWA, the multilayer theory and Snell's law as presented in various bidirectional simulations. The position of a reflected Gaussian beam at a single interface perfectly agrees with the results from theory while the BPM shows a significant deviation which arises from the paraxial limitation as shown in chapter 3. In case of multiple reflections, the analysis of Fabry-Perot resonators provides a criterion for a minimum number of iterations which are necessary to obtain a desired degree of accuracy. In homogeneous medium, the VWPM perfectly agrees with the vectorial version of the plane wave decomposition (PWD). Therefore, the unidirectional and bidirectional VWPM utilizes the vectorial PWD in homogeneous medium to reduce the simulation time. A parallel algorithm is presented in appendix C to further enhance the simulation speed in inhomogeneous medium. The center equations of the parallel VWPM scale linear with the number of threads and the sequential code sequences possess a time-complexity of a one- or two-dimensional Fast Fourier transformation. This yields a significant reduction in simulation time as shown in appendix C.

In chapter 6, the Whittaker Kotelnikov Shannon (WKS) sampling theorem is discussed and the effect of aliasing in the spectrum is shown in a simulation of an undersampled propagating Gaussian beam through vacuum.

The diffraction order efficiency (DOE) is utilized to investigate the influence of the discretization of oblique interfaces in the axis of propagation on the accuracy of the simulation. It is shown, that the amplitude deviates, depending on the wavelength in the medium and the discretization of the system in the axis of propagation δz . The normalized sampling interval δz_λ is introduced and it is shown that the amplitude deviation is below one percent by selecting a sampling interval δz which is in the range of one tenth of the wavelength (i.e. $\delta z_\lambda \leq 0.1$). Figure 5.3 shows a series of graphs to get the number of iterations from a desired accuracy in the amplitude and a given configuration of the refractive index.

Chapter 7 provides a detailed discussion of the energy conservation in lossless and the absorption in lossy medium. The simulated power flux perfectly agrees with the results from theory for homogeneous layers and longitudinal index variations. In layers with lateral changes in the refractive index (i.e. inhomogeneous layers), evanescent modes are generated in the spectrum of the electric field which arise from local discontinuities the electric field in agreement with Gibb's phenomenon. It is shown that these evanescent modes cause an increase in the power flux which violates the conservation law. This observation agrees to various publications on the treatment of evanescent modes in the BPM. As shown in chapter 7, the electric field in a waveguide is dominated by growing evanescent modes, if the entire spectrum is treated like propagating modes, using a purely complex calculation as introduced in Appendix B.

Several methods of stabilization, which are partially known in the BPM, are presented: First, a low-pass filtering of the system is utilized, which can not stabilize the simulation under all circumstances. Due to the reduction of discontinuities in the refractive index, the generation of high order modes is

reduced. This is shown in simulations of step-index and GRIN waveguides. The violation of the conservation law is not completely suppressed and a stabilization of the power flux can therefore be only obtained for small lateral variations in the refractive index and for small propagation distances in agreement with the results in [29, 45].

Second, a clipping of evanescent modes at the space-dependent evanescent boundary $k_{\perp} = n(\mathbf{r})k_0$ is suggested to maintain the conservation law. The method improves the stability of the power flux, but the energy which is contained in the evanescent modes depends on the distribution of the refractive index $n(\mathbf{r})$. Dependent on the contrast of lateral index changes, more or less energy is removed from a propagating electromagnetic field by clipping at the space-dependent evanescent boundary. Since the power of the electric field is distributed over the entire spectrum according to Parseval's theorem, it is shown that the clipping of evanescent modes yields to a loss of energy and thus a violation of the conservation law. A high index change causes a high drop in the power flux in lossless medium. This dependency to the index distribution can be removed with a clipping of modes at the evanescent boundary in vacuum $k_{\perp} = k_0$. The conservation law is then maintained for a wide range of contrast in the lateral variations of the refractive index but a drop in the energy flux in lossless media is still observed.

Third, the conservation law is maintained under all circumstances from an energy-balanced clipping of modes. A constant power flux in lossless media is obtained in agreement with the theory under all circumstances but the distribution of the electric field shows discontinuities due to the controlled clipping of modes since the maximum angle of propagation changes from layer to layer. Due to the varying angle of propagation and the inho-

mogeneities in the electric field, the dynamic clipping is primarily of academic interest.

Forth, the evanescent transfer in the VWPM from chapter 3 is utilized to maintain the conservation law. A stabilization of the power flux in lossless media is obtained from an identification of eligible configurations of the propagation vectors as presented in chapter 3. The conservation law is maintained from a suppression of evanescent-to-evanescent propagation at longitudinal interfaces. A stabilization of BPM-simulations from a modified treatment of evanescent modes, compared to the treatment of propagating modes, is also presented in the literature as described (refer to chapter 7). The clipping at the evanescent boundary in vacuum and the evanescent transfer in the VWPM provides the best results for maintaining of the conservation law.

An optimization problem of practical interest is investigated with the VWPM in chapter 8. The local absorption in a thin absorbing layer is derived from the distribution of the electric field and from the distribution of the refractive index to optimize the efficiency of thin film solar cells by using one- and two-dimensional diffraction gratings. In the first section, the discrete calculation of the local absorption is introduced. Then, the principle for the detection of light in semiconductors is discussed and a brief overview on solar cells is given. Referring to various publications, the use of diffractive structures for an enhancement in the absorption is then described. The VWPM is subsequently utilized to determine the parameters of a two-dimensional micrometer grating which yields an enhanced average absorption rate over a wide spectral range. The results are compared to the absorption rates without a grating and it is shown that the enhancement of the absorption efficiency is in the range of 50 percent over nearly the entire spectrum by

using an optimized twodimensional micrometer grating. The optimization and control of the local absorption in thin films furthermore is desirable in a wide range of other applications like wavelength division multiplexers, add-drop filters, photo detectors and electro-optical modulators as shown in [80, 81, 82].

9.1 Closing

The VWPM is suggested for the simulation of fully three-dimensional micro-optical systems such as lenses, lens arrays, prisms, plastic structures, absorption filters etc. With rigorous solvers like the FDTD, the whole three-dimensional E- and H-field has to be store in computer memory. For a system which is 1024x1024x4000 pixels in size this means 4 Gigasamples for each field component. With the Yee-scheme, three time slices and three real field components for x, y and are needed. This requires 3x3x8 Bytes per sample for double precision, resulting in 288 GBytes of memory, not counting the perfectly matched layers (PML). By cashing out to hard disk, a speed factor of approximately 100 would be lost. Thus a wave optical simulation with FDTD is practically not possible for this system size. With the proposed VWPM, it would be possible, because the system is calculated slice by slice. Also, the processing time is still reasonable, compared to RCWA, since the time only grows with the forth order of the samples while the time for the RCWA grows with the sixth order of the modes. The threedimensional simulation of an electromagnetic vector field which is composed from ten modes is then a hundred times faster with the VWPM than with the RCWA.

Bibliography

- [1] Max Born and Emil Wolf, *PRINCIPLE OF OPTICS*, 7th expanded edition, Cambridge University Press, ISBN 0-521-46222-1, 2003.
- [2] Eugene Hecht, *OPTICS*, Fourth International Edition, Addison Wesley, ISBN 0-321-18878-0, 2002.
- [3] Allen Taflove, Susan C. Hagness, *Computational Electrodynamics: The Finite-Difference Time-Domain Method*, Third edition, Artech House Inc., ISBN-10:1-58053-832-0, 2005.
- [4] Ting-Chung Poon and Taegeun Kim, *Engineering optics with Matlab*, ISBN 981-256-873-5, World Scientific Publishing, 2006
- [5] G. Bao, L. Cowsar and W. Masters, *Mathematical Modeling in Optical Science*, SIAM, 2001.
- [6] K. Yee, *Numerical solutions of initial boundary value problems involving Maxwell's equations in isotropic media*, IEEE Transactions on Antennas and Propagation, vol. AP-14, pp. 302-307, 1966.
- [7] J. Berenger, *A perfectly matched layer for the absorption of electromagnetic waves*, Journal of Computational Physics 114: 185200, 1994.

- [8] S.D. Gedney, *An anisotropic perfectly matched layer absorbing media for the truncation of FDTD lattices*, Antennas and Propagation, IEEE Transactions on 44: 16301639, 1996.
- [9] G. Mur, *Absorbing boundary conditions for the finite-difference approximation of the time-domain electromagnetic field equations*, Electromagnetic Compatibility, IEEE Transactions on 23: 377382, 1981.
- [10] Z. P. Liao, H. L. Wong, B. P. Yang, and Y. F. Yuan, *A transmitting boundary for transient wave analysis*, Scientia Sinica a 27: 10631076, 1984.
- [11] C.B. Burkhardt, *Diffraction of a Plane Wave at a Sinusoidally Stradied Diffractive Grating*, J. Opt. Soc. Am. 56 (1966), Nr. 11, S. 1502
- [12] Ir. van Kraaij, *A more Rigorous Coupled-Wave Analysis*, Dissertation, NOD number OND1321799, Technische Universiteit Eindhoven, Department of Mathematics and Computer Science, 2005.
- [13] M. Feit, J. Fleck, *Light propagation in graded index fibers*, Appl. Opt., vol. 24, pp. 3390-3998, 1978.
- [14] G.R.Hadley, *Wide-Angle beam propagation method using Pade approximant operators*, Opt Lett, Vol 17, No. 20, pp 1426-1428, 1992.
- [15] Changbao Ma and Edward Van Keuren, *A three-dimensional wide-angle BPM for optical waveguide structures* in OPTICS EXPRESS, (22 January 2007), Vol. 15, No2.
- [16] P. Lee, E. Vogoies, *Three-dimensional semi vectorial wide-angle beam propagation method*, J. Lightwave Tech., vol. 12, no. 2, pp. 215-225, Feb. 1994.

- [17] T. Anada, T. Hokazono, T. Hiraoka, J. Hsu, T. Benson, P. Sewell, *Very-wide-angle beam propagation methods for integrated optical circuits.*, IEICE Trans Electron, Vol E82-C, No. 7, pp. 1154-1158, 1999.
- [18] Junji Yamauchi, Yuta Nito and Hisamatsu Nakano, *A modified semivectorial beam propagation method retaining the longitudinal field component* in Integrated Photonics and Nanophotonics Research and Applications, (Optical Society of America, 2008), paper IWB5.
- [19] P. Liu and B.J. Li, *Semivectorial beam-propagation method for analyzing polarized modes of rib waveguide.*, IEEE J. Euumant Electron, Vol. 28, pp 778-782, April 1992.
- [20] J. Wanguemert-Perez, I. Molina-Fernandez, *A novel Fourier based 3D full-vectorial beam propagation method*, Optical Quantum Electronics, vol. 36, pp. 285-301, Kluwer Academic Publishers 2004, Netherlands.
- [21] Y. Tsuji, M. Koshiba, N. Takimoto, *Finite element beam propagation method for anisotropic optical waveguides.*, Journal Lightwave Technology, Vol. 17, No. 4, pp.723-828, Apr. 1999.
- [22] M. Stern, *Semivectorial polarized finite difference method for optical waveguides with arbitrary index profiles*, IEEE Proceedings, Vol. 135, Pt.J, No 1, Feb 1988.
- [23] H. Pinheiro, A. Barbero, H. Hernandez-Figueroa, *Full-vectorial FE-BPM approach for the analysis of anisotropic medium with off-diagonal permittivity terms*, Mic. Opt. Tech. Letters, V.25, No 1, pp. 12-14, April 2000.

- [24] S.Obayya, B. Rahman, *New vectorial numerically efficient propagation algorithm based on the finite element method.*, IEEE Journal Lightwave Technology, Vol. 18, No. 3, pp. 409-415, Mar 2000.
- [25] P. Sewell, J. Wykes, A. Vukovic, D. W. P. Thomas, T.M.Benson, C. Christopoulos *Multi-grid interface in computational electromagnetics*, Elec. Lett. Vol.40 No.3, pp 162-163, 2004.
- [26] Y. Lu, S. Wei, *A new iterative bidirectional beam propagation method*, IEEE Photon. Technol. Lett. 14, 1533-1535 (2002)
- [27] P. Ho and Y. Lu, *A stable bidirectional propagation method based on scattering operators*, IEEE Photon. Technol. Lett. 13, 1316-1318 (2001)
- [28] H. Rao, M. Steal, R. Scarmozzino and R. M. Osgood, *Complex propagator for evanescent waves in bidirectional beam propagation method*, J. Lightwave Technol., Vol. 18, No. 8, (2000)
- [29] S. Chui and Y. Lu, *A propagator- θ beam propagation method*, Photonics Technology Letters, IEEE, Vol. 16(3), pp. 822-824 (2004)
- [30] K.-H. Brenner, *Aspects for calculating local absorption with the rigorous coupled-wave method*, Optics Express, Vol. 18, Issue 10, pp. 10369-10376 (2010)
- [31] K.-H. Brenner and W. Singer, *Light propagation through microlens: a new simulation method* in Applied Optics 32, (1993), 4984-4988
- [32] T. Schuster, *Simulation von Lichtbeugung an Kreuzgitterstrukturen und deren Anwendung in der Scatterometrie*, Dissertation am Institut für technische Optik, Universität Stuttgart, Januar 2010, ISBN 978-3-923560-63-9

- [33] R. Berger, J. Kauffmann, N. Kerwien, W. Osten, H.J. Tiziani, *Rigorse Beugungssimulation: Ein Vergleich zwischen RCWA, FDTD und der Finiten Elemente Methode*, Institut für Technische Optik, Universität Stuttgart, DGaO-Proceedings 105 p.59, 2004
- [34] F. Wyrowski, H. Schimmel, *Elektromagnetisches Optikrechnen - Design zur Lichtformung* in Photonik 3/2007, page 54-57.
- [35] H. Scheffers, *Vereinfachte Ableitung der Formeln für die Fraunhoferschen Beugungserscheinungen*, Physikalisch-Technische Reichsanstalt, Berlin-Charlottenburg, Oktober 1942.
- [36] A. Siegman, *Fresnel reflection and evanescent gain*, Optics and Photonics News, Vol. 21, Issue 1, pp. 38-45 (2010).
- [37] S. Ziolkowski, K.-H. Brenner, "Vectorial analysis and optimisation of ideal focusing lenses", EOS Topical Meeting On Advanced Optical Imaging Techniques, 29.06.-01.07.2005, London, p. 91-92, ISBN 3-00-016360-3 (2005)
- [38] H. Weyl, "Ausbreitung elektromagnetischer Wellen über einem ebenen Leiter", Ann. d. Phys. IV. 60. S. 481. 1919
- [39] N. Fliege, *Systemtheorie*, B.G. Teubner Stuttgart, 1991, ISBN 3-519-06140-6.
- [40] P. Török, P. Varga, *Electromagnetic diffraction of light focused through a planar interface between materials of mismatched refractive indices: an integral representation*, Vol. 12, No. 2, Feb 1995, J. Opt. Soc. Am. A
- [41] S. Csutak, S. Dakshina-Murthy, and J. Campbell, *CMOS-Compatible Planar Silicon Waveguide-Grating-Coupler Photodetectors Fabri-*

- cated on Silicon-on-Insulator (SOI) Substrates*, IEEE Journal of quantum electronics, Vol. 38, No. 5, (2002)
- [42] W.Huang, C. Xu, S. Chu and S. Chaudhuri, *The finite difference vector beam propagation method: analysis and assessment*, J. Lightwave Technology, Vol 10, pp. 295-305, 1992.
- [43] C. Vasallo, *Limitations of the wide-angle beam propagation method in non-uniform systems*, J. Opt. Soc. Am., Vol. 13, pp. 761-770, 1996.
- [44] D. Yevick, *The application of complex Pade approximants to vector field propagation*, IEEE Photon. Technol. Lett., Vol. 12, pp. 1936-1638, 2000.
- [45] Y. Lu and P. Ho, *Beam Propagation Method Using a $[p/(p+1)]$ Pade Approximant of the Propagator*, submitted to IEEE Photon Technol. Lett.
- [46] P. Kaczmarek and P. Lagasse, *Bidirectional beam propagation method*, Electron. Lett., Vol. 24, No. 11, pp. 675-676, May 1988.
- [47] C. Yu and D. Yevick, *Application of the bidirectional parabolic equation method to optical waveguide facets*, J. Opt. Soc. Am. A, Vol. 14, pp. 14488-1450, 1997.
- [48] H. El-Rafaei, I. Betty and D. Yevick, *The application of complex Pade approximants to reflection at optical waveguide facets*, IEEE Photonics Technology Letters, Vol.12, pp. 158-161, 2000.
- [49] H. Rao, R. Scarmozzino and R. Osgood, *A bidirectional beam propagation method for multiple dielectric interfaces*, IEEE Photonics Technology Letters, Vol. 11, No. 7, pp. 830-832, 1999.

- [50] H. El-Refaei, D. Yevick and I. Betty, *Stable and noniterative bidirectional beam propagation method*, IEEE Photonics Technology Letters, Vol. 12, pp. 389-391, 2000.
- [51] H. Rao, M. Steal, R. Scarmozzino and R. Osgood, *Complex propagator for evanescent waves in bidirectional beam propagation method*,
- [52] Joseph W. Goodman, *FOURIER OPTICS*, Third edition, Roberts and Company Publishers, ISBN 0-9747077-2-4, 2004.
- [53] H.-P. Nolting, Reinhard Maerz, *Results of Benchmark Tests for different Numerical BPM Algorithms*, Journal of Lightwave Technology, Vol 13, No. 2, Feb 1995
- [54] A.P. Hibbins, J.R. Sambles and C.R. Lawrence, *Surface plasmon-polariton study of the optical dielectric function of titanium nitride*, Journal of modern optics, Vol 45, No. 10, 2051-2062, 1998
- [55] L. Jozefowski, J. Fuitowski and T. Kawalec, H.-G. Rubahn, *Direct measurement of the evanescent-wave polarization state*, J. Opt. Soc. Am. B/Vol. 24, No. 3/March 2007.
- [56] B. Trauter, *Untersuchungen zum inversen, elektromagnetischen Gitterbeugungsproblem mit Anwendungen in der Gittercharakterisierung*, Dissertation, Department of Optoelectronics, University of Heidelberg, 2009
- [57] D. Guel, J. Palicot, *Analysis and comparison of clipping techniques from OFDM peak-to-average power ration reduction*, Santorini, Greece, Pages: 862-867, 2009, ISBN:978-1-4244-3297-4 DSP 2009, IEEE Press

- [58] J. Van Roey, J. van der Donk, and P. Lagasse, *Beam-propagation method: analysis and assessment*, J. Opt. Soc. Am. 71, 803-810 (1981)
- [59] D. Yevick and D. Thomson, *Complex Pade approximants for wide-angle acoustic propagators*, J. Acoust. Soc. Am., Vol. 108(6), pp. 2784-2790 (2000)
- [60] Mitsubishi Electric Corporation, Public Relations Division, *Mitsubishi Electric develops practical-use multi-crystalline silicon solar cell with world's highest conversion efficiency rate of 18.6%*, No. 2432, Mitsubishi Electric Corporation, Tokyo, March 19, 2008
- [61] Michael Niggemann, Benedikt Bisi, Andreas Gombert, Andreas Hirsch, Harald Hoppe, Philippe Lalanne, Dieter Meissner and Volker Wittwer, *Trapping Light in Organic Plastic Solar Cells with integrated Diffraction Gratings*, Fraunhofer Institute for Solar Energy Systems (ISE), Heidenhofstr.2 , 79110 Freiburg, Germany.
- [62] Bett, A.W.; Dimroth, F.; Guter, W.; Hoheisel, R.; Oliva O.; Philipps, S. M.; Schöne, J., *Highest Efficiency Multi-Junction Solar Cell for Terrestrial and Space Applications*, 24th European Solar Energy Conference and Exhibition, September 2009, Hamburg, Germany
- [63] Aramoto, T. et. al., *16.0% Efficient thin-film CdS/CdTe solar cells*, PV Research and Development Center, Matsushita Battery Industrial Co., Ltd., 1-1 Matsushita-cho, Moriguchi, Osaka 570, JAPON, Japanese journal of applied physics ISSN 0021-4922 CODEN JJAPA5, 1997, vol. 36 (1), no10, pp. 6304-6305
- [64] Ingrid Repins, Miguel A. Contreras, Brian Egaas, Clay DeHart, John Scharf, Craig L. Perkins, Bobby To, Rommel Nouf, *19.9%-efficient*

ZnO/CdS/CuInGaSe₂ solar cell with 81.2% fill factor, Progress in Photovoltaics: Research and Applications. 16, Nr. 3, 2008, S. 235-239

- [65] Jef Poortmans, Vladimir Arkhipov, *Thin Film Solar Cells: Fabrication, Characterization and Applications: Design, Fabrication, Characterization and Applications*, John Wiley & Sons, ISBN-13: 978-0470091265
- [66] Shanalyn A. Kemme, Saleem H. Zaidi and James M. Gee, *Sub-micron Diffractive Gratings for Thin Film Solar Cell Applications*, Technical Reports About PV Cells. Sandia National Laboratories, and University of New Mexico at Albuquerque: Oct 1999 <http://www.sandia.gov/pv/pvc.htm>.
- [67] Saleem H. Zaidi, James M. Gee, and Douglas S. Ruby, *DIFFRACTION GRATING STRUCTURES IN SOLAR CELLS*, IEEE, ISBN 0-7803-5772-8, 2000
- [68] M. Peters, J. C. Goldschmidt, P. Löper and B. Blsi, *PHOTONIC STRUCTURES AND SOLAR CELLS*, Technical report, Fraunhofer Institute for Solar Energy Systems ISE, Heidenhofstr. 2, D-79110 Freiburg, Germany
- [69] Yeonsang Park, Emmanuel Drouard, Ounsi El Daif, Xavier Letartre, Pierre Viktorovitch, Alain Fave, Anne Kaminski, Mustapha Lemiti, Christian Seassal, *Absorption enhancement using photonic crystals for silicon thin film solar cells*, Optical Society of America, 2009
- [70] R.H. Morf, *Diffraction Gratings for Thin Amorphous Silicon Solar Cells*, technical report, Condensed Matter Theory, Paul Scherrer Institute, CH-5232 Villigen, Switzerland

- [71] S.A. Boden, W. Zhang, A Papakostas, A. Potts and D.M. Bagnall, *Nanostructured optical metamaterials*, technical report, Electronics and Computer Science, University of Southampton, Southampton, UK.
- [72] Franz-Josef Haug, Thomas Söderström, Oscar Cubero, Vanessa Terrazoni-Daudrix, Xavier Niquille, Stephanie Perregeaux, and Christophe Ballif, *Periodic textures for enhanced current in thin film silicon solar cells*, technical report, Institute of Microtechnology, University of Neuchatel, Rue A.-L. Breguet 2, Neuchatel, Switzerland
- [73] V.G. Weizer, M.P. Godlewski, *A 25.5 percent AMO Gallium Arsenide Grating Solar Cell*, NASA Technical Memorandum 87134, Nov 1985.
- [74] Christian Haase and Helmut Stiebig, *Thin-film silicon solar cells with diffractive elements*, 10.1117/2.1200602.0150, SPIE 2006.
- [75] Albert Lin and Jamie D. Phillips, *Optimization of Random Diffraction Gratings in Thin-Film Solar Cells Using Genetic Algorithms*, SSEL Annual Report 2007
- [76] Xiaomin Jin, Simeon Trieu, *Improvement of Light Transmission using Photonic Lattices for Solar Cells*, Electrical Engineering Department, California Polytechnic State University, published in OSA, 2008
- [77] Kamaruzzaman Sopian, Nilofar Asim, Nowshad Amin, Saleem H. Zaidi, *Enhancement of Optical Absorption in Thin-Film Silicon Solar Cells in Silicon-On-Insulator (SOI) Configuration*, European Journal of Scientific Research ISSN 1450-216X Vol.24 No.3 (2008), pp.358-364, <http://www.eurojournals.com/ejsr.htm>
- [78] N. Moll, T. Morf, M. Fertig, T. Stoeflerle, B. Trauter, R. Mahr, J. Weiss, T. Pflueger, K.-H. Brenner, *Polarization-Independent Photo-Detectors*

with Enhanced Responsivity in a Standard SOI CMOS Process. in IEEE of Lightwave Technology, (2009).

- [79] M. Auer, K.-H. Brenner, N. Moll, T. Morf, M. Fertig, T. Stoeferle, R.F. Mahrt, J. Weiss, T. Pflueger *Enhancement of Photo-Detector Responsivity in Standard SOI CMOS Processes by introducing Resonant Grating Structures*, EOS Topical Meeting on Diffractive Optics, 14.-18.02.2010, Koli/Finnland, ISBN 978-3-00-024193-2, 2010
- [80] M. Fertig, N. Moll, T. Morf, T. Pflueger, J. Weiss *Photo detector device*, INTERNATIONAL BUSINESS MACHINES CORPORATION, Patent Publication No.: US 2009/0179225 A1
- [81] M. Fertig, T. Morf, J. Weiss, T. Pflueger, N. Moll *Photo detector*, INTERNATIONAL BUSINESS MACHINES CORPORATION, Patent Publication No.: US 20090140362
- [82] M. Fertig, T. Pflueger, T. Morf, N. Moll *Method and apparatus for designing a device for electro-optical modulation of light incident upon the device*, INTERNATIONAL BUSINESS MACHINES CORPORATION, Patent application number: 20100122221
- [83] M. Fertig, T. Pflueger, T. Morf, N. Moll *Using 3d integrated diffractive gratings in solar cells*, INTERNATIONAL BUSINESS MACHINES CORPORATION, USPTO Patent Application, International Application No.: PCT/EP2009/050094
- [84] M. Fertig, K.-H. Brenner, *The vector wave propagation method (VWPM)*, JOSA A, Vol. 27, Issue 4, pp. 709-717 (2010)

Appendices

Appendix A

Fundamentals

A.1 Speed of light

The product $\mu_0\epsilon_0\mu\epsilon$, with $[\epsilon_0] = As/(Vm)$ and $[\mu_0] = Vs/(Am)$, relates to the velocity v [m/s] of the EM wave

$$v^2 = \frac{1}{\mu_0\epsilon_0\mu\epsilon}$$

The speed of light in vacuum c [m/s] is then

$$c = \frac{1}{\sqrt{\mu_0\epsilon_0}}$$

$\epsilon_0 = 1/36 \cdot \pi \cdot 10^{-19}$ and $\mu_0 = 4\pi \cdot 10^{-7}$. The speed of light in a medium with a refractive index n is

$$v^2 = \left(\frac{c}{n}\right)^2$$

A.2 Transversality

With equation 2.29, the identical result is obtained for the magnetic field \mathbf{H} and the vectors wave equations are then

$$\begin{aligned}\mathbf{E} &= \hat{\mathbf{E}}_0 e^{i(\mathbf{k}\cdot\mathbf{r}-\omega t)} \\ \mathbf{H} &= \hat{\mathbf{H}}_0 e^{i(\mathbf{k}\cdot\mathbf{r}-\omega t)}\end{aligned}$$

With these expressions, the rotation on the left side of the third (eq. 2.3) and fourth (eq. 2.4) Maxwell equation transforms to

$$\begin{aligned}(\nabla \times \mathbf{E})_x &= \frac{\partial E_z}{\partial y} - \frac{\partial E_y}{\partial z} = (\mathbf{k} \times \mathbf{E})_x \\ (\nabla \times \mathbf{E})_y &= -\left(\frac{\partial E_z}{\partial x} - \frac{\partial E_x}{\partial z}\right) = (\mathbf{k} \times \mathbf{E})_y \\ (\nabla \times \mathbf{E})_z &= \frac{\partial E_y}{\partial x} - \frac{\partial E_x}{\partial y} = (\mathbf{k} \times \mathbf{E})_z\end{aligned}$$

and

$$\begin{aligned}(\nabla \times \mathbf{H})_x &= \frac{\partial H_z}{\partial y} - \frac{\partial H_y}{\partial z} = (\mathbf{k} \times \mathbf{H})_x \\ (\nabla \times \mathbf{H})_y &= \frac{\partial H_z}{\partial x} - \frac{\partial H_x}{\partial z} = (\mathbf{k} \times \mathbf{H})_y \\ (\nabla \times \mathbf{H})_z &= \frac{\partial H_y}{\partial x} - \frac{\partial H_x}{\partial y} = (\mathbf{k} \times \mathbf{H})_z\end{aligned}$$

Assuming a time independent ϵ and μ and $\mathbf{J}_c = 0$ the equations transform to

$$\begin{aligned}\mathbf{k} \times \mathbf{E} &= -\mu_0 \mu \omega \mathbf{H} \\ \mathbf{k} \times \mathbf{H} &= -\epsilon_0 \epsilon \omega \mathbf{E}\end{aligned}$$

With a division by $|bfk| = nk_0$, the expression transforms to

$$\begin{aligned}\mathbf{s} \times \mathbf{E} &= -\mu_0 \mu v \mathbf{H} \\ \mathbf{s} \times \mathbf{H} &= -\epsilon_0 \epsilon v \mathbf{E}\end{aligned}$$

using $v = \omega/k$ and with $c/n = 1/\sqrt{\epsilon_0\epsilon\mu_0\mu}$ yield

$$\mathbf{E} = -\sqrt{\frac{\mu}{\epsilon}} \mathbf{s} \times \mathbf{H}$$

$$\mathbf{H} = -\sqrt{\frac{\epsilon}{\mu}} \mathbf{s} \times \mathbf{E}$$

and with a scalar multiplication with \mathbf{s}

$$\mathbf{E} \cdot \mathbf{s} = \mathbf{H} \cdot \mathbf{s} = 0$$

the transversality of the field is shown. The components \mathbf{E} , \mathbf{H} and \mathbf{k} span an orthogonal Cartesian coordinate system.

A.3 Discrete spatial derivatives

The space derivatives ϵ_x and ϵ_y , with $\epsilon = n^2$ are derived from the symmetric average

$$\epsilon_x(m\delta x, n\delta y) = \frac{n^2((m+1)\delta x, n\delta y) - n^2((m-1)\delta x, n\delta y)}{2\delta x}$$

$$\epsilon_y(m\delta x, n\delta y) = \frac{n^2(m\delta x, (n+1)\delta y) - n^2(m\delta x, (n-1)\delta y)}{2\delta y}$$

A.4 Absorption coefficient

The absorption coefficient $\alpha = 2\kappa k_0$, with $k_0 = 2\pi/\lambda$ is the propagation constant in vacuum, is derived from the irradiance $I \approx \mathbf{E}\mathbf{E}^*$ and the complex refractive index $\hat{n} = n + i\kappa$ according to

$$\begin{aligned}
 |\mathbf{E}(\delta z)|^2 &= \hat{\mathbf{E}}_0 \hat{\mathbf{E}}_0^* e^{i2\hat{n}k_0\delta z} \\
 &= \hat{\mathbf{E}}_0 \hat{\mathbf{E}}_0^* e^{i2(n+i\kappa)k_0\delta z} \\
 &= \hat{\mathbf{E}}_0 \hat{\mathbf{E}}_0^* e^{i(2nk_0+i2\kappa k_0)\delta z} \\
 &= \hat{\mathbf{E}}_0 \hat{\mathbf{E}}_0^* e^{-2\kappa k_0\delta z} e^{i2nk_0\delta z} \\
 &= \hat{\mathbf{E}}_0 \hat{\mathbf{E}}_0^* e^{-\alpha\delta z} e^{i2k\delta z}
 \end{aligned}$$

A.5 Evanescent modes

A discrete mode $(k_x, k_y) = (p\delta k_x, q\delta k_y)$, with $p \in \{0, \dots, n_x - 1\}$ and $q \in \{0, \dots, n_y - 1\}$ is called *evanescent* if

$$\begin{aligned}
 0 &> (nk_0)^2 - (k_x^2 + k_y^2) = k^2 - k_\perp^2 \\
 \Leftrightarrow k_\perp^2 &> (nk_0)^2 \\
 \Leftrightarrow ((p\delta k_x)^2 + (q\delta k_y)^2) &> (nk_0)^2 \\
 \Leftrightarrow 4\pi^2(p^2/X^2 + q^2/Y^2) &> 4\pi^2(n/\lambda)^2 \\
 \Leftrightarrow p^2/X^2 + q^2/Y^2 &> (n/\lambda)^2 \\
 \Leftrightarrow_{X=Y} p^2 + q^2 &> (n/\lambda X)^2
 \end{aligned}$$

The evanescent radius of a square aperture is then Xn/λ , with n is the real part of the complex refractive index $\hat{n} = n + i\kappa$.

A.6 Snell's law

Snell's law can be derived from the continuity of the tangential component k_{\perp} of the incident (subscript 'e') and transmitted (subscript 't') propagation vector \mathbf{k} according to

$$\begin{aligned} k_{\perp,e} &= k_{\perp,t} \\ \Leftrightarrow k_e \sin \theta_i &= k_t \sin \theta_t \\ \Leftrightarrow n_e k_0 \cdot \sin \theta_i &= n_t k_0 \cdot \sin \theta_t \\ \Leftrightarrow n_e \cdot \sin \theta_i &= n_t \cdot \sin \theta_t \end{aligned}$$

A.7 Total internal reflection

In case of $n_i < n_t$ the critical angle of total internal reflection (TIR) θ_c is derived from Snell's law according to

$$\begin{aligned} n_i \sin \theta_i &= n_t \sin \theta_t \\ \Leftrightarrow n_i \sin \theta_i &= n_t \\ \Leftrightarrow \sin \theta_c &= \frac{n_t}{n_i} \end{aligned}$$

with $\theta_t = \pi/2$.

This assumption yields the evanescent modes

$$\begin{aligned}
0 &> (n_t k_0)^2 - (k_x^2 + k_y^2) = k^2 - k_{\perp}^2 \\
\Leftrightarrow 0 &> 1 - (k_x^2 + k_y^2)/(n_t k_0)^2 \\
\Leftrightarrow (k_x^2 + k_y^2)/(n_t k_0)^2 &> 1 \\
\Leftrightarrow ((\sin \theta_t \cos \phi)^2 + (\sin \theta_t \sin \phi)^2) &> 1 \\
\Leftrightarrow \sin^2 \theta_t (\cos^2 \phi + \sin^2 \phi) &> 1 \\
\Leftrightarrow \sin^2 \theta_t &> 1 \\
\Leftrightarrow \sin \theta_t &> 1
\end{aligned}$$

with $\theta_t = \sin^{-1}(n_e/n_t \sin \theta_e)$ is the angle of transmission and ϕ is the yaw angle of the electromagnetic wave.

A.8 Fresnel coefficients for evanescent waves

The amplitude of a wave is derived from the conservation law $(1 - r) = t$ according to

$$\begin{aligned}
k_{z,t} t &= k_{z,e} (1 - r) \\
\Leftrightarrow k_{z,t} t &= k_{z,e} - r k_{z,e} \\
\Leftrightarrow k_{z,t} t &= k_{z,e} - (t - 1) k_{z,e} \\
\Leftrightarrow k_{z,t} t &= k_{z,e} - t k_{z,e} + k_{z,e} \\
\Leftrightarrow k_{z,t} t + k_{z,e} t &= k_{z,e} + k_{z,e} \\
\Leftrightarrow t (k_{z,t} + k_{z,e}) &= 2 k_{z,e} \\
\Leftrightarrow t &= \frac{2 k_{z,e}}{(k_{z,t} + k_{z,e})}
\end{aligned}$$

with $\hat{k}_{z,e} = \sqrt{(nk_0)^2 - k_{\perp}^2} + i0$ and $\hat{k}_{z,t} = 0 + i\sqrt{k_{\perp}^2 - (nk_0)^2}$ (i.e. an evanescent wave). The amplitude of the reflected wave is then

$$r = \frac{\hat{k}_{z,e} - \hat{k}_{z,t}}{\hat{k}_{z,e} + \hat{k}_{z,t}}$$

derived from the substitution $r = t - 1$.

A.9 Energy flux in evanescent waves

The z-component of the propagation vector of an evanescent wave is purely imaginary

$$\cos \theta_t = i\sqrt{1 - k_{\perp}^2/(n_t k_0)^2}$$

because $k_{\perp}^2/(n_t k_0)^2 > 1$ for evanescent modes. In the two-dimensional xz-case this transforms to

$$\begin{aligned} \cos \theta_t &= \sqrt{1 - k_x^2/k_t^2} \\ &= \sqrt{1 - \sin^2 \theta_t} \\ &= \sqrt{1 - n_e^2/n_t^2 \sin^2 \theta_i} \\ &= \sqrt{1 - \sin^2 \theta_i/\sin^2 \theta_c} \end{aligned}$$

according to Snell's law with θ_c is the critical angular of total internal reflection.

Hence, for all angles θ_i greater than θ_c an evanescent mode is obtained due to the negative argument in the square root. Then, the z-component of the propagation vector $k_{z,t} = n_t k_0 \cos \theta_t = n_t k_0 \sqrt{1 - \sin^2 \theta_i/\sin^2 \theta_c}$ is a

purely complex quantity which yields a purely complex cosines $\cos \theta_t = i\sqrt{1 - k_{\perp}^2 / (n_t k_0)^2}$. The purely complex cosines is now applied to a three-dimensional vector wave, **propagating in the z -direction**, which is composed from forward (+) and backward (-) propagating TE- and a TM-components of the E-field

$$\begin{aligned} \mathbf{E}(\mathbf{r}) &= \mathbf{E}_{TM}(\mathbf{r}) + \mathbf{E}_{TE}(\mathbf{r}) \\ &= (\mathbf{e}_x \cos \theta_t - \mathbf{e}_z \sin \theta_t) E_{0,TM}^+ e^{i\mathbf{k}^+ \cdot \mathbf{r}} + \\ &\quad (\mathbf{e}_x \cos \theta_t + \mathbf{e}_z \sin \theta_t) E_{0,TM}^- e^{i\mathbf{k}^- \cdot \mathbf{r}} + \\ &\quad \mathbf{e}_y (E_{0,TE}^+ e^{i\mathbf{k}^+ \cdot \mathbf{r}} + E_{0,TE}^- e^{i\mathbf{k}^- \cdot \mathbf{r}}) \end{aligned}$$

and H-field

$$\begin{aligned} \tilde{\mathbf{H}}(\mathbf{r}) &= \sqrt{\epsilon/\mu} \mathbf{e}_y (E_{0,TE}^+ e^{i\mathbf{k}^+ \cdot \mathbf{r}} + E_{0,TE}^- e^{i\mathbf{k}^- \cdot \mathbf{r}}) + \\ &\quad \sqrt{\epsilon/\mu} [(\mathbf{e}_x \cos \theta_t - \mathbf{e}_z \sin \theta_t) E_{0,TM}^- e^{i\mathbf{k}^- \cdot \mathbf{r}} - \\ &\quad (\mathbf{e}_x \cos \theta_t + \mathbf{e}_z \sin \theta_t) E_{0,TM}^+ e^{i\mathbf{k}^+ \cdot \mathbf{r}}] \end{aligned}$$

The energy flux across the interface is calculated according to $\int S d\mathbf{A}$ with $d\mathbf{A}$ is $\mathbf{n} \delta A$ and $\delta A = \delta x \delta y$ is the area element. \mathbf{n} is the surface normal and \mathbf{S} is the Poynting vector. Since the wave propagates along the z -axis, the flux at location \mathbf{r}_{\perp} is

$$P(\mathbf{r}_{\perp}) = \mathbf{S}_z(\mathbf{r}_{\perp}) \delta x \delta y = (E_x(\mathbf{r}_{\perp}) H_y(\mathbf{r}_{\perp})^* - E_y(\mathbf{r}_{\perp}) H_x(\mathbf{r}_{\perp})^*) \delta x \delta y$$

with S_z is the z -component of the Poynting vector, which is gained from the scalar multiplication of \mathbf{S} with $\mathbf{n} = \mathbf{e}_z$. The energy flux for evanescent waves is zero in average due to purely imaginary cosines terms and the phase shift of $\pm\pi/2$ between $E_x = \cos \theta_t (E_{0,TM}^+ e^{i\mathbf{k}^+ \cdot \mathbf{r}} + E_{0,TM}^- e^{i\mathbf{k}^- \cdot \mathbf{r}})$ and $H_y^* = E_{0,TE}^+ e^{i\mathbf{k}^+ \cdot \mathbf{r}} + E_{0,TE}^- e^{i\mathbf{k}^- \cdot \mathbf{r}}$ as well as $E_y = E_{0,TE}^+ e^{i\mathbf{k}^+ \cdot \mathbf{r}} + E_{0,TE}^- e^{i\mathbf{k}^- \cdot \mathbf{r}}$ and $H_x^* = \sqrt{\epsilon/\mu} \cos \theta_t (E_{0,TM}^- e^{i\mathbf{k}^- \cdot \mathbf{r}} - E_{0,TM}^+ e^{i\mathbf{k}^+ \cdot \mathbf{r}})$.

Appendix B

Vector wave propagation method

B.1 Complex Fresnel coefficients of transmission

With the conservation law $t = 1 + r$, the Fresnel amplitude coefficients can be derived and then transformed to an expression which shows the dependency to the surface normal \mathbf{n} and the propagation vector \mathbf{k}

$$\begin{aligned} t_{TE}(\mathbf{k}_\perp, \mathbf{r}_\perp) &= \frac{2n_e \cos \theta_e}{n_e \cos \theta_e + n_t \cos \theta_t} \\ &= \frac{2n_e k_0 \cos \theta_e}{n_e k_0 \cos \theta_e + n_t k_0 \cos \theta_t} \\ &= \frac{2\mathbf{n} \cdot \mathbf{k}_e}{\mathbf{n} \cdot \mathbf{k}_e + \mathbf{n} \cdot \mathbf{k}_t} \\ &= \frac{2k_{z,e}}{k_{z,e} + k_{z,t}} \end{aligned}$$

with n_e is the refractive index before and n_t is the refractive index behind a longitudinal interface along the axis of propagation. θ_e is the angle of incidence and θ_t the angle of transmission. For lossy or gaining medium, the refractive index $\hat{n}_t = n_t + i\kappa_t$ is complex and by consideration of a complex $\hat{k}_z = k_z + i\gamma_z$, a complex transmission coefficient for the TE-component of the field is obtained

$$\hat{t}_{TE}(\mathbf{k}_\perp, \mathbf{r}_\perp) = \frac{2\hat{k}_{z,e}}{\hat{k}_{z,e} + \hat{k}_{z,t}}$$

with $k_{z,t}^2 = n^2 k_0^2 - (k_x^2 + k_y^2)$. In case of a positive sign in the square root of $k_{z,t}$, *Fresnel transmission* is obtained. A negative sign yields *Lenserf transmission* as discussed in [36].

The real-valued Fresnel coefficient of transmission for the TM-component is

$$\begin{aligned} t_{TM}(\mathbf{k}_\perp, \mathbf{r}_\perp) &= \frac{2n_e \cos \theta_e}{n_e \cos \theta_t + n_t \cos \theta_e} \\ &= \frac{2n_e n_t \mathbf{n} \cdot \mathbf{k}_e}{n_t^2 \mathbf{n} \cdot \mathbf{k}_e + n_e^2 \mathbf{n} \cdot \mathbf{k}_t} \\ &= \frac{2n_e n_t k_{z,e}}{n_e^2 k_{z,t} + n_t^2 k_{z,e}} \end{aligned}$$

and then transforms to the complex Fresnel coefficient

$$\hat{t}_{TM} = \frac{2\hat{n}_e \hat{n}_t \hat{k}_{z,e}}{\hat{n}_t^2 \hat{k}_{z,e} + \hat{n}_e^2 \hat{k}_{z,t}}$$

in case of a lossy or gaining medium and including the range of k for evanescent waves. The complex treatment of the Fresnel coefficients yields an interesting detail. In case of a lossy or gaining medium (i.e. $\kappa \neq 0$), the refractive index always introduces a phase shift because $\kappa/n \neq 0$. This is the reasoning for the so called *Goos-Hänchen Shift*.

B.2 Transfer matrix of transmission

Using the complex quantities in the transformations in chapter 3 and 5, the propagation for the entire range of spatial frequencies can be calculated. Then, evanescent modes are treated like propagating modes. Inserting the unity vectors of the TE- and TM-component in equation 3.20 to 3.22 and **using the complex refractive index and the complex propagation vector**, equation 3.19 is expressed by

$$\begin{aligned}
 \tilde{E}_{TE,e} &= \tilde{\mathbf{E}}(\mathbf{k}_\perp) \cdot \mathbf{e}_{TE} \\
 &= \begin{pmatrix} \tilde{E}_x \\ \tilde{E}_y \\ \tilde{E}_z \end{pmatrix} \cdot \frac{1}{k_\perp} \begin{pmatrix} -k_y \\ k_x \\ 0 \end{pmatrix} \\
 &= \frac{1}{k_\perp} (\tilde{E}_y k_x - \tilde{E}_x k_y) \\
 \tilde{E}_{TM,e} &= \tilde{\mathbf{E}}(\mathbf{k}_\perp) \cdot \mathbf{e}_{TM,e} \\
 &= \begin{pmatrix} \tilde{E}_x \\ \tilde{E}_y \\ \tilde{E}_z \end{pmatrix} \cdot \frac{1}{k_e k_\perp} \begin{pmatrix} k_x \hat{k}_{z,e} \\ k_x \hat{k}_{z,e} \\ -k_\perp^2 \end{pmatrix} \\
 &= \frac{1}{k_\perp k_e} (\tilde{E}_x k_x \hat{k}_{z,e} + \tilde{E}_y k_y \hat{k}_{z,e} - \tilde{E}_z k_\perp^2)
 \end{aligned}$$

Eliminating the z -component with the *transversality condition* then gives

$$E_{TM,e} = \frac{1}{k_\perp k_e \hat{k}_{z,e}} \left(\tilde{E}_x (k_x k_{z,e}^2 + k'_x k_\perp^2) + \tilde{E}_y (k_y k_{z,e}^2 + k'_y k_\perp^2) \right)$$

and by inserting the terms into equation 3.17 the expression transforms to

$$\begin{aligned} \tilde{\mathbf{E}}_t(\mathbf{k}_\perp, \mathbf{r}_\perp) &= \frac{\tilde{E}_x}{k_\perp^2} \left(\frac{\hat{t}_{TM}}{\hat{k}_e \hat{k}_t \hat{k}_{z,e}} (k_x \hat{k}_{z,e}^2 + k'_x k_\perp^2) \begin{pmatrix} k_x \hat{k}_{z,t} \\ k_y \hat{k}_{z,t} \\ -k_\perp^2 \end{pmatrix} - \hat{t}_{TE} k_y \begin{pmatrix} -k_y \\ k_x \\ 0 \end{pmatrix} \right) + \\ &\frac{\tilde{E}_y}{k_\perp^2} \left(\frac{\hat{t}_{TM}}{\hat{k}_e \hat{k}_t \hat{k}_{z,e}} (k_y \hat{k}_{z,e}^2 + k'_y k_\perp^2) \begin{pmatrix} k_x \hat{k}_{z,t} \\ k_y \hat{k}_{z,t} \\ -k_\perp^2 \end{pmatrix} + \hat{t}_{TE} k_x \begin{pmatrix} -k_y \\ k_x \\ 0 \end{pmatrix} \right) \end{aligned}$$

This expression depends on the transversal components of the electrical field vector. Inserting expressions for k'_x and k'_y (eq. 3.16) and reordering by the transversal components \tilde{E}_x and \tilde{E}_y , the complex 3x3 *transfer matrix of transmission* \mathbf{M} is

$$\hat{\mathbf{M}}^{(3)}(\mathbf{k}_\perp, \mathbf{r}_\perp) = \frac{1}{k_\perp^2} \begin{pmatrix} k_y^2 \hat{t}_{TE} + k_x^2 \hat{t}'_{TM} (1 - i\hat{\epsilon}_{x,e}) & k_x k_y (\hat{t}'_{TM} (1 - i\hat{\epsilon}_{y,e}) - \hat{t}_{TE}) \\ k_x k_y (\hat{t}'_{TM} (1 - i\hat{\epsilon}_{x,e}) - \hat{t}_{TE}) & k_x^2 \hat{t}_{TE} + k_y^2 \hat{t}'_{TM} (1 - i\hat{\epsilon}_{y,e}) \\ -\hat{t}'_{TM} k_x (1 - i\hat{\epsilon}_{e,x}) k_\perp^2 / \hat{k}_{z,t} & -\hat{t}'_{TM} k_y (1 - i\hat{\epsilon}_{e,y}) k_\perp^2 / \hat{k}_{z,t} \end{pmatrix}$$

with

$$\begin{aligned} \hat{\epsilon}_{x,t} &= f_t \frac{\epsilon_{x,t}}{k_x}, \quad \hat{\epsilon}_{y,t} = f_t \frac{\epsilon_{y,t}}{k_y} \\ f_t &= \left(\frac{k_\perp}{n_t k_t} \right)^2, \quad k_t = n_t k_0 \end{aligned}$$

and

$$\hat{t}'_{TM} = \frac{\hat{n}_e \hat{k}_{z,t}}{\hat{n}_t \hat{k}_{z,e}} \hat{t}_{TM}$$

The VWPM utilizes the 2x2 sub-matrix and derives the z-component after the propagation step. With the definition of \hat{t}_{TM} , equation 3.26 simplifies to

$$\hat{t}_{TM} = \frac{2\hat{n}_e^2 \hat{k}_{z,t}}{\hat{n}_t^2 \hat{k}_{z,e} + \hat{n}_e^2 \hat{k}_{z,t}}$$

In case of vertical incidence (i.e. $k_{\perp} = 0$), the transfer matrix is singular and the transfer is obtained from the diagonal matrix

$$\hat{\mathbf{M}}(0, \mathbf{r}_{\perp}) = \begin{pmatrix} \hat{t}(\mathbf{r}_{\perp}) & 0 \\ 0 & \hat{t}(\mathbf{r}_{\perp}) \end{pmatrix}$$

with $\hat{t}(\mathbf{r}_{\perp}) = \hat{t}_{TE}(\mathbf{r}_{\perp}, \mathbf{k}_{\perp} = 0) = \hat{t}_{TM}(\mathbf{r}_{\perp}, \mathbf{k}_{\perp} = 0)$ is the space-dependent complex Fresnel transmission coefficient for vertical incidence.

B.3 Magnetic vector

For plane waves, the magnetic vector \mathbf{H} is derived from the electric vector \mathbf{E} from equation 2.40 on page 34 according to

$$\begin{aligned} \mathbf{H} &= q(\mathbf{s} \times \mathbf{E}) \\ &= q/k \begin{pmatrix} k_y E_z - k_z E_y \\ -(k_x E_z - k_z E_x) \\ k_x E_y - k_y E_x \end{pmatrix} \end{aligned}$$

with $q = \sqrt{\epsilon_0 \epsilon / \mu_0 \mu} = n / \mu / Z_0$ and $k = nk_0$. A substitution of E_z with the expression in equation 3.16 yields

$$\begin{aligned} \mathbf{H} &= q/k \begin{pmatrix} k_y/k_z(E_x k'_x + E_y k'_y) - k_z E_y \\ -(k_x/k_z(E_x k'_x + E_y k'_y) - k_z E_x) \\ k_x E_y - k_y E_x \end{pmatrix} \\ &= q/k/k_z \begin{pmatrix} -k_y k'_x & -(k_y k'_y + k_z^2) \\ (k_x k'_x + k_z^2) & k_x k'_y \\ -k_y k_z & k_x k_z \end{pmatrix} \cdot \mathbf{E}^{(2)} \end{aligned}$$

which is equal to the matrix \mathbf{T} in equation 3.40.

B.4 Energy Flux

On complex fields \mathbf{E} and \mathbf{H} , the time average of the Poynting vector $\langle \mathbf{S} \rangle_T$ is derived according to

$$\langle \mathbf{S} \rangle_T = \frac{1}{2} \text{Re} \{ \mathbf{E} \times \mathbf{H}^* \} \quad [J/s/m^2 = W/m^2]$$

and the energy flux through an aperture A in is then

$$P = \int_A \langle \mathbf{S} \rangle_T d^2 \mathbf{A} \quad [W]$$

With the definition of $\langle \mathbf{S} \rangle_T$ and $d^2 \mathbf{A} = \mathbf{n} d^2 \mathbf{r}_\perp = \mathbf{e}_z d^2 \mathbf{r}_\perp$, with \mathbf{e}_z is the surface normal and with $\hat{\mu} = \mu + i0$ and $\hat{k}_z = k_z + i0$, the energy flux of plane waves per area is then

$$\begin{aligned} \frac{\partial P}{\partial A} &= \langle \mathbf{S} \rangle_T \cdot \mathbf{e}_z \\ &= \langle 0S_x + 0S_y + 1S_z \rangle_T \\ &= \frac{1}{2} \text{Re} \{ E_x H_y^* - E_y H_x^* \} \\ &= \frac{1}{2\mu Z_0 k_z k_0} \text{Re} \{ E_x [E_x^*(k_x^2 + k_z^2) + E_y^*(k_x k_y)] + E_y [E_x^*(k_x k_y) + E_y^*(k_y^2 + k_z^2)] \} \\ &= \frac{1}{2\mu Z_0 k_z k_0} \text{Re} \{ k_z^2 (E_x E_x^* + E_y E_y^*) + k_x^2 (E_x E_x^*) + 2k_x k_y (E_x E_y^*) + k_y^2 (E_y E_y^*) \} \\ &= \frac{1}{2\mu Z_0 k_z k_0} \text{Re} \{ k_z^2 (E_x E_x^* + E_y E_y^*) + (k_x E_x + k_y E_y^*)^2 \} \\ &= \frac{1}{2\mu Z_0 k_z k_0} \text{Re} \{ k_z^2 (E_x E_x^* + E_y E_y^*) + k_z^2 (E_z E_z^*) \} \\ &= \frac{1}{2\mu Z_0 k_0} k_z \mathbf{E} \mathbf{E}^* \\ &= \frac{1}{2\mu Z_0 k_0} k_z |\mathbf{E}|^2 \quad [W/m^2] \end{aligned}$$

with $Z_0 = 376.82 [\Omega]$ is the impedance of the vacuum.

B.5 Fresnel coefficients of reflection

The complex Fresnel coefficients or reflection for the TE-component \hat{r}_{TE} and the TM-component \hat{r}_{TM} are derived from the surface normal \mathbf{n} and the propagation vector \mathbf{k} according to

$$\begin{aligned}\hat{r}_{TE}(\mathbf{k}_\perp, \mathbf{r}_\perp) &= \frac{\mathbf{n} \cdot \mathbf{k}_e - \mathbf{n} \cdot \mathbf{k}_t}{\mathbf{n} \cdot \mathbf{k}_e + \mathbf{n} \cdot \mathbf{k}_t} \\ \hat{r}_{TM}(\mathbf{k}_\perp, \mathbf{r}_\perp) &= \frac{\hat{n}_t^2 \mathbf{n} \cdot \mathbf{k}_e - \hat{n}_e^2 \mathbf{n} \cdot \mathbf{k}_t}{\hat{n}_t^2 \mathbf{n} \cdot \mathbf{k}_e + \hat{n}_e^2 \mathbf{n} \cdot \mathbf{k}_t}\end{aligned}$$

With the surface normal \mathbf{n} and $\mathbf{n} \cdot \mathbf{k} = k_z = |\mathbf{n}||\mathbf{k}| \cos \theta$, $|\mathbf{n}| = 1$ and $|\mathbf{k}| = nk_0$, the well known formulation from equation 2.68 can be obtained from a division by k_0 . Another formulation which depends on the the complex z -component of the propagation vector $\hat{k}_z = nk_0 \cos \theta$ is

$$\begin{aligned}\hat{r}_{TE}(\mathbf{k}_\perp, \mathbf{r}_\perp) &= \frac{\hat{k}_{z,e} - \hat{k}_{z,t}}{\hat{k}_{z,e} + \hat{k}_{z,t}} \\ \hat{r}_{TM}(\mathbf{k}_\perp, \mathbf{r}_\perp) &= \frac{\hat{n}_t^2 \hat{k}_{z,e} - \hat{n}_e^2 \hat{k}_{z,t}}{\hat{n}_t^2 \hat{k}_{z,e} + \hat{n}_e^2 \hat{k}_{z,t}}\end{aligned}$$

with $\hat{n}_t = n_t + i\kappa_t$ and a complex $\hat{k}_{z,t} = \sqrt{(n_t k_0)^2 - (k_x^2 + k_y^2)}$ which is also defined for negative arguments in the square root. Again, in case of a gaining or absorbing medium, a positive sign for $\hat{k}_{z,t}$ yields the laws of Fresnel transmission and reflection and with a negative sign Lensef transmission and reflection is obtained. In the latter case all observations on gain and decay of waves are reverted as shown in [36].

B.6 Transfer matrix of reflection

The transfer matrix of reflection is calculated from equation 5.16 on page 99. The subscript e indicates the incident layer and the subscript t indicates the transmitted layer. The vectors of unity for the TE- and TM-component are taken from 3.20 and 3.21 on page 61 and the z-component of the electric field is substituted by equation 3.16. The scalar TE- and TM-components are then equal to the transmitted, which are introduced above. Eliminating the z -component in the scalar TM-component gives

$$E_{TM,e} = \frac{1}{k_{\perp} \hat{k}_e \hat{k}_{z,e}} \left(\tilde{E}_x \left(k_x \hat{k}_{z,e}^2 + k'_x k_{\perp}^2 \right) + \tilde{E}_y \left(k_y \hat{k}_{z,e}^2 + k'_y k_{\perp}^2 \right) \right)$$

and inserting the terms into equation 5.16 yields

$$\begin{aligned} \tilde{\mathbf{E}}_e^- &= \frac{\hat{r}_{TE}}{k_{\perp}^2} \left(\tilde{E}_y k_x - \tilde{E}_x k_y \right) \begin{pmatrix} -k_y \\ k_x \\ 0 \end{pmatrix} + \frac{\hat{r}_{TM}}{k_e^2 k_{\perp}^2} \\ &\quad \left(\tilde{E}_x k_x \hat{k}_{z,e} + \tilde{E}_y k_y \hat{k}_{z,e} + k_{\perp}^2 \frac{\tilde{E}_x k'_x + \tilde{E}_y k'_y}{\hat{k}_{z,e}} \right) \begin{pmatrix} k_x \hat{k}_{z,e} \\ k_y \hat{k}_{z,e} \\ -k_{\perp}^2 \end{pmatrix} \end{aligned}$$

Reordering the expression by the x- and y-component of $\tilde{\mathbf{E}}_e$ yields the complex transfer matrix of reflection $\hat{\mathbf{R}}$

$$\begin{aligned} \tilde{\mathbf{E}}_e^- &= \hat{\mathbf{R}} \cdot \tilde{\mathbf{E}}_e^{(2)} \\ &= \frac{1}{k_{\perp}^2} \begin{pmatrix} \hat{r}_{TE} k_y^2 + \hat{r}_{TM} k_x^2 (1 - i\hat{\epsilon}_x) & (\hat{r}_{TM} (1 - \hat{\epsilon}_y) - \hat{r}_{TE}) k_x k_y \\ (\hat{r}_{TM} (1 - \hat{\epsilon}_x) - \hat{r}_{TE}) k_x k_y & \hat{r}_{TE} k_x^2 + \hat{r}_{TM} k_y^2 (1 - i\hat{\epsilon}_y) \\ -\hat{r}_{TM} k_x (1 - i\hat{\epsilon}_x) k_{\perp}^2 / \hat{k}_{z,e} & -\hat{r}_{TM} k_y (1 - i\hat{\epsilon}_y) k_{\perp}^2 / \hat{k}_{z,e} \end{pmatrix} \cdot \tilde{\mathbf{E}}_e^{(2)} \end{aligned}$$

with $\mathbf{E}^{(2)}$ is the transversal subvector of \mathbf{E} and $\hat{\epsilon}_x = \epsilon_x k_{\perp}^2 / \epsilon / k_e^2 / k_x$, $\hat{\epsilon}_y = \epsilon_y k_{\perp}^2 / \epsilon / k_e^2 / k_y$, $k'_x = k_x - i\epsilon_x / \epsilon$, $k'_y = k_y - i\epsilon_y / \epsilon$ and $\epsilon_x = \partial\epsilon / \partial x$, $\epsilon_y = \partial\epsilon / \partial y$ are the space derivatives of $\epsilon(\mathbf{r}_{\perp})$ (i.e. the x- and y-component of $\text{grad}(\epsilon)$). This is the transfer matrix of reflection as shown in equation 5.20 on page 100.

B.7 Energy flux of a TE-polarized wave in homogeneous medium

Let a TE-polarized wave be assigned to the y-component E_y of the electric field due to the definition of the coordinate system. Then, $k_y = 0$ and the energy flux per area is

$$\begin{aligned}
\frac{\partial P_{TE}(\mathbf{r}_\perp, \mathbf{k}_\perp)}{\partial A} &= \frac{1}{2} \text{Re} \left\{ \mathbf{E} \times \left(\frac{1}{\hat{\mu} Z_0 k_0} (\mathbf{k} \times \mathbf{E}) \right)^* \right\} \cdot \mathbf{n} \\
&= \frac{1}{2} \text{Re} \left\{ \begin{pmatrix} E_x \\ E_y \\ E_z \end{pmatrix} \times \left(\frac{1}{\hat{\mu} k_0 Z_0} \left(\begin{pmatrix} k_x \\ k_y \\ \hat{k}_z \end{pmatrix} \times \begin{pmatrix} E_x \\ E_y \\ E_z \end{pmatrix} \right) \right)^* \right\} \cdot \mathbf{n} \\
&= \frac{1}{2 Z_0 k_0} \text{Re} \left\{ \begin{pmatrix} 0 \\ E_y \\ 0 \end{pmatrix} \times \left(\frac{1}{\hat{\mu}} \begin{pmatrix} -\hat{k}_z E_y \\ 0 \\ k_x E_y \end{pmatrix} \right)^* \right\} \cdot \mathbf{n} \\
&= \frac{1}{2 k_0 Z_0} (E_y E_y^*) \text{Re} \left\{ \frac{\hat{k}_z^*}{\hat{\mu}^*} \right\}
\end{aligned}$$

with $\mathbf{n} = (0 \ 0 \ 1)^T$, $\hat{k}_z = k_z + i\gamma_z$, a complex $\hat{\mu}$ and by setting $E_x = E_z = 0$. For perpendicular incidence $\hat{k}_z = \hat{n} k_0$ and then

$$\frac{\partial P_{TE}(\mathbf{r}_\perp, 0)}{\partial A} = \frac{1}{2 Z_0} (E_y E_y^*) \text{Re} \left\{ \frac{\hat{n}^*}{\hat{\mu}^*} \right\}$$

B.8 Energy flux of a TM-polarized wave in homogeneous medium

Let a TM-polarized wave be assigned to the E_x - and E_z -component of \mathbf{E} due to the definition of the coordinate system. Then, $k_y = 0$ and the energy flux is

$$\begin{aligned}
 \frac{\partial P_{TM}(\mathbf{r}_\perp, \mathbf{k}_\perp)}{\partial A} &= \frac{1}{2} \text{Re} \left\{ \mathbf{E} \times \left(\frac{1}{\hat{\mu} Z_0 k_0} (\mathbf{k} \times \mathbf{E}) \right)^* \right\} \cdot \mathbf{n} \\
 &= \frac{1}{2Z_0 k_0} \text{Re} \left\{ \begin{pmatrix} E_x \\ E_y \\ E_z \end{pmatrix} \times \left(\frac{1}{\hat{\mu}} \begin{pmatrix} k_y E_z - \hat{k}_z E_y \\ -(k_x E_z - \hat{k}_z E_x) \\ k_x E_y - k_y E_x \end{pmatrix} \right)^* \right\} \cdot \mathbf{n} \\
 &= \frac{1}{2Z_0 k_0} \text{Re} \left\{ \begin{pmatrix} E_x \\ 0 \\ E_z \end{pmatrix} \times \left(\frac{1}{\hat{\mu}} \begin{pmatrix} k_y E_z \\ \hat{k}_z E_x - k_x E_z \\ -k_y E_x \end{pmatrix} \right)^* \right\} \cdot \mathbf{n} \\
 &= \frac{1}{2Z_0 k_0} \text{Re} \left\{ E_x \left(\frac{(\hat{k}_z E_x - k_x E_z)}{\hat{\mu}} \right)^* \right\} \\
 &= \frac{1}{2Z_0 k_0} \text{Re} \left\{ E_x \left(\frac{1}{\hat{\mu}} \left(\hat{k}_z E_x + \frac{k_x^2 E_x}{\hat{k}_z} \right) \right)^* \right\} \\
 &= \frac{1}{2Z_0 k_0} \text{Re} \left\{ E_x \left(k_x^2 + (\hat{k}_z^*)^2 \right) \frac{E_x^*}{\hat{\mu}^* \hat{k}_z^*} \right\} \\
 &= \frac{k_0}{2Z_0} E_x E_x^* \text{Re} \left\{ \frac{(\hat{n}^*)^2}{\hat{\mu}^* \hat{k}_z^*} \right\}
 \end{aligned}$$

with $\mathbf{n} = (0 \ 0 \ 1)^T$, $\hat{k}_z = k_z + i\gamma_z$, a complex $\hat{\mu}$ and by setting $E_y = 0$. For perpendicular incidence, $\hat{k}_z = \hat{n}k_0$ and then

$$\frac{\partial P_{TM}(\mathbf{r}_\perp, 0)}{\partial A} = \frac{1}{2Z_0} (E_x E_x^*) \text{Re} \left\{ \frac{\hat{n}^*}{\hat{\mu}^*} \right\}$$

Hence, for equal amplitudes, the energy flux of a TE- and TM-polarized wave is equal at perpendicular propagation.

B.8. ENERGY FLUX OF A TM-POLARIZED WAVE IN HOMOGENEOUS MEDIUM 245

Figure B.1: *Fresnel coefficient of reflection (top) and transmission (bottom) for internal reflection with $n_e = 1 + i0$ and $n_t = 1.1 + i0$.*

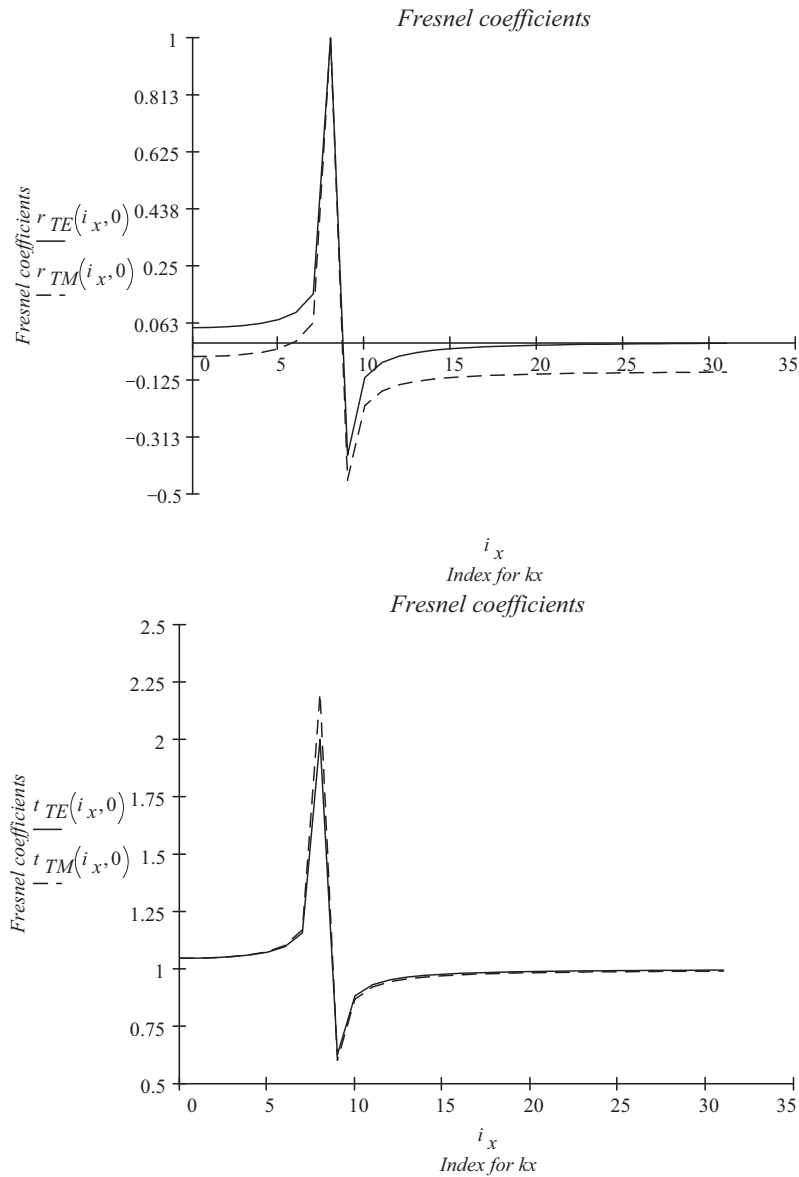
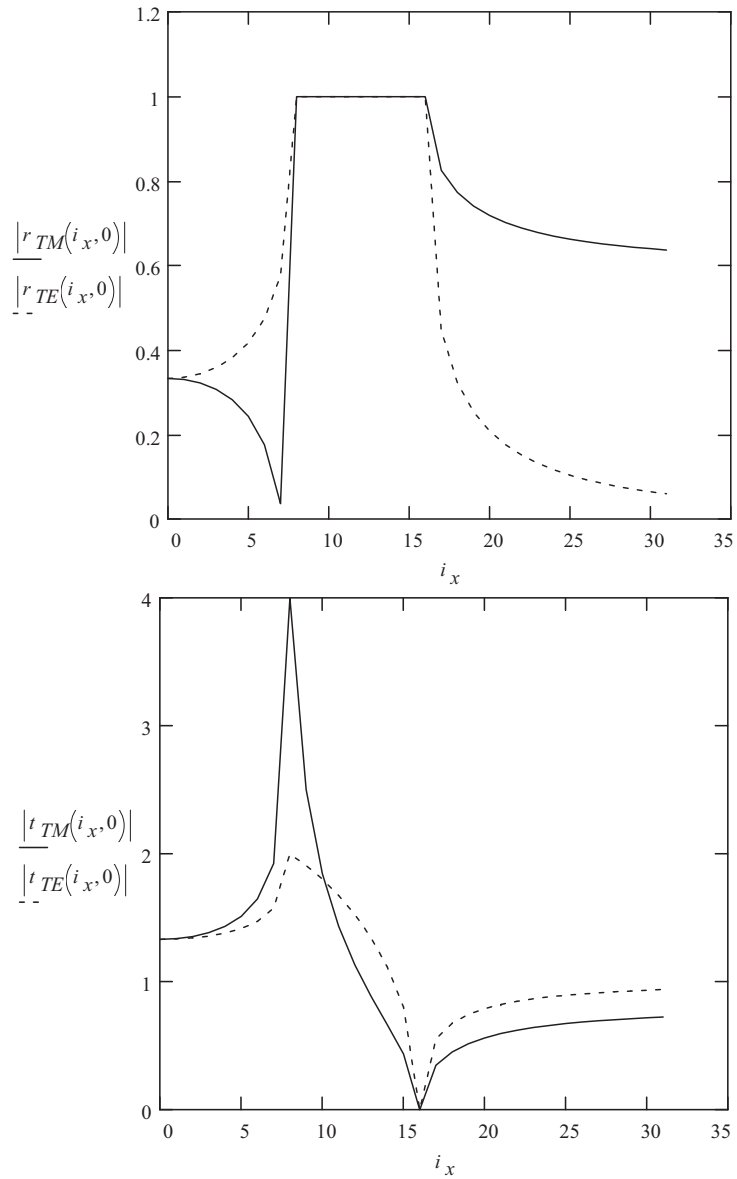


Figure B.2: *Absolute of the Fresnel coefficient of reflection (top) and transmission (bottom) for internal reflection with $n_e = 1 + i0$ and $n_t = 2 + i0$.*



B.8. ENERGY FLUX OF A TM-POLARIZED WAVE IN HOMOGENEOUS MEDIUM 247

Figure B.3: Fresnel coefficients, mode index i_x , angle of incidence τ and transmitted complex z-component of the propagation vector $\hat{k}_{z,t}$ for $i_y = 0$ (i.e. 2D-case) for $X = 8$ [μm], $n_x = 32$, $\lambda = 1$ [μm], $n_e = 1$ and $n_t = 1.1$.

$t_{TM}(i_x, 0)$	$t_{TE}(i_x, 0)$	$r_{TM}(i_x, 0)$	$r_{TE}(i_x, 0)$	i_x	$\tau(i_x, 0)$	$k_{zt}(i_x, 0)$
1.04762	1.04762	-0.04762	0.04762	0	0	6283185.30718
1.04837	1.04831	-0.04693	0.04831	1	7.181	6233904.66155
1.05078	1.05049	-0.04475	0.05049	2	14.478	6083668.01396
1.05531	1.0546	-0.04063	0.0546	3	22.024	5824668.67116
1.06306	1.06164	-0.03358	0.06164	4	30	5441398.0927
1.07659	1.07389	-0.02128	0.07389	5	38.682	4904809.95836
1.10297	1.0977	0.0027	0.0977	6	48.59	4155936.44103
1.17099	1.15859	0.06454	0.15859	7	61.045	3041834.00698
2.2	2	1	1	8	90	0
0.60371	0.6279	-0.45117	-0.3721	9	90 - 28.358i	3238279.58585i
0.87008	0.88369	-0.20902	-0.11631	10	90 - 39.714i	4712388.98038i
0.92277	0.93287	-0.16112	-0.06713	11	90 - 48.187i	5929626.09942i
0.94561	0.95405	-0.14036	-0.04595	12	90 - 55.143i	7024814.73104i
0.95829	0.96577	-0.12883	-0.03423	13	90 - 61.119i	8047936.31201i
0.96629	0.97316	-0.12155	-0.02684	14	90 - 66.395i	9023537.90423i
0.97177	0.97821	-0.11657	-0.02179	15	90 - 71.137i	9965585.4964i
0.97573	0.98186	-0.11297	-0.01814	16	90 - 75.456i	10882796.18541i
0.97872	0.9846	-0.11026	-0.0154	17	90 - 79.429i	11780972.45096i
0.98103	0.98673	-0.10815	-0.01327	18	90 - 83.112i	12664164.8567i
0.98287	0.98842	-0.10648	-0.01158	19	90 - 86.548i	13535306.85634i
0.98436	0.98979	-0.10513	-0.01021	20	90 - 89.771i	14396586.13779i
0.98559	0.99093	-0.10401	-0.00907	21	90 - 92.807i	15249673.88834i
0.98662	0.99187	-0.10307	-0.00813	22	90 - 95.679i	16095872.62402i
0.98749	0.99267	-0.10228	-0.00733	23	90 - 98.404i	16936214.98171i
0.98823	0.99335	-0.10161	-0.00665	24	90 - 100.998i	17771531.75263i
0.98887	0.99394	-0.10103	-0.00606	25	90 - 103.473i	18602499.94794i
0.98943	0.99445	-0.10052	-0.00555	26	90 - 105.839i	19429677.51512i
0.98991	0.9949	-0.10008	-0.0051	27	90 - 108.108i	20253528.90042i
0.99034	0.99529	-0.09969	-0.00471	28	90 - 110.286i	21074444.19312i
0.99072	0.99564	-0.09934	-0.00436	29	90 - 112.38i	21892753.68079i
0.99106	0.99595	-0.09904	-0.00405	30	90 - 114.399i	22708739.06576i
0.99136	0.99623	-0.09876	-0.00377	31	90 - 116.345i	23522642.21417i

Appendix C

Multithreaded bidirectional VWPM

The WPM performs an integration of locally deformed plane waves over each location \mathbf{r}_\perp and the entire range of spatial frequencies \mathbf{k}_\perp . Therefore, the time-complexity of the WPM and the VWPM is higher than the time-complexity of the BPM. The VWPM and the WPM is in $\mathcal{O}(n^2)$ in the two-dimensional and in $\mathcal{O}(n^4)$ in the three-dimensional case, with n is the number of samples.

C.1 Multithreaded wave propagation

The wave propagation scheme provides an intuitive and efficient way to distribute the calculation. The parallel algorithm utilizes the concept of

spatial parallelism which is introduced in the next section.

C.1.1 Spatial and spectral parallelism

A parallel algorithm identifies a set of parameters and associated memory which is suitable to be distributed over T processes. The parameters are selected such that a minimum of identical information needs to be calculated by each thread. The number of synchronization points (i.e. communication) should be small in order to take the most benefit from the parallelization and avoid locking situations and communication overhead. The complexity of the code sequences for each thread should be balanced in order to ensure the fastest progress and avoid starving.

C.1.2 Spectral parallelism

In the *spectral parallelism* a set of transversal spatial frequencies \mathbf{k}_\perp is distributed over T threads or distributed processes according to

$$\begin{aligned}\mathbf{k}_\perp^{(t,x)} &\in \left\{ \mathbf{k}_\perp\left(t\frac{n_x}{T}, 0\right), \dots, \mathbf{k}_\perp\left(\left(t+1\right)\frac{n_x}{T} - 1, n_y - 1\right) \right\} \\ \mathbf{k}_\perp^{(t,y)} &\in \left\{ \mathbf{k}_\perp\left(0, t\frac{n_y}{T}\right), \dots, \mathbf{k}_\perp\left(n_x - 1, \left(t+1\right)\frac{n_y}{T} - 1\right) \right\} \\ \mathbf{k}_\perp^{(t,xy)} &\in \left\{ \mathbf{k}_\perp\left(t\frac{n_x}{T_x}, t\frac{n_y}{T_y}\right), \dots, \mathbf{k}_\perp\left(\left(t+1\right)\frac{n_x}{T_x} - 1, \left(t+1\right)\frac{n_y}{T_y} - 1\right) \right\}\end{aligned}$$

with $T_x T_y = T$ and $0 \leq t < T$ and n_x, n_y are the number of samples in the x and y axis. The first and second distribution of the spectral parallelism is one-dimensional, the third describes a two-dimensional parallelism. The

spectral parallelism is of interest in a parallel version of the BPM. The WPM and VWPM prefer the concept of spatial parallelism since each position in the aperture considers the entire spectrum.

C.1.3 Spatial parallelism

In the *spatial parallelism*, a set of transversal locations \mathbf{r}_\perp is distributed over T threads or distributed processes according to

$$\begin{aligned}\mathbf{r}_\perp^{(t,x)} &\in \left\{ \mathbf{r}_\perp\left(t\frac{n_x}{T}, 0\right), \dots, \mathbf{r}_\perp\left(\left(t+1\right)\frac{n_x}{T} - 1, n_y - 1\right) \right\} \\ \mathbf{r}_\perp^{(t,y)} &\in \left\{ \mathbf{r}_\perp\left(0, t\frac{n_y}{T}\right), \dots, \mathbf{r}_\perp\left(n_x - 1, \left(t+1\right)\frac{n_y}{T} - 1\right) \right\} \\ \mathbf{r}_\perp^{(t,xy)} &\in \left\{ \mathbf{r}_\perp\left(t\frac{n_x}{T_x}, t\frac{n_y}{T_y}\right), \dots, \mathbf{r}_\perp\left(\left(t+1\right)\frac{n_x}{T_x} - 1, \left(t+1\right)\frac{n_y}{T_y} - 1\right) \right\}\end{aligned}$$

with $T_x T_y = T$ and $0 \leq t < T$ and n_x, n_y are the number of samples in the x and y axis. The first and second distribution of the spectral parallelism is one-dimensional, the third describes a two-dimensional distribution which can be used to apply a useful clustering of the system to maximize homogeneous areas which are then computed with the faster PWD (eq. 3.10).

C.2 Algorithm

In the parallel algorithm of the VWPM, a main thread performs the Fourier transformation and distributes the system \mathcal{N} (chapter 3) to the worker threads prior to the processing of a layer. In case of a propagation through homogeneous medium in the incident and transmitted layer, the main thread

gathers the phase adjusted Fourier coefficients and then performs the inverse Fourier transformation according to equation 3.5.1. In inhomogeneous medium, the system is distributed according to the spatial parallelism and each thread performs the algorithm of the VWPM in chapter 3 and 5.

The system \mathcal{N} is identical to the system in chapter 3 and 5. Each layer j has a layer of incidence $j - 1$ and a layer of propagation j . In case of bidirectional propagation, all reflected waves $\mathbf{E}^-(\mathbf{r})$ at all interfaces are initialized to zero.

The incident wave is considered in front of and in direct contact with the boundary between layer $j - 1$ and j . The *first step* performs the Fourier transformation of the propagating $\mathbf{E}_{j-1}^{(2)}$ and reflected $\mathbf{E}_j^{(2)-}$ electric field according to

$$\mathbf{E}_{j-1}^{(2)}(x, y) = \begin{pmatrix} E_{x,j-1} \\ E_{y,j-1} \end{pmatrix} \xRightarrow{FFT} \begin{pmatrix} \tilde{E}_{x,j-1} \\ \tilde{E}_{y,j-1} \end{pmatrix} = \tilde{\mathbf{E}}_{j-1}^{(2)}(k_x, k_y)$$

and

$$\mathbf{E}_j^{(2)-}(x, y) = \begin{pmatrix} E_{x,j} \\ E_{y,j} \end{pmatrix} \xRightarrow{FFT} \begin{pmatrix} EX_j^-(k_x, k_y) \\ EY_j^-(k_x, k_y) \end{pmatrix} = \tilde{\mathbf{E}}_j^{(2)-}(k_x, k_y)$$

with $x = m\delta x$, $y = n\delta y$ and $k_x = p\delta k_x$, $k_y = q\delta k_y$. The layers $j - 1$ and j of the system \mathcal{N} are then accessed in shared memory by the worker threads and in a *second step* the space- and frequency-dependent transformation matrix of reflection $\mathbf{R}^{(t)}$ and transmission $\mathbf{M}^{(t)}$ is calculated **by each thread for the assigned locations** $\mathbf{r}_\perp^{(t)} = (x, y)^{(t)} = (m\delta x, n\delta y)^{(t)}$ and for the **entire range of spatial frequencies** $\mathbf{k}_\perp = (k_x, k_y) = (p\delta k_x, q\delta k_y)$. The reflected amplitudes in layer $j - 1$ and the transmitted amplitudes in layer

j are then derived by each child thread from the spectrum according to

$$\begin{pmatrix} WX_{j-1}^-(p, q, (m, n)^{(t)}) \\ WY_{j-1}^-(p, q, (m, n)^{(t)}) \end{pmatrix} := \left(\mathbf{R}^{(t)} \cdot \tilde{\mathbf{E}}_{j-1}^{(2)} \right) e^{+i\mathbf{k}_\perp \cdot \mathbf{r}_\perp}$$

and

$$\begin{pmatrix} EX_j^+(p, q, (m, n)^{(t)}) \\ EY_j^+(p, q, (m, n)^{(t)}) \end{pmatrix} := \mathbf{M}^{(t)} \cdot \tilde{\mathbf{E}}_{j-1}^{(2)}$$

The spatial derivatives $\epsilon_{j,x}$ and $\epsilon_{j,y}$ in $\mathbf{R}^{(t)}$ and $\mathbf{M}^{(t)}$ are derived from equation 3.33.

After the transfer at the interface with $\mathbf{M}^{(t)}$, the reflected two-dimensional spectrum in layer j , EX_j^- and EY_j^- is accumulated to the transmitted spectrum EX_j^+ and EY_j^+ and the two-dimensional plane wave components are then

$$\begin{pmatrix} WX_j^+(p, q, (m, n)^{(t)}) \\ WY_j^+(p, q, (m, n)^{(t)}) \end{pmatrix} = \left(\begin{pmatrix} EX_j^+ \\ EY_j^+ \end{pmatrix} + \begin{pmatrix} EX_j^- \\ EY_j^- \end{pmatrix} \right) e^{+i\mathbf{k}_\perp \cdot \mathbf{r}_\perp} \mathcal{P}^{(t)}$$

with the thread-specific (i.e. space-dependent) phase element

$$\begin{aligned} \mathcal{P}^{(t)} &:= \mathcal{P}(k_x, k_y, (x, y)^{(t)}) \\ &:= e^{i\delta z k_{z,j}} \\ &:= e^{i\delta z \sqrt{(n_j(x,y)k_0)^2 - ((k_x)^2 + (k_y)^2)}} \end{aligned}$$

With WX_j^+ and WY_j^+ , the electric field of a mode \mathbf{k}_\perp at a distance δz behind the interface at a location \mathbf{r}_\perp in the aperture is known. The z -component WZ_j^+ in layer j and for each spatial frequency is then obtained by each thread for the assigned locations from equation 3.16.

The propagated magnetic field vector of a spatial frequency is then derived

from the x - and y -component of the electric field according to

$$\begin{pmatrix} HX_j(p, q, (m, n)^{(t)}) \\ HY_j(p, q, (m, n)^{(t)}) \\ HZ_j(p, q, (m, n)^{(t)}) \end{pmatrix} := \mathbf{T}^{(t)} \cdot \begin{pmatrix} WX_j^{+(t)} \\ WY_j^{+(t)} \end{pmatrix}$$

The spatial three-dimensional electrical \mathbf{E}_j and magnetic \mathbf{H}_j field in layer j is then obtained by each thread from a summation over all frequencies

$$\mathbf{E}_j((x, y)^{(t)}) := \frac{1}{n_x n_y} \sum_p \sum_q \begin{pmatrix} WX_j^{+(t)} \\ WY_j^{+(t)} \\ WZ_j^{+(t)} \end{pmatrix}$$

$$\mathbf{H}_j((x, y)^{(t)}) := \frac{1}{n_x n_y} \sum_p \sum_q \begin{pmatrix} HX_j^{+(t)} \\ HY_j^{+(t)} \\ HZ_j^{+(t)} \end{pmatrix}$$

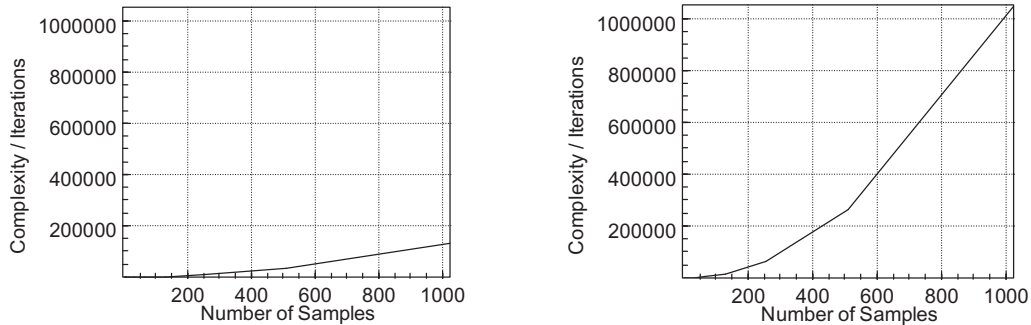
The reflected electric field in layer $j - 1$ is obtained from a parallel calculation of equation 5.33 and a summation of all space-dependent fields

$$\mathbf{E}_{j-1}^-((x, y)^{(t)}) := \frac{1}{n_x n_y} \sum_p \sum_q \begin{pmatrix} WX_{j-1}^{-(t)} \\ WY_{j-1}^{-(t)} \\ WZ_{j-1}^{-(t)} \end{pmatrix}$$

The propagated $\mathbf{E}_j((x, y)^{(t)})$ and reflected wave $\mathbf{E}_{j-1}^-((x, y)^{(t)})$ is then passed to the main thread. The algorithm then proceeds with the next layer $j + 1$.

Again, the $(j - 1)$ -th reflected field contributes to the processing of the j -th layer in the opposite direction. In the program code, the index $j - 1$ is replaced with $j - d$ with $d \in \{-1, 1\}$ indicates the direction of propagation. The algorithm iterates with an increasing order of layers for $d = 1$ and with a decreasing order of layers for $d = -1$. d is negated (i.e. $d = -d$) if $j = 1$ or $j = n_z - 1$.

Figure C.1: *Time-complexity of the multithreaded two-dimensional VWPM with eight threads (left) versus singlethreaded VWPM (right) for up to 1024 samples.*



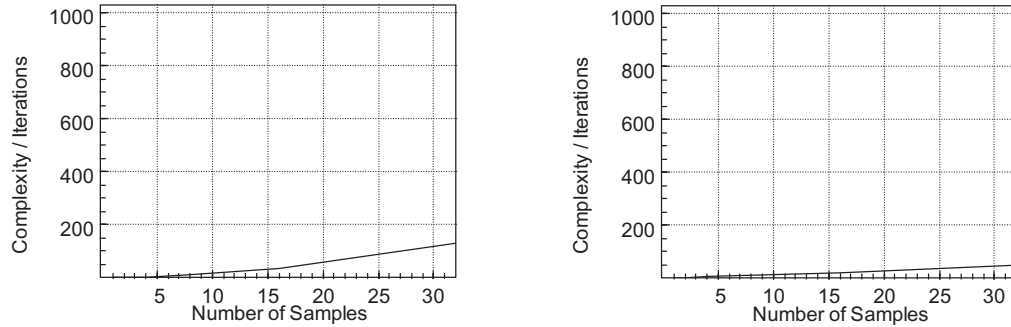
C.3 Time-Complexity

By using T worker threads, the complexity for the multithreaded VWPM is still in $\mathcal{O}(n^2)$ in the two-dimensional and in $\mathcal{O}(n^4)$ in the three-dimensional case but the computation time for the calculation of the electric fields at each location in the aperture \mathbf{r}_\perp divides by the number of child threads T and thereby scales linear with the number of threads.

The Fourier transformation at the beginning of each iteration is the only synchronization point with a sequential program code. The comparison of the time-complexity in iterations, based on the number of samples n , for the multithreaded and singlethreaded algorithm is shown in figure C.1.

In figure C.2, the comparison to the VBPM from chapter 4 shows that the split step propagation scheme is still faster. This is reasonable because the logarithmic complexity of the Fast Fourier Transformation cannot be reached with a linear clustering of $n_x n_y$ samples.

Figure C.2: *Time-complexity of the multithreaded two-dimensional VWPM and eight threads (left) versus singlethreaded VBPM (right) for the simulation of one iteration and up to 32 samples.*

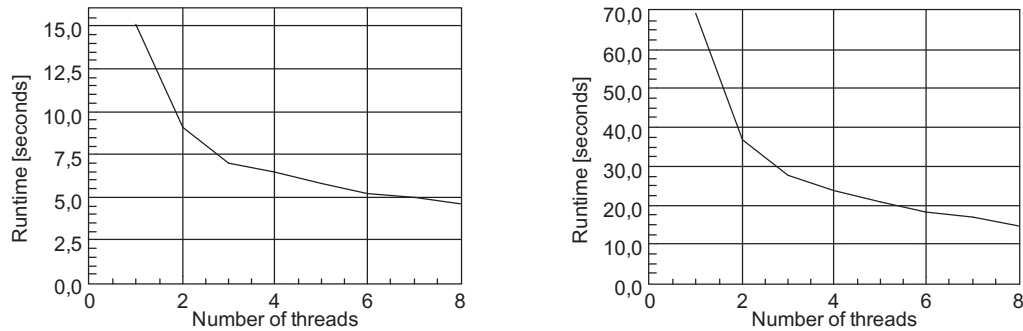


C.3.1 Selected scenarios

Figure C.3 compares the runtimes for the bidirectional three-dimensional simulation of the two-dimensional grating which is shown figure 3.6 in chapter 5 for two different algorithms. The runtimes in seconds over the number of threads for the multithreaded bidirectional VWPM which uses the PWD in homogeneous medium in the left subplot are compared to the results which are obtained from a multithreaded bidirectional VWPM in the right subplot. The combined use of the VWPM and the PWD yields a faster simulation since the two-dimensional grating scene contains large homogeneous areas.

In case of the oblique interfaces from chapter 5, less homogeneous area exist and the combined use of VWPM and PWD does not show such a significant improvement. A two-dimensional simulation in the x - and z -axis for one up to eight threads is compared in figure C.4. The runtime of the simulations with the PWD in homogeneous medium in the left subplot is

Figure C.3: Comparison of runtimes for a multithreaded simulation of a two-dimensional grating with 64^2 modes, utilizing the multithreaded VWPM with PWD in homogeneous medium (left) and the multithreaded VWPM (right).

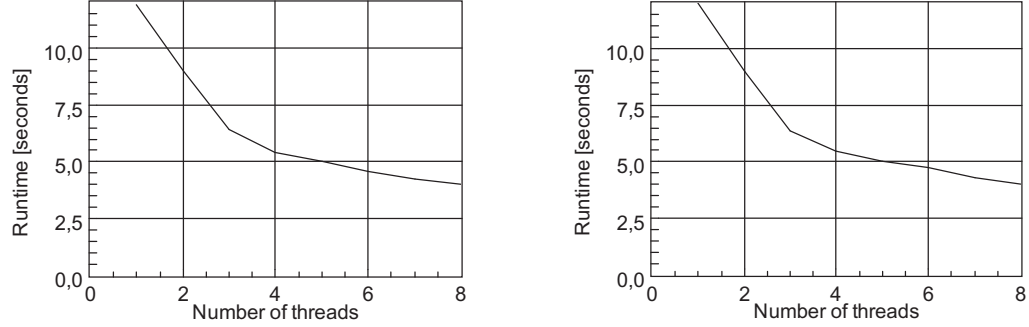


compared to the runtime of the multithreaded unidirectional VWPM without the PWD in the right subplot. The runtimes are almost identical due to the absence of large homogeneous areas.

C.4 Multithreaded split step propagation

The parallel algorithm of the wave propagation scheme distributes each layer over a number of T threads according to the *spatial parallelism*. In case of the split step propagation scheme, this approach is only applicable to the phase adjust operator \mathcal{S} , because \mathcal{S} operates in the spatial domain. The concept of spatial parallelism is not applicable to the spatial frequency domain and the use of the diffraction operator \mathcal{D} , because \mathcal{D} operates in the spatial frequency domain and on the average refractive index \bar{n} . Hence, no space-dependent information exists. The concept of

Figure C.4: Comparison of runtimes for a multithreaded unidirectional simulation of a slanted boundary with 512 modes, utilizing the PWS (left) and the VWPM (right) in homogeneous layers.



spectral parallelism is therefore recommended to distribute the calculation of the diffracted spectrum in a homogeneous medium as performed in the parallel version of the PWD (eq. 2.62), which is utilized in the simulations of the previous section. The phase adjustment in the second step of the split step scheme is performed in the spatial domain and the calculation is therefore distributed over a number of threads by using the spatial parallelism.

The twofold application of spatial and spectral parallelism generates two synchronization points in the algorithm - the forward Fourier transformation (\mathcal{F}) prior to the application of \mathcal{D} and the inverse Fourier transformation (\mathcal{F}^{-1}) prior to the application of \mathcal{S} . This reduces the benefit of the parallel approach for a low number of samples. The equation for the multithreaded BPM is then

$$E(\vec{r}_{\perp}; z + d_z) = \mathcal{S}(\mathbf{r}_{\perp}^{(t)}, d_z) \mathcal{F}^{-1} \left\{ \tilde{\mathcal{D}}(\nu_{\perp}^{(t)}, d_z) \mathcal{F} \{ E(\mathbf{r}_{\perp}; z) \} \right\}$$

using spatial ($\mathbf{r}_{\perp}^{(t)}$) and spectral ($\nu_{\perp}^{(t)}$) parallelism.

Index

- absorptance, 51
- absorption (VWPM), 178
- absorption coefficient, 229
- absorption length, 183
- accuracy, 68, 70, 72, 94, 104, 105, 108, 109, 111, 132
- algorithm
 - bidirectional VWPM, 101
 - evanescent modes, 78, 113
 - multithreaded VWPM, 251
 - VWPM, 63
- aliasing, 123
- amplitude vector, 26
- angular frequency, 29

- Beam Propagation Method, 18
- bidirectional VWPM, 96
 - iterations, 96
 - stabilization, 96
- boundary condition, 63
- BPM, 18
 - power flux, 154
- BPM and WPM, 16

- conduction band, 183
- conservation law, 135
- convolution theorem, 42
- coupled resonators, 94
- depletion region, 183
- detection of light, 183
- diffraction (BPM), 84
- diffraction order efficiency (DOE), 127
- dimensionless field strength, 182
- DOE, 127

- electric permittivity, 24
- energy flux, 35, 66, 240
 - TE-mode in homogeneous medium, 244
 - TM-mode in homogeneous medium, 245
- energy flux per time and through an area element, 35
- evanescent modes, 230
- evanescent wave, 45, 49, 73, 112
 - energy flux, 48, 233
 - Fresnel amplitude coefficients, 232

- transversal propagation, 47
- Fabry-Perot resonator, 90
- Fast Fourier methods, 10, 16
- FDTD, 12
- Fermi level, 184
- finesse, 92
- Finite Difference Time Domain, 12
- Fourier transformation, 38
- Fresnel amplitude coefficients, 43, 241
 - complex, 235
 - evanescent wave, 232
- Gaussian beam, 130
- Gibb's phenomenon, 154
- Goos Hähnchen Shift, 50
- Helmholtz equation, 26
- homogeneous medium, 24
- homogeneous scalar wave equation, 29
- impedance of vacuum, 182
- intensity, 33
- inverse Fourier transformation, 39
- irradiance, 33
- isotropic medium, 24
- Laplace operator, 26
- linear medium, 24
- local absorptance
 - algorithm, 183
 - local absorption, 35, 181
 - applications, 190
 - power ratio, 182
- magnetic permeability, 24
- magnetic vector, 66, 239
- Maxwell equations, 24
- microstructured geometries, 188
 - diffractive approach, 188, 189
 - physical optics approach, 188
- modified transmission coefficient, 62
- normalized sampling rate, 129
- Nyquist frequency, 122
- Nyquist index, 123
- OPL, 190
- optical path length, 190
- optical tunneling, 49
- phase adjustment (BPM), 85
- phase element, 58
 - evanescent wave, 76
- photo current, 183
- photo-electric effect, 183
- Plane Wave Decomposition, 41, 65
- pn-junction, 183
- polarization, 30
- power flux, 35, 136
 - at lateral index variations, 151

- at longitudinal index variations, 143
 - Gaussian beam, 141
 - in an aperture, 141
 - of a spectrum, 141
 - of a TE-polarized wave, 138
 - of a TM-polarized wave, 138
 - of polarized waves, 140
 - through area element, 182
- power ratio, 182
- Poynting vector, 34, 66, 136
- propagation, 62, 98
- propagation constant, 30, 46
- propagation vector, 29
- PWD, 41, 65
- quantum efficiency, 184
 - external, 184
 - internal, 184
- Ray Tracing, 21
- RCWA, 14
- RCWA and FDTD, 10
- recombination, 184
- reflectance, 51
- Rigorous Coupled Wave Analysis, 14
- sampling, 40, 119, 124
 - angle of propagation, 123
- scalar wave equation, 28
- scalar wave propagation method, 57
 - simulation methods, 8
 - single resonator, 89
 - Snell's law, 231
 - solar cell, 185
 - CIGS, 185, 187
 - efficiency, 186
 - flexible, 185
 - GaAs, 186
 - materials, 185
 - mono-crystalline, 186
 - multi-crystalline, 186
 - organic, 187
 - thin film, 185, 187
 - space derivative (discrete), 229
 - space vector, 29
 - speed of light, 26, 30, 227
 - split step propagation, 19, 55
 - Stabilization of the VWPM
 - clipping at the evanescent boundary, 167
 - clipping at the evanescent boundary in vacuum, 171
 - energy balanced clipping, 168
 - low pass filtering of the system, 162
 - sampling-induced clipping, 173
 - transfer of evanescent modes, 175
 - total internal reflection, 231

- transfer matrix of reflection, 100, 242
- transfer matrix of transmission, 62, 83, 98, 237
- transmittance, 51
- transversality, 32, 60, 100, 228
- valence band, 183
- VBPM, 82, 86
- Vector Beam Propagation Method, 86
- vector of unity
 - TE-polarization, 61, 100
 - TM-polarization, 61, 100
- vector wave equation, 26
- vector wave equation in a source-free medium, 26
- vectorial amplitude, 26
- Vectorial BPM, 82
- Vectorial Plane Wave Decomposition (VPWD), 86
- vectorial PWD, 65
- vectorial split step propagation, 81
- VPWD, 86
- VWPM, 53, 59
 - energy flux of evanescent waves, 79
 - instability in the power flux, 156
 - multithreaded, 249
 - propagation, 249
 - power flux, 154
 - stabilization of the power flux, 160
- wave equation
 - inhomogeneous, 27
- Wave Propagation Method, 20
- WPM, 20
 - power flux, 154